DOE/PC/80524--T15

DE89 015741

PIPE AND BEND EROSION BY PNEUMATIC TRANSPORT OF SOLIDS AT HIGH TEMPERATURE

FINAL REPORT

Contract DE-FG2-85PC80524

by

George E. Klinzing (P.I.) and Luis A. Borzone

Chemical/Petroleum Engineering Department

University of Pittsburgh, Pittsburgh, PA 15261

and

Wen-Ching Yang

Westinghouse Research and Development Center

1310 Beulah Road, Pittsburgh, PA 15235

June, 1989

ABSTRACT

The erosion of various components of a pneumatic transport line has been studied through basic experiments, commercial-scale test runs and computer simulation. The main objective was to study the effect of the operating variables on the erosion rates of refractory lined straight pipe sections and bends. Temperatures ranging from 22 to 830°C, gas velocities from 12.9 to 34 m/s and solid flow rates from 48 to 225 kg/h were tested in a High Temperature Pneumatic Transport Test Facility, in which refractory samples were placed forming a 0.0508 m. ID. (2 in.) vertical pipe. Four kinds of refractory concretes were used as targets. The erodent materials were river sand, coal slag and alumina. The effect of gas velocity and solids flow rate on the erosion rate was correlated in terms of power laws, while temperature effects proved to be more complex, since mechanical properties of both erodent and target materials change with temperature. Analysis of the samples revealed a selective erosion pattern in which the concrete matrix was preferentially eroded, followed by the release of the undercutted aggregates. The resulting topology modified the particle dynamics inside the pipe, as shown by pressure drop measurements.

The erosion of circular bends was evaluated using a computer model that combines computational particle dynamics and experimental data to predict the erosion pattern inside the bend. Experiments on the erosion of wedge samples, performed in the erosion test facility, and data on particle-wall collisions, obtained with the help of high-speed photographic tecniques, were the basic set of data used in the simulation. As an alternative to circular radius bends, an experimental study of wear and flow patterns in blinded T-bends was performed. The internal geometry in this kind of bends was determined by the solids deposition, and complex erosion patterns appeared as the operating variables were manipulated.

Descriptors

Bend Erosion

Blinded T-Bends

Castables

Erosion

High Temperature

Particle Impact

Pipe Erosion

Pneumatic Transport

Pressure Drop

Refractory Concrete

Simulation

TABLE OF CONTENTS

LIST OF FIGURES

LIST OF TABLES

NOMENCLATURE

A_E	Area exposed to erosion	(m^2)
A_p	Transversal area of a particle	(m^2)
C_D	Drag coefficient	(-)
d_p	Particle diameter	(m)
D_t	Pipe diameter	(m)
e	Specific erosion rate	($cm^3/cm^2/kg$)
e_p	Volume eroded per impact	(cm^3)
E	Erosion rate	($cm^3/cm^2/h$)
E_Y	Young's modulus	(GPa)
f_g	Gas friction factor	(-)
f_r	Kinetic friction factor	(-)
f_s	Solids friction factor	(-)
F_D	Drag force	(N)
H	Hardness	(GPa)
HMOR	Hot modulus of rupture	(MPa)
K_c	Toughness	(MPa $m^{1/2}$)
K_{ep}	Kinetic energy	(J)
m_p	Mass of a particle	(kg)
MOR	Modulus of rupture	(MPa)
r_p	Particle radius	(m)
Re_g	Gas Reynolds number	(-)

Re_p	Particle Reynolds number	(-)
Re_t	Terminal Reynolds number ($\rho_g U_t d_p/\mu$)	(-)
t	Time	(s), (h)
T	Temperature	(°C)
U_g	Superficial gas velocity	(m/s)
U_p	Particle velocity	(m/s)
U_s	Slip velocity	(m/s)
U_t	Terminal velocity	(m/s)
W_g	Gas flow rate	(kg/s)
W_s	Solids flow rate	(kg/s)

Greek Letters

ε	Gas voidage	(-)
ε_r	Coefficient of restitution	(-)
μ	Gas viscosity	(k/m-s)
κ	Pipe roughness	(m)
ρ_g	Gas density	(kg/m^3)
ρ_p	Particle density	(kg/m^3)

1.0 INTRODUCTION

The pneumatic conveying of solids at high temperatures is an operation of growing importance in the area of coal technology. Coal combustion and gasification units must handle solid-loaded streams at high temperatures, close to slagging conditions. Coal gasificatiom processes are in various stages of development. Processes like Lurgi, Hy-gas, Bi-gas, Synthane, CO_2 acceptor, Steam-Iron Hydrogen and Cogas, have all stages that operate in a temperature range from 500°C to 1000°C[1]*. Under these conditions, erosion and corrosion processes become major problems, affecting the continuous operation of such systems[2]. Ceramic materials, in virtue of their high refractoriness and low chemical reactivity, are often used as linings in conveying lines, valves and cyclones. The development of high purity and high strength monolithic refractories has given the designer greater flexibility to control these problems. High alumina castables are now being used as lining materials for vessels and transport lines of gasification units[1]. Silicon carbide castables are suggested as an alternate lining material.

An improved design requires not only a wise selection of lining materials, but also an assessment of the role played by the design parameters on the material's performance. Current research in solid particle erosion is centered on the fundamental understanding of such parameters, developing models for the erosion process and improving the methods of material's testing and selection of standards[3]. Still, the predictive capability of these models is poor and the proper scaling factors should be measured in commercial scale units under actual operating conditions.

The time scale for the erosion processes in commercial units is measured in terms of hours or days. The current methodology has been to accelerate the erosion process using

---

*Parenthetical references placed superior to the line of the text refer to the bibliography

extreme conditions. These tests, while useful to evaluate the relative erosion resistance of different materials, cannot be applied directly to predict wear in transport lines, since the erosion parameters are sensitive to the actual geometry and fluid dynamics. There is a number of studies [4,5] in commercial scale units, where the erosive wear is evaluated under actual conditions and geometries over a long period of time, ranging from a few hours, up to 30 days.

The objective of this work is to provide data and scaling factors for the erosion rates of refractory linings in commercial scale units operating at high temperatures. The work is organized into three main chapters: Chapter 2 covers the literature review on the erosion process of brittle materials and the most important properties of refractory concretes. Chapter 3 presents the experimental results and analysis on pipe erosion at high temperatures. Chapter 4 deals with the prediction of erosion rates in pipe bends and other components, followed by a discussion on the alternatives now available to minimize wear in bends.

2.0 EROSION OF REFRACTORY MATERIALS

The understanding of the complex process of erosion requires the background of several fields in the area of fluid mechanics and material science. The literature review presented here is concerned mainly with the erosion of brittle materials, in particular, of refractory concretes, followed by a revision of the most relevant properties of this type of materials. The literature review on particle dynamics is presented for specific cases in the next two chapters.

2.1 THE EROSION PROCESS

Erosion is a type of wear caused by the interaction between particles being carried by a fluid and a target. The amount of material removed in each impact is the result of multiple phenomena, beginning in the flow field and ending during the unload period after the impact. The most important factors involved in the erosion process are presented in Table 1. They can be classified into four main categories: impact parameters, erodent properties, target properties and environmental factors. Their diversity makes the erosion process particularly complex.

Impact parameters are determined by the fluid dynamics and geometry of the system. The drag force exerted by the gas on the particles determines the particle motion. Geometry plays a major role by generating the flow field, angles of impact and collision rates.

For a given impact velocity, particle size and shape determine the kinetic energy, impact radius, stress distribution and even mechanism of wear. Mechanical properties of the erodent become an important issue when they are comparable to the target properties, particularly in high temperature environments, where significant variations in material's strength occur.

Table 1. Factors involved in erosion.

1. Impact Parameters
   - Particle velocity
   - Impingment angle
   - Collision rate
2. Particle Properties
   - Size and shape
   - Density
   - Hardness
   - Friability
   - Strength
3. Target Properties
   - Microstructure
   - Surface hardness
   - Composition
   - Strength
4. Environmental Factors
   - Temperature
   - Carrier gas composition

The target properties will define the mechanism of erosion and will determine the amount of material to be removed under impact conditions. These properties can be very sensitive to the temperature and composition of the carrier gas. In reactive atmospheres there exist the possibility of gas-solid reactions that may enhance the erosion process.

2.1.1 Mechanisms of Erosion in Ceramics

Solid particle erosion is a discrete and accumulative process, and its study requires the understanding of single impact events. The response of a material to an impact is a complex function of the physical properties of the target and projectile. The specific responses, or impact damage, are manifested as crack evolution, void formation and coalescence, adiabatic shear zones, etc[6]. The basis to understand impact damage lies in the understanding of high strain elastic and inelastic phenomena. The dynamic stress fields and fracture characteristics are too complex to expect a fully analytical model of impact fracture. The approach is to apply simplified postulates with the result of a group of dimensionless functions relating the most important material and impact parameters. The prediction of the erosion rates starting from these models is not straightforward since mechanisms of material removal are often dependent on multiparticle effects.

A material under load can deform elastically (perfectly brittle materials) or elastically and plastically (ductile materials). Figure 1 shows the erosion rates of ductile and brittle materials as a function of the impingment angle[7]. This typical behavior can be explained in terms of the various mechanisms of wear, like cutting, chipping and deformation. Surface and subsurface characteristics play an important role. Brittle materials like glass suffer little erosion at low angles of impingment and maximum erosion at frontal impact. Aluminum shows a typically ductile behavior and has excellent erosion resistance at high angles of impact whilst its erosion is maximum at an angle of about 14°. Other materials, like 11% chromium steel present both types of behavior, having a maximum at about 20° with moderate erosion at 90°.

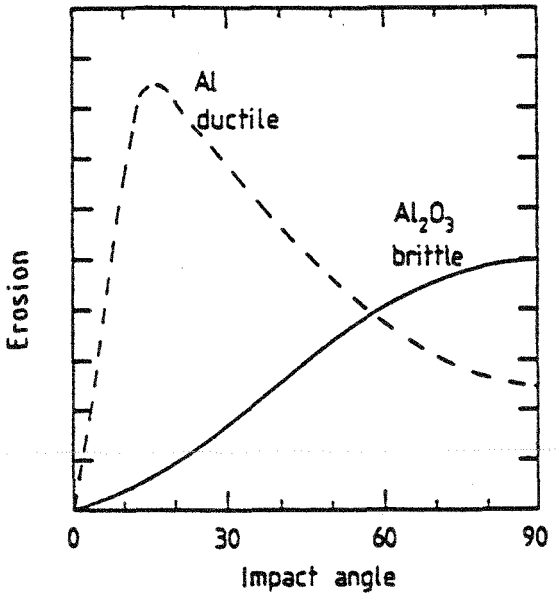

Figure 1. Ductile and brittle erosion

This work deals mainly with the erosion of ceramic materials. Although ceramic erosion is considered a brittle process, recent studies have shown that plastic deformation plays a crucial role in the chipping process. Two types of responses to the impact of hard

solid projectiles have been found in ceramics[8]: an elastic response regime and an elastic/plastic response regime.

In the elastic response regime the interaction between particle and target is purely elastic, resulting in ring (Hertzian) cracks around the indentation that initiate from preexisting flaws that lie just outside the area of contact between the particle and the target[9]. This process is well described by linear elastic fracture mechanic, being typical of large and blunt particles. The material removal is caused by the intersection of Hertzian-type cracks[10]. The volume removed per particle can be written as:

$$e_p \ \alpha \ r_p^a \, U_p^b \tag{2-1}$$

where a and b are constants determined from Weibull's statistical analysis.

In an elastic/plastic regime, a plastic zone is formed in the impacting area and three types of cracks are formed: median, radial and lateral. These cracks intersect or propagate to the surface causing the material removal.

The median/radial crack system model is based on a strictly dynamic contact between a spherical particle of radius r_p and the target. As contact forces increase above the level determined by the hardness of the material, plastic deformation occur beneath the impacting particle and a set of cracks forms normal to the target surface[9]. This set of cracks is typical of impact by sharp particles. The removal zone is assumed to be governed by the radial crack dimensions. This model predicts [11]:

$$e_p \ \alpha \ K_c^{-4/3} H^{-1/4} U_p^{19/6} r_p^{11/3} \rho_p^{1/4} \tag{2-2}$$

A second type of cracks, oriented primarily parallel to the target surface, generates upon impact by sharp particles. They are called the lateral crack system. Radial cracks are generated by the wedging action of the impacting particle, while lateral cracks are formed as a result of residual plastic deformation at the point of contact. The lateral crack system model was proposed by Evans et al.[12] assuming that a plastic deformation

zone is formed under the impacting area. Figure 2 shows the sequence of crack formation. Lateral cracks initiate during the unloading period from cracks that appear as a balance between irreversible residual forces (opening components) and the reversible elastic (closing) components. The contact area at load P_r leads to a crack of characteristic radius c at a depth h below the surface. The lateral cracks curve and propagate to the target surface resulting in a chip formation. The volume eroded per impact results in:

$$e_p \;\alpha\; [(E_Y/H)^{5/4} / (K_c H^{1/6})] K_{ep}^{7/6} \tag{2-3}$$

Another lateral crack system model by Wiederhorn and Lawn[13], which assumes that all the kinetic energy carried by the particle is dissipated in the irreversible plastic deformation process, and that the lateral crack size is proportional to the radial crack size, predicts the following erosion rate per impact:

$$e_p \;\alpha\; U_p^{22/9} r_p^{11/3} K_c^{-4/3} H^{1/9} \tag{2-4}$$

When a flux of particles is impinging on a surface many new complex aspects are added to the basic problem of erosion. Interparticle collisions within the incident stream, enhanced particle fragmentation, subsurface fatigue, wide range of angles of impact, surface shielding due to rebounding or embedded particles, are among the various possibilities[9].

2.1.2 Effect of Temperature

Studies of erosion at elevated temperatures have been carried out to a limited extent in recent years, however, no adequate theory giving the temperature dependence on erosion has emerged[9]. The erosion behavior of materials with temperature depends on the variation of mechanical properties with temperatures of both erodent and target materials. Wiederhorn and Roberts[14] have found that changes in the mechanisms of erosion are possible at high temperatures, in which ceramic materials begin to show a ductile behavior. This behavior has been documented for porcelain and glass. At high

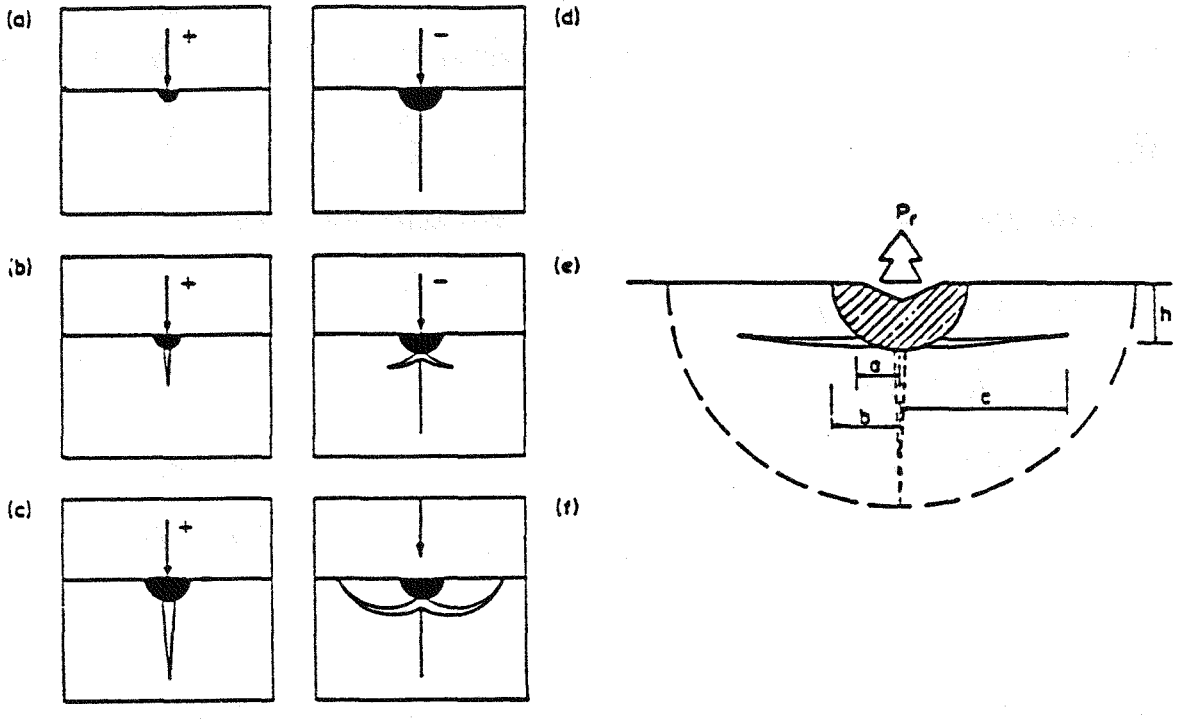

Figure 2. The lateral crack system

temperatures there is a significant enhancement of the erosion rate at low angles of impingment[9], suggesting that cutting mechanisms may become important.

Surface melting has been reported by several authors[9] as a result of localized energy release on impact. Hutchings[15] has reported an increase of 500°C in metals by particles impacting at 100(m/s). In ceramic materials, due to the low thermal conductivity, this local increase in temperature may be even more dramatic. Yust[16] has calculated and found evidence of local melting of alumina targets by particles impacting at 24 m/s, at ambient temperatures of 470 °C. The calculated maximum local temperature was of the order of 2700°C. This effect becomes more important as the particle velocity and temperature increase.

2.1.3 Effect of Particle Velocity

The effect of particle velocity is very much related to the dissipation of kinetic energy of the impacting particles in the target. The dependence of erosion rate on particle velocity has been measured for many materials over at least three orders of magnitude in velocity[9] , and it seems well correlated by a power law:

$$E \ \alpha \ U_p^m \tag{2-5}$$

The velocity exponent has been reported not to depend on the type of erodent material, but to be dependent on angle of attack and temperature. Its value apparently bears little relation to composition or microstructure of the material. Castable refractories, which are about 30% porous and have a multiphase structure exhibit the same range of velocity exponents as dense homogeneous ceramics. The erosion models discussed in Section 2.1.1 predict exponents in the range of 2 to 3.2. Finnie[17] has found that the exponents may vary from 2, for ductile materials, up to 6, for brittle materials. Arundel et al.[18] found experimentally exponents in the range of 3.3 (mild steel) to 8 (rubber). Morrison and Routbert [19] studied the erosion of mullite by sharp alumina particles, finding the exponent to be a function of the erodent's particle diameter (from 2.2 for 270μm particles up to 2.8 for 37 μm particles). The exponents also showed variations at small angles of impingment, becoming constant at angles greater than 30°.

2.1.4 Effect of Solids Concentration

The influence of particle concentration in the erosive stream has been examined in a few instances. As particle concentration increases, particle interference or shielding effects become important and the specific erosion rate, measured as mass or volume loss per unit mass of impinging particles decreases, as has been reported by several authors[9]. Mills and Mason[20] found that in the case of bend erosion the concentration effects on the specific erosion rates are well correlated by a power law:

$$e \propto (W_s/W_g)^n \tag{2-6}$$

where n varies between -0.16 and -0.38.

2.2 REFRACTORY CONCRETES

The erosion of refractory concretes presents distinctive characteristics due to their heterogeneous nature. The proper understanding of this process requires a knowledge of the structure and properties of each phase.

A refractory concrete, usually called "castable", is a highly porous multiphase material, often containing large aggregate grains embedded in a fine grained matrix. Castables allow a wide range of physical, chemical and electric properties assuring engineers unlimited design freedom. There are many advantages in the use of refractory concretes over conventional refractories, listed in Table 2.

Table 2. Advantages of refractory concretes

- Quick installation and low construction costs
- No brick joints to fall
- Minimized leaks of gas and heat
- Good thermal shock resistance
- High strength at room temperature
- Greater flexibility in design
- Low thermal conductivity
- No cut to fit work

Because of a wide variety of aggregates and cements used, the range of properties of available refractory concretes is large.

2.2.1 The Cement Phase

The cement phase usually consists of submicron size refractory particles, such as aluminum oxide, mixed with a binder material. The most common binder is calcium aluminate [21]. There are other chemicals such as sodium silicates and certain phosphates used as binders in specialized applications. The main active ingredient in all calcium aluminate cements is monocalcium aluminate $CaO\text{-}Al_2O_3$, or CA. Other cementitious constituents* such as $C_{12}A_7$, CA_2 may occur in some commercial cements, while silica and iron containing compounds such as C_2AS_5, C_2S, C_6A_2F, CF_2, etc, are present in less pure cements. Inert materials, such as Al_2O_3 or $CaTiO_3$ are often added to the cement. The properties of the binder are influenced by such physical factors as particle size, crystallite size and amount of glassy phase present.

Calcium aluminate cements can be divided into three classes:

1. Low purity cements: These products are manufactured from relatively high iron bauxites and limestones by fusion or sintering. They contain 5-10% of Fe_2O_3 or FeO and SiO_2 as the main impurities and can be used in refractory concretes with service limits up to about 2500°F.

2. Intermediate purity cements: These products are manufactured from low iron bauxite, mostly by sintering with limestone. They contain 5% silica but only 1-2 % iron oxide as the main impurities. Usage of this type of concrete is limited to a service limit of 2900°F.

3. High purity cements: These products are made from Bayer alumina and high purity limestones or hydrated lime. These cements have a service limit above 2900°F and are used in applications were very low iron content is required, as in coal gasification units.

---

*C=CaO, A=Al_2O_3, S=SiO_2, F=FeO, H=H_2O

2.2.2 Aggregate phase

In principle all refractory grains can be used as aggregates in refractory cements. In practice, most aggregates contain mainly alumina or silica in various forms. They range from crushed fire brick, containing 35-40% alumina to high purity sintered or fused alumina.

2.2.3 Casting and Curing

Casting is the most common method of installation of refractory concretes. Good installation practices must achieve a homogeneous casting while using the highest cement/water ratio. Formulation of the concrete should allow good flowability at low water content, showing a slight thixotropic behavior. The amount of water strongly modifies the strength and high temperature volume stability of the concrete[22]. The setting is achieved by hydration of the cement compounds[23]:

$$CA + H \xrightarrow{T < 21°C} CAH_{10}$$

$$\xrightarrow{T\ [21\text{-}35°C]} C_2AH_8 + AH_3$$

$$\xrightarrow{T > 35°C} C_2AH_6$$

These hydration reactions are exothermic. In Figure 3 are shown the mineral species present during the hydration and dehydration of CA[23]. The conventional practice has been to keep the concrete cool to improve the formation of hexagonal hydrates CAH_{10} and C_2AH_8. However, experiments with membrane curing[24] have shown that it is only necessary to maintain a high humidity to assure good properties.

During the initial heat up the hydraulic bond is destroyed at 200 - 350°C. For most cements this result in a significant decrease in strength, except for high purity cements, in which the decrease is less marked when the concrete is properly cured and heated.

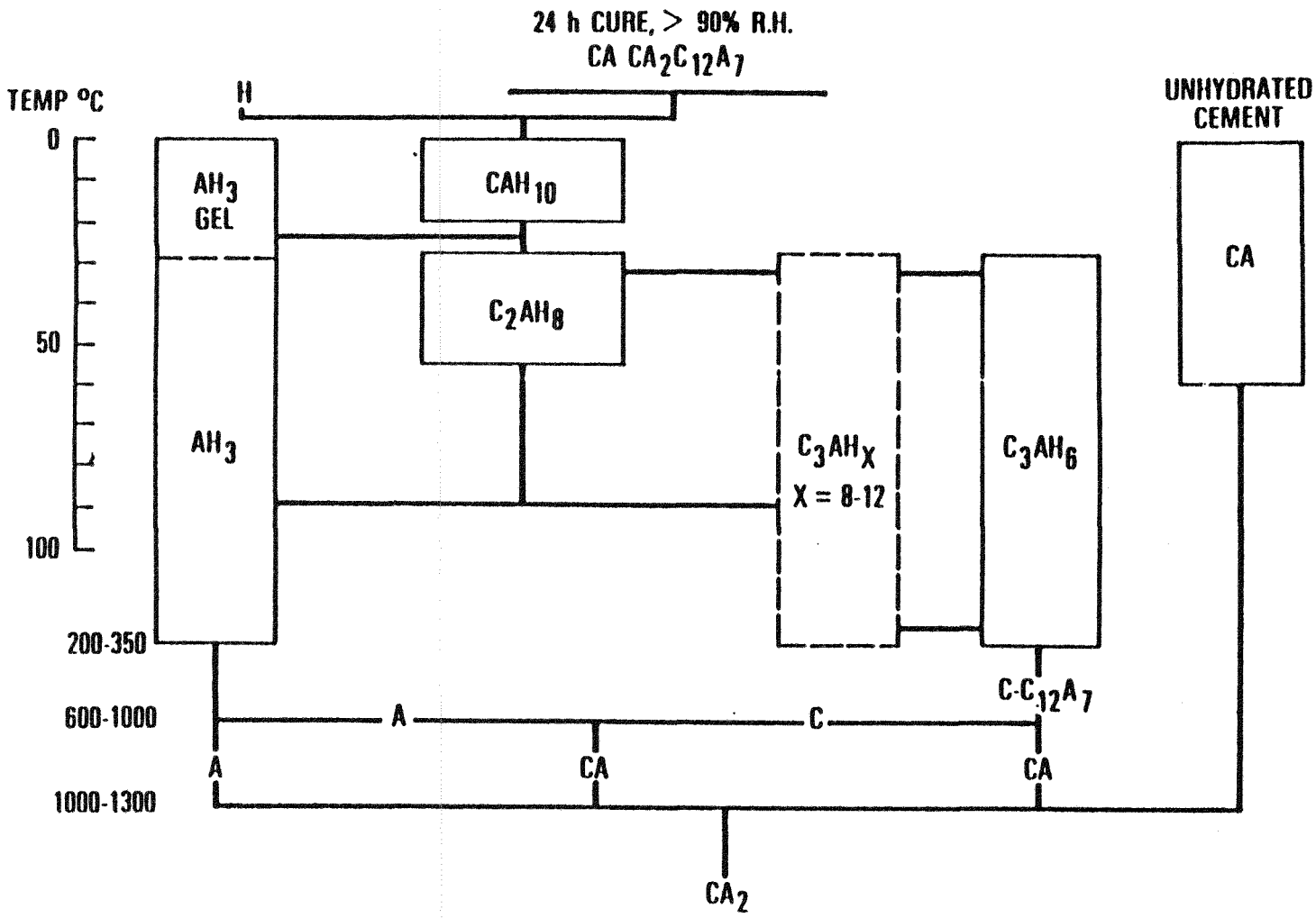

Figure 3. Hydration and dehydration of calcium aluminate cement

2.2.4 Physical Properties of Refractory Concretes

Physical and chemical properties are sensitive to the method of casting, curing and drying. It is necessary to keep in mind that all the properties of refractory concretes are likely to be time and temperaure dependent.

Porosity and permeability. Since the density of refractory concretes depends mainly on the type of aggregates, it varies widely, from 480 to 2800 kg/m^3. Generally, the porosity of the refractory concrete is high compared to most bricks, but its permeability is very low because of a very small average pore diameter. This is true up to the temperature at which the cement reacts with the aggregates to form a ceramic bond. Since permeability is low, care must be taken to heat the concrete slowly the first time to prevent cracking during the dehydration stage. Heating rates below 150°C/h are safe for shapes of 22x10x8 cm.[25]. Thermal shock resistance of refractory concretes is excellent, in agreement with their very fine pore distribution.

Thermal Conductivity. Thermal conductivities of refractory concretes are low compared with the equivalent brick because of their lower density. There is a significant drop in thermal conductivity after the first heat up due to dehydration of the binder[21].

Strength. Strength properties generally measured in refractory concretes are the crushing strength and modulus of rupture (MOR). Most measurements are made at room temperatures after heating to various temperatures, but the measurement of the hot modulus of rupture (HMOR) is becoming increasingly popular. The cold MOR generally decreases significantly during the dehydration of the cement, although to a much less extent when using a high purity cement. In this intermediate range the hydraulic bond has been destroyed while the ceramic bond is not fully developed. This drop in strength is not present to the same degree in the hot modulus of rupture. The greatest difference in MOR's occur at high temperatures, where a glassy phase is formed. Here, the cold MOR becomes very large, while the HMOR decreases rapidly with increasing viscosity of the glassy phase. In general, the modulus of rupture of a dense refractory concrete varies

from about 5 to 12 MPa after drying at 110°C[21]. In Figure 4 are shown typical HMOR curves for intermediate and high purity alumina castables[26].

The cold crushing strength of castables is usually three to five times that of the cold MOR. The hot compressive strength is usually not determined. The modulus of elasticity as a function of temperature correlates very well with the HMOR[27].

Corrosion resistance. A starting point in the design of a refractory lining is its compatibility with the process atmosphere. In gasification units this atmosphere consists of hydrogen, steam, carbon monoxide and dioxide, methane and other gases at high temperatures and pressures. Unless the lining is designed to stand this environment, the coupling of corrosion and erosion will shortly destroy it. Typical refractory corrosion by steam involves the formation of silicic acid from aluminosilicates. Experience in ammonia plants has shown that steam leaches SiO_2, (possibly as H_4SiO_4) from ceramic materials at temperatures as low as 800°C[1]. As SiO_2 is leached a weak skeletal structure is created and the concrete properties are degraded. The content of Fe_2O_3 in refractories exposed to CO atmospheres should be low to prevent the formation of carbon inside the refractory according to:

$$2CO \xrightleftharpoons{Fe} CO_2 + C$$

This reaction may cause spalling of the surface.

These two problems have been solved through the use of high purity alumina castables, with a very low silica and iron content. Both calcium aluminate and phosphate bonds have proved to be effective in gasification systems[28].

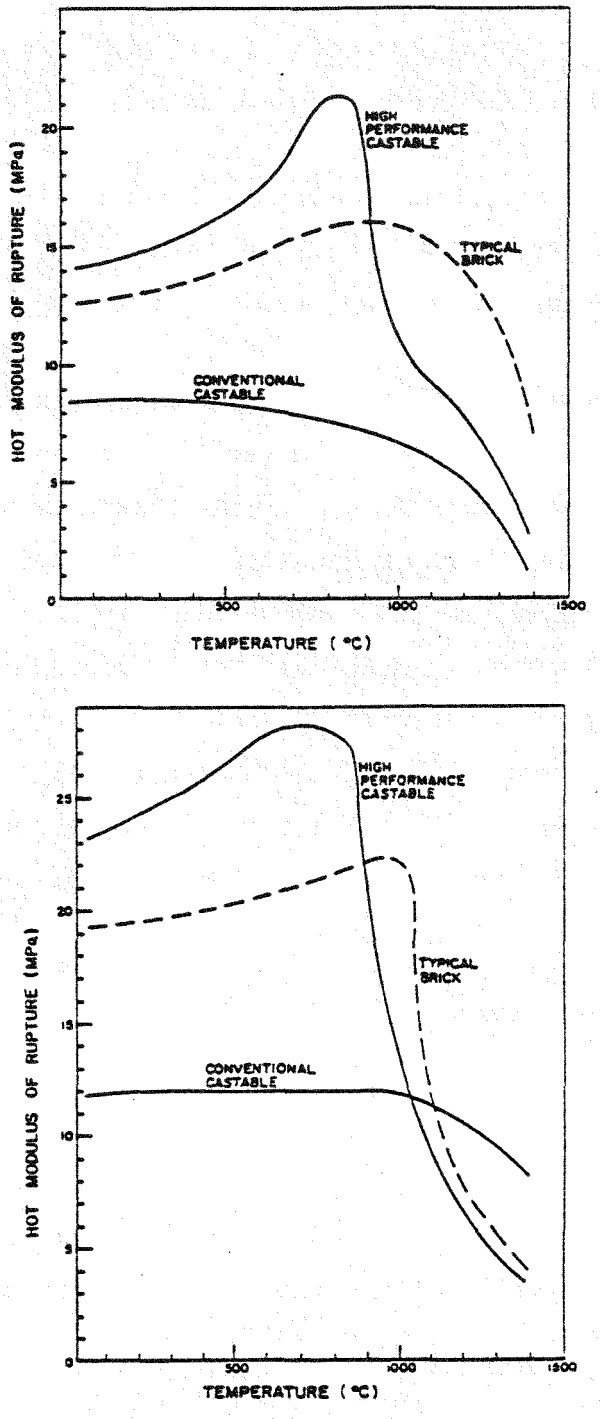

Figure 4. Effect of temperature on the hot modulus of rupture for: a) 75-85% alumina castables, b) 90-95% alumina castables

2.2.5 Erosion of Refractory Concretes

Because of the fine grain structure and porous nature, the cement phase is more susceptible to erosive wear than the aggregate phase. Therefore, the erosion resistance of the matrix plays a major role in the overall resistance of the concrete; the aggregates simply fall from the surface of the refractory as the cement bond is cut away by the impacting stream of particles. In Figure 5 is shown the erosion rate of a high alumina concrete compared with a metal and a dense ceramic material. Erosion rates in castables are generally much higher, but this difference is less marked as the development of high performance castables proceeds.

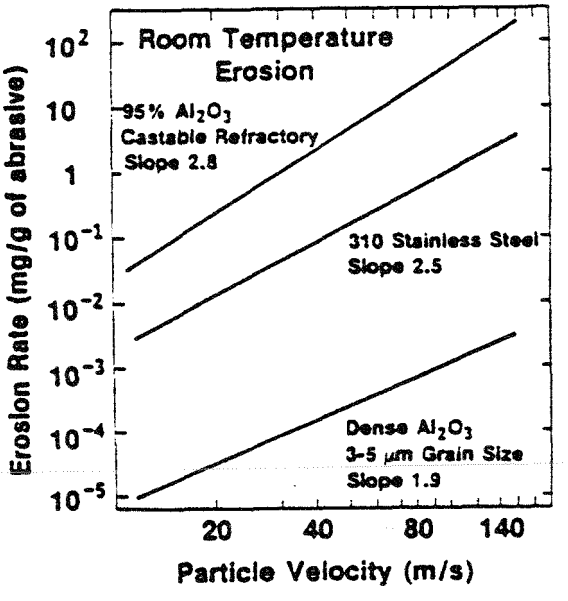

Figure 5. Erosion of engineering materials

Three stages can be observed in the erosion of refractory concretes (Figure 6).

During the early stage of wear the cement phase is attacked preferentially and the smallest aggregate particles are removed from the surface of the refractory (Stage I). As the erosion proceeds, medium size aggregates are removed and the largest aggregates are

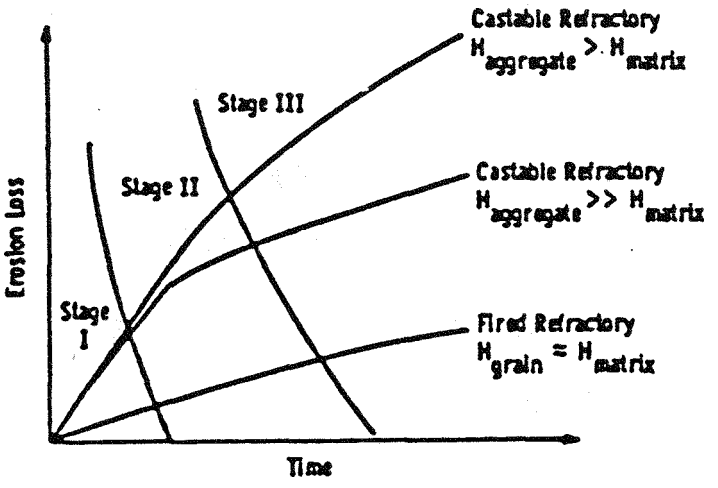

Figure 6. Stages in the erosion of refractory concretes

being undercutted (Stage 2). A final stage proceeds as large aggregates are cut loose from the surface by particle impacts, exposing additional matrix (Stage III)

The extent of undercutting depends on the shadowing of the matrix by the aggregates. Shadowing is a geometrical effect that has been modeled to give predictions of the dependence of the erosion rate on impact angle. Assuming that the aggregates can be approximated by spheres, the relative erosion rate of a refractory as a function of the impingment angle is then expressed by[3]:

$$E / E_{90} = (1 - R/sin\alpha) / (1 - R) \qquad (2\text{-}7)$$

where E_{90} is the erosion rate for a 90 degrees impingment, α is the impingment angle and R is the ratio of sphere diameter to interparticle spacing. The most important prediction of this model is that in the case of refractory concretes the erosion rate does not depend strongly on the impingment angle for a wide range of angles. This facilitates and reduces the amount of data required for design.

As the erodent's particle size becomes comparable to the interparticle spacing of the aggregates, the extent of undercutting rapidly decreases and the impacts begin to be resisted by the aggregates. Crowley[29] has found differences of up to one order of magnitude in the erosion rates by 400 microns sand and 40 microns catalyst particles impacting on alumina concrete under the same conditions.

Micrographic studies of eroded samples of refractory concretes show a topology completely different from the one observed in dense ceramics. Chipping mechanisms are observed only in the aggregates, while the erosion of the cement occurs primarily by localized crushing and removal of the cement phase grains. A model developed by Bitter[30], based on elastic/plastic modeling gives the following amount of material removed per impact:

$$e_p \ \alpha \ 1/2\, m_p[U_p \sin\alpha - U_{pel}]^2 / [\sigma^2/E_Y] \qquad (2\text{-}8)$$

where U_{pel} is the particle velocity at which the elastic limit is just reached during the collision. If U_{pel} is small compared to the particle velocity, Equation 2-8 becomes the ratio of the kinetic energy to the elastic energy at the fracture, a conclusion reached by Vojnovich et al.[31] in an independent work.

Although the authors have confirmed the role played by the strength (σ), measured as the crushing strength, and modulus of elasticity, this equation fails to predict the correct exponent for the particle velocity which, for refractory concretes, has been found to be in the range of 2 to 4. The importance of cement strength to the erosion process has also been demonstrated on castable refractories that have been exposed to hydrothermal treatments[32].

3.0 PIPE EROSION

The erosion of straight pipe sections of pneumatic transport units is not usually regarded as a serious problem [33]. However, there are some cases in which pipeline wear becomes important, such as in the handling of extremely abrasive materials, as occurs in pneumatic waste rock backfill[34], or when the capital cost of pipelines is very important, as in long distance conveying. Another situation of enhanced wear occurs in refractory lined transport lines of gasification and combustion units, as shown by Yang[5], who studied the erosion rates by dead burned dolomite on different types of refractory materials.

At this point the modeling of the erosion rates in straight pipes is limited by the difficulty to predict the erosion parameters inside the pipe: collision rates, impact velocities and angles of impingment. These parameters can be solved in theory through flow modeling. However, present models for the flow of solid particles in gases are only good to predict average quantities, but do not represent accurately the behavior of individual particles in the flow or answer questions about the interaction between particles[35]. The situation of pneumatic conveying is different to other types of two-phase flow, since particle-wall collisions play an important role. The collisions reduce the kinetic energy of the particles, which are then reaccelerated by the drag forces, with the result of a loss of pressure energy.

There have been many attempts to simulate the motion of single particles on pipes[36]. The major problem in this type of simulation is to find a suitable mechanism to avoid particles to slide, in the horizontal case, or go straight, in the vertical case. In horizontal simulations this problem has been overcome by considering a slight roughness in the walls, or particle shapes different from spheres. More recently it has been introduced the "abnormal bouncing" model, based in the concept of virtual wall[37]. These concepts,

while useful to make the models work, do not provide physical explanations for the radial component of the particle velocity inside straight pipes.

There is a number of experimental studies on particle trajectories inside pipes. Scott[38] has found that the average radial particle velocity is proportional to the average axial particle velocity. Ottjes[39] came to the same conclusion using 3600 μm polypropylene particles in a 0.082 m (3 1/4 in.) pipe, showing that the ratio of radial to axial average velocities is constant. This constant was calculated as 0.03, which gives average impinging angles (or deviation from axial trajectory) of 1.8 degrees. Brauer[40] found this angle to be 2.2 degrees in the case of 400 μm steel spheres. This angle, or the ratio of average radial to axial velocities, was independent of pipe diameter and average axial particle velocity in the range of 22 to 77 m/s.

Still, the formulation of a mechanism or mechanisms to explain the radial diffusion of particles is not conclusive. The existence of aerodynamic forces cannot explain the trajectories observed in pipes[36], neither the effects of turbulence[40], which are important only in the case of hydraulic transport. Vaux et al.[41] performed a high speed cinematography study of particles moving in a vertical pipe and found that interparticle collisions played a significant role in generating radial components of particle trajectory. Their movies showed small particles colliding with big particles (which move slower in upward vertical flow), and rebounding at different angles from the axis of the pipe.

As far as erosion modelling is concerned, the knowledge of impact angles and impact velocities solves just half of the problem. Particle-wall collision rate is another important parameter to be considered. As the solids concentration increases shielding effects become important and the calculation of collision rates is not straightforward[41]. As the particle concentration increases, contact times become also important, particularly in the case of very rough surfaces.

3.1 EXPERIMENTAL METHOD

3.1.1 The High Temperature Erosion Test Facility

The test unit consists essentially of a main burner coupled to an insulated pneumatic transport system. The unit is designed to maintain the operating conditions required in the long duration tests. Figure 7 shows a diagram of the high temperature pneumatic transport test facility.

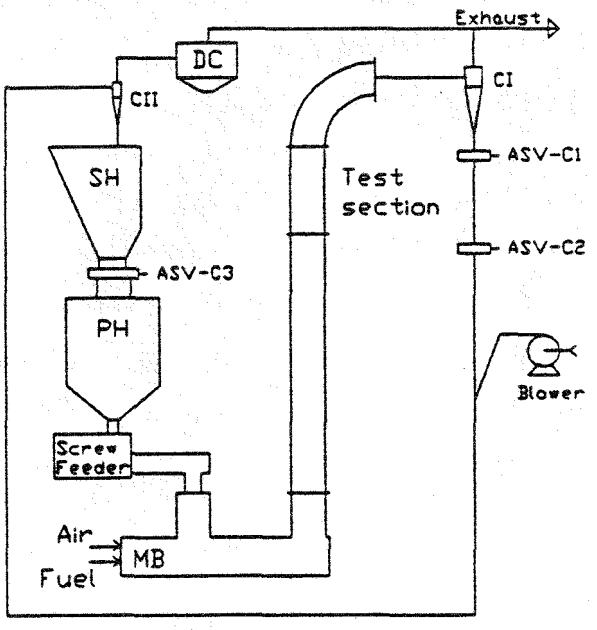

Figure 7. The erosion test facility

A combustible mixture of natural gas and air in excess is injected into the main burner (MB). The solids are fed through a T pipe placed immediately after the main burner. The gas/solids mixture passes through an acceleration section to the test section, where the samples are placed. The solids are recovered by a hot cyclone (CI) and stored temporarily in the water cooled 0.089 m (3 1/2 inch) pipe that connects valves ASV-C1

and ASV-C2. The solids are removed in a batch operation by manipulating these valves, falling into the blower line. The recycle line is designed to operate using room air. The solids being recycled are separated in a second cyclone (CII) and stored in the secondary hopper (SH). Valve ASV-C3 is opened at regular intervals to dump the solids into the primary hopper (PH). The dusty stream coming from cyclone II passes through a dust collector (DC) and is sent to the exhaust line coming from cyclone I.

The test facility has an adequate instrumentation to provide a safe and continuous operation as well as data acquisition. The test section allows any combination of thermocouples or pressure probes. Skin thermocouples monitor the wall temperatures of the steel shell of the burner and transport leg to check the integrity of the refractories. Details of the different components of the test facility are presented in Appendix A.

Particle velocities were measured using a technique in which the electric signals of two ring probes are cross-correlated. In the high temperature set-up these metallic probes, made of carbon steel, were embedded in a refractory concrete sample. The signals coming from the probes were displayed in an oscilloscope, photographed and digitized for cross-correlation. Direct data acquisition, using a PC was avoided since past experience indicates that a burn out of the data acquisition components may occur as the electrostatic level increases. The dimensions of the high temperature velocity meter are shown in Figure 8.

3.1.2 Refractory Samples

Five different types of refractory concretes were ordered from two companies: Kaotab-95, Kaocrete HS and Kaolite 2000HS from Babcock&Wilcox; and Fraxcast ES and Carbofrax 11LI from Carborundum. These concretes were prepared following the instructions of the manufacturer. Properties of these concretes and preparation instructions are included in Appendix B.

The erosion samples were made by pouring the concrete mixture into a cast. The cast

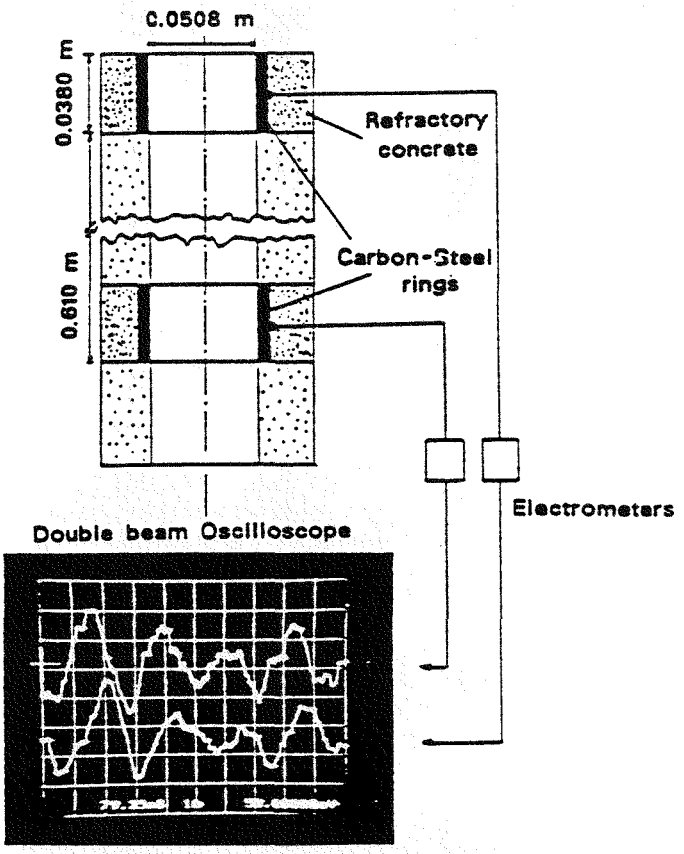

Figure 8. The high temperature particle velocity meter

cast consisted of an external 0.102 m. (4 in.) I.D. x 0.381 m. long Excelon pipe and an internal 0.0508 m. (2 in.) O.D. x 0.356 m. long PVC pipe. The two pieces were held in position by a refractory sample which serves as a base (Figure 9). The whole cast was water tight, with the internal surfaces lined with celluloid to facilitate the removal of the samples from the cast. The samples were left in the cast for 24 hours at room temperature, and then in a saturated ambient for another 24 hours. They were then cutted using a high speed diamond saw and dried at 110 °C for 48 hours.

The texture of the refractory concretes so prepared is shown in Figures 10a.b and 11a.b. These pictures correspond to magnified cross sections of the samples taken after the slag tests. Kaotab, a 95 % alumina concrete, bonded with a high purity calcium aluminate cement, presents a wide aggregate size distribution resulting in a closely

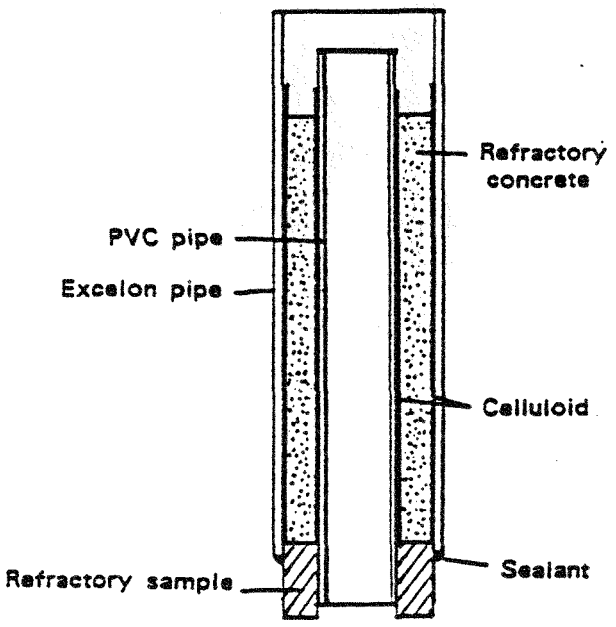

Figure 9. The cast

packed structure. This packing allows to use a minimum amount of cement in the concrete (Figure 10a). Fraxcast is an aluminosilica type of concrete, bonded with calcium aluminate plus other additives which give this material a very high strength at low and intermediate temperatures. Its structure contains both large and intermediate size aggregates, as shown in Figure 10b. Carbofrax is a silicon carbide concrete. The aggregates are predominantly silicon carbide crystals, bonded by a low iron calcium aluminate cement. Its structure, shown in Figure 11a, looks less compact than the previous two concretes, with large aggregates surrounded by a fine grained matrix. Kaocrete is an aluminosilica concrete, bonded with low purity calcium aluminate cement. This material is not abrasion resistant and in this work is used mainly to show the relation between erosion, geometry and flow patterns. Its structure consists of large and intermediate size aggregates, packed closely and held together by a weak matrix (Figure 11b). Kaolite 2000 is an insulating concrete and it was used with the same purpose than Kaocrete.

3.1.3 Erodent Materials

The erodent materials used in this work were river sand, coal slag and alumina. River sand was chosen since it is the standard material for erosion tests. Coal slag is a coal related material which allows a realistic study of the effect of temperature on the erosion rates. Alumina is a very stable material in the range of temperatures studied. Properties of these materials are presented in Appendix B.

All three materials have a similar average particle size, measured as 50 % below sieve, but they differ considerably in particle size distribution and shape. River sand, with a particle diameter of 240 microns, presents a narrow size distribution and a relatively rounded shape (Figure 12a). Its main mineral constituent is quartzite. Alumina particles also present a narrow size distribution, with a particle size of 400 microns and a shape more irregular than the river sand (Figure 12b). This material has been sintered at high temperatures and the main constituent is tabular α-alumina. Coal slag presents a wide size distribution and very irregular shapes (Figure 13a). Slag particles have extremely sharp edges and they are a combination of knife-like plates, rods and other irregular shapes. The variety of sizes is shown clearly in a cross section of an epoxide mixture of slag (Figure 13b).

3.1.4 The Erosion Tests

A total of 32 experimental test runs were performed to study the effect of gas velocity, solids flow rate and temperature on the erosion rates of straight pipe sections. A summary of test durations, operating conditions and measured erosion rates is presented in Appendix C. Ten tests were performed with river sand as erodent, three of which had to be repeated. The test run duration varied from 5.5 hours up to 36.8 hours, and the ranges of the operating variables varied from 12.9 to 26 m/s for the actual gas velocity, 50 to 159 Kg/h for the solids flow rate and 23 to 830°C for the temperature. The highest temperature was limited by the maximum burner temperature attainable under those

a)

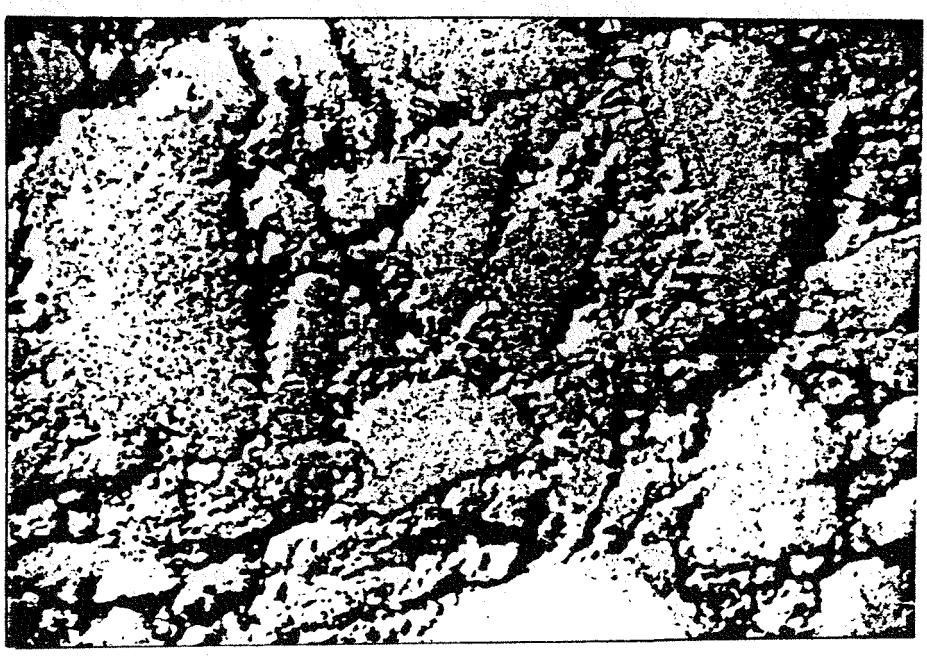

1000 µm

b)

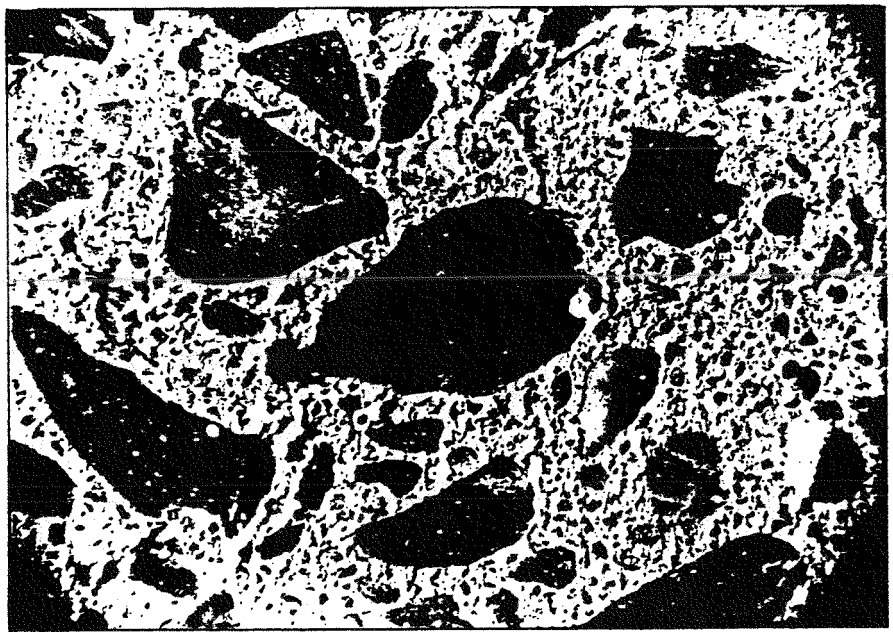

Figure 10. Photomacrographs of cross-sections showing the texture of: a) Kaotab sample, b) Fraxcast sample

a)

1000 µm

b)

Figure 11. Photomacrographs of cross-sections showing the texture of: a) Carbofrax sample, b) Kaocrete sample

a)

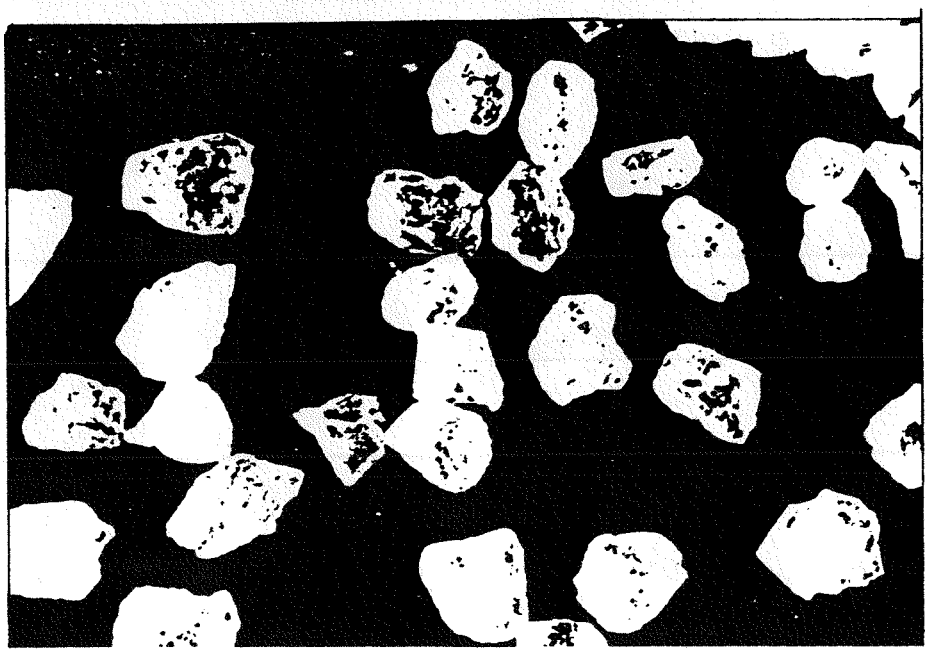

500 µm

b)

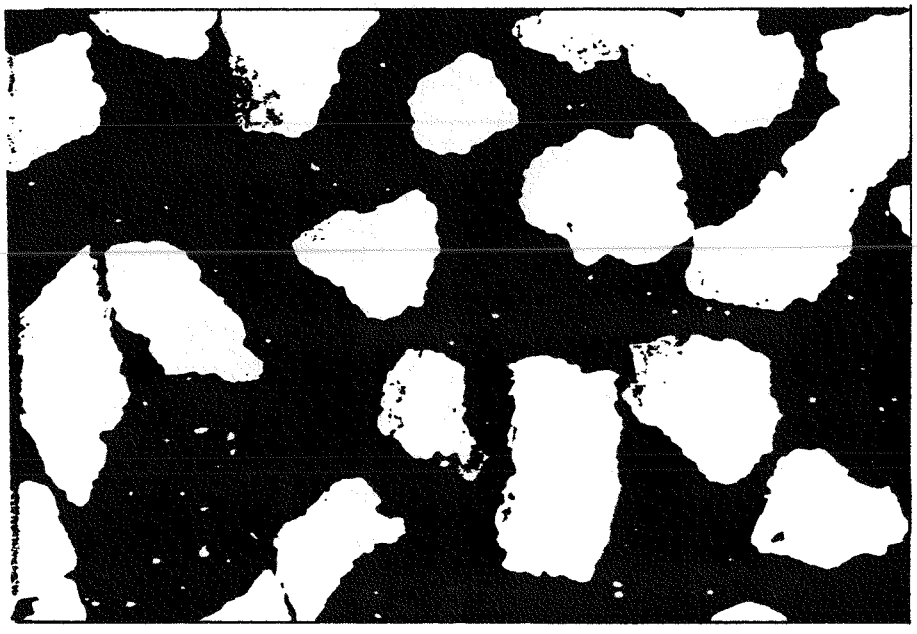

Figure 12. Photomacrographs of a) River sand particles, b) Alumina T-64 particles

a)

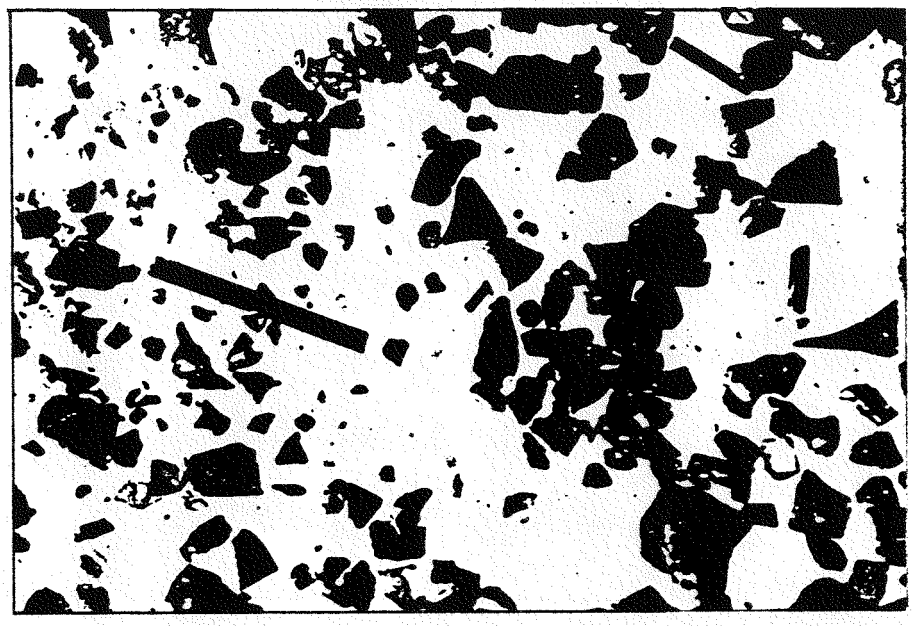

500 µm

b)

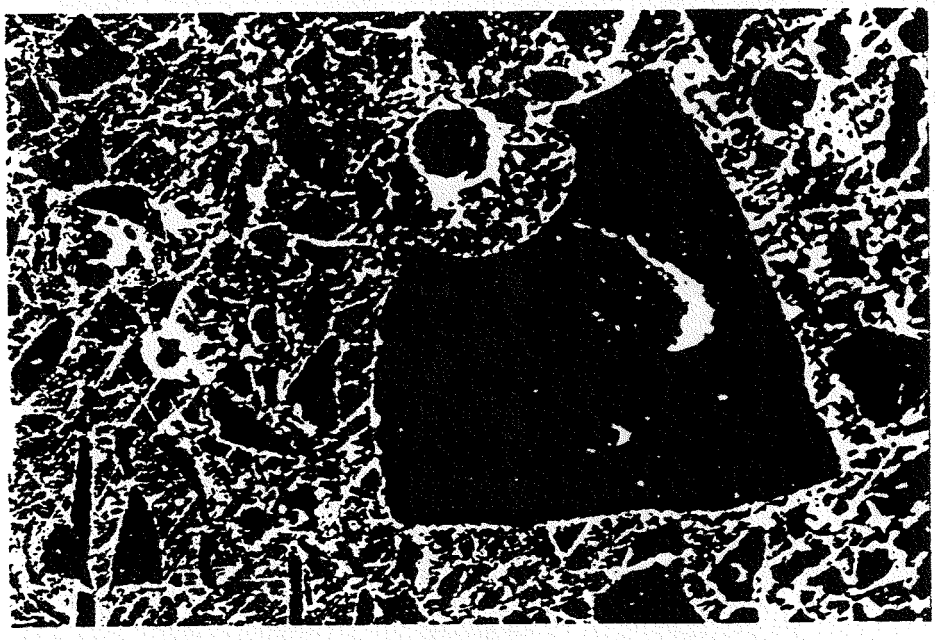

Figure 13. Photomacrographs of a) Coal slag particles.
b) Cross section of coal slag particles in epoxide

conditions. Curing conditions for the concrete samples in the sand test series were different to the other cases. Samples were heated up to 530°C for 18 hours and weighed. No solids were fed during this curing operation so that the first two tests fell into the unsteady state erosion period, where the matrix is eroded preferentially. These two tests had to be repeated along with test #8 (830°C). The erosion rates measured in sand test #8 were too large, as it was verified, and the reason was that water is still present in a crystal state at temperatures of 530°C (curing temperature), being released as the samples were heated up to 830°C.

For the coal slag tests the curing procedure was different, to prevent unsteady processes or dehydration. The samples were heated to 950°C for a total of 9.5 hours. The erosion data were consistent and no repetitions were required. Operating conditions ranges for the coal slag test series were 17.8 to 34.0 m/s for the gas velocity, 64 to 225 kg/h for the solids flow rate and 22 to 630°C for the temperature. The temperature range varied depending on the gas velocity. The lower temperature limit was given by the maximum volumetric air flow rate that the erosion test facility can handle. The upper limit was restricted by the burner temperature, which should not exceed 900°C to avoid slagging conditions and plugging of the transport line.

The test matrix for the alumina test runs included gas velocities from 17.8 to 34.0 m/s, solids flow rates from 48 to 172 kg/h and temperatures from 530 to 850°C. The test at the maximum temperature was repeated to assure consistency in the data.

3.2 MECHANISM OF EROSION

The erosion of the refractory samples begins with a transient period in which major changes in the surface topology occur. The samples coming out from the cast show a smooth surface, in which only the cement phase is present. As the erosion proceeds, the aggregates begin to appear and a steady state regime of erosion develops. The final surface topology, which persists during the test runs, depends on the microstructure of the concrete and, to a less degree, on the characteristics of the erodent material.

The sequence for the erosion of the high alumina concrete (Kaotab) is shown in Figures 14a,b and 15a. These figures correspond to the first series of test runs, using sand as erodent material. After 17.5 hours at 530°C (Sand test run #1) the matrix has been preferentially eroded and the aggregates begin to show up (Figure 14a). By the end of sand test run #2, with a total running time of 38.8 hours, the superficial matrix has been completely eroded and intermediate and large size aggregates are clearly visible (Figure 14b). Since the cement phase is receding, it is possible to observe some undercutting of the intermediate size alumina aggregates: large size aggregates are still well embedded in the matrix. The steady state morphology is shown in Figure 15a, where it can be seen a great deal of undercutting of the large aggregates. These aggregates were removed upon impact, since they were actually observed mixed with the sand particles. In summary, during the initial period the erosion proceeds from finer to coarser grain size. The steady state erosion rate is determined by the final topology, that is, the degree of undercutting of large size aggregates. The extent of this undercutting depends not only on the microstructure of the concrete, but also on the ability of the erodent particles to penetrate and remove the cement phase and intermediate size aggregates. In Figure 15b is shown the final topology of the Kaotab samples during the alumina test series. Although the undercutting of coarse aggregates is still important, it occurs to a less degree than in the case of sand erosion. In the case of alumina it is possible to observe extended regions of intermediate size aggregates completely embedded in the matrix, resisting further undercutting. This difference can be explained in terms of the difference of particle sizes of the erodent materials (240 μm for sand compared with 400 μm for alumina). The bigger alumina particles find more difficult to penetrate and reach the matrix. In the case of coal slag, the surface looks very similar to the case of sand erosion.

A quantitative analysis of surface morphology of the eroded samples is presented on Section 3.3.

a)

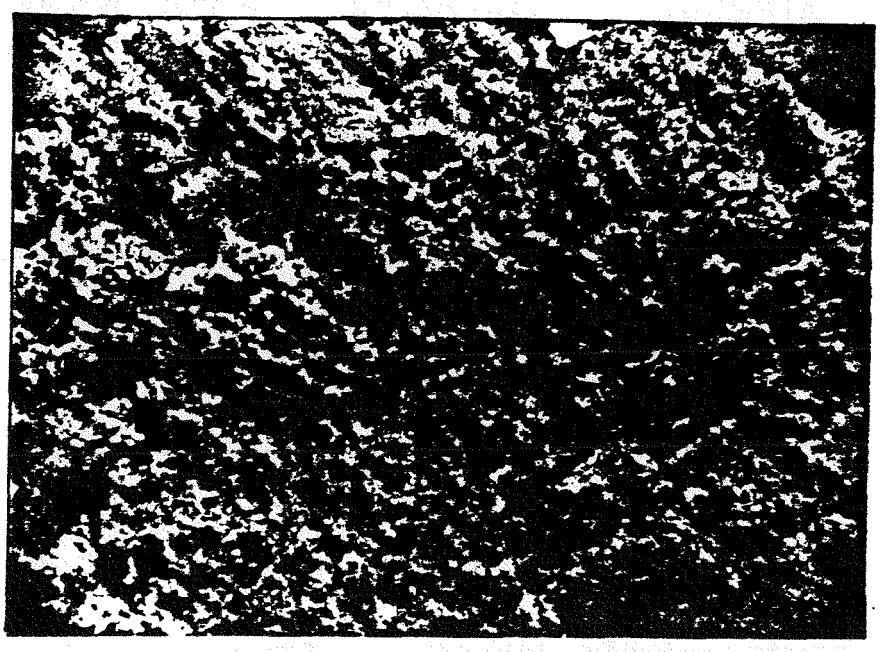

1000 μm

b)

Figure 14. Photomacrographs of the surface Kaotab samples eroded by sand. a) After exp. #1, b) After exp. #2

a)

1000 µm

b)

Figure 15. Photomacrographs of the steady state surface of Kaotab samples. a) Sand erosion. b) Alumina erosion

3.2.1 Effect of Temperature

The effect of temperature on the erosion rates was measured at constant gas velocities and solids flow rates. Although in the pneumatic transport literature the solids concentration is expressed as the solids/gas mass ratio, this last quantity is not constant when the temperature changes (at constant actual gas velocity). A fixed value for the solids flow rate assures a constant number of particles circulating in the test section.

In the sand test series the gas velocity was 17.8 m/s and the solids flow rate 50 kg/h. The erosion rates are plotted in Figure 16a, and compared to the results of coal slag tests performed under similar conditions. In the range from 23 to 530 °C the erosion rates changed very little. At the third temperature level (830°C) there is a significative increase in the erosion rates. In the case of the alumina tests, shown in Figure 16b, the low temperature range was not studied. The actual gas velocity in these series was 34 m/s and the solids flow rate 48 kg/h. Above 530°C, a steady increase of the erosion rates was also observed. This behavior is completely different to the one shown by the coal slag (Figure 16b), where the erosion rates sharply go down above 450 °C. This decrease cannot be attributed to changes in the target properties because, as it is shown by the erosion rates by the stable alumina, the target erosion resistance starts degrading above 530 °C. The erosion rates by coal slag were measured at three different gas velocities: 17.8, 26.0 and 34.0 m/s (Figure 17). The solids flow rate was kept at 64 kg/h. The widest range of temperatures was covered at the highest gas velocity. Initially, there is an increase of the erosion rates with temperature, followed by a sharp decrease starting at 450 °C. This is the point where the slag softens. The rate of increase of the erosion rates in the intermediate range (200-450 °C) is a function of the gas velocity.

3.2.2 Effect of Gas Velocity

The effect of gas velocity is shown in Figures 18, 19 and 20. The solids flow rates were kept constant: 50 kg/h for sand, 64 kg/h for coal slag and 48 kg/h for the alumina. In all cases, the erosion rate is well correlated by a power law:

$$E = k_1 U_g^n \tag{3-1}$$

were k_1 is a constant and n is the gas velocity exponent, whose value is listed in Table 3.

Table 3. The gas velocity exponent, n

Refractory	Sand	Slag			Alumina
	530°C	200°C	350°C	450°C	530°C
Fraxcast	2.6	2.5	2.9	2.9	2.5
Kaotab	3.5	3.4	3.2	3.2	3.4
Carbofrax	4.0	2.5	2.2	2.4	2.4
Kaocrete	2.5	-	-	-	-

This exponent seems to be independent of the type of erodent, with the exception of Carbofrax eroded by sand, which is high compared with the values for slag and alumina. This difference can be explained noticing that curing conditions were different in the sand test series, and that this particular concrete is very sensitive to prefiring conditions. In the case of coal slag, the exponent is not very much sensitive to temperature .

3.2.3 Effect of Solids Flow Rate

As in the case of gas velocity, the effect of solids flow rate is well correlated by a power law:

$$E = e\,W_s = k_2\,W_s^{1+m} \tag{3-2}$$

The specific erosion rates, e, are shown in Figures 21, 22 and 23. These erosion rates were measured at constant actual gas velocity, equal to 17.8 m/s, so that the results show the effect of solids concentration. The values for the exponent m are presented in Table 4.

Table 4. The solids flow rate exponent, m

Refractory	Sand 530°C	Slag 200°C	Alumina 530°C
Fraxcast	-0.43	-0.48	-0.57
Kaotab	(-0.09)	-0.36	-0.39
Carbofrax	-0.30	-0.90	-0.68
Kaocrete	-0.30	-	-

The value of this exponent seems to be a function of both type of target and erodent material.

A detailed discussion of the results is presented in the last section of this chapter.

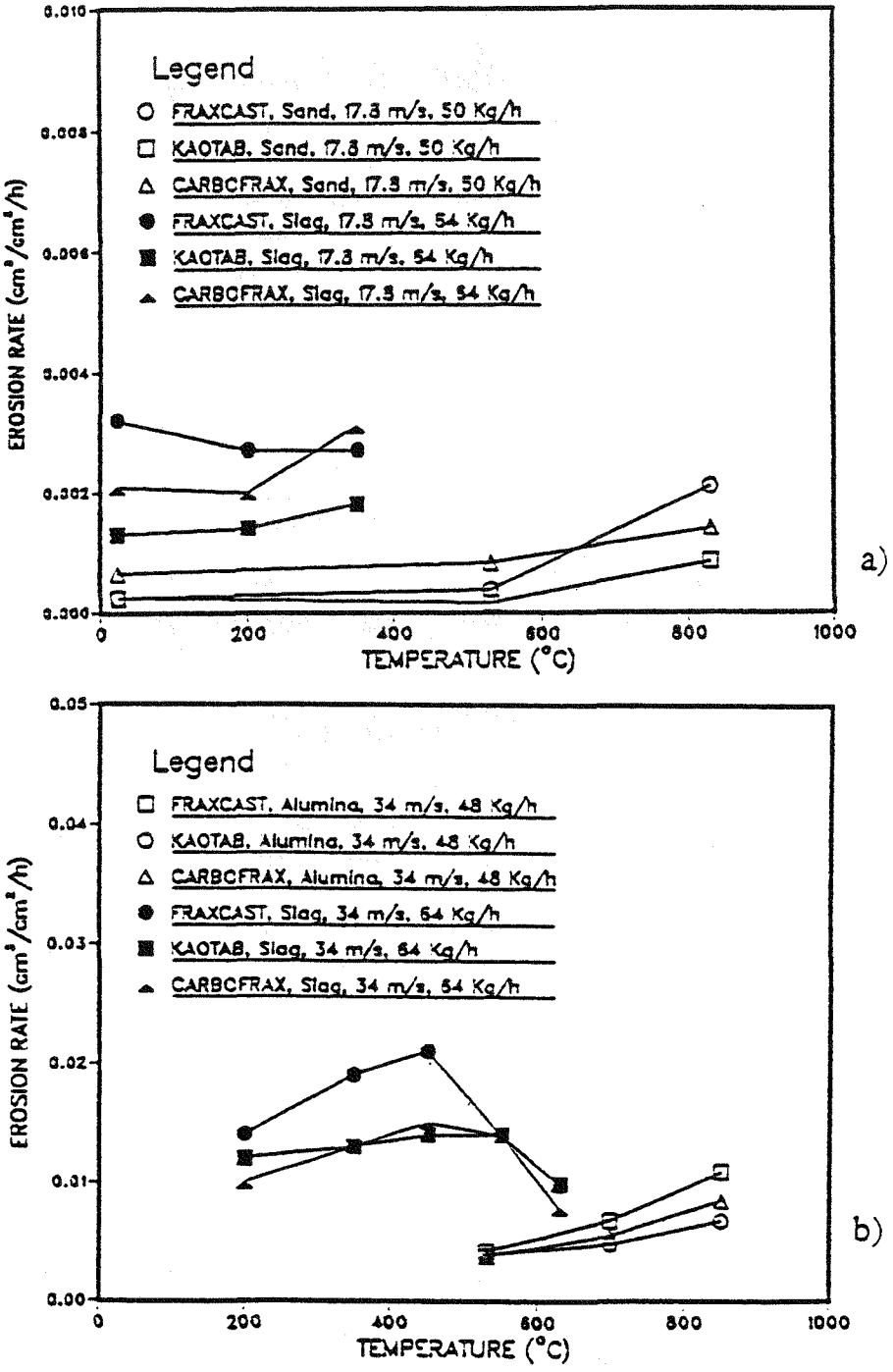

Figure 16. Effect of temperature on the erosion rate by a) River sand and coal slag, b) Alumina and coal slag

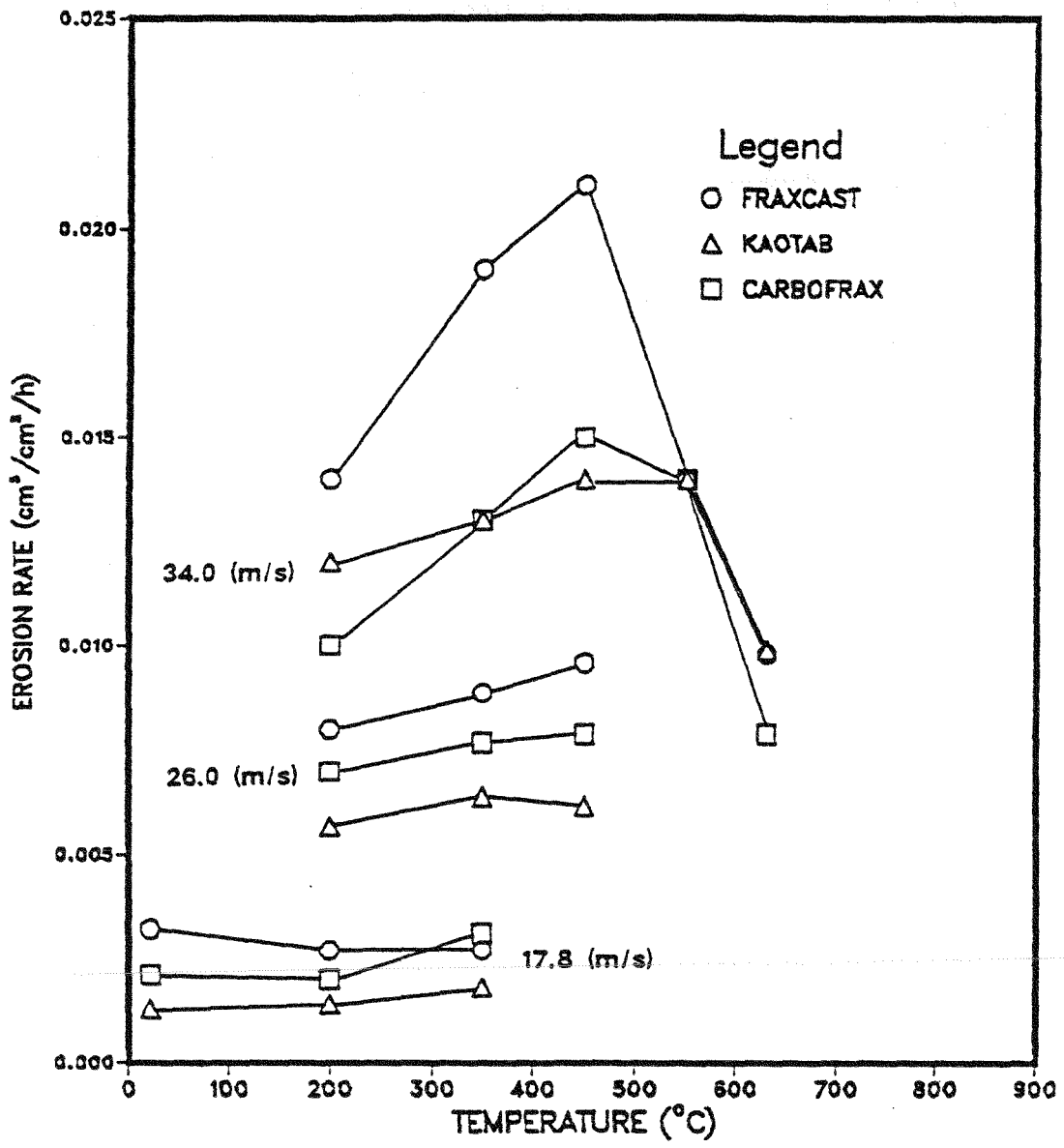

Figure 17. Effect of temperature on the erosion rate by slag

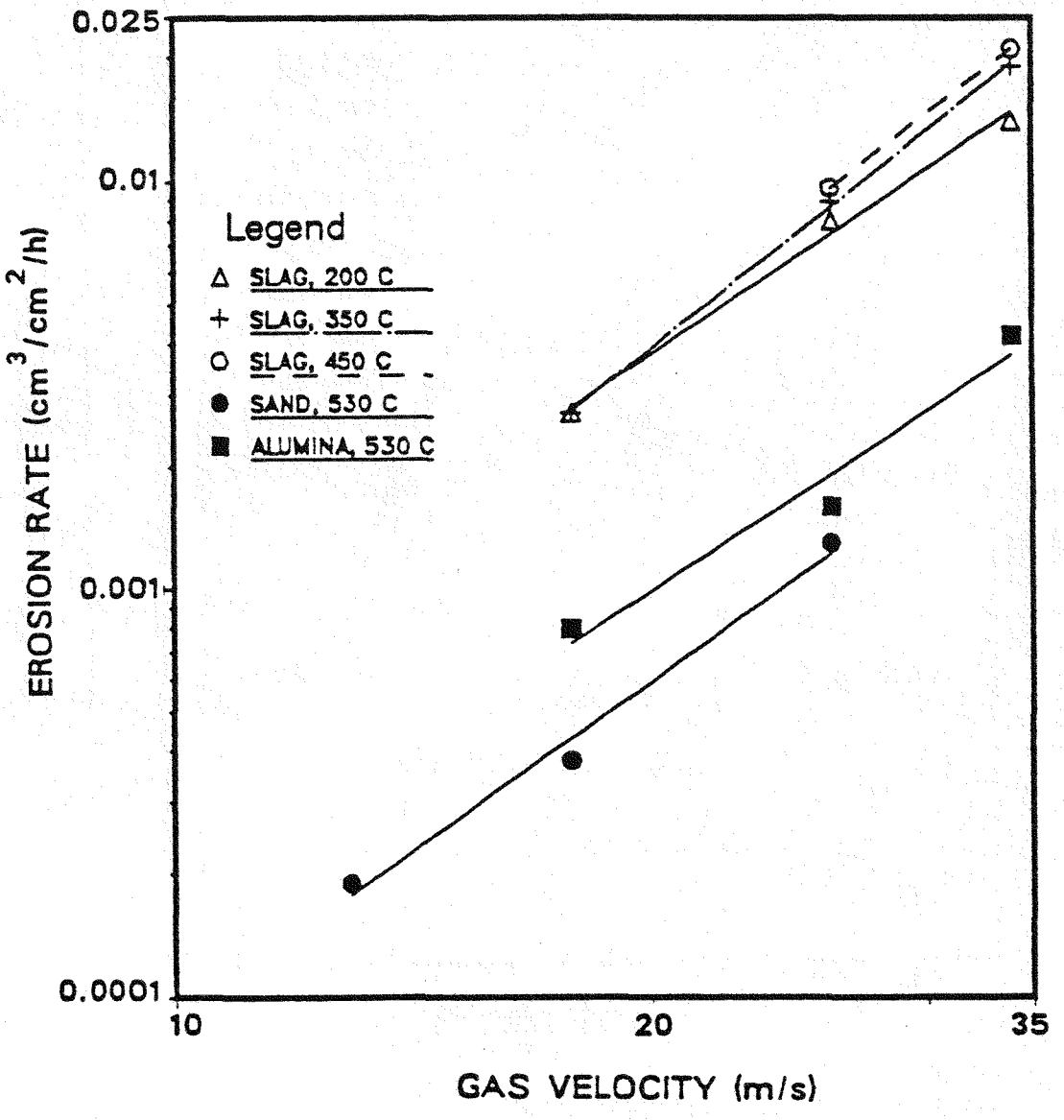

Figure 18. Effect of gas velocity on the erosion rate of Fraxcast concrete

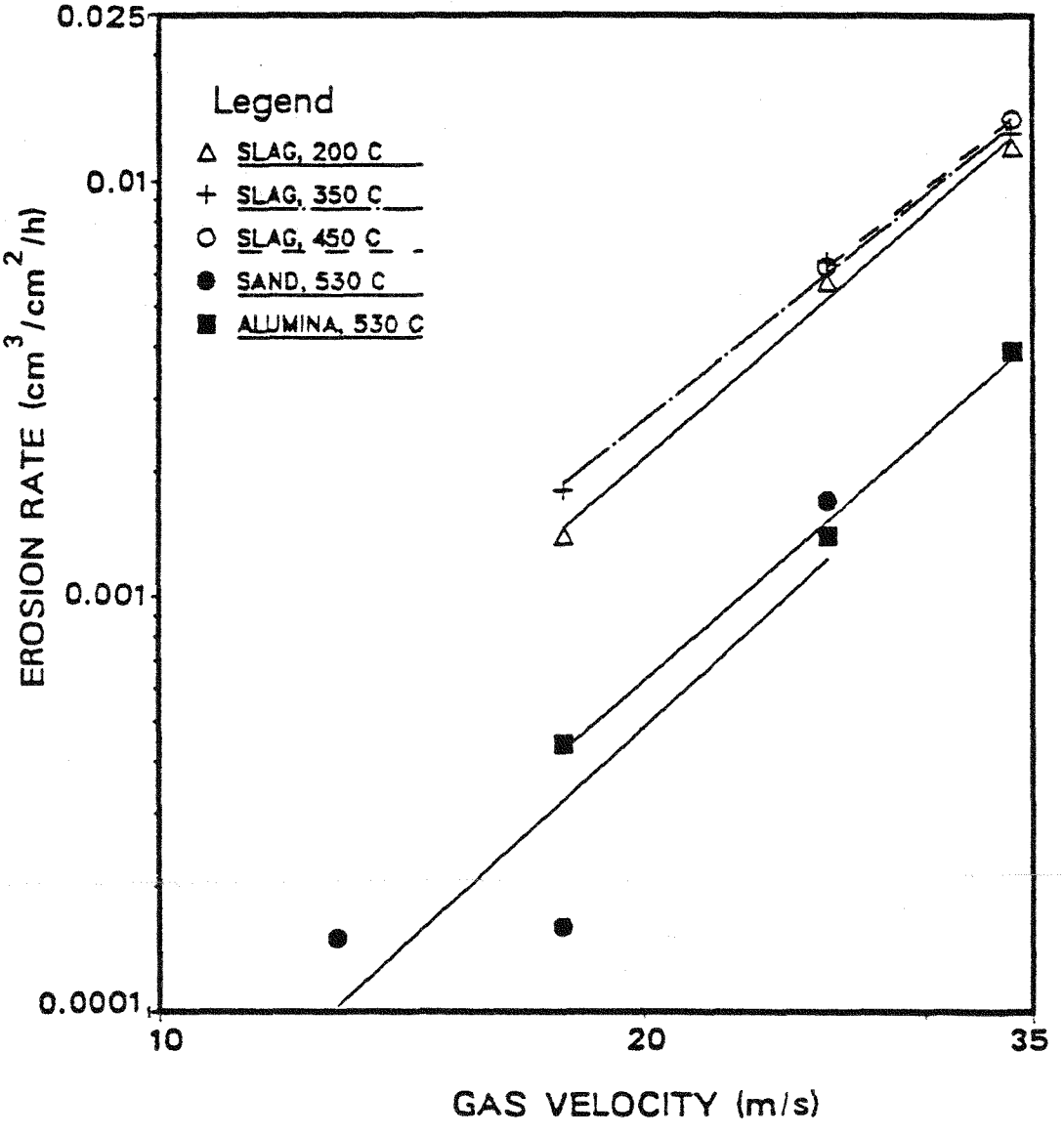

Figure 19. Effect of gas velocity on the erosion rate of Kaotab concrete

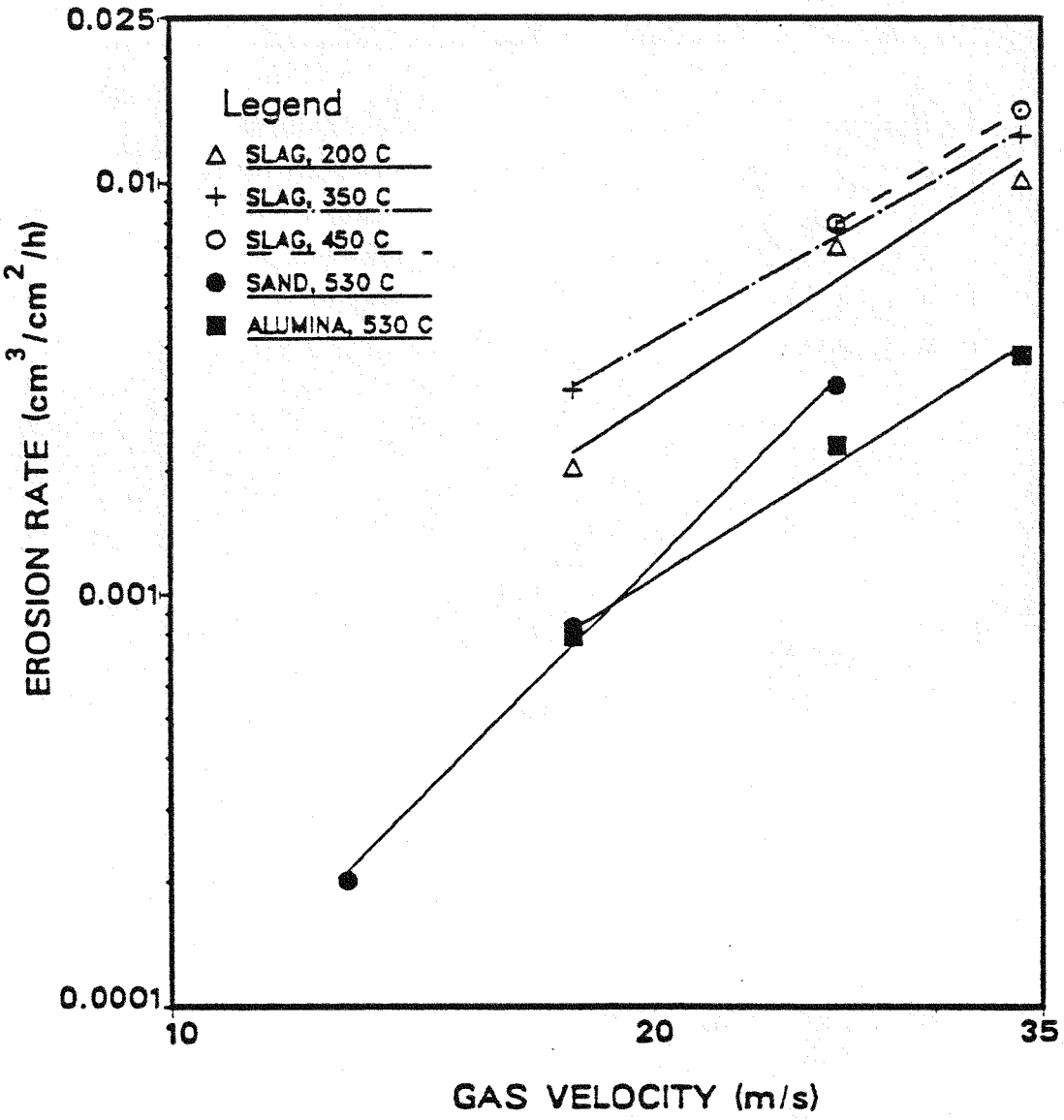

Figure 20. Effect of gas velocity on the erosion rate of Carbofrax concrete

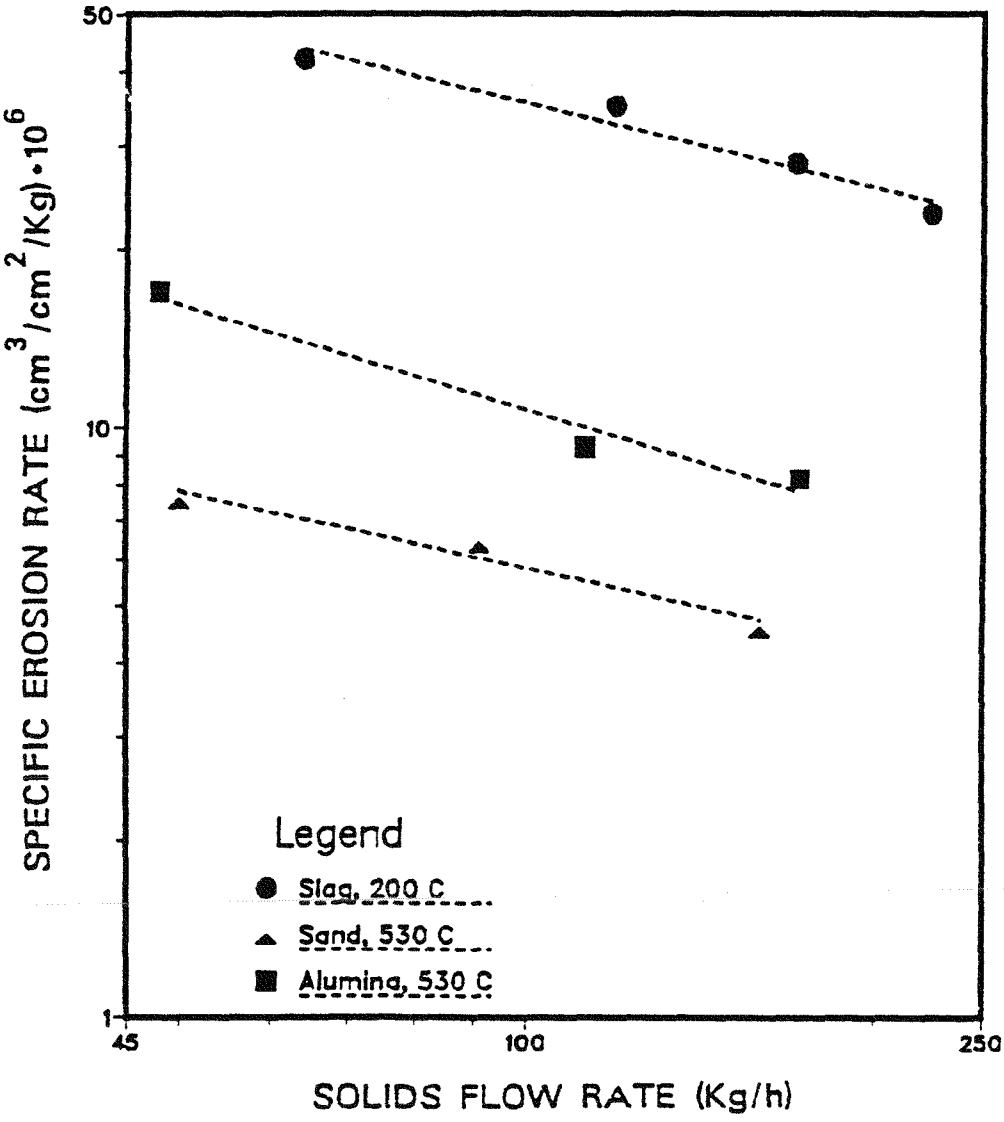

Figure 21. Effect of solids flow rate on the erosion rate of Fraxcast concrete

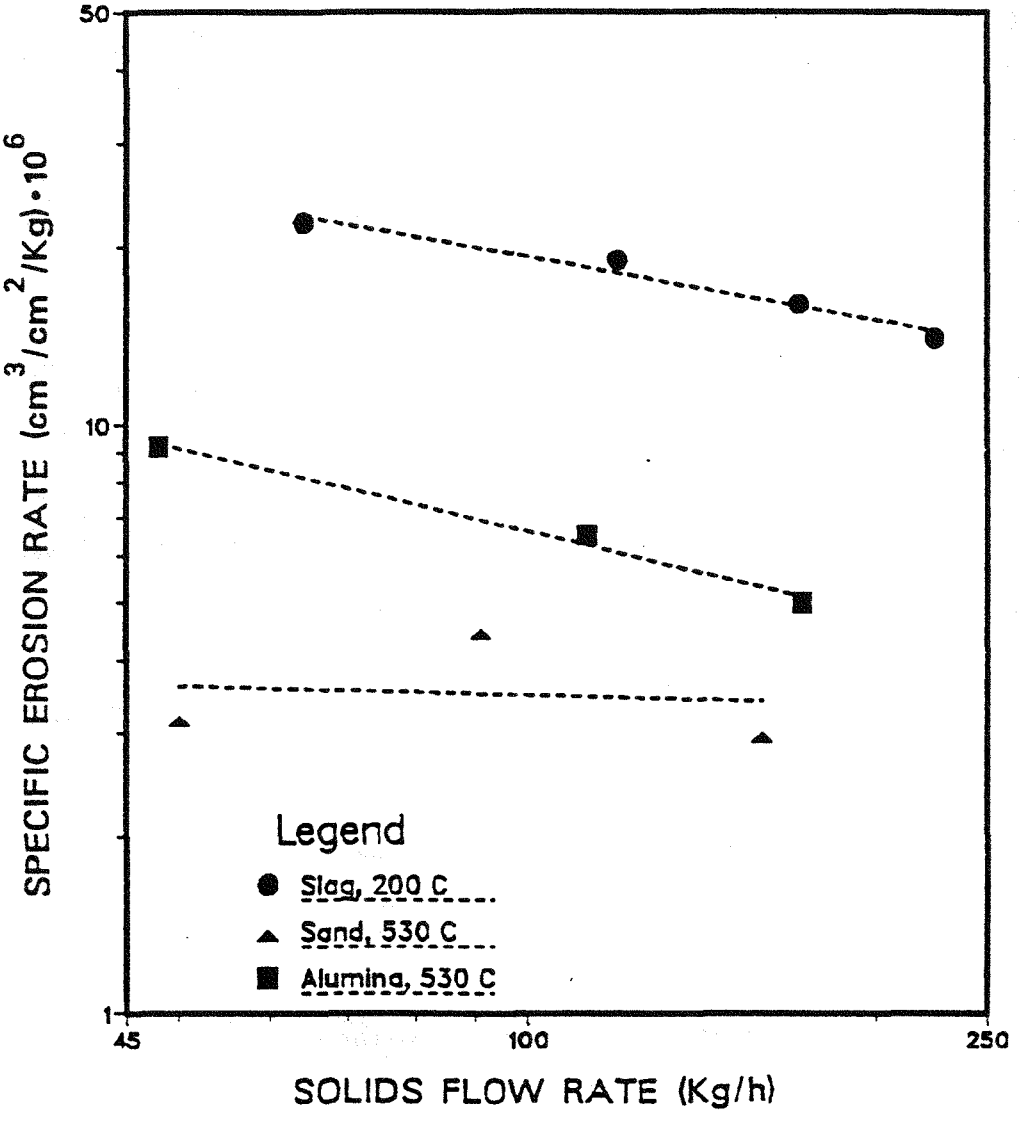

Figure 22. Effect of solids flow rate on the erosion rate of Kaotab concrete

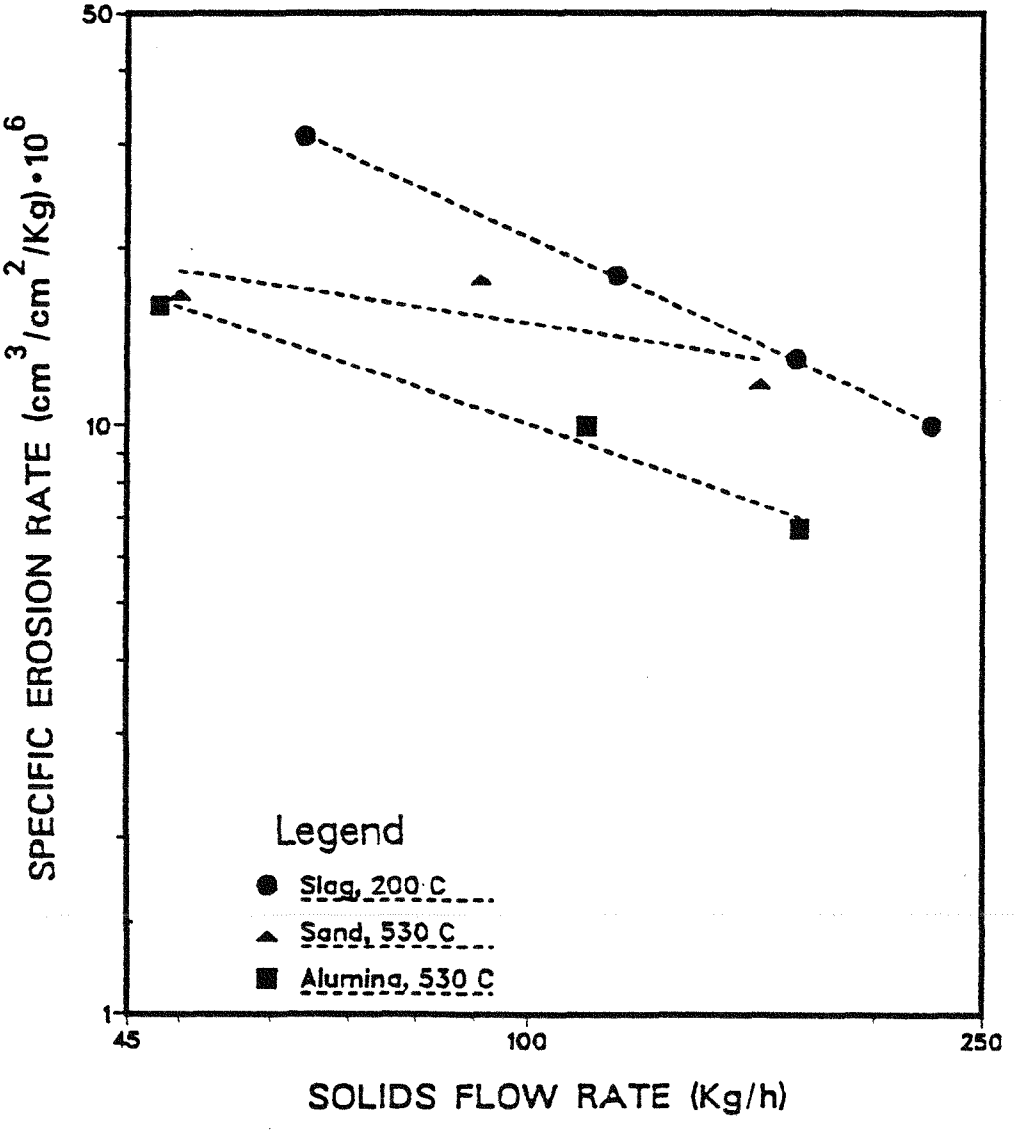

Figure 23. Effect of solids flow rate on the erosion rate of Carbofrax concrete

3.3 SURFACE TOPOLOGY

The concrete surfaces generated by the erosion process are characterized by their high roughness. A novel way to treat this kind of surfaces is using the concept of fractals[42]. This tool has the advantage of providing information about scale and shape at the same time[43]. The fractal dimension of a surface can be determined by covering it with area elements of decreasing size ε_3, and noting how the area changes with the resolution of these elements. If some order prevails in the sense that the surface observes scale similarity, that is, the surface looks statistically the same at all levels of resolution, then it is a self-similar fractal and the increase in the area follows a power law. In a more restricted sense, a real surface may show self-similarity in a bounded region, and a fractal dimension can still be defined for that region. For a fractal surface of dimension D_3 (a surface embedded in a three dimensional space), the number of area elements to cover the surface will increase according to:

$$N_3 \ \alpha \ \varepsilon_3^{-D_3} \tag{3-3}$$

If the fractal is isotropic, its fractal dimension can be evaluated by an intersection of a plane with the surface[44], generating a boundary of dimension $D_b = D_3 - 1$.

3.3.1 Surface Characterization

A wax cast of the concrete eroded surface was made by pouring melted wax on the samples. The best results were obtained when the wax temperature was 60 °C, and the sample was standing at room temperature. After cooling, the cast was carefully removed, cut and photographed. The photographs were digitized and analyzed numerically. Cross sections and digitized images for the two Kaotab samples shown in Figures 14b and 15a are presented in Figures 24 and 25. Figure 24 corresponds to a transient state of erosion of a Kaotab sample, while Figure 25 shows the steady state surface boundary. The Coastline Method was used for the analysis[42]. This method consists in measuring the

perimeter of the eroded boundary using different lengths of step, ε_b. The total length of the boundary is then:

$$L = N \varepsilon_b \tag{3-4}$$

where N is the number of steps to cover the boundary line. From Equation 3-3 it is known that N is proportional to $\varepsilon_b^{-D_b}$, so that:

$$L = K \varepsilon_b^{1-D_b} \tag{3-5}$$

The fractal dimension D_b of the eroded boundary can be calculated by plotting the perimeter L versus length of step ε_b in a log-log scale. The plots for the cases shown in Figures 24 and 25 are presented in Figures 26 a and b respectively. A straight line (smooth surface) should have a fractal dimension of 1.000, by definition. As the surface begins to be eroded a definite slope develops, starting at a point ε_c (Figure 26a) . This is the resolution scale at which self-similarity begins to develop. At steady state (Figure 26b) a maximum fractal dimension and critical step characterize the surface. The value of the fractal dimension is very small but still useful to differentiate between steady state and transient surfaces. Fractal dimensions and critical step length for different samples in a steady state of erosion are presented in Table 6. Some of the wax cross sections are included in Appendix D. The critical step length seems to be related to the maximum aggregate size in the concrete.

Fractal analysis then appears as a purely geometrical tool to quantify the initial stage of erosion. During this period, the variation of the fractal parameters is related to the development of the concrete surface. The erosion rate of a Kaotab sample by alumina was measured as a function of time along with its fractal dimension. The values are presented in Figure 27. The begining of the steady state period of the erosion coincides with the stabilization of the fractal parameters.

3.3.2 Effect of Aggregate Size

During the alumina tests, the aggregate size distribution of the Kaotab concrete was varied to see its effect on the erosion rates and mechanisms of erosion. The concrete mixture was sieved in three fractions: over 2000 μm, between 2000 μ and 600 μm and below 600 μm. The larger fractions were in a ratio 1:1, so the finer fraction which contains the small aggregates and the cement was divided in two and mixed again with the others. The refractory samples were then prepared in the same way as the original concrete and cutted to size and in half. These half samples were inserted together in the test section, cured at 950°C for 10 hours without feeding solids. Then solids were fed at 48 kg/h, 34 m/s and 530 °C. The samples were removed every day and weighted. The erosion rates were calculated as a function of time. Photographs of the final surfaces are included in Figure 28a,b. The results for the samples containing the intermediate and large size aggregates are included in Figure 27, were they are compared with the original sample of Kaotab (all eroded under the same conditions). The initial erosion rates for the three types of samples are very similar, since they all start from the same surface condition. The castable with the original formulation reaches the lowest value of erosion rate, followed by the one containing the intermediate fraction. Both surfaces look alike, with large aggregates surrounded by smaller ones, which are embedded in the cement matrix. The fraction containing the large fraction presents very high erosion rates and extreme undercutting (compare Figures 15a and 28 b). There is a minimum that occurs at about 8 hours. At this point the matrix has receded enough to be protected by the large aggregates. As the erosion proceeds, undercutting continues and whole aggregates are hit loose, increasing the erosion rate.

Table 5. Fractal dimensions and critical step length for various concrete samples

Sample	D_b	ε_c (mm)
Kaotab, Sand	1.066	3.8
Kaotab, Slag	1.078	3.6
Kaotab, Alumina	1.062	3.9
Fraxcast, Sand	1.035	2.9
Fraxcast, Slag	1.045	3.4
Fraxcast, Alumina	1.031	3.5
Carbofrax, Sand	1.031	4.5
Carbofrax, Slag	1.040	4.2
Carbofrax, Alumina	1.042	4.0

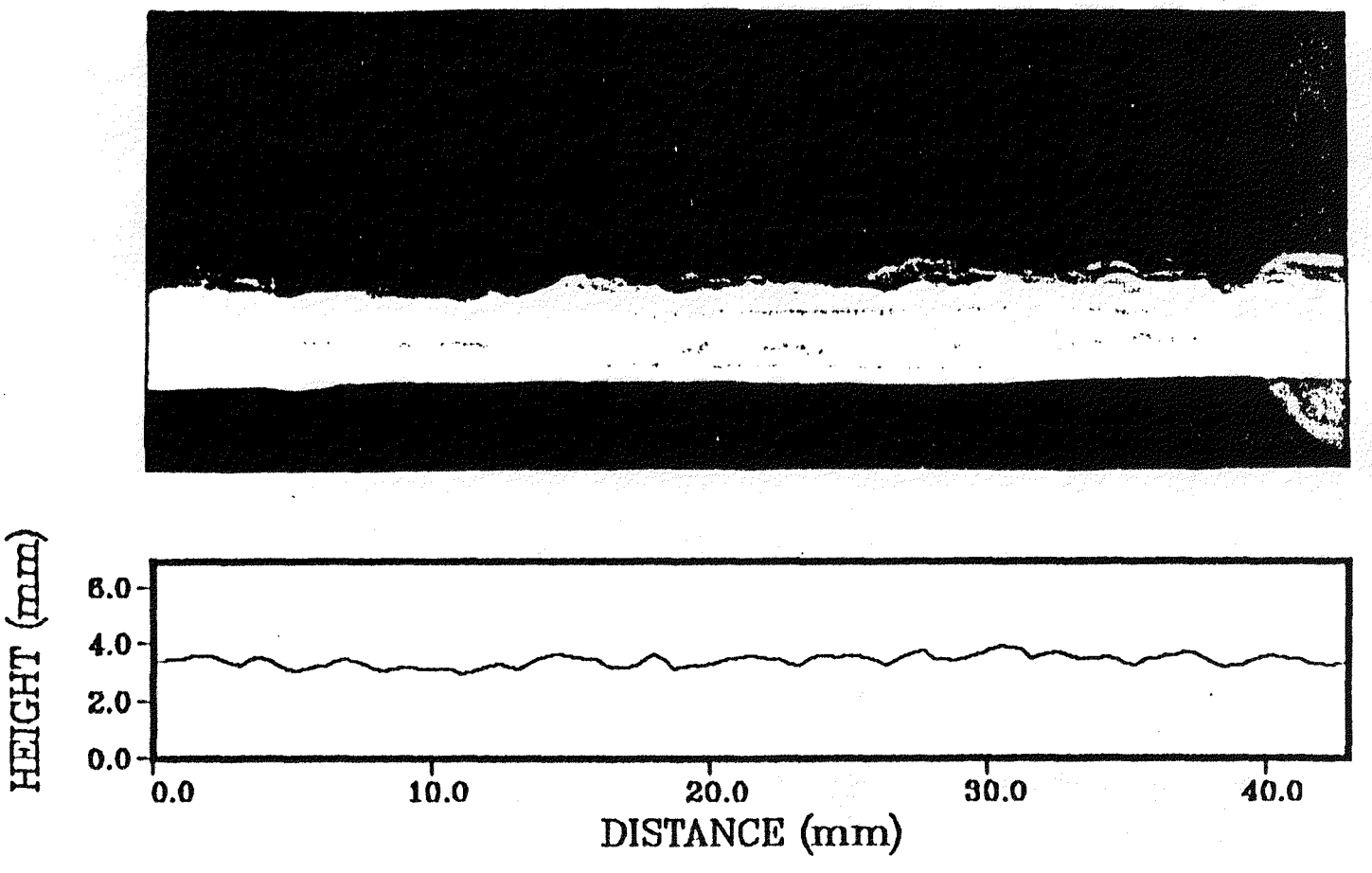

Figure 24. Wax cast and digitized boundary for the transient surface of Kaotab concrete

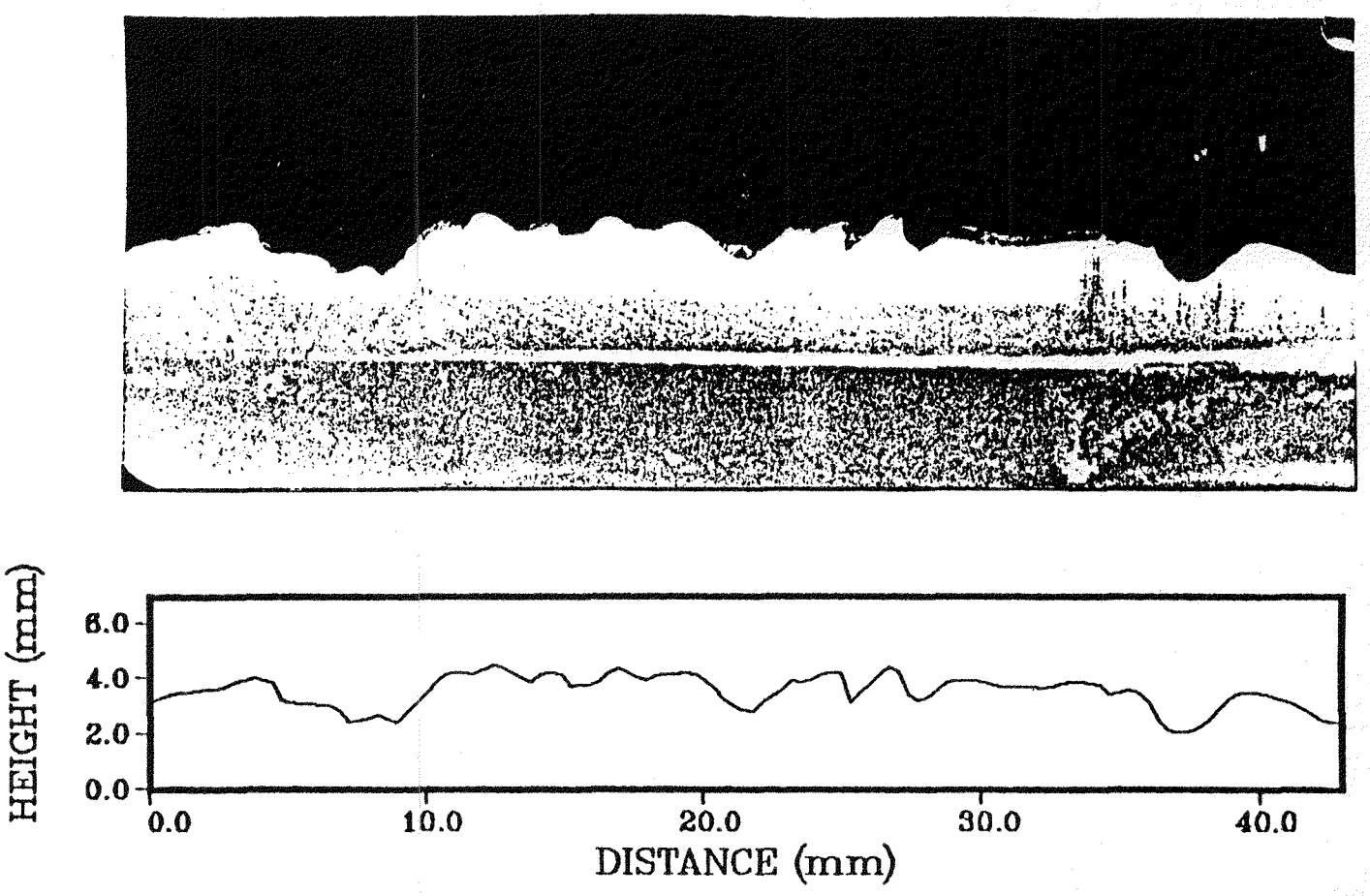

Figure 25. Wax cast and digitized boundary for the steady state surface of Kaotab concrete

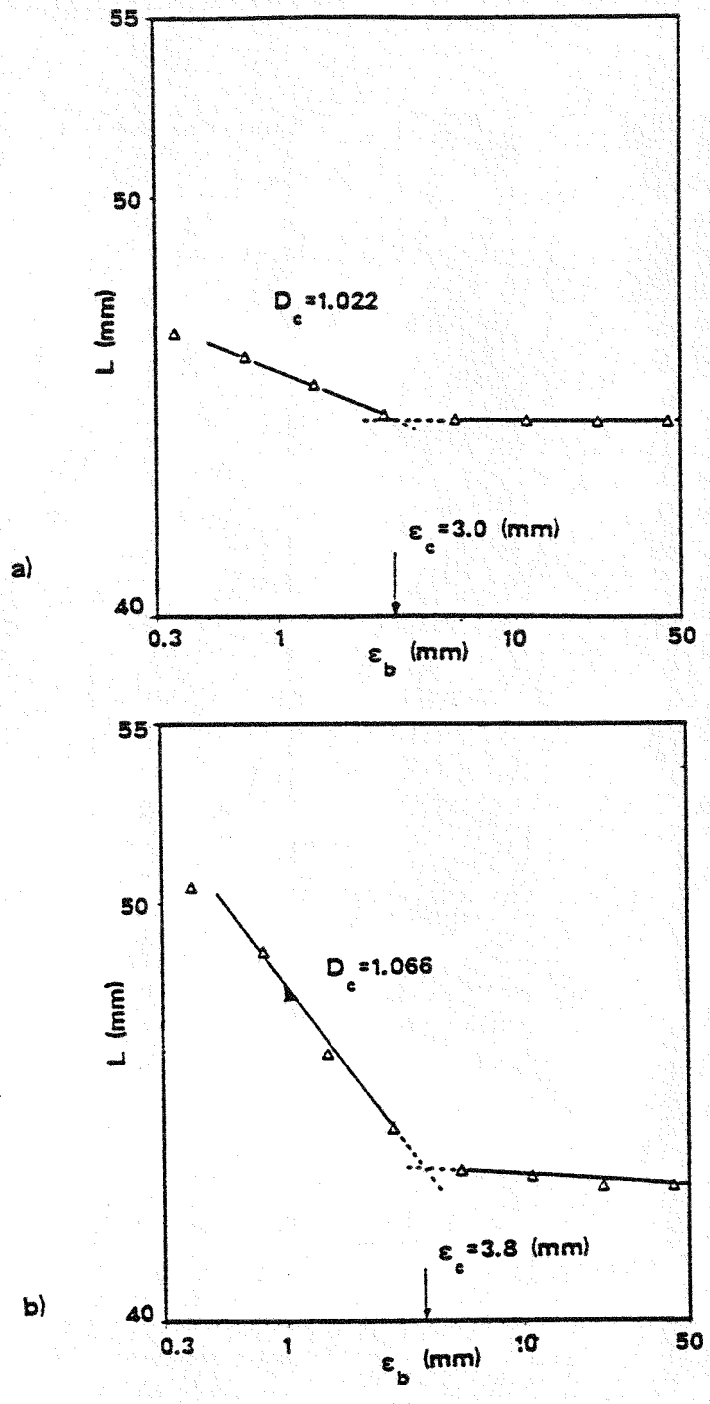

Figure 26. Fractal analysis for a) Transient Kaotab surface, b) Steady state Kaotab surface

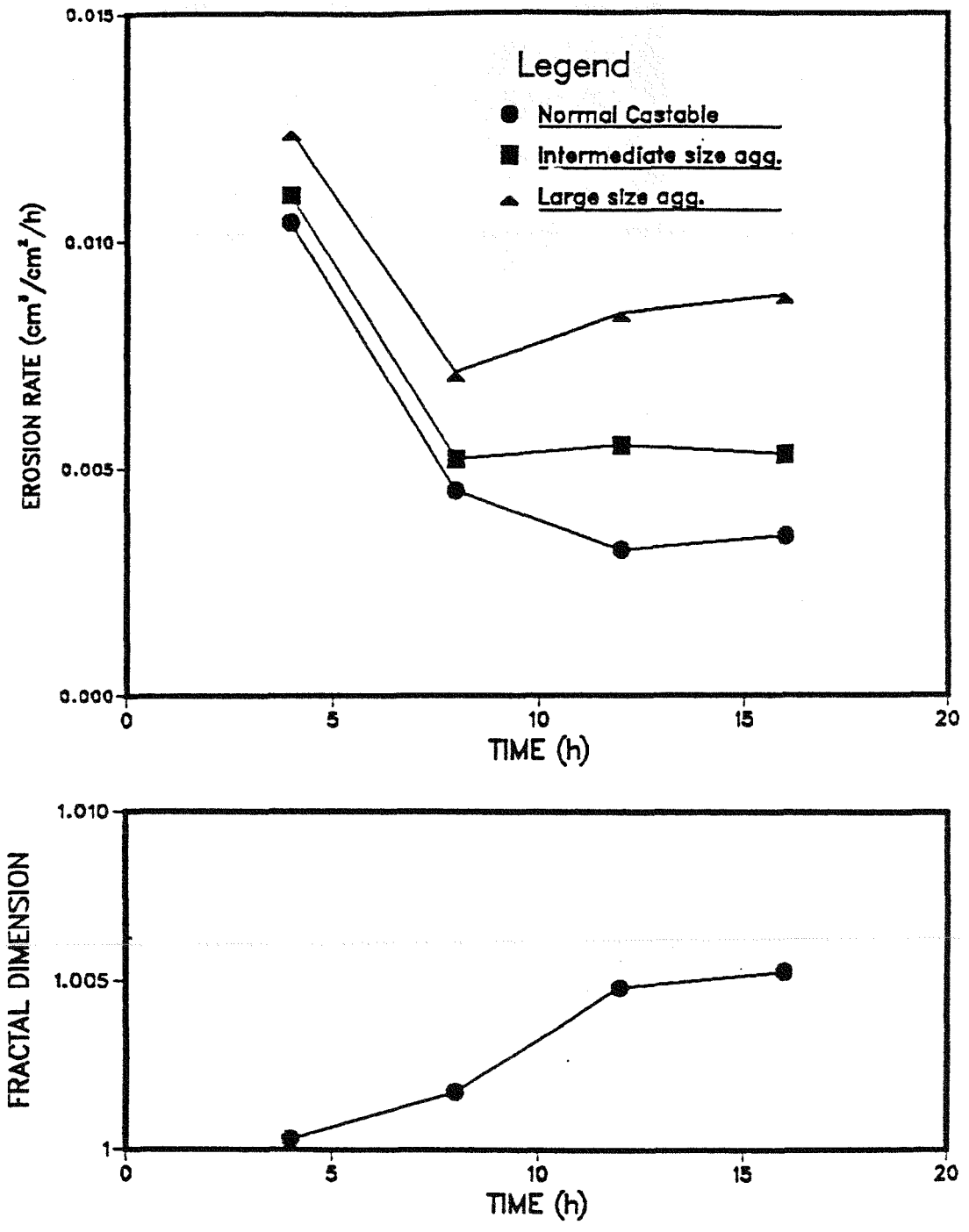

Figure 27. a) Erosion rates for a Kaotab sample as a function of time, compared to samples with modified aggregate size, b) Variation of fractal dimension with time for Kaotab concrete

a)

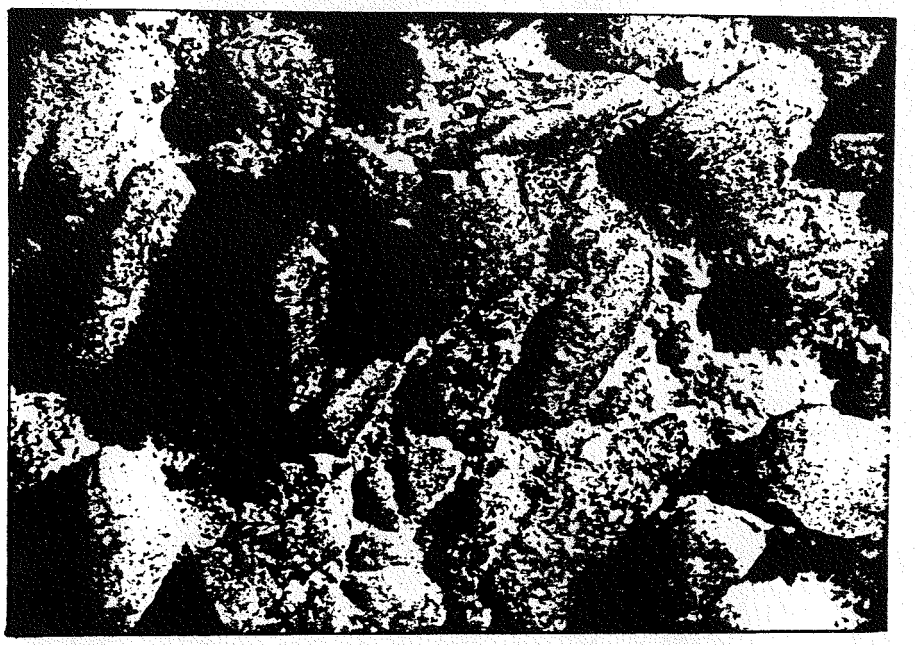

1000 μm

b)

Figure 28. Photomacrographs of the steady-state surface of Kaotab samples. a) Intermediate aggregate size. b) Large aggregate size

3.4 TRANSPORT ENERGY LOSSES

Transport energy losses are an important parameter in the design and evaluation of pneumatic transport lines. Most studies of pressure drops in pipes have been conducted at ambient temperatures in conventional pipes (copper, carbon-steel, stainless-steel, PVC). Data for pressure drop of gas-solids mixtures circulating at high temperatures in rough pipes are scarce. In this work this type of data were obtained and compared with predictions of different correlations and models available in literature.

3.4.1 Pressure Drop in Vertical Pipes

In steady state conditions the total pressure drop in vertical pneumatic conveying lines can be decomposed in two parts: a static term and a frictional term[45].

$$\Delta P_T = \Delta P_{static} + \Delta P_{friction} \tag{3-6}$$

The total static contribution is given by:

$$\Delta P_{static} = [(1-\varepsilon)\rho_p + \varepsilon\rho_g] L g \tag{3-7}$$

where the voidage is given by

$$\varepsilon = 1 - 4W_s/(\pi D_t^2 U_p \rho_p) \tag{3-8}$$

The frictional contribution can be splitted in two parts, considering gas and solids separately. The gas frictional term is given by:

$$\Delta P_{fg} = 2 f_g \rho_g \varepsilon U_g^2 L / D_t \tag{3-9}$$

and the solids frictional term is

$$\Delta P_{fs} = 2 f_s \rho_p (1 - \varepsilon) U_p^2 L / D_t \tag{3-10}$$

The friction factors f_g and f_s must be calculated from correlations. The gas friction factor is commonly calculated from Koo's equation[46] :

$$f_g = 0.0014 + 0.125\, Re_g^{-0.32} \tag{3-11}$$

For concrete pipes the roughness is very high and the expression for the gas friction factor should account specifically for it [47]:

$$f_g^{-1/2} = -3.6\, log_{10}[6.9/Re_g + (0.27\kappa/D_t)^{1.11}] \tag{3-12}$$

Several expressions are available in literature for the solids friction factor in vertical pipes. The most successful are the correlations by Yang[48] and Konno and Saito[49]. Yang's correlation results in the following expression for the solids flow friction factor:

$$f_s = 0.00315(1-\varepsilon)/\varepsilon^3\, [(1-\varepsilon)(Re_t/Re_p)]^{-0.979} \tag{3-13}$$

where the particle velocity is calculated from the following equation:

$$U_p = U_f - U_t[(1+2f_s U_p^2/(gD_t))\varepsilon^{4.7}]^{1/2} \tag{3-14}$$

In the correlation by Konno and Saito the solids friction factor is:

$$f_s = 0.0285(gD_t)^{1/2}/U_p \tag{3-15}$$

and the paricle velocity is

$$U_p = U_g - U_t \tag{3-16}$$

3.4.2 Experimental Method

Pressure drop measurements were carried out in the test section of the pneumatic transport test facility, substituting the small samples (normally 0.065 m long) by 0.3048 m (1 ft) long samples. Fraxcast was chosen as the wall material. A total of five samples formed a 1.52 m long pipe section, with pressure probes and thermocouples connected in both ends. Coal slag was circulated under different operating conditions. Two series of tests were performed. In the first one, the solids were circulated through the smooth samples, before the rugged morphology was developed. Using this wall condition, combustion gases alone were circulated varying temperature and actual gas velocity. The sequence was repeated using different solids flow rates. The total number of experiments was limited, since wall conditions would change due to the erosive wear by the coal slag. The duration of each experiment was about one minute, and the pressure drop was registered in a chart recorder. Once this part was finished, solids at high velocity (34 m/s) were circulated for a total of 24 hours, modifying the surface of the test pipe (steady-state erosion). Using this new wall condition, all the previous experiments were repeated. Experimental data for the pressure drops are tabulated in Appendix E.

The pressure drop for gas alone circulating in the initial or rough pipe is grossly underpredicted by Koo's equation (Appendix E) The rough pipe equation (Equation 3-12) does an excellent job once the roughness parameter has been adjusted. A single parameter can be used then to predict accurately the pressure drop as a function of gas velocity and temperature (Figures 29 and 30). As the solids are fed, temperature effects become less important, as shown by Figures 31 and 32. In this case, the frictional and static contributions of the solids control the pressure drop behavior. Konno and Saito's correlation underpredicts the pressure drop by as much as 50 % in the case of the initial pipe, becoming worse in the case of the rough pipe (Appendix E). Yang's correlation does a better job for the initial pipe, or for the rough pipe at high gas velocities, but underpredicts at low gas velocities by as much as 50%.

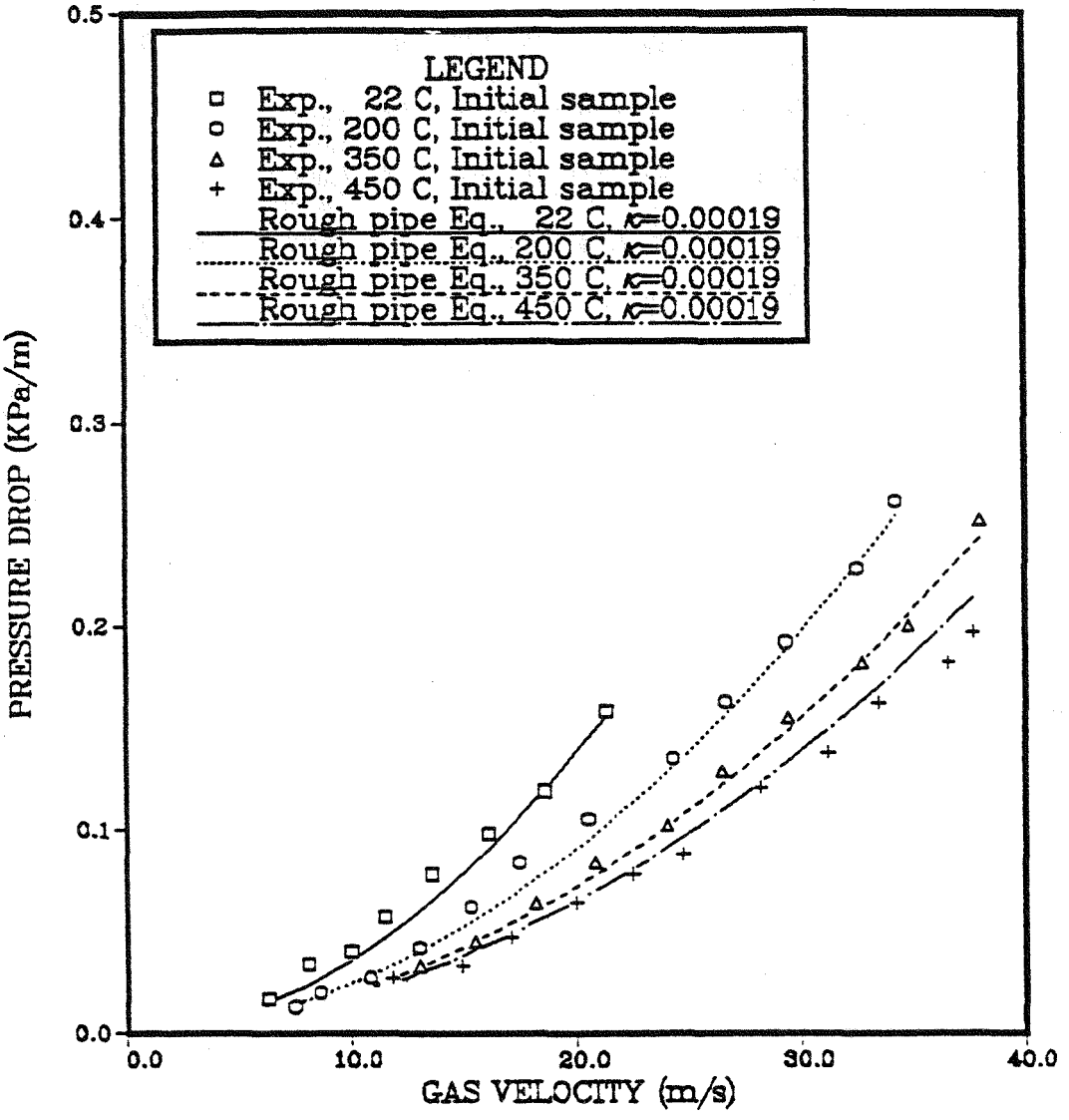

Figure 29. Pressure drop by combustion gases on initial pipe compared with rough pipe equation

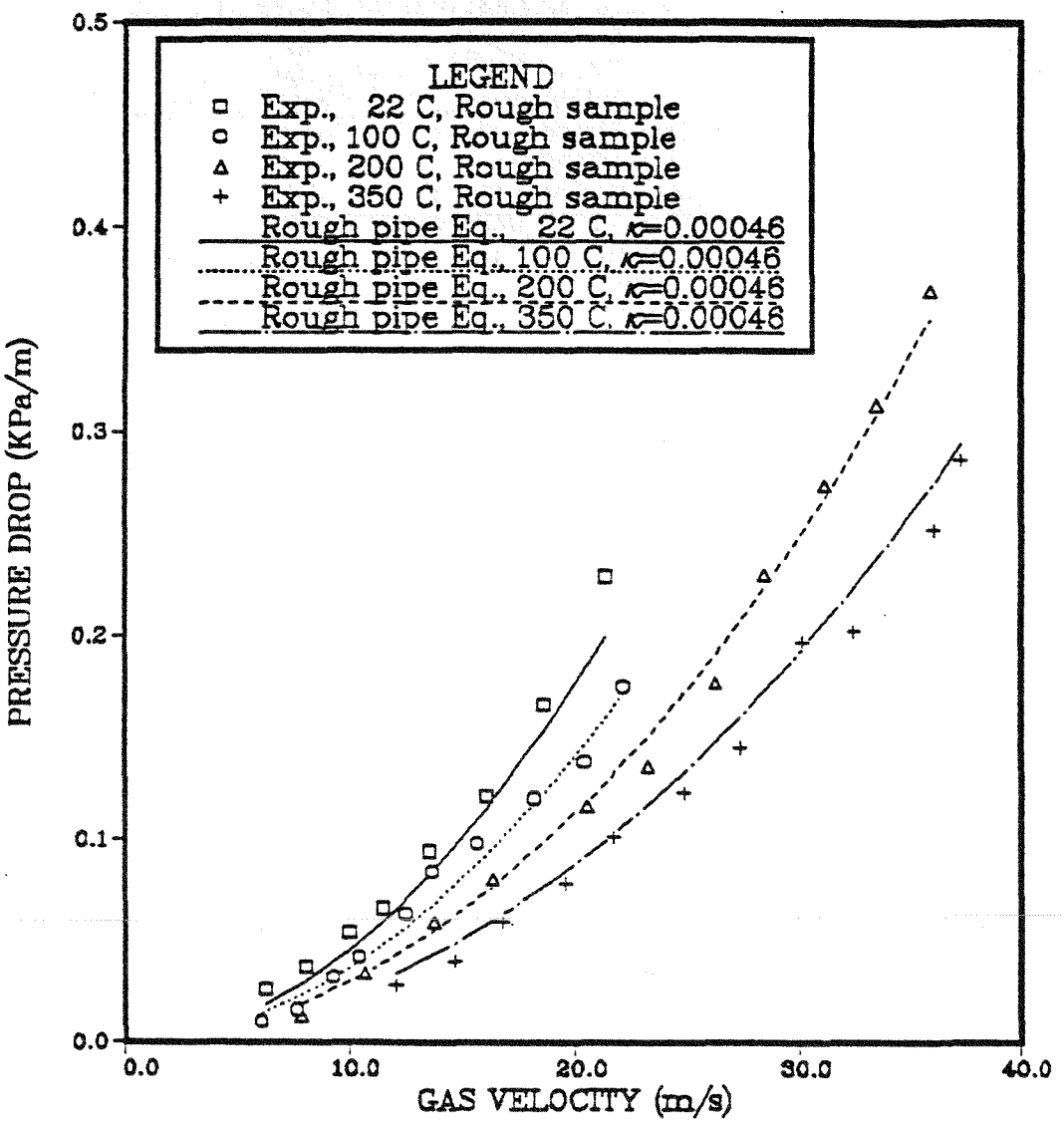

Figure 30. Pressure drop by combustion gases on rough pipe compared with rough pipe equation

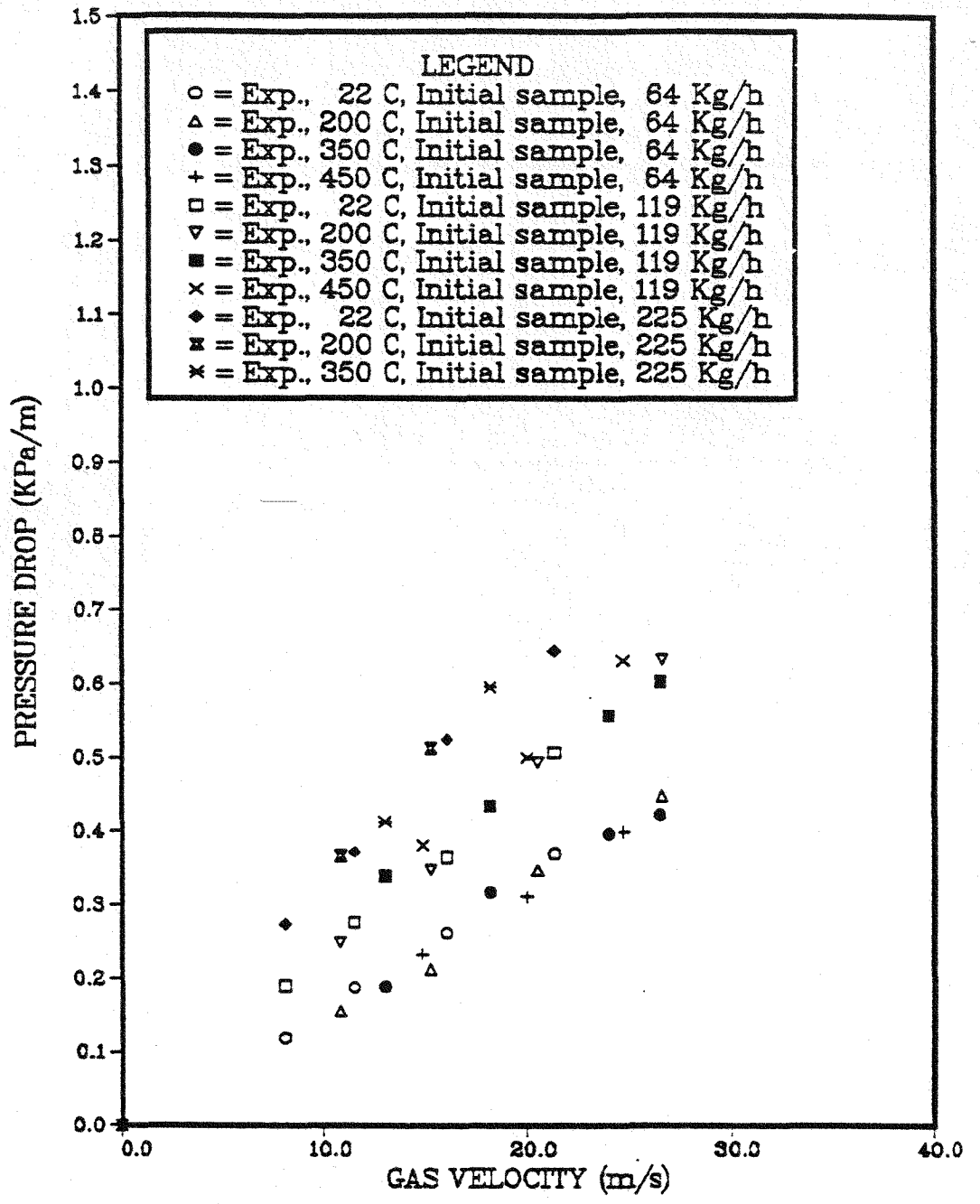

Figure 31. Pressure drop by coal slag on initial pipe

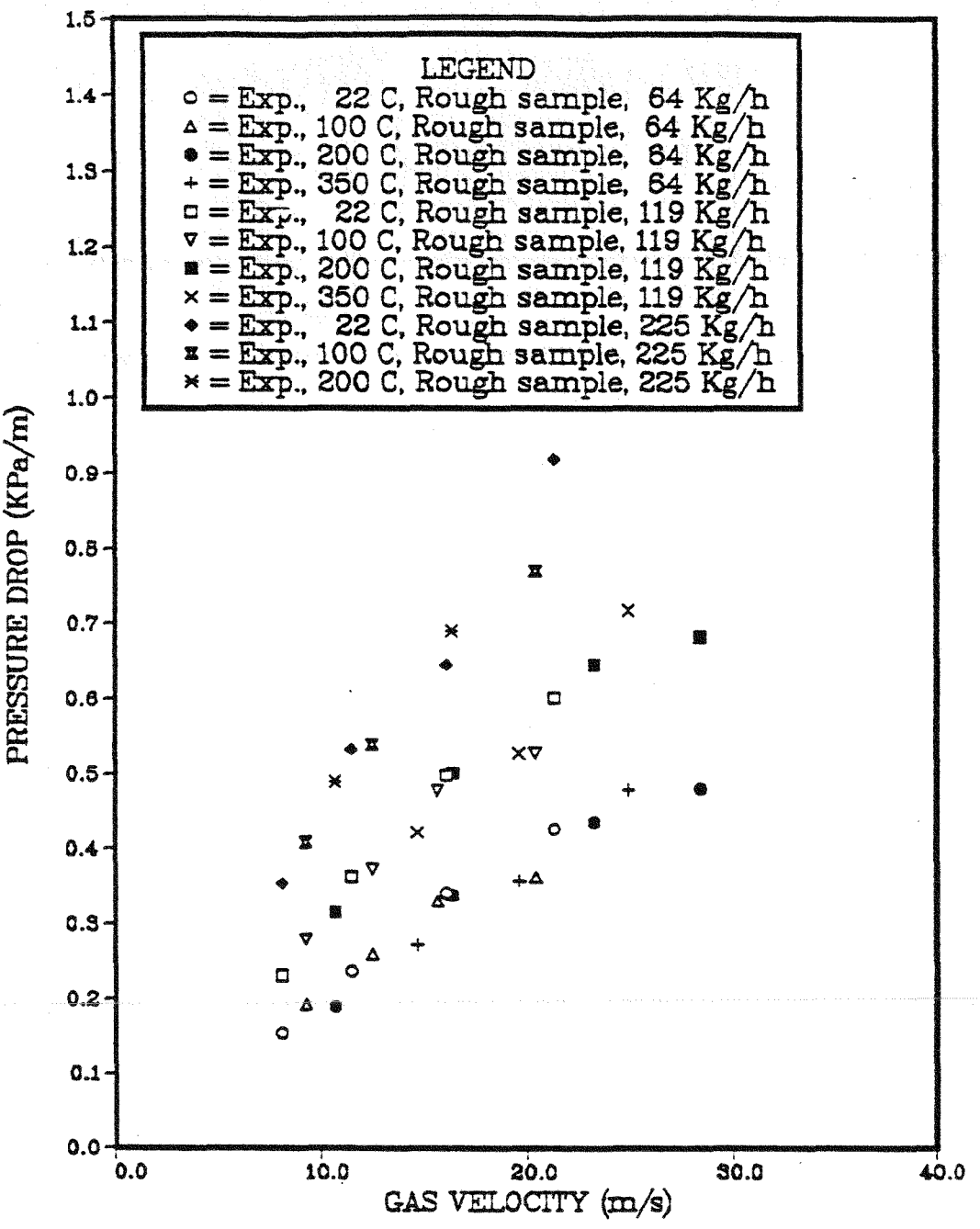

Figure 32. Pressure drop by coal slag on rough pipe

3.5 DISCUSSION

A comparison of the erosive wear caused by river sand, coal slag and alumina shows a trend that can be explained in terms of particle shape and particle size distribution. This trend can be observed in Figures 18, 19 and 20, where the lowest erosion rates correspond to river sand, followed by the alumina (10% to three times higher) and the coal slag (about one order of magnitude higher than the sand erosion rates). For sand and alumina, the erosion rates do not vary significantly below the temperature level of 530 °C, so the data are still comparable. At temperatures above 500°C, this trend changes, as the slag softens. The difference in solids flow rates (about 30 % higher for the coal slag) cannot explain the difference in the erosion rates. From the point of view of mechanisms, the erosion proceeds in a similar way for the three erodent materials: erosion of the cement phase, undercutting and release of the medium size aggregates, undercutting and release of the large size aggregates. Sharp-edged particles may enhance the erosive wear in two ways: by causing more damage upon impact, since the small radius of contact generates intense stresses in the target surface, and by their geometrical advantage to reach the cement phase and fine grains that lie around the aggregates. This enhanced erosion behavior is more dramatic when the particle size distribution is wide, because smaller particles can penetrate more easily to reach the matrix, and large particles have enough kinetic energy to release the aggregates upon impact. Thus, the combination of both sharp edges and wide particle size distribution of the slag can explain the high values for the erosion rates compared with sand and alumina. The same trend can be seen in the case of sand and alumina, since the last material is tabular. with relatively sharp edges, while in the case of river sand these edges are rounded. Density and particle size differences between these two materials are compensated in part by changes in the number of particles circulating in the transport line, since mass flow rates are nearly the same. Differences may arise due to the fact that the particle velocities are dependent on both density and particle diameter. The terminal velocity for the alumina particles is 55% higher than for the sand particles. Since the erosion rates are very sensitive to impact velocities, even small changes in velocity can translate into significant variations of the wear rates.

The effect of the gas velocity on the erosion is well correlated by a power law (Equation 3-1). Gas velocity is the variable that can be normally measured in a pneumatic transport facility. The determination of the actual average particle velocity in this kind of systems is not straightforward. This is particularly true for impact velocities. The ratio of average particle velocity to gas velocity normally increases until it reaches a point in which it remains constant [50]. This point occurs at velocities lower than 10 m/s, varying according to the particle size. After this point the particle velocity becomes proportional to the gas velocity, and the power law then applies to both variables. Particle velocities measured with the cross-correlation technique support this statement in the case of the test facility used in this work. For river sand conveyed at 530°C the ratio of particle to gas velocity remained the same in the range of 12 to 26 m/s, being equal to 0.74. Therefore, in this case the exponent measured for the gas velocity also applies for the effect of average particle velocity on the erosion rates. Still, the variable that is relevant in the erosion models is the kinetic energy of the particle at impact, which is directly related to the impact velocity. In the case of smooth pipes, this variable can be considered to be the average particle velocity, but in the case of concrete samples the case is different. In Figure 33 is shown a magnification of the eroded boundary of a Kaotab sample impacted by sand during the period of steady erosion. The cross section was obtained by immersing part of a sample in a mixture of epoxide and fine coal, and cutting it. In that way the surface remained intact and the undercutting of the aggregates could be measured. The diagram of this figure includes some probable trajectories of the impacting particles (the dot corresponds to a 200 μm sphere). As it is shown in the diagram, the only way for a particle to reach the matrix is either by penetrating through the aggregates in the correct angle, or by mutiple collision with them. Measurements of particle trajectories in smooth pipes result in deviations from axial direction of the order of 2°. Still, higher deviations are possible when the walls are rough, as it was shown by high speed photographs taken in eroded samples. Figure 34 shows two milimeter alumina particles impacting with a smooth and a rough wall (smooth and eroded carbofrax surfaces) at a velocity of about 2 m/s. The stream impacting the smooth surface shows a degree of dispersion due to the irregular particle shape of the alumina. This dispersion is

extremely high in the case of the rough surface, and as a result, very large deviations from the axial trajectory may result. In the case of a pipe, particles rebounding in such a way can collide directly with the matrix in the opposite side. Neglecting drag forces by the fluid, the impact velocity will be related to the average particle velocity by the restitution coefficient of the impact. The same applies to the case in which the particles rebound directly towards the matrix. Since the restitution coefficient presents a flat behavior over a range of impact angles, the impact velocity can be considered proportional to the average particle velocity, and for hence to the gas velocity. Then, the power law behavior of the erosion rates with the gas velocity can be seen as a manifestation of the power law behavior of the impact velocity, although the last one cannot be known without more extensive work on collisional behavior inside this type of systems. From a point of view of design it is the gas velocity the most important variable, while from a modeling point of view, it is the impact velocity the relevant one.

The fact that the gas velocity exponents and, as follows from the previous discussion, the particle impact exponents are greater than two indicates that as the velocity increases a proportionally larger fraction of the kinetic energy is used in the wear process. Values of these exponents indicate that they are not very sensitive to the type of erodent material neither to temperature (below the range in which dramatic changes in mechanical properties of the erodent occur). The exponent is clearly not sensitive to particle shape or particle size distribution. This means that once the proportionality constant in Equation 3-1 is known, the scaling of the gas velocity can be done with data for other types of materials impacting that surface. Previous experimental work by other authors has shown that these exponents are valid in a wide range of velocities, so extrapolations can be made. In the range of low gas velocities this relation may break down because the particle velocity is not proportional to the gas velocity. Still, the extrapolated predictions will be on the safe side.

The effect of solids concentration shows a clear trend that can be used in design to minimize wear. The erosion tests indicate that as the solids concentration increases, the

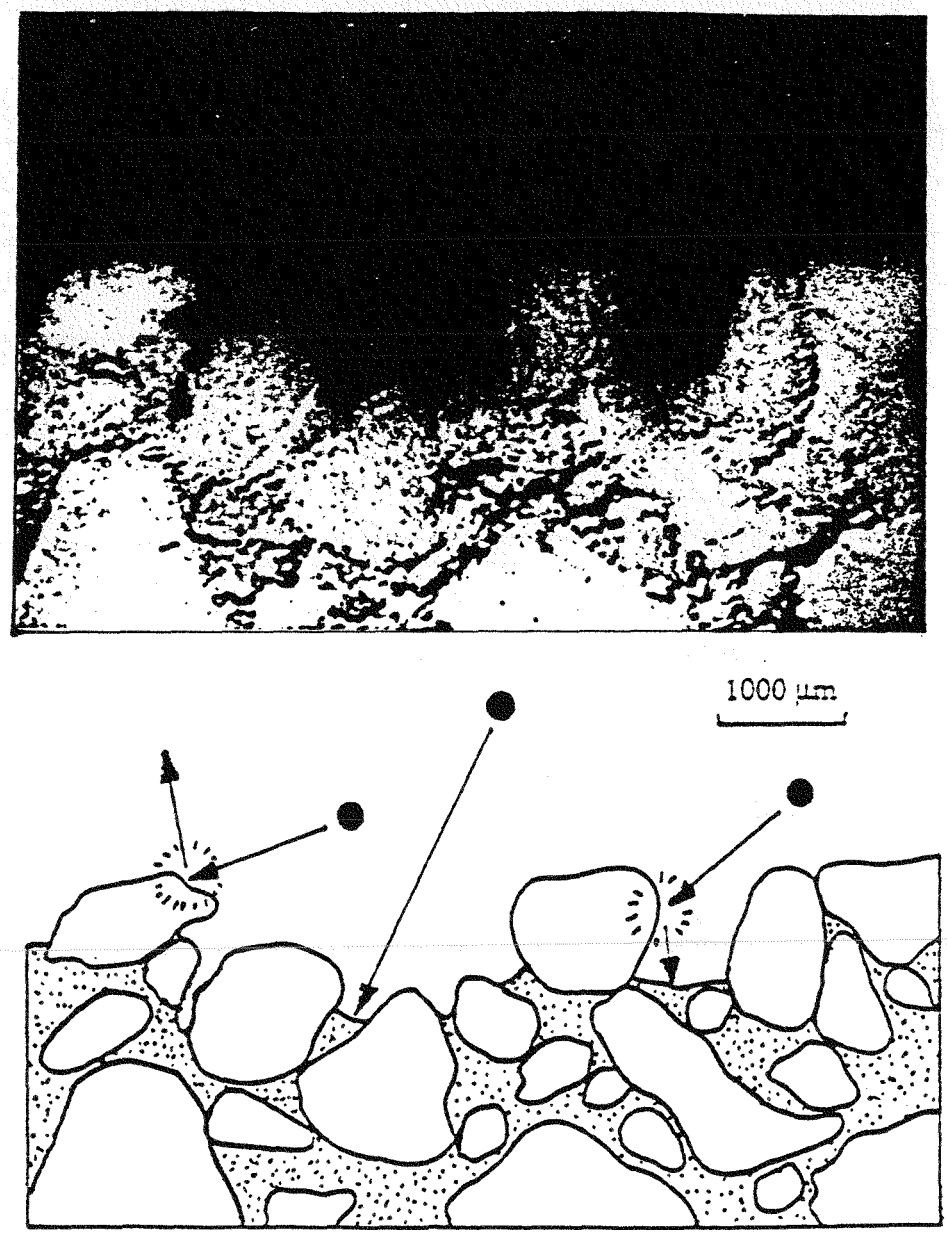

Figure 33. Photomacrograph and diagram of the eroded boundary of a Kaotab sample

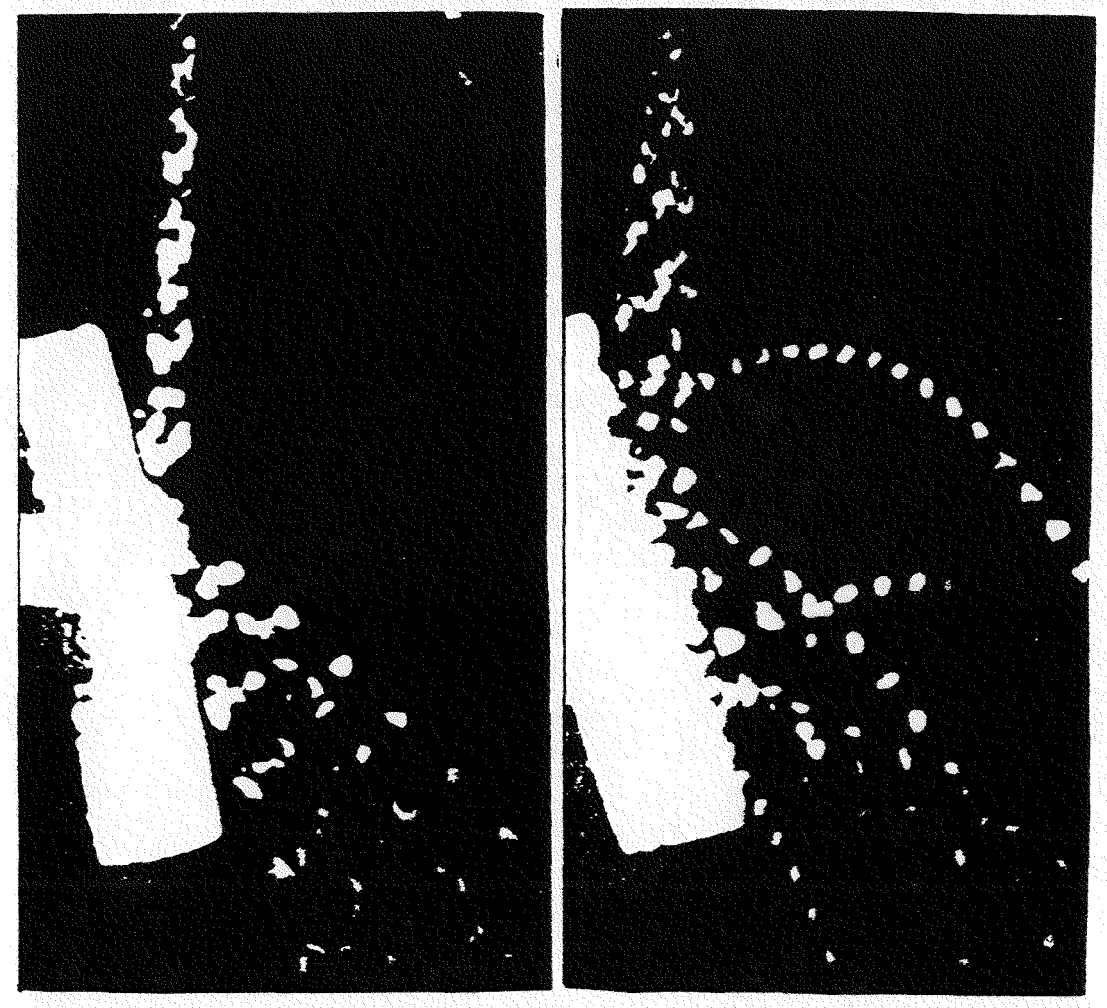

a) b)

Figure 34. Solids dispersion upon impact on
a) Smooth wall, b) Rough wall

amount of material removed from the walls per unit mass of solids circulating in the unit decreases. So, for highly abrasive materials, such as the coal slag, the choice is towards high solids concentration. The reasons for this type of behavior have not been fully explained. A similar behavior has been reported in other collisional processes such as heat transfer[51] and frictional losses[52] in gas-solids flow. The phenomenon has been explained in terms of an effect of reduction in the scale of turbulence due to the inertia of the particles. In the case of rough samples other effects should be taken into consideration, such as interparticle collisions, which reduce both particle velocity and collision efficiency. Shielding by particles residing temporarily in the region being undercut is also likely to occur. The values of the solids concentration exponents (m) show no clear tendency and they vary with type of erodent and target material. The big jump in the value of this exponent in the case of Carbofrax samples going from river sand (prefired at 530°C) to slag and alumina (prefired at 950°C) suggests that the cement phases play an important role in this type of behavior. Surface morphology in the three test series were very similar, so that shadowing and shielding effects were similar too. The presence of different phases will determine the response of the matrix under multiple impacts, such as crack propagation, as well as the rates of release of the bigger aggregates when hit by more than one particle. In the case of the Fraxcast concrete, which in accordance to Table 3 (gas velocity exponents) showed a similar response for the three types of erodent materials, the solids concentration exponent varies to a much lesser extent. The same can be said for Kaotab, except that measurements were not very consistent as to give a good value for this exponent. In fact, considering only the last two points, measured under similar conditions, it can be seen that the exponent is smaller, in agreement with the Fraxcast behavior.

Temperature effects are complex because target and erodent properties depend on temperature. In the case of river sand the erosion rates remain constant in the range of 22 to 530°C, showing a significant increase at 830°C. Despite the fact that quartz, the main mineral component of river sand, suffers a phase transformation at 573°C (α to β quartz), the behavior of the erosion rates with temperature can still be attributed to the variation of

the concrete's properties, since previous work indicates that, above certain level, the mechanical properties of the erodent are not very important. This fact was confirmed by the alumina test series. Alumina is a very stable material in the range of temperatures studied. The erosion rates still show a significant increase above the 530°C level. The case of coal slag is completely different, since there is a drastic change in the mechanical properties starting at about 450°C. After this point the erosion rates decrease sharply, as the slag softens. When this happens, the sharp edges easily deform upon impact, relaxing the stresses in the contact area. This fact also illustrates the importance of the presence of sharp edges as related to the wear process. It then follows that in the case of coal related materials with low softening points, the closer to slagging conditions the better, since the erosive wear is less severe. For the other two erodent materials the opposite occurs. This result shows that care must be taken in the selection of erodents for standard tests of target materials at high temperatures.

Comparing the erosion rates by sand, coal slag and alumina at high temperatures (Figures 16 and 17), it comes that there is a trend in the rates of increase of the erosion rates for the different concretes. At high temperatures the slopes for the high alumina concrete (Kaotab) are consistently smaller than for the other materials. There is an exception in the case of Carbofrax eroded by sand, but that can still be explained in terms of the sensitivity of this concrete to prefiring conditions. This behavior is consistent with the variation of the hot modulus of rupture of this type of materials at high temperature. Examining the behavior of the HMOR presented in Figure 4 for the case of a conventional intermediate alumina and high alumina concrete (like kaotab), and in Appendix B for a 50-60% alumina concrete (like Fraxcast), it follows that this variable correlates very well with the high temperature behavior of the erosion rates. Still, this relation is not straightforward since the slopes are also a function of the gas velocity (Figure 17), or, how comes from a previous discussion in this section, of the impact velocity. This increase in the slopes may be a consequence of a liquid phase formation in the concrete matrix, which occurs to a greater extent in intermediate or low alumina castables. The apparition of a liquid phase will enhance the rates of release of the

undercutted aggregates, being the low alumina concretes the most affected ones. Thermal effects, caused by conversion of part of the kinetic energy of the particle into heat during the impact, will also contribute to the behavior of the slopes as the impact velocity increases. A local increase in temperature will generate more liquid phase in the case of low alumina concretes, with the result of an increased erosion rate.

The topology generated during the erosion process is determined mainly by the grained structure of the concrete. The surface morphology of a particular concrete is visually the same for the three types of erodent materials. This observation was confirmed quantitatively by fractal analysis, which showed no significative variation for the different erodents. There are minor differences in the amount of matrix exposed, being higher in the case of alumina and coal slag. The first case can be explained by the larger particle size of the alumina compared with the river sand, becoming geometrically more difficult for it to reach the matrix. In the case of coal slag, this is a consequence of the higher erosion rates. Since the aggregates are being removed more frequently, it is easier to see portions of fresh matrix. An important point is that the surface morphology gives no information on how was the sample placed with respect to the flow direction. This observation gives support to the hypothesis that the particles rebound in the aggregates before colliding with the matrix. In other words, the cement phase is bombarded from all directions. Once the particle reaches the matrix, the amount of cement being crushed will be controlled by the other phases present on it (intermediate and small size aggregates). A wise design of an erosion resistant concrete should optimize the particle size distribution of the aggregates. As it is shown in Figure 27, the elimination of any size fraction in the Kaotab concrete resulted in an immediate degradation of the erosion resistance. Without an intermediate phase fraction the cement becomes more vulnerable to the impact, while without a large size fraction, the shadowing and the reduction of impact velocity (because primary impact occurs with the hard aggregates) effects are greatly reduced.

Although the fractal parameters are not directly related to the erosion rates, they can

be used to characterize the transient stages of erosion. The fractal dimension of the eroded boundary remains relatively unchanged during the removal of the superficial matrix, and then rapidly increases as the undercutting proceeds, becoming constant when the large size aggregates are fully exposed. This is a purely geometrical measurement which allows to predict the end of the initial stages of erosion. The technique is useful in the case when drying and erosion of the castable occur simultaneously, or when the transient period is long, as will occur with the development of high performance castables.

When the surface morphology changes, so does the particle dynamics inside the pipe as the number of interactions grows. This was shown by the measurements of the pressure drop under two different surface conditions. Going from an initial surface to a fully developed one (steady-state) the pressure drop increased in 25 to 30%. Particle-wall interactions affect the pressure drop because the kinetic energy dissipated in the impacts has to be restored from the pressure energy of the fluid. Since the average particle velocity has decreased due to the interactions, the solids concentration inside the pipe tends to increase. The final result is an increase of the solids frictional and static terms of the pressure drop. Present correlations are not formulated to take into account this type of situations and, even adjusting one parameter in some of the present correlations is not enough to predict the measured pressure drops (Appendix E). Perhaps the most promising correlation to be used in this type of situations is the one proposed by Yang[48]. The advantage of this correlation is that, unlike other correlations, the particle velocity is expressed as a function of the solids friction factor (Equation 3-14). This functionality cannot be neglected when frictional effects are important. The expression for the solids friction factor (Equation 3-13) has the potential to include a geometrical parameter in the same way as the rough pipe equation (Equation 3-12) does for single phase flow. Such task must begin by choosing a representative set of geometrical parameters, such as the fractal parameters.

Refractory linings are not the only elements suffering degradation during particle

impact: particles are also worn in the process. Particle attrition has been recognized as an important factor to consider in the design of coal conversion processes and utilization systems[53]. The fluid dynamic behavior and the efficiency of the particle collection systems are closely related to particle size. Finer particles are produced from the surface of the particle rather than by fracture of it into intermediate fragments. In pneumatic conveying systems, particle wall collision is the main cause for attrition. In the case of the erosion experiments, where the materials were recirculated several times, the particle size distributions for the erodents were measured at different times. River sand and alumina showed no evidence of attrition. In the case of coal slag, there was a difference, and the particle size varied from 300 μm to 210 μm after the slag experimental run #10 (Figure 35). The fines produced in this process are not fully counted in this plot since collection efficiency of fine particles in the cyclone is poor.

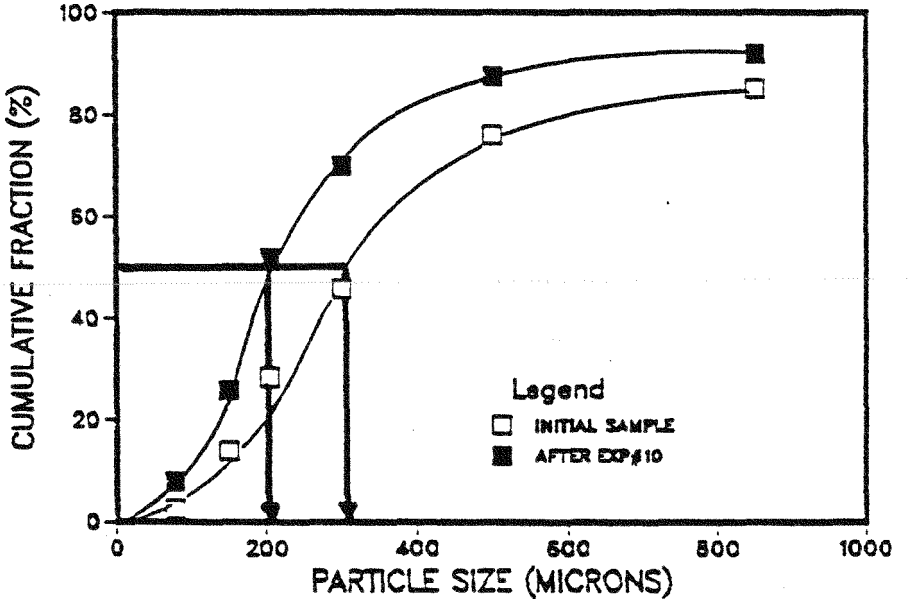

Figure 35. Coal slag attrition

Table 6. Summary of results

$E = K\ U_g^{n}\ W_s^{1+m}$

E ($cm^3/cm^2/h$)
U_g (m/s)
W_s (Kg/h)

Erodent	Target	n	1+m	T (°C)	K
River Sand	Kaotab			22	2.9E-10
		3.5	0.91	530	1.9E-10
				830	10.2E-10
	Fraxcast			22	1.5E-8
		2.6	0.57	530	2.3E-8
				830	12.7E-8
	Carbofrax			22	4.2E-10
		4.0	0.70	530	5.3E-10
				830	9.0E-10
Coal Slag	Kaotab			22	1.1E-8
		3.3	0.52	200	1.2E-8
				350	1.3E-8
				450	1.4E-8
				550	1.4E-8
				630	1.0E-8
	Fraxcast			22	7.0E-8
		2.8	0.64	200	5.0E-8
				350	6.8E-8
				450	7.6E-8
				550	5.0E-8
				630	3.5E-8
	Carbofrax			22	1.4E-6
		2.4	0.10	200	1.4E-6
				350	1.8E-6
				450	2.1E-6
				550	1.9E-6
				630	1.1E-6
Alumina	Kaotab	3.4	0.43	530	4.6E-9
				700	5.6E-9
				850	7.6E-9
	Fraxcast	2.5	0.61	530	5.9E-8
				700	9.5E-8
				850	15.4E-8
	Carbofrax	2.4	0.32	530	2.3E-7
				700	3.4E-7
				850	5.2E-7

The coal slag particle shapes at the beginning and end of the slag test series showed no appreciable differences, so that the mode of fracture regenerated continuously the sharp edges.

A summary of the erosion results is presented in Table 6, where the proportionality constant for the erosion rate expression is tabulated as a function of temperature. A more graphic interpretation of the effect of the different variables on the erosion rates can be obtained by using the expression on Table 6 to calculate the life (wear thru) of a 0.0254 m (1 inch) refractory lining, assuming that the change in gas velocity due to variations of the pipe diameter is corrected. The results are as follows:

Fraxcast eroded by river sand at 530°C, 50 kg/h

U_g = 10 m/s, lining life is 30,000 hours (3.5 years)
U_g = 25 m/s, lining life is 2,800 hours (4 months)

Fraxcast eroded by coal slag at 450°C, 50 kg/h

U_g = 10 m/s, lining life is 4,300 hours (6 months)
U_g = 25 m/s, lining life is 300 hours (12 days)

Fraxcast eroded by coal slag at 630°C, 50 kg/h

U_g = 10 m/s, lining life is 9,300 hours (1 year)
U_g = 25 m/s, lining life is 650 hours (1 month)

From these numbers it comes that if castable concretes are the choice as a low cost lining alternative, the operating variables should be carefully chosen, in particular, the gas velocity. Although high performance castables are being developed at the present time, the high cost of these materials still make conventional castables competitive.

The selection of the gas velocity is bounded by other considerations, such as transport energy losses. The pressure drop in conveying systems tends to decrease with decreasing gas velocity, reaching a minimum point and then increasing, as the phase density increases. The operation of the system near this point seems to be the best choice, regarding both erosion and pressure drop. However, the pressure fluctuations generated

near this point should be also taken into consideration. Attempts to reach this minimum point during the sand experiments in the transport test facility failed because pressure fluctuations caused shut down of the unit, since the flame was no longer stable.

The results presented in Table 6 are expected to be valid in the case of larger pipe diameters, particularly the gas velocity exponents and the effect of temperature, both related to local processes, while there will be differences in the effect of the solids concentration, since shielding effects depend on the pipe diameter. A first approximation can be obtained by correcting the value of the solids flow rate by the ratio of 0.0254 m (2 inch) to the new pipe diameter, and using this value in the expression for the erosion rates.

4.0 BEND EROSION

The erosion process is more severe when sudden changes in the flow direction occur. The particles, due to their own inertia, tend to follow their trajectory until they collide with the wall. The same effect can be seen when obstacles are placed in the flow stream. The erosion rate is very sensitive to the particular geometry. The erosion profile obtained experimentally in a given bend can hardly be used to predict the erosion pattern in other geometries. Besides, geometry itself is modified by the erosion process. In more complex cases, like in blinded T-bends, where solids are deposited in the bend, the geometry is determined by the operating conditions of the transport units.

All the factors mentioned in Table 1 for pipe erosion apply to bend erosion. In the case of bends, the erosion pattern is not uniform but depends on the spatial coordinates. Erosion can be quantified as the total mass loss of the bend, or as the local depth of wear, the last one directly related to the bend life [20]. The effect of phase density on the specific erosion and depth of wear has been investigated by several authors [20,54,55]. They have found that for sand impacting mild steel in a circular bend, it follows the power law:

$$e \propto (W_s/W_g)^m$$

Mills and Mason [20] found exponents varying on time from -0.16 for fresh sand, up to -0.38 for degraded sand. Agarwal[55] has found the exponent to be -0.25 for sand in mild steel bends.

Unlike pipes, the wear of the bend walls is not uniform; mass losses are not directly related to the bend's life. Wear thru occurs normally at a primary wear point, where a combination of high kinetic energy and collision rates dominates. Mason[54] has introduced the concept of mean wear rate, w, defined as the mass of erodent material

which, when pneumatically conveyed around a 90° bend, results in unit depth of wear at the primary wear point. A suitable unit for this variable is milimiter per ton of material (mm/ton). He found this mean wear rate to be a power law function of gas velocity and solids to air mass ratio.

The flow pattern inside a circular bend is characterized by a relatively well dispersed layer of particles sliding around the outer radius of the bend, with particles traveling much slower than the conveying air. The trajectories between wall collisions have been reported as straight lines or distinct curves, depending on the particle size [56]. The flow behavior is further complicated by the secondary motion of the carrier fluid, which is induced by centrifugal effects. Twin eddies are formed in the radial plane which, coupled to the main flow, produce a spiral motion inside the bend. The mathematical modeling of this motion is considered unpromising[57]. As the erosion proceeds, the internal geometry of the bend changes and secondary wear points begin to develop. The geometric irregularities generate an increased turbulence and swirling flow inside the bend, causing premature failure.

Until recently, the universal solution to bend wear has been the use of long radius circular bends. This came from the idea that long radius bends behave like straight pipe sections with minimum particle-wall interactions and, for that reason, they present minimum energy losses and material degradation (erosion and attrition)[58]. However, experimental studies in long radius circular bends have shown pressure drops in excess of short radius bends and the presence of multiple wear points, indicating that collisional processes are more severe inside the long radius version[59]. Other considerations in the design of pipe bends include cost, installation and weight, variables that have brought interest to new bend alternatives, such as blinded T-bends and dirt boxes.

There have been several attempts to simulate the flow of particles in bends[36,60]. The approach has been to solve the equations of motion of the particles taking various external forces into consideration, such as drag, frictional, gravitational and centrifugal (inertial) forces. Among them, friction has been treated rather ambiguously. The friction

term has been given by an expression similar to the Fanning friction formula, with the coefficient determined empirically. A more realistic approach has been the use of the impulsive equations, assuming that frictional losses are due mainly to particle wall interactions. Trajectories, velocities and forces on the particles are then calculated after a collision, as well as the energy transferred from the fluid to the particle during the reacceleration period. The simulations presented in this chapter use the same approach, but the amount of material removed on each collision is computed. Besides motion and impulsive equations, a relation for the mass loss of the target upon impact is required. This relation was obtained empirically by using angular refractory samples which allowed to correlate the amount of material removed as a function of the impingment angle.

4.1 WEDGE EROSION

The effect of angle of impact on the erosion rates is very sensititive to the target properties and, in the case of heterogeneous materials, to the surface topology. At the present time there is no theoretical way to predict this behavior due to the complexity of the phenomena involved in the erosion process. In the case of refractory concretes this response has to be measured for a given set of conditions. The advantage in doing so is that the erosion can be considered as a statistically averaged local phenomena, and the data can be applied in many situations.

4.1.1 Experimental method

The experiments on wedge erosion were carried out in the test section of the High Temperature Pneumatic Transport Test Facility, described in Chapter 3. Methods of sample preparation and type of targets and erodent materials are the same that the ones used in the pipe erosion experiments. The only difference was the geometry of the test samples, which in this case were triangular or prismatic bars, presenting different angles

to the flow stream. Impact angles of 22.5, 30, 45 and 90 degrees were tested using wedges of 45, 60, 90 and 180 (prism) degrees. The wedges were mounted and secured in cilindrical refractory samples, like the ones used in pipe erosion. The mass loss was measured as a function of time for sand and alumina. In the case of coal slag, the high erosion rates and the repeated impact by large particles on eroded samples was too severe, and some of the wedges disintegrated. The time intervals could not be reduced since these tests were coordinated with pipe erosion tests.

4.1.2 Results and Discussion

In Figure 36 are shown some of the eroded wedge samples used during the sand tests. Figure 36a shows one of the eroded faces of a 90 degrees Fraxcast wedge (45° impingment angle). The surface morphology is identical to the one formed in the case of pipe erosion. In Figures 36b and c are shown different views of a prismatic sample in an advanced state of erosion. The amount of material removed is not radially uniform but presents a maximum in the middle region. This can be explained in terms of the radial velocity and concentration profile inside the pipe. There is a number of studies describing concentration, mass flow and particle velocity distributions in vertical pipes[61] showing a decrease in all these quantities as approaching the pipe walls. The eroded profile is more likely to be caused by the particle velocity distribution because, as follows from the last chapter, velocity is the most sensitive variable when considering erosion rates.

In Figure 37a is shown the wedge's weight loss as a function of time for two different impingment angles, using sand as erodent. The gas velocity was 17.8 m/s, the solids flow rate 50 kg/h and the temperature 530°C. There is an initial period in which the matrix is eroded away and the edges of the wedge are rounded, after which the erosion rate becomes constant. This steady value of the erosion is plotted for the different wedge samples in Figure 37b. The erosion rate is expressed in terms of unit mass but, unlike the specific erosion rates, this mass correspond to the mass of particles hitting the sample, calculated assuming a uniform particle concentration distribution. The erosion presents a

behavior similar to brittle materials, with a minimum erosion rate at low angles of impact, being maximum at frontal impact. The same is the case of alumina, shown in Figure 38, being similar for the three target materials. However, a brittle behavior cannot explain these curves, since the variation in the erosion rates is too abrupt, occurring between 20 and 30 degrees. These curves can be better explained in terms of a shadowing mechanism, expressed quantitatively in Equation 2-7. For low angles of impingment, the large aggregates protect the matrix from impact. As the angle increases, the erodent can reach the matrix directly. This kind of behavior is well described by Equation 2-7, which is written in terms of two parameters: the maximum erosion rate (at 90 degrees, E_{90}) and the ratio of sphere diameter to interparticle spacing (R). The first parameter can be evaluated by reading the value of the erosion rate at frontal impact directly from the plot. The second one can be accurately calculated by knowing the angle at which E/E_{90} takes half its maximum value. In the case of Kaotab and Fraxcast samples eroded by alumina, this occurs at about 28°. Replacing the values in Equation 2-7, it comes R=0.3, that is an interparticle spacing about three times the size of a spherical aggregate. Looking at Figure 15, and considering only protruding aggregates, it follows that this value is not unreasonable, suggesting that the behavior shown by the erosion rate versus impingment angle is not a manifestation of material's response to impact, as suggested by Figure 1, but a consequence of the surface topology. In fact, the information obtained in this section can be used as a characterization of surface topology in concretes, specifically for shadowing effects. Keeping in scope the purpose of these tests, Equation 2-7 is then used as a correlation for the effect of impingment angle on the erosion rate, to be used in the bend erosion simulation.

a)

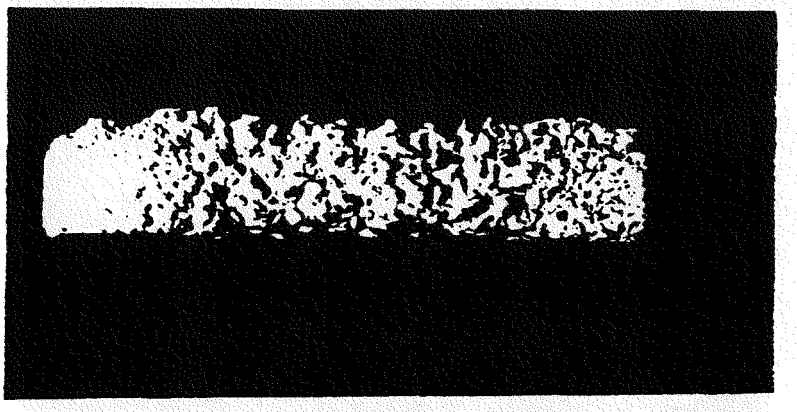

b)

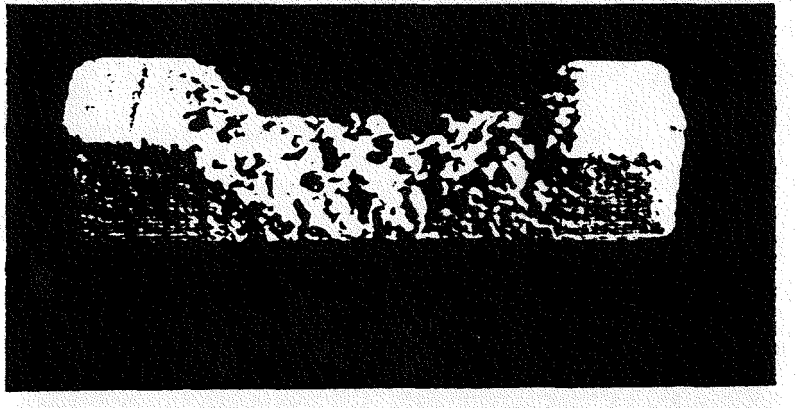

c)

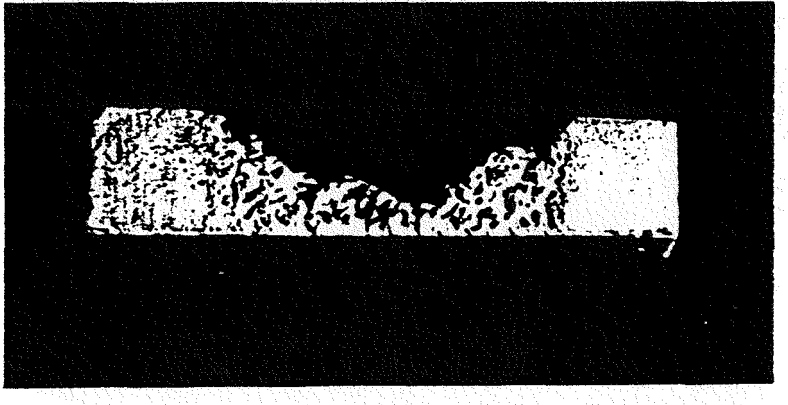

Figure 36. Eroded wedge samples: a) Fraxcast 45° wedge, b) and c) Fraxcast 90° wedge

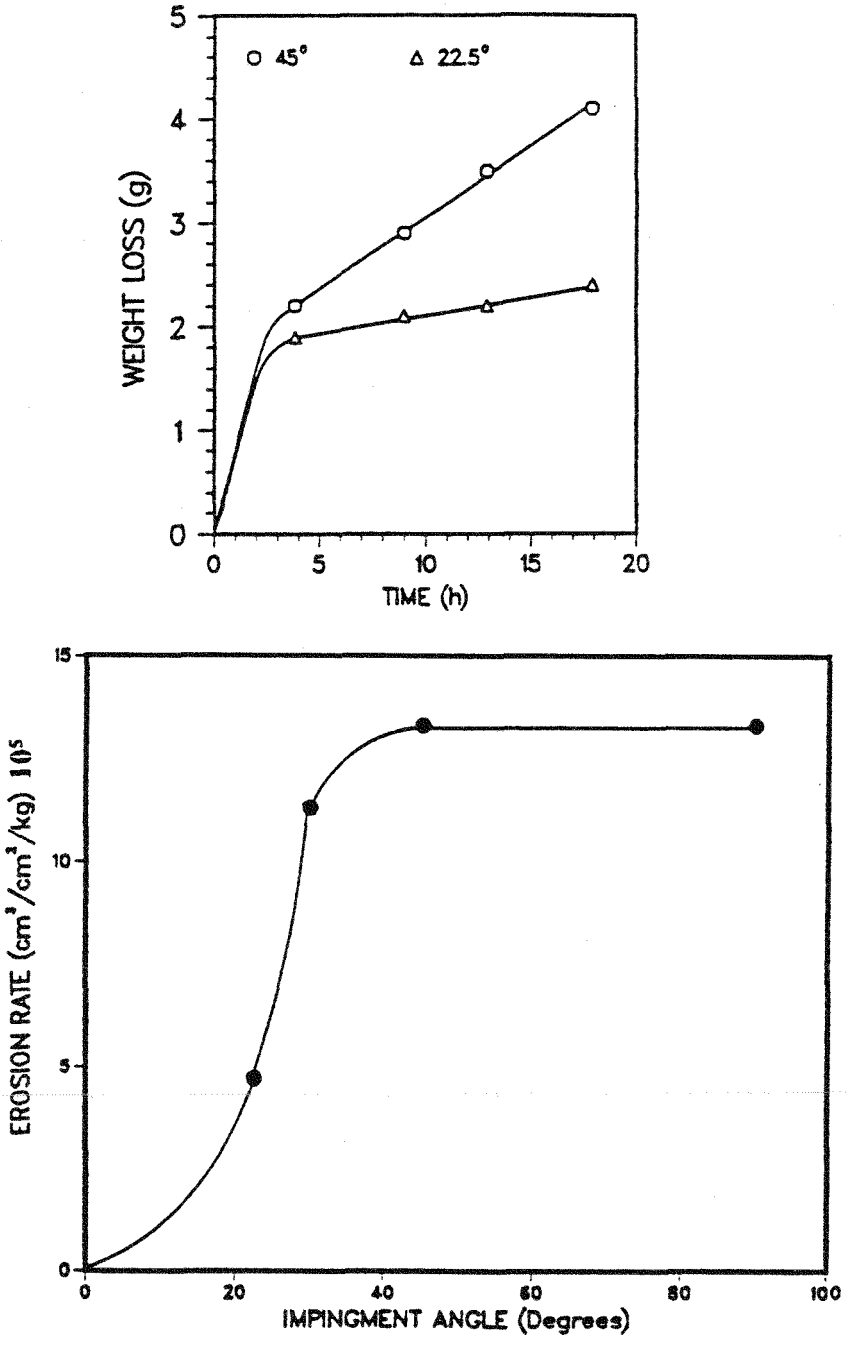

Figure 37. Effect of impingment angle on the erosion rate of a Fraxcast sample at 530°C using river sand as erodent material

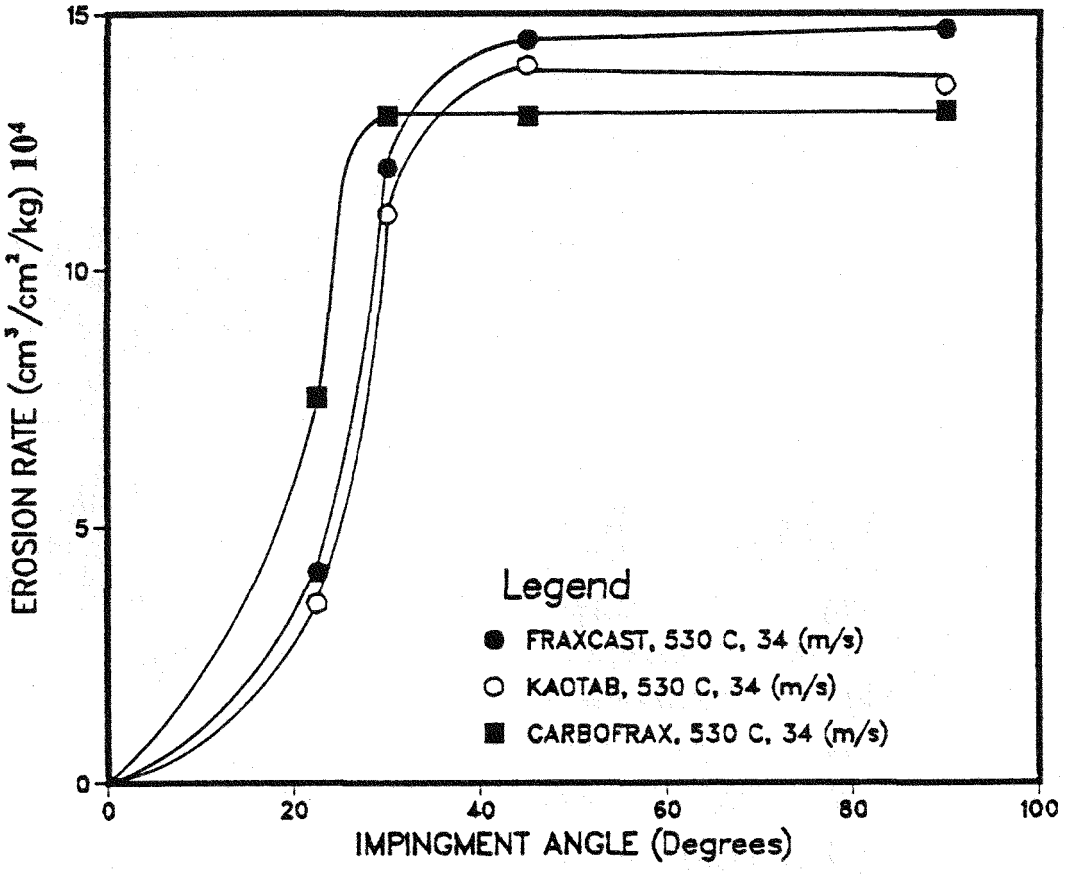

Figure 38. Effect of impingment angle on the erosion rate of refractory concretes using alumina as erodent material

4.2 PARTICLE IMPACT

Particles retain a significant fraction of their kinetic energy after a wall collision. This energy, along with the energy gained during the reacceleration by the drag forces, will cause further material removal from the target surface at secondary or tertiary wear points. The prediction of these points requires the solution of the particle dynamic equations after impact, for which the particle velocity and direction of rebound are the initial conditions. Rebound parameters depend on both target and erodent characteristics. These parameters have been the subject of study in many areas[62], and there is a number of measurements using high speed photography for larger particles and Laser Doppler Velocimetry (LDV) for small particles.

A direct central impact proceeds in two stages. There is an initial period of deformation, beginning when the particle and surface make contact and ending at the time of maximum deformation, and a period of restitution, which continues until the bodies separate. The ratio of impulse during the restitution period to impulse during the deformation period is defined as the restitution coefficient[63], ε_r. For a particle impacting a massive body, this ratio can be written in terms of the impact and rebound velocities:

$$\varepsilon_r = U_{p,rebound} / U_{p,impact} \tag{4-1}$$

The coefficient of restitution gives a measure of how much kinetic energy is lost by the particle during the impact. This energy is lost as vibrations, plastic deformation and removal of material at the target surface. This coefficient depends on particle size, shape and velocity. When particles hit the surface at an angle α, there is a tangential component of the impulse which can be evaluated according to Coulomb's law in terms of the kinetic friction factor f_r[64]. For the particle velocity components then follows:

$$U_{p,rebound,normal} / U_{p,impact,normal} = \varepsilon_r \tag{4-2}$$

$$U_{p,rebound,tangential} / U_{p,impact,tangential} = 1 - f_r(1 + \varepsilon_r \tan(\alpha_i)) \tag{4-3}$$

This model alone has not been successful when used in simulations mainly because of the poor understanding of levitation and dispersion mechanisms inside pipes. The problem has been overcome by using the Abnormal Bouncing Model[65]. In this model, the pipe wall is replaced by a virtual wall inclined at a certain angle. The effect is a generation of momemtum in the radial direction which works as a mechanism for particle dispersion inside the pipe. This model is intended to take care of the irregularities in both particle shape and wall roughness, however, it requires a number of assumptions about the angle of inclination of the virtual wall.

The rebound dynamics in surfaces that have suffered erosion can only be described in a statistical sense. This becomes evident when examining the number of possible geometric situations at impact. The local impact angle between a relatively small particle and the eroded surface may deviate considerably from the geometric average. For this type of situations Tabakoff[62] has used a polynomial correlation in which the ratio of rebound and impingment angles and velocities is expressed as a function of the impinging angle:

$$U_{p,r} / U_{p,i} = 1.0 + a_1\alpha_i + b_1\alpha_i^2 + c_1\alpha_i^3 + d_1\alpha_i^4 \qquad (4\text{-}4)$$

$$\alpha_r / \alpha_i = 1.0 + a_2\alpha_2 + b_2\alpha_i^2 + c_2\alpha_i^3 + d_2\alpha_i^4 \qquad (4\text{-}5)$$

This type of correlations includes a statistical average of many particular situations and for that reason is useful in the simulation of erosion processes, where many particles are involved. The relation between restitution coefficients and erosion has been investigated [66] and it has been concluded that the kinetic energy lost during impact does not give sufficient information regarding erosion.

4.2.1 Experimental Method and Results

Particle impact and rebound parameters were determined using a high speed photographic technique in which single particles were gunned, using an eductor, into a ceramic surface. The light source was a strobe which produced flashes at a frequancy ranging from 1 to 500 Hz. Particles were fed into the eductor and their trajectory photographed. Particle velocities and angles were measured from the pictures, since magnification and strobe frequency were known. A considerable number of points had to be measured in order to obtain the correlations for rebound angles and velocities, because of the dispersion in the data. This variation was attributed to shape irregularities, as it can be seen from Figure 39, where the rebound of spherical and irregular particles impacting under the same conditions is compared. The ratio of rebound to impingment angles and velocities for 2 mm. alumina particles, impacting a smooth Fraxcast surface at a velocity of about 5 m/s are shown in Figures 40 and 41. The data are well correlated by cubic polynomia:

$$\alpha_r / \alpha_i = 1.0 - 1.09\ 10^{-2}\ \alpha_i - 4.66\ 10^{-5}\ \alpha_i^2 + 1.86\ 10^{-6}\ \alpha_i^3 \qquad (4\text{-}6)$$

$$U_{p,r} / U_{p,i} = 1.0 - 4.35\ 10^{-3}\ \alpha_i - 1.17\ 10^{-4}\ \alpha_i^2 + 8.00\ 10^{-7}\ \alpha_i^3 \qquad (4\text{-}7)$$

The rebound particle velocity ratio presents a small dispersion at all angles, while the rebound angle ratio is very much dispersed, particularly at very small and very large (close to 90 degrees) angles. This means that the kinetic energies after impact are well determined, while trajectories are not. Data of impact on rough surfaces were also taken but in this case the dispersion was higher and the amount of data did not allow for a good polynomial fit. This enhanced dispersion in fact causes an increased collision rate in the pipe, and it can be assumed to be the cause of enhanced wear in refractory lined pipes.

Figure 39. Particle rebound on a smooth Fraxcast surface.
a) Glass spheres. b) Alumina particles

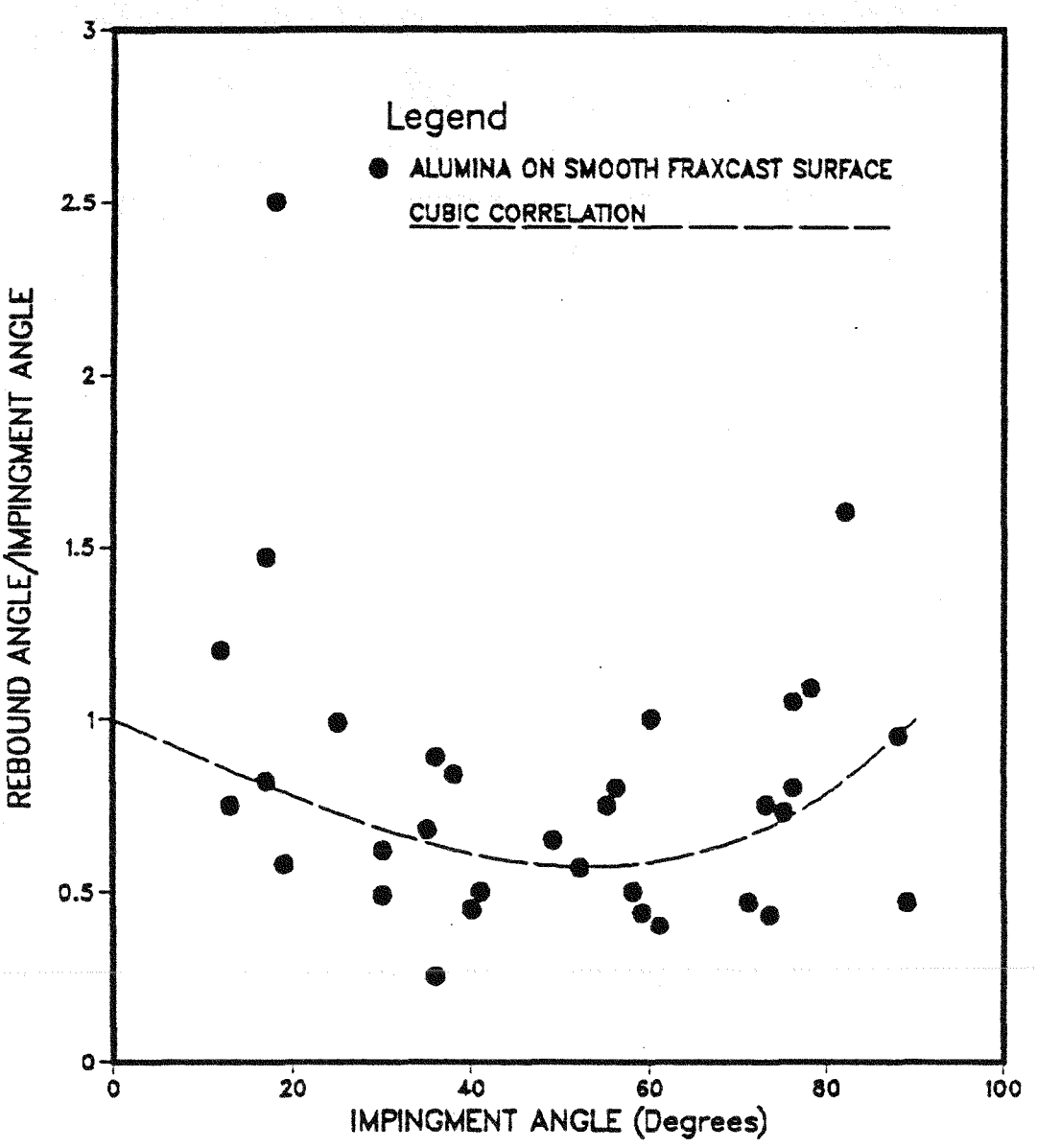

Figure 40. Ratio of rebound to impingment angles as a function of the impingment angle for alumina particles impacting Fraxcast concrete

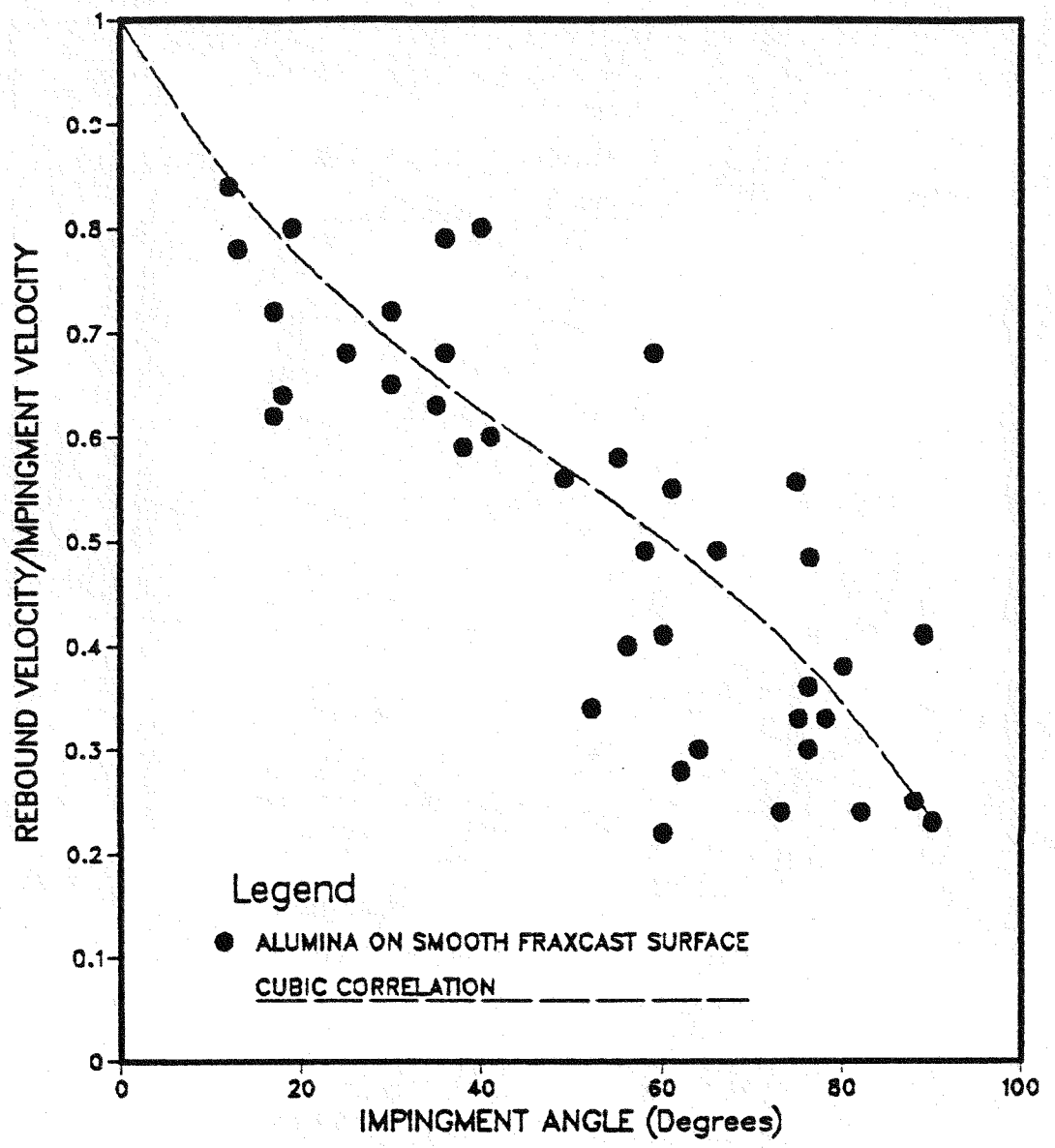

Figure 41. Ratio of rebound to impingment velocities as a function of the impingment angle for alumina particles impacting Fraxcast concrete

4.3 BEND EROSION SIMULATION

A two-dimensional model for the erosion of 90° circular bends is presented in this section. The basic approach has been to couple particle dynamic calculations inside this type of bends with the fundamental measurements of erosion rates at different angles of impingment and particle rebound correlations to develop a working model which predicts wear rates as a function of time and space. The structure of the model is presented in the diagram on Figure 42. A number of assumptions had to be made in order to simplify the formulation of the model:

1. Particles are considered to be spheres in the calculation of trajectories and erosion parameters. Effects of particle shape on the erosion rates are already included in the correlations used to calculate material removal rates.
2. Particle concentration is uniform upstream the bend.
3. Gravity and drag are the only important forces acting on the particles during flight. Aerodynamic lifting, turbulence and particle rotation effects are neglected.
4. Interparticle collisions are not important in the calculation of trajectories for dilute phase conditions. In the case of the erosion rates, interparticle collisions are considered in the exponent of the solids concentration correction.
5. The flow pattern is not affected by the presence of the particles.

4.3.1 Particle Dynamics

Particle trajectories are calculated following an Eulerian approach. For any time element, the drag force on the particle is calculated from the slip velocity and the equations of motion are integrated to obtain the particle trajectory. Refering to Figure 43, the components of the slip velocity vector for each particle are calculated from the gas velocity field and instant particle velocity for each particle.

$$|U_s| = (U_{sx}^2 + U_{sy}^2)^{1/2} \tag{4-8}$$

$$U_{sx} = U_{gx} - U_{px} \tag{4-9}$$

$$U_{sy} = U_{gy} - U_{py} \tag{4-10}$$

The drag force depends on the slip velocity and drag coefficient, which is a function of the particle's Reynolds number.

$$Re_p = D_p U_s \rho_g / \mu_g \tag{4-11}$$

$$C_D = 24/Re_p \qquad for\ Re_p<0.3 \tag{4-12}$$

$$C_D = 18.5/Re_p^{0.6} \quad for\ Re_p<1000 \tag{4-13}$$

$$C_D = 0.44 \qquad for\ Re_p>1000 \tag{4-14}$$

$$|F_D| = C_D A_p \rho_g |U_s|^2 \tag{4-15}$$

The components of the gas velocity field are calculated according to a 1/7 power law . Refering to the nomenclature given in Figure 43:

$$|U_g| = U_{gmax}(1 - |r_{i,k}|/r_o)^{1/7} \tag{4-16}$$

In the program, the value of U_{gmax} is corrected by multiplying by the ratio of local eroded to initial pipe radius.

Having solved the force balance, particles trajectories are calculated integrating numerically the equations of motion of each particle:

$$x_p(t+\Delta t) = x_p(t) + U_{px}(t)\,\Delta t + F_{Dx}\,(\Delta t)^2 / (2\,m_p) \tag{4-17}$$

$$y_p(t+\Delta t) = y_p(t) + U_{py}(t)\,\Delta t + F_y\,(\Delta t)^2 / 2 \tag{4-18}$$

where

$$F_y = F_{Dy}/m_p - g\,(\rho_p - \rho_g) / \rho_p \tag{4-19}$$

Initial conditions for these equations are calculated assuming that the particles come from the pipe uniformly distributed and with a vertical velocity resulting from a balance between drag forces and gravity, that is, U_{px} is zero and U_{py} varies according to the radial gas velocity profile at the entrance.

The pipe walls are divided into equal area elements, each one expressed as a function of an angular coordinate and time. $B_1(\zeta_k,t)$ and $B_2(\zeta_k,t)$ represent the distance from the center of the original bend at angle ζ_k and time t for the outer and inner surfaces respectively. At time zero, they correspond to the outer and inner bend radius.

The model proceeds integrating the equations of motion for each particle, calculating the particle positions at each time interval. For each position and each particle there is a check, in which particle coordinates are compared to the coordinates of the wall element at that particular angular position. A particle radial distance from the center of the bend in excess of $B_1(\zeta_k,t)$ or smaller than $B_2(\zeta_k,t)$ is indicative of a collision with the outer or inner wall respectively. If this happens, the subindex of the wall element, particle velocity and angle of impact before impact are saved. The angle of impact is calculated from the angle of trajectory of the particle and the slope of the bend wall at the moment of impact. The slopes of the wall are determined numerically using their cartesian coordinates, $b_{ix}(\zeta_k,t)$, $b_{iy}(\zeta_k,t)$, i=1 or 2. Rebound angles and velocities are calculated based on the restitution coefficients or correlations.

The integration proceeds until the particles reach the end of the bend. Integration times for this part of the simulation are of the order of tenths of a milisecond. The result is a collection of data on number of collisions, as well as angles and velocities of impact, for each wall element. The wall recession of each element is calculated by adding the contributions of each impact, measured in the wedge experiments.

$$E = (4/3)\pi\rho_p(D_p/2)^3/W_s\, E_{wedge}(\alpha_i)\,(U_p/U_{p,wedge})^n\,(W_s/W_{s,wedge})^{(1+m)}\,c_p \qquad (4\text{-}20)$$

In this equation, $E_{wedge}(\alpha)$ is the correlation obtained for the wedge samples,

expressed in units of $cm^3/cm^2/h$, and it is corrected for particle velocity and solids concentration. The correction for particle velocity uses the actual particle velocity at impact related to the particle velocity at which the wedge experiments were performed, while the particle concentration correction does not uses local concentrations but the concentration in the pipe section before the bend, in agreement with the method as the exponent m is calculated. c_p in the expression is the number of particles that can be found aligned in the pipe diameter, calculated from the cubic root of the particle concentration in the pipe.

The values calculated for wall recession are very small, since only a limited number of particles is used in the simulation, normally between 200 and 400 particles, flowing through the pipe in miliseconds. The methodology was to assume that particle trajectories and wall collisions remained constant for many hours, so that the values for wall recession were amplified several orders of magnitude, given by the ratio of a fixed real time interval (of the order of hours) to the time that takes the number of particles used in the simulation to flow through a given cross section in the pipe, assuming the particles to be uniformly distributed. The new walls generated were characterized by a very high roughness, so a convolution technique was used to smooth them. In this technique, five area elements in positions k-2 to k+2 were taken, their positions averaged and the result assigned to position k. This was repeated through the whole wall, with the result of a smoother surface that presented no convergence problems in the calculations.

The detailed calculations used in this model are presented in Appendix F. In Figure 44 are shown the trajectories of single particles inside a circular bend. Figure 44a shows the behavior of a 200 μm sand particle compared with a 50 μm one at a gas velocity of 20 m/s in a two inch pipe. Large particles are not very sensitive to the flow field inside the bend, while smaller particles are easily deviated from their trajectories. From this it comes that wear patterns inside the bend will be more dependant on the fluid dynamics when the particles are smaller. Examining Figures 44b and c it can be seen that inside these kind of bends there are important radial variations in voidage. This result agrees with visual observations reported for circular bends.

In Figure 45 has been simulated one of the experiments by Mason[54] on the erosion of perspex bends. The erodent material was 60 μm alumina circulating in a stream at 88 m/s, and solids to air ratio of 3.3. The primary and secondary wear points are very well predicted by the model, with differences in the tertiary wear point. The model predicted angles of 24 and 33 degrees for these points, as compared to 22 and 36 degrees measured by Mason. Data for the simulation were taken from other sources[18].

The development of secondary wear points occurs in stages. In Figure 46 are shown the results of a simulation for a bend lined with Fraxcast concrete at four time intervals. The gas velocity for this simulation was 17.8 m/s, the solids flow rate 51 kg/h and the temperature 530°C. Four hundred particles were used in the simulation, but only a few of them were plotted in the diagram. The initial flow pattern is characterized by a layer of solids circulating near the outer wall of the bend, with no significant interaction with the inner wall of the bend (Figure 44 a). Two hundred hours later (Figure 44b) the geometry at the primary wear point has changed significantly and particles are rebounding towards the inner wall. As the geometry keeps changing (Figure 44c and d) so does the particle dynamics inside the bend.

From a practical point of view, the primary wear point is the most critical one because this is the point where the bend will fail. This point can be easily evaluated without information about rebound characteristics of the particles. In Figure 46 is compared the simulation of a Fraxcast lined bend when drag forces and rebound are present or not. The eroded patterns before the primary wear point are not totally different and the wear thru point, as well as useful life of the bend, can be well predicted in both cases. As pointed before, drag forces should be included when dealing with small size particles, or when the gas velocity is high. The big advantage of the complete formulation of this type of models is in the development of new bends alternatives. Long radius circular bends present a number of disadvantages, and there is now more interest in other types of bends, such as blinded tees and dirt boxes. In these cases, most of the wear is caused by secondary impacts and their simulation requires the complete basic

approach given in this section to circular bends. The most time consuming and challenging part of this type of simulation is the evaluation of the erosion parameters, that is, number of collisions, angles and velocities of impact. Even in two dimensional modeling, the solution of the motion equations for irregular geometries may require the development of new algorithms. The problem is even worse when small particles and flow circulations occur, where a higher level of simulation, including turbulence effects, is required. This task still may be accomplished with the use of supercomputers. Once the erosion parameters are determined, the amount of material removed can be calculated using data or correlations for the erosion rates.

The high concentration layer generated in the outer region of the bend can be seen as a shield that protects the bend against direct impact of the incoming particles. This shielding effect has been discussed in the chapter of Pipe Erosion as one of the causes of the decrease of the specific erosion rates as the solids concentration increases but, being unknown the particle dynamics in straight pipe sections, no calculations could be made to prove it. This is not the case of circular bends, in which the particle dynamics is well determined. To gain insight into this problem, one of the assumptions made in the formulation of this model (no interparticle collisions) was relaxed. The time interval for the integration of the particle trajectories was decreased and, besides wall collision checking, particle to particle collisions were monitored. To do this, the distance between each particle and its neighbors was evaluated at each time increment and compared to the particle radius. The particle trajectories were not changed upon impact. Instead, particles were allowed to continue until hitting the wall, but the impact event was registered and saved. The geometry and operating conditions used in the simulation are the ones shown in Figure 47. The solids flow rate, and for that, the particle spacing and amount of particles circulating inside the bend were increased. A plot, showing the fraction of particles hitting the wall between angles of 20 and 30 degrees (where primary wear occurs) and that have not been intercepted by other particles, is shown in Figure 48. The ordinate axis is expressed in term of number of high energy collisions against the wall (20 to 30 degrees) divided by the number of particles used in the simulation. This is an

analogous of the specific erosion rates and, in fact, the behavior of collisional rates shows a power law of negative exponent, equal to -0.2, consequence of the shielding effect of the particles. The wear rates at the wear point can be assumed to be closely related to these high energy collisions.

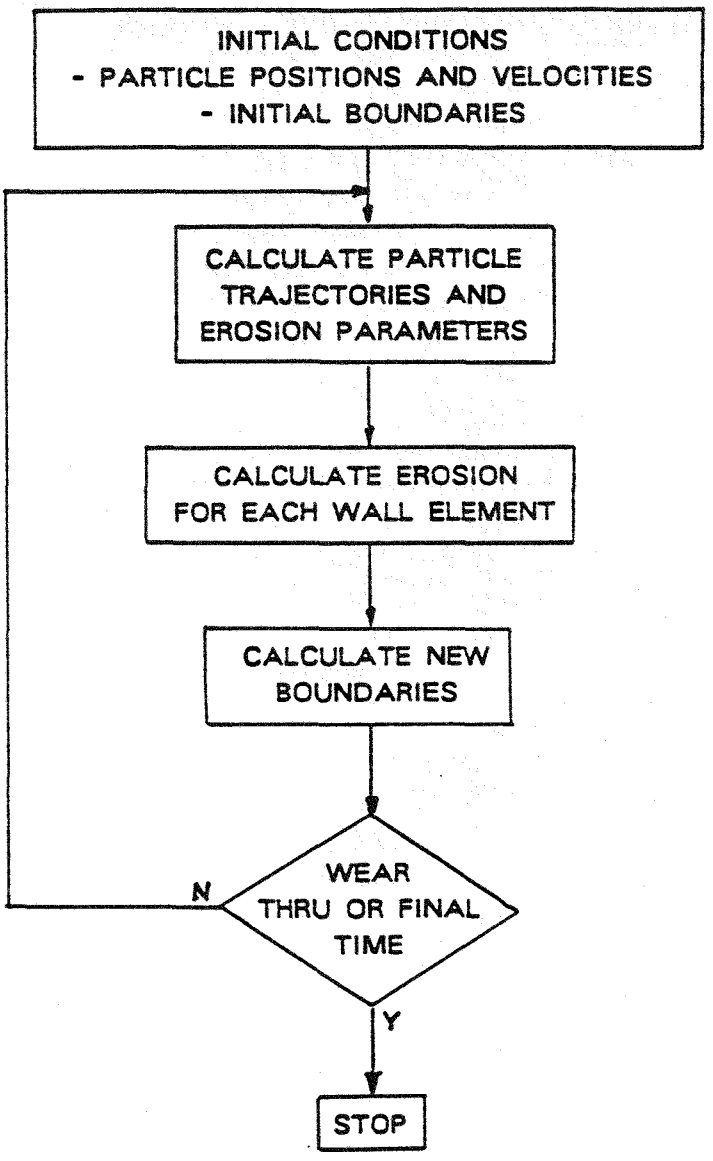

Figure 42. Flow diagram for the bend erosion model

Slip Velocity $\vec{U}s = \vec{U}g - \vec{U}p$

Drag Force $\vec{F}_D = \dfrac{(C_D\ Ap\ \rho_g\ Us^2)}{2} \dfrac{\vec{U}s}{|\vec{U}s|}$

Gravity $\vec{F}_g = (\rho_p - \rho_g)/\rho_p\ \vec{g}$

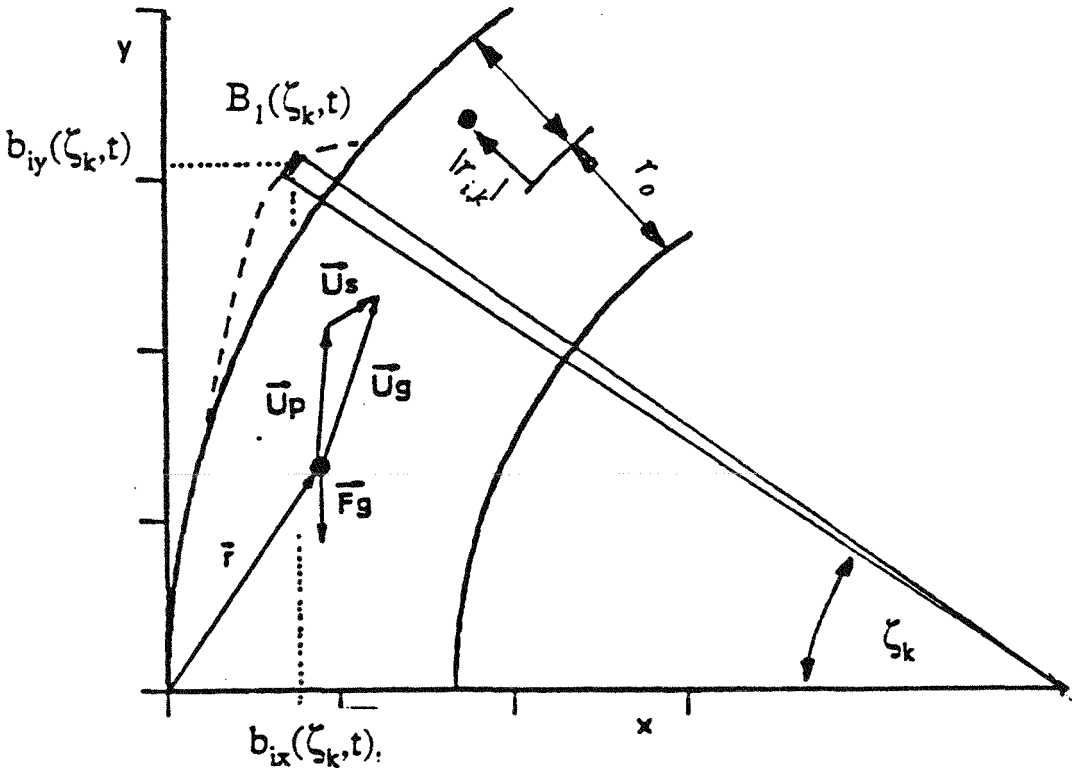

Figure 43. Variables of the model

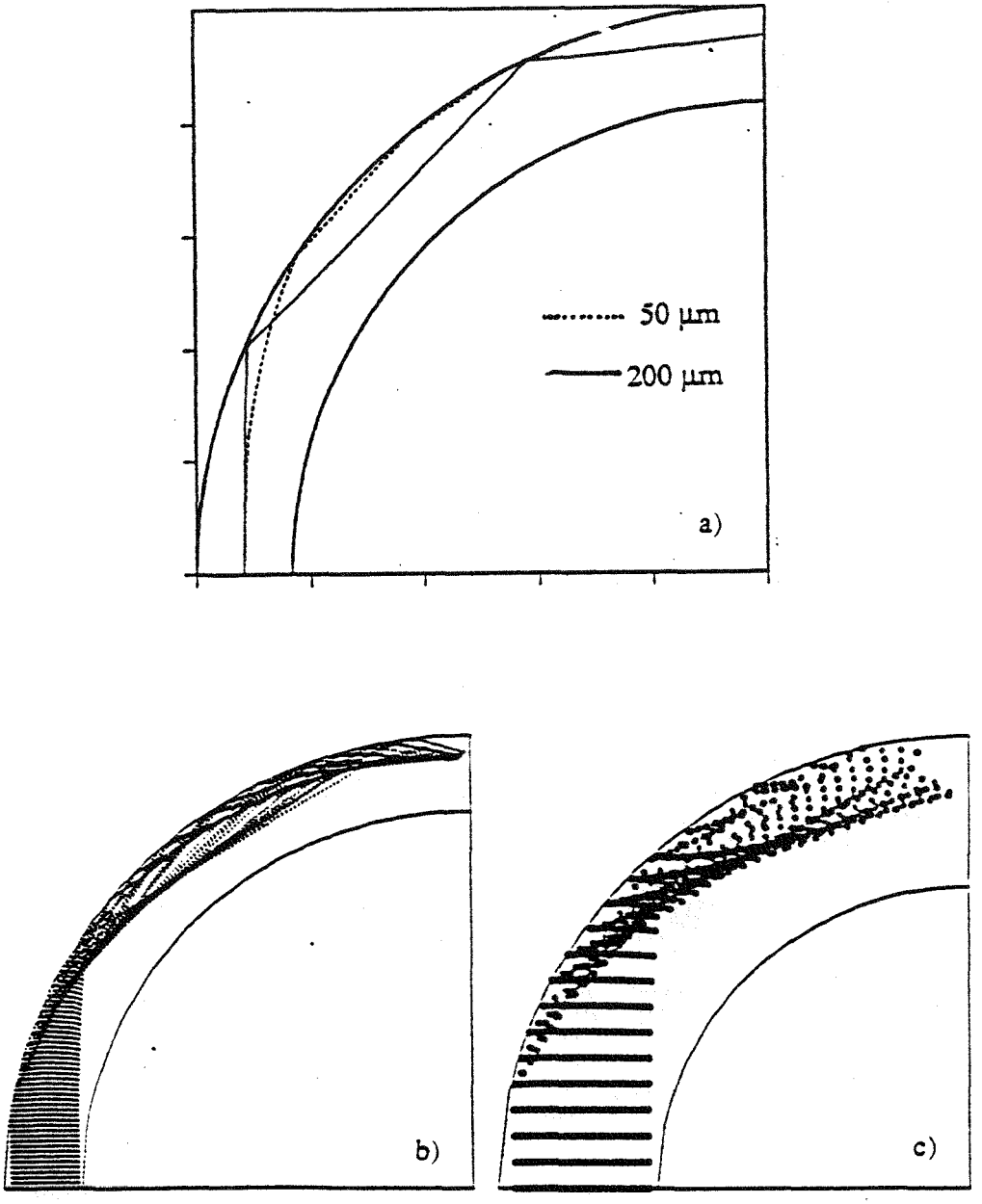

Figure 44. Trajectories of single particles inside a circular bend

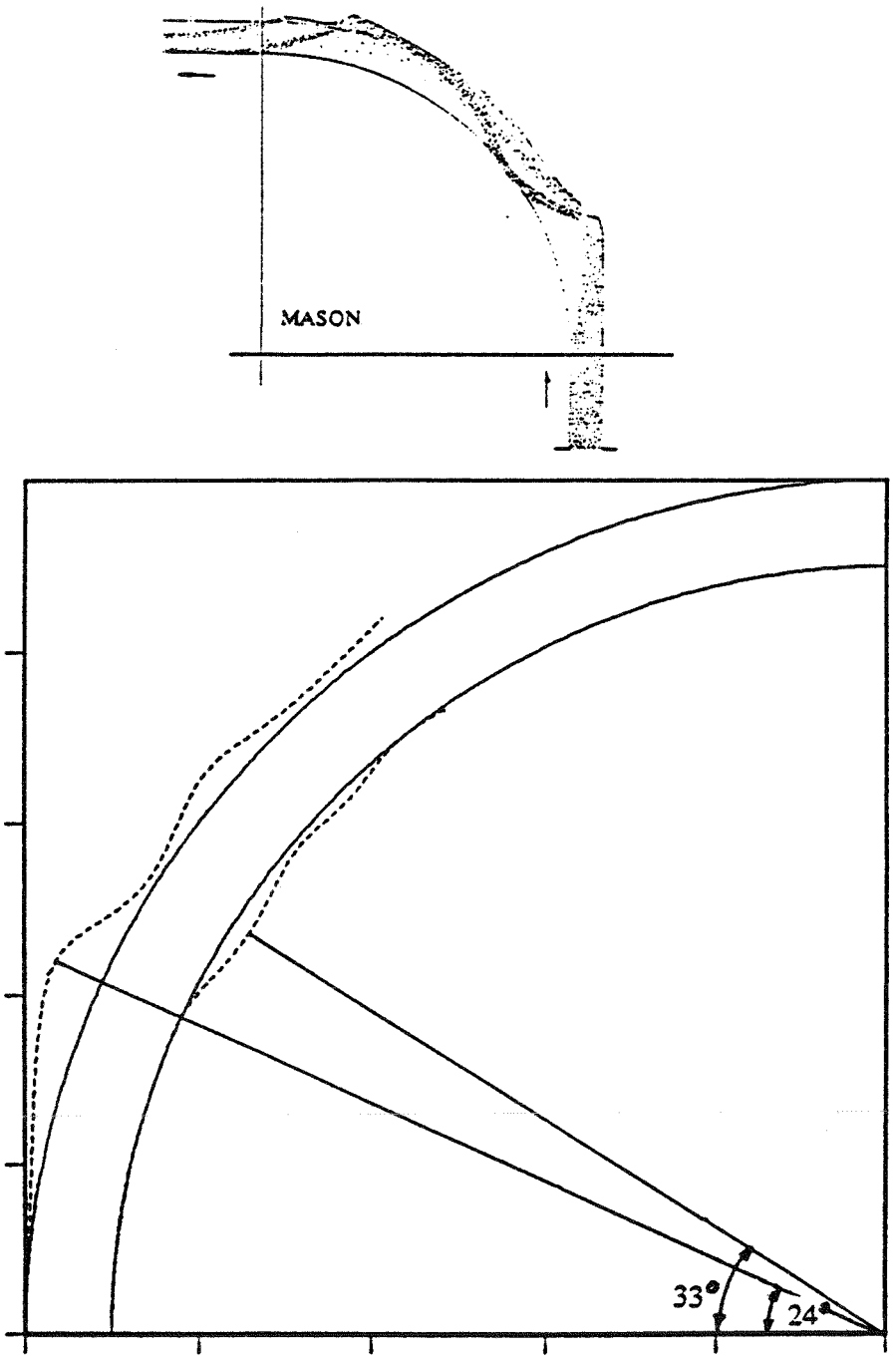

Figure 45. Comparison with experimental data

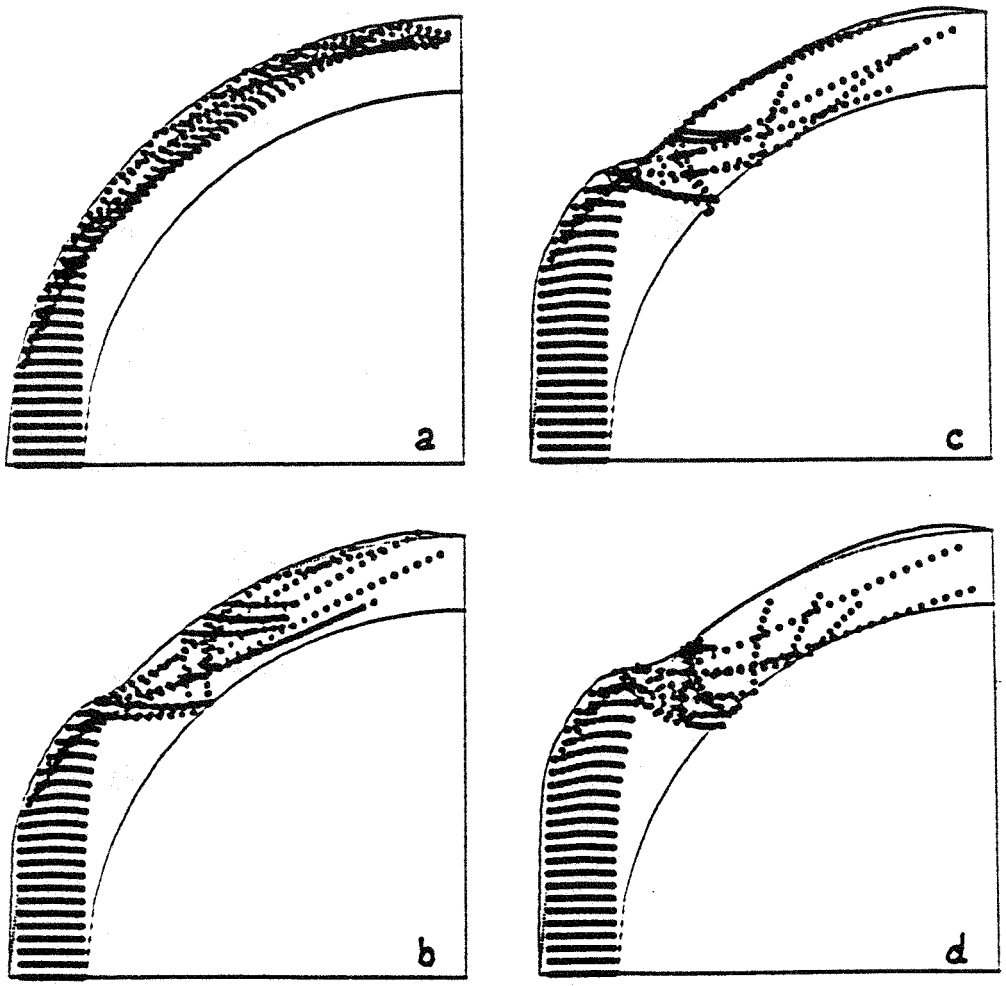

Figure 46. Development of secondary wear points

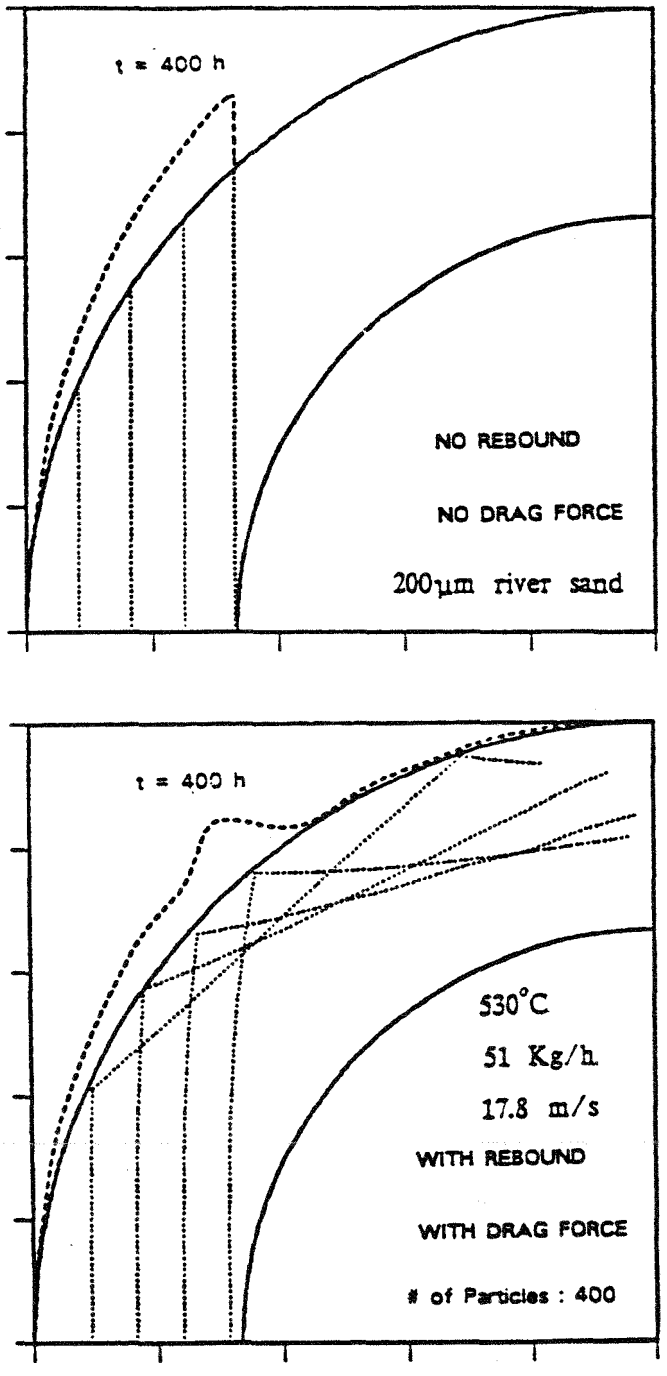

Figure 47. Simulation of a Fraxcast lined circular bend

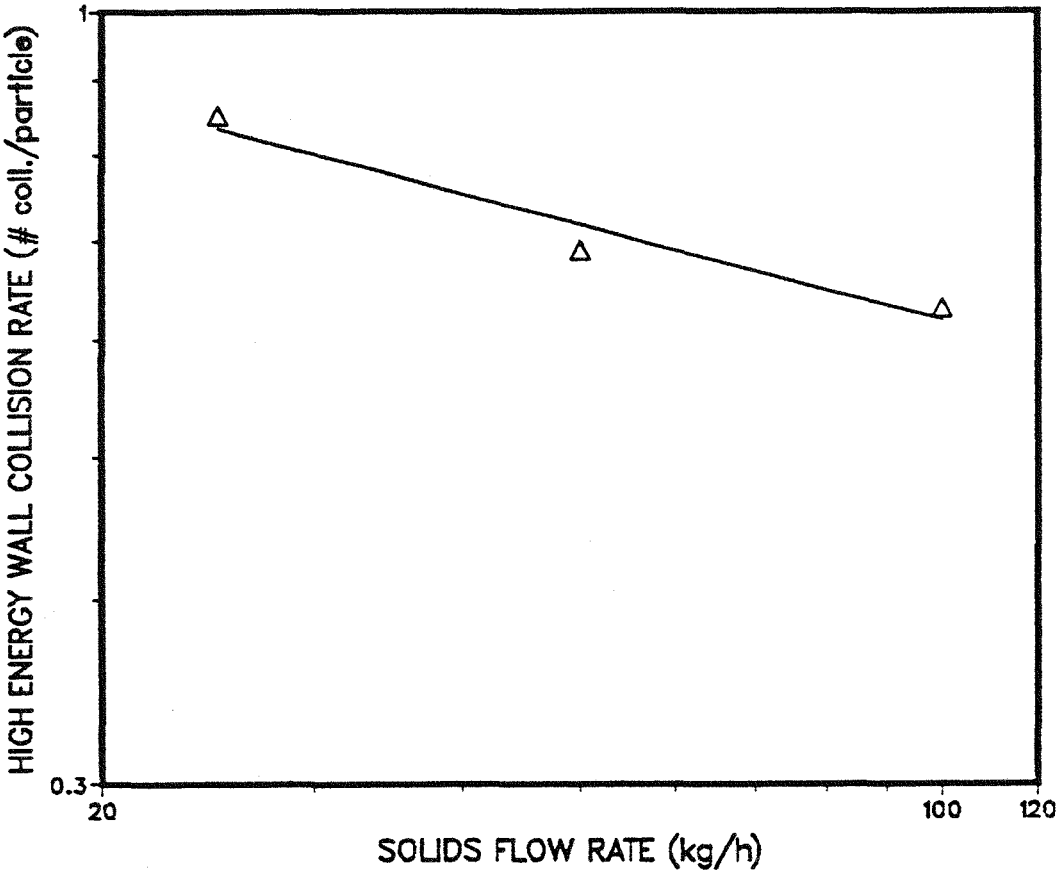

Figure 48. Effect of solids concentration on collisional rates

4.4 WEAR OF BLINDED T-BEND

Blinded T-bends are becoming an important alternative to the use of long radius circular bends in pneumatic conveying units handling abrasive materials. They are characterized by a very long service life (easily, ten times the life of a long radius bend) and pressure losses comparable to those of short radius elbows[67]. One of the drawbacks with T-bends is the scarcity of data available for design. T-bends are particulary complex due to the solids deposition, which depends on the gas velocity and solids flow rate. This means that the internal geometry of the bend is a function of the operating conditions. Since gravity plays a major role in particle deposition, the orientation of the T-bend is very important. In this section is addressed the effect of the operating variables on the internal geometry of a particular bend, including descriptions of flow and wear patterns.

4.4.1 Experimental Method

The experimental apparatus is shown in Figure 49. Glass beads, with a weight mean particle diameter of 450 μm were fed through a live-bin vibrating-screw feeder unit into a 0.0508 m (2 inch) diameter Excelon pipe. The air was provided by a 7.5 HP Roots blower. The gas-solids mixture moved through a 5 m. acceleration section, at the end of which was placed a glass T-bend, with an end blinded in the flow direction. The dimensions of this glass bend are given in Figure 50. This bend could be positioned in two ways: horizontal to horizontal or horizontal to vertical. A third orientation, vertical to horizontal, was achieved by extending the acceleration section upwards. In all cases, the solids were recovered in a settling chamber. Both, gas velocity and solids flow rate, were manipulated to obtain the different flow regimes for each orientation. Flow patterns were visually observed and photographed. For the wear tests, the internal surface of the bend was painted in strips with black ink, as shown in Figure 50. The removal of this paint was then mapped into a three dimensional diagram of the T-bend.

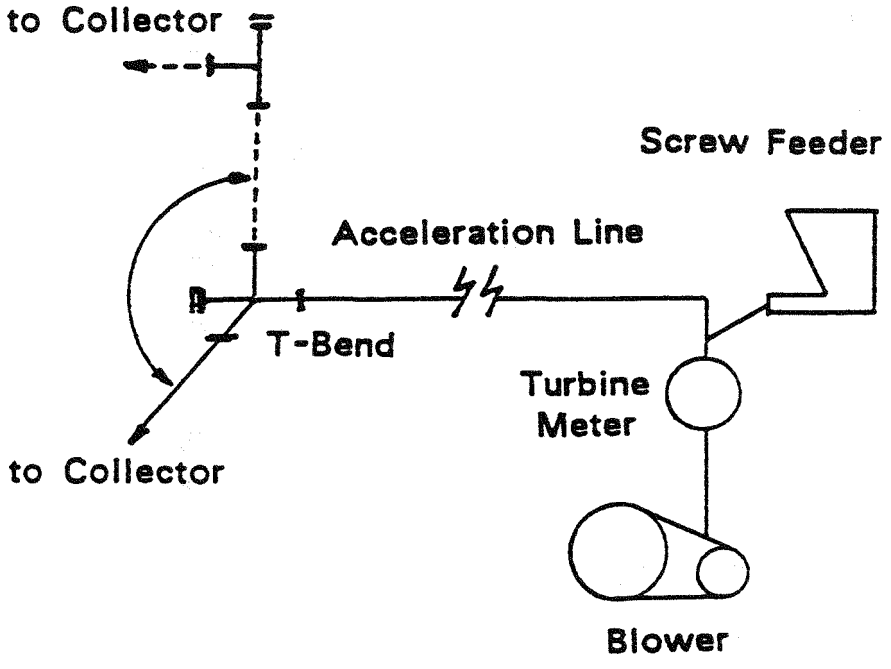

Figure 49. The test unit

4.4.2 Flow Patterns

The flow patterns were studied for three orientations: horizontal to horizontal, horizontal to vertical upwards and vertical upwards to horizontal. In all cases the patterns described correspond to a steady state operation.

In the horizontal to horizontal orientation the solids began to accumulate in the dead end of the T-bend. In Figure 51 are shown pictures of the bend for two different operating conditions. Depending on the values of gas velocity and solids concentration, different regimes were possible, as it is shown in Figure 52. At high air velocities and low solid flow rates the dead end is depleted of solids. An increase of the solids flow or a decrease in the gas velocity caused the solids to deposit, filling the end zone and

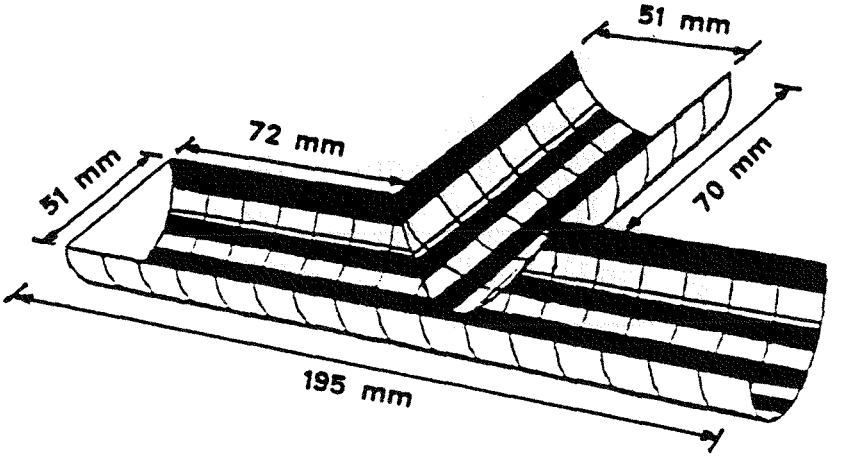

Figure 50. The glass T-bend

ultimately the outlet branch of the T. This configuration was very stable and the boundary lines shown in Figure 52 were very well defined.

In the horizontal to vertical orientation the same kind of behavior was observed (Figure 53), and the boundary lines were still well defined, though there was a small oscillation, in which the surface of the wedge formed at the dead end moved a few millimeters back and forth. This oscillation increased at high air velocities. Figure 54 shows the shapes of the wedges in two different cases. Picture (a) corresponds to a gas velocity of 10.6 m/s and 21 kg/h. in which the surface of the wedge is almost planar. In Picture (b) the gas velocity is 10.8 m/s and the solids flow rate is 98 kg/h. After reaching the outlet branch of the bend, the wedge developed two slopes. The steepest one faced the inlet branch of the T, where the shear by the gas counteracted the weight of the solids. and angles much higher than the angle of repose of the solids were possible. The point of change of slope was not stationary. This is an important result since T-bends in this orientation are commonly assumed to behave as a short radius elbow, in which the dead end becomes a concave surface. In this study was observed that when the dead end is

filled a convex surface is always generated. The result of this constriction is an increase of the local gas velocity and drag on the particles in this point.

The vertical upwards to horizontal orientation was the most unstable. There was no solids accumulation in any operating condition tested (gas velocities from 8 to 30 m/s, solids flow from 4 to 100 kg/h). In Figure 59 (Case 5, wear tests) is shown the flow pattern at 11 m/s and 37 kg/h. A cloud of solids was located in the center of the T, rotating in the direction shown in the figure. The particle concentration inside the cloud increased as the solid flow rate increased. The dead end was relatively depleted of solids at all times, and particles in this region were rotating and rebounding in all directions. At very high solid flow rates, there was a cyclone effect, in which the solids in the end zone slide over the walls following a helical path towards the cloud in the center.

4.4.3 Wear Patterns

The wear patterns are directly related to the flow pattern and internal geometry. Five cases and three orientations, shown in Table 7, were considered.

The wear pattern for Case 1 is shown in Figure 55. Under these operating conditions a wedge of solids formed in the dead end, protecting it from the particle bombardment. The big advantage of this layer is that it resists the first impact of the particles, which is the one with the highest kinetic energy. Subsequent impacts will cause much less damage. The zones marked in black correspond to high wear rates (ink removed in the first 5 to 10 minutes of test). Dotted regions indicate moderate wear (ink removed at the time indicated by Table 7), The solids impacting the wedge rebounded upwards, causing moderate wear in most of the free end region. There was significant wear in the plane of the wedge, caused probably by both erosive and abrasive wear, since the solids in this plane move downwards to be carried again by the air. The particles then followed a helical path, causing moderate wear in the region of the outlet branch that opposses the dead zone.

a)

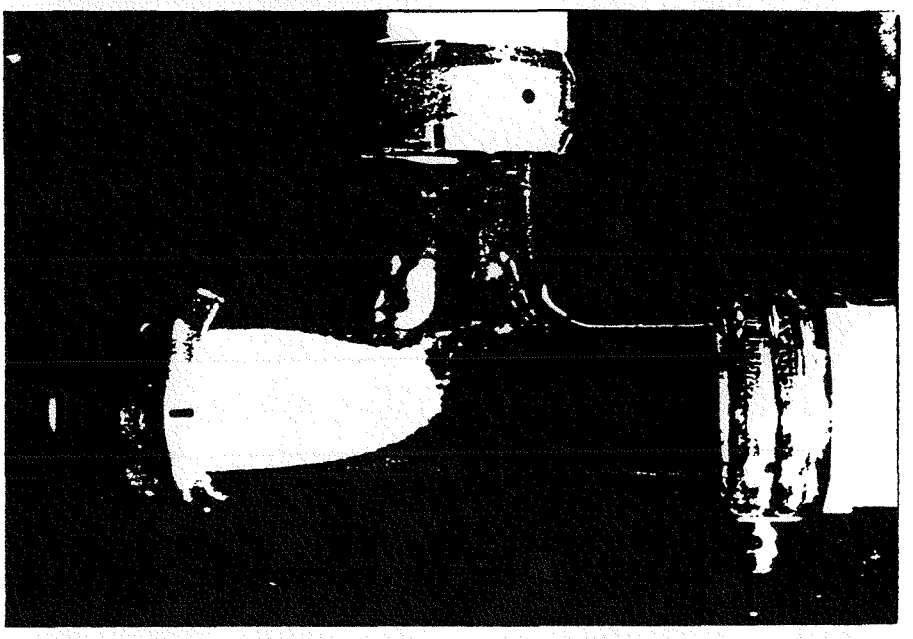

b)

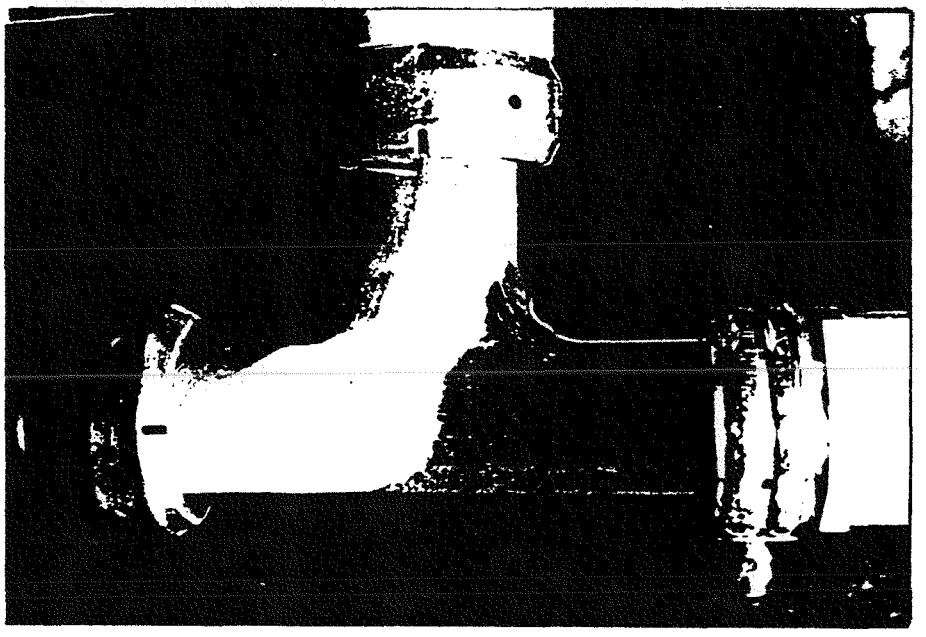

Figure 51. Solids deposition in an horizontal to horizontal orientation, a) U_g= 8.0 m/s, W_s= 18 kg/h, b) U_g= 8.0 m/s, W_s= 77 kg/h

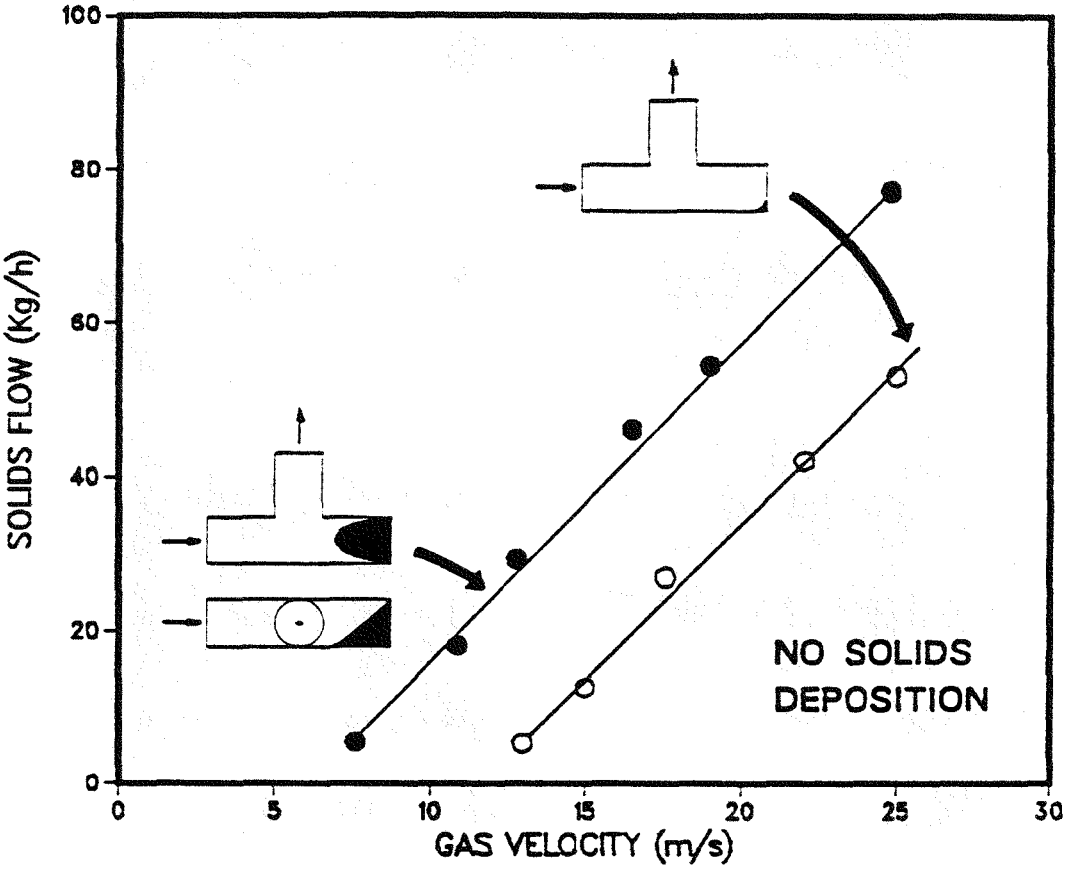

Figure 52. Flow pattern diagram for the horizontal to horizontal orientation.

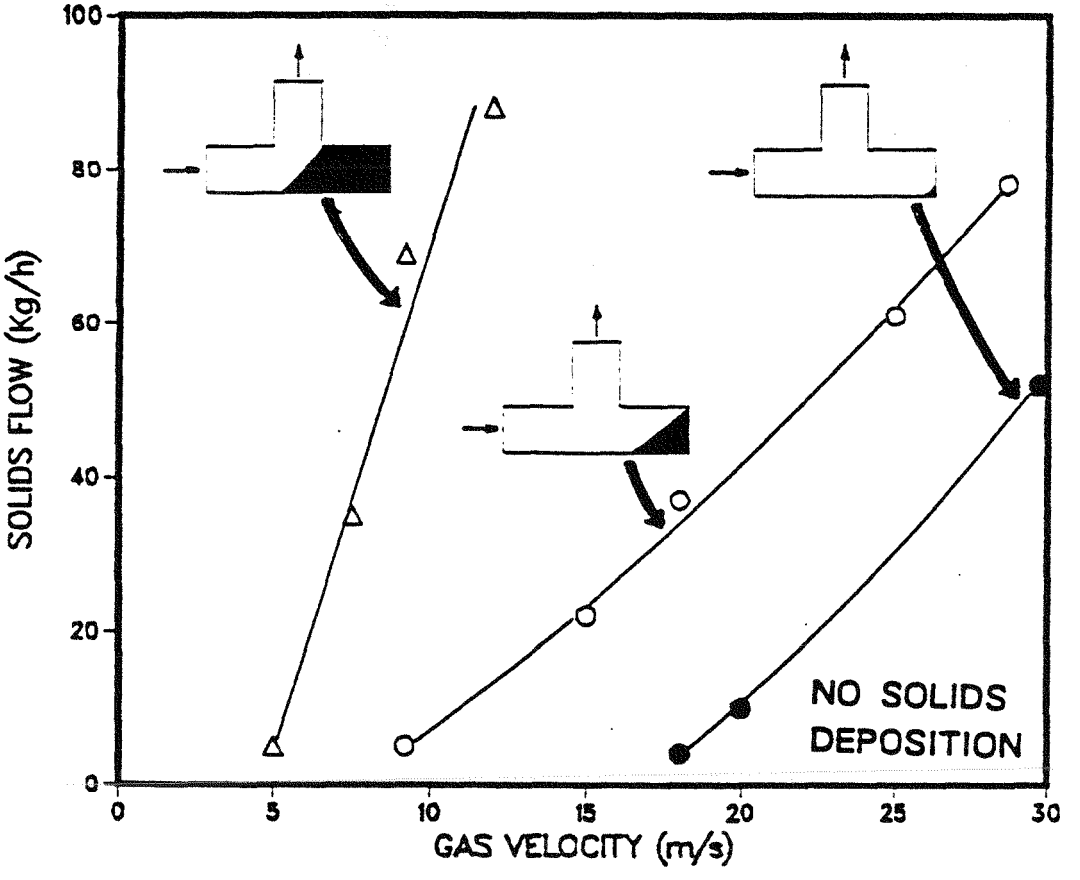

Figure 53. Flow pattern diagram for the horizontal to vertical upwards position.

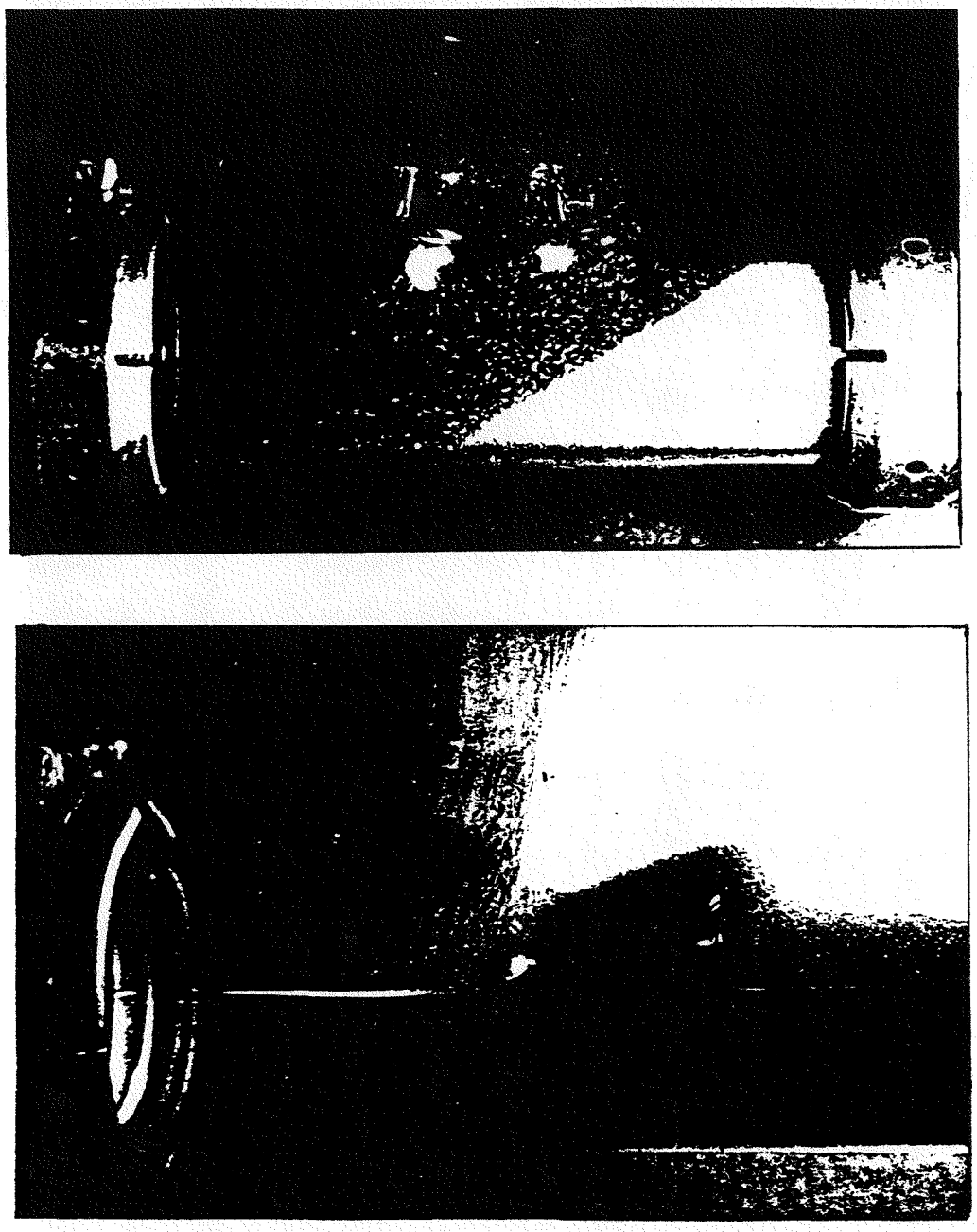

Figure 54. Solids deposition in an horizontal to vertical upwards position, a) U_g= 10.6 m/s, W_s= 21 kg/h, b) U_g= 10.8 m/s, W_s= 98 kg/h

Table 7. Conditions for the wear tests.

Case	Orientation	U_g(m/s)	W_s(kg/h)	t (min)
1	H - H	10.8	18.	40
2	H - H	27.0	18.	20
3	H - V	10.6	37.	40
4	H - V	10.8	98.	40
5	V - H	11.0	37.	40

where t = Running time
H = horizontal direction
V = vertical upwards direction

As the air velocity increased, the layer of solids deposited in the dead zone was depleted (Figure 56, Case 2). Being unprotected, the end of the T-bend was heavily eroded. Moderate erosion occured in the end branch and in the outlet branch of the T due to secondary impacts. Since the gas velocity was high, some of the particles deviated from their trajectories, impacting the junction of the outlet and end branches, causing considerable erosion at this point.

In Cases 3 and 4 (Figures 57 and 58) were studied the wear patterns for the horizontal to vertical upwards orientation. In both cases the end zone was protected from the direct impact of the particles. One important observation that the wear zones were completely different in each case, and that change was achieved by increasing the solids flow rate at constant gas velocity. Then, it can be seen that the wear points in this kind of bend can be changed by manipulating the operating conditions.

Case 5 (Figure 59) was very similar to Case 2. In both cases there was no solids deposition to protect the end plate of the bend, or to modify the flow pattern. The vertical upwards to horizontal orientation has the advantage of a cloud formation in the center, which dampens the first impact. A very high particle to particle interaction was visually observed in this region.

The particular shape of the wedges, whenever solids deposition occur, depends on the external shear by the gas, as well as on the bulk properties of the solid. Further research is necessary to address the effect of particle size and type of material on the internal bend geometry, since these variables determine angles of repose and drag characteristics of the particles.

4.4.4 Discussion

Blinded T-bends present various flow regimes that can be measured and represented in a gas velocity - solids flow rate diagram. The spatial orientation of the bend, along with the operating conditions determines the type of flow patterns that will develop, as well as their stability. The horizontal to horizontal orientation is the most stable configuration, while in the case of vertical upwards to horizontal orientation no solids accumulation was observed.

The wear pattern is determined by the internal geometry of the bend and flow pattern. Solids deposition is an effective shield against direct impact, decreasing the kinetic energy of the particles and, for that reason, minimizing the material removal on subsequent impacts. The internal geometry and flow patterns can be manipulated to change the wear points inside the bend.

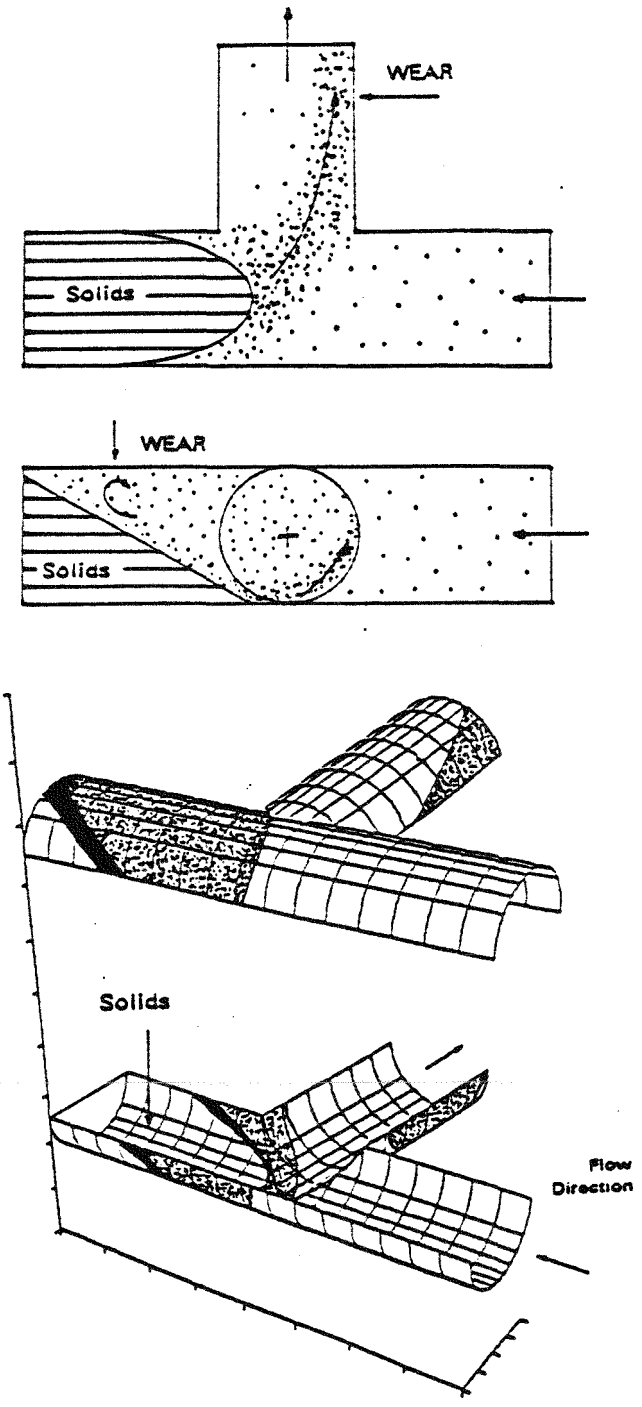

Figure 55. T-Bend wear pattern. Case 1 : Horizontal to Horizontal

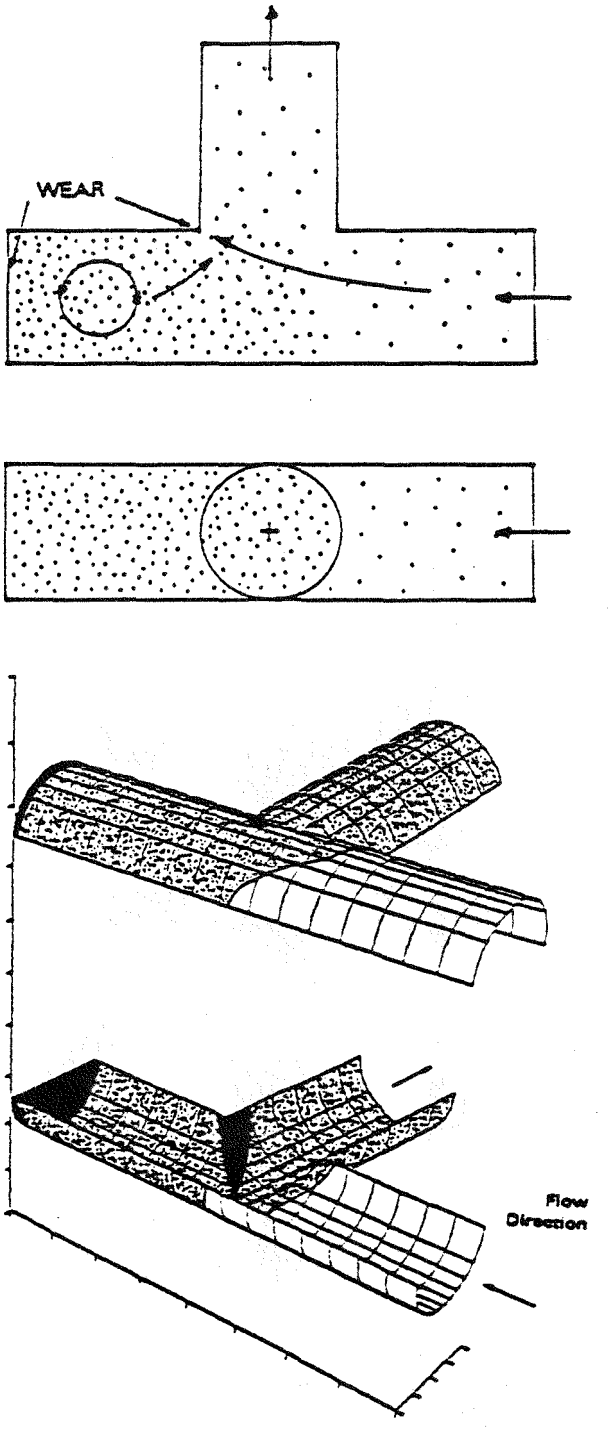

Figure 56. T-Bend wear pattern. Case 2 : Horizontal to Horizontal

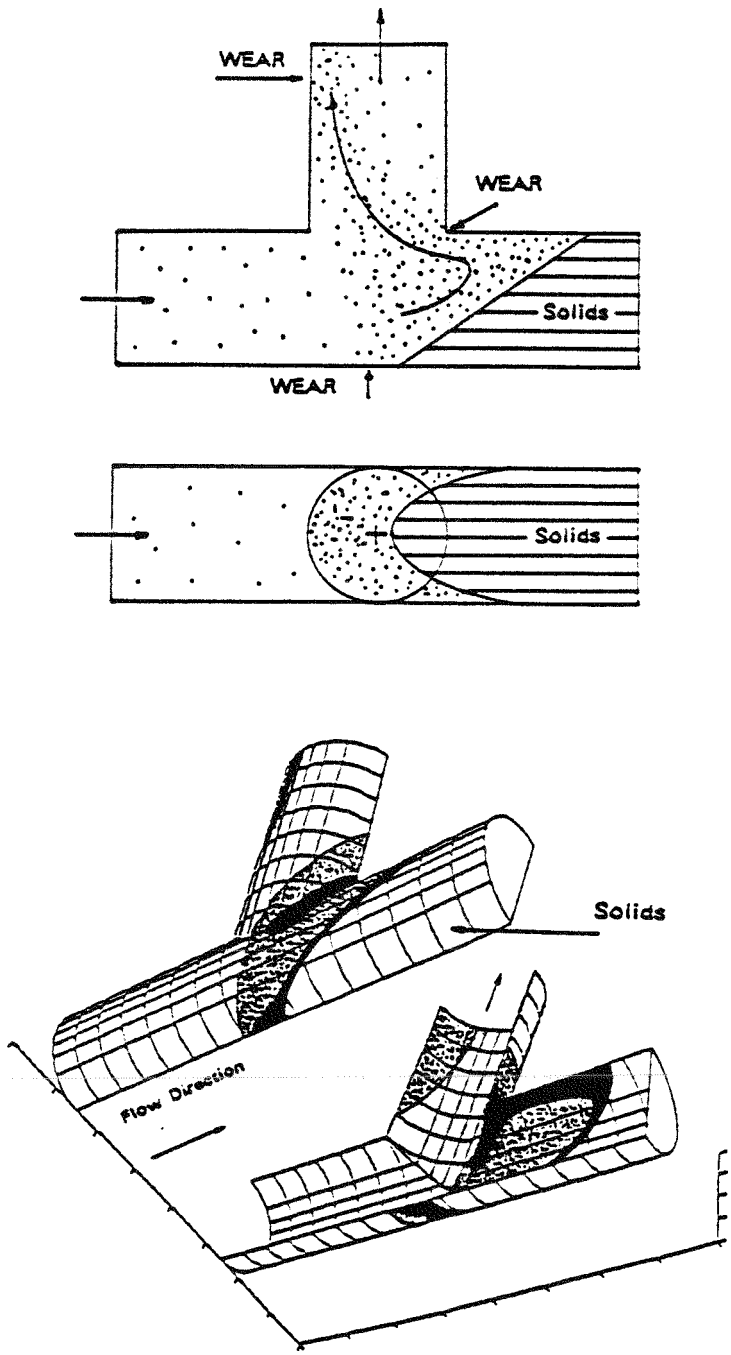

Figure 57. T-Bend wear pattern. Case 3 : Horizontal to Vertical Upflow

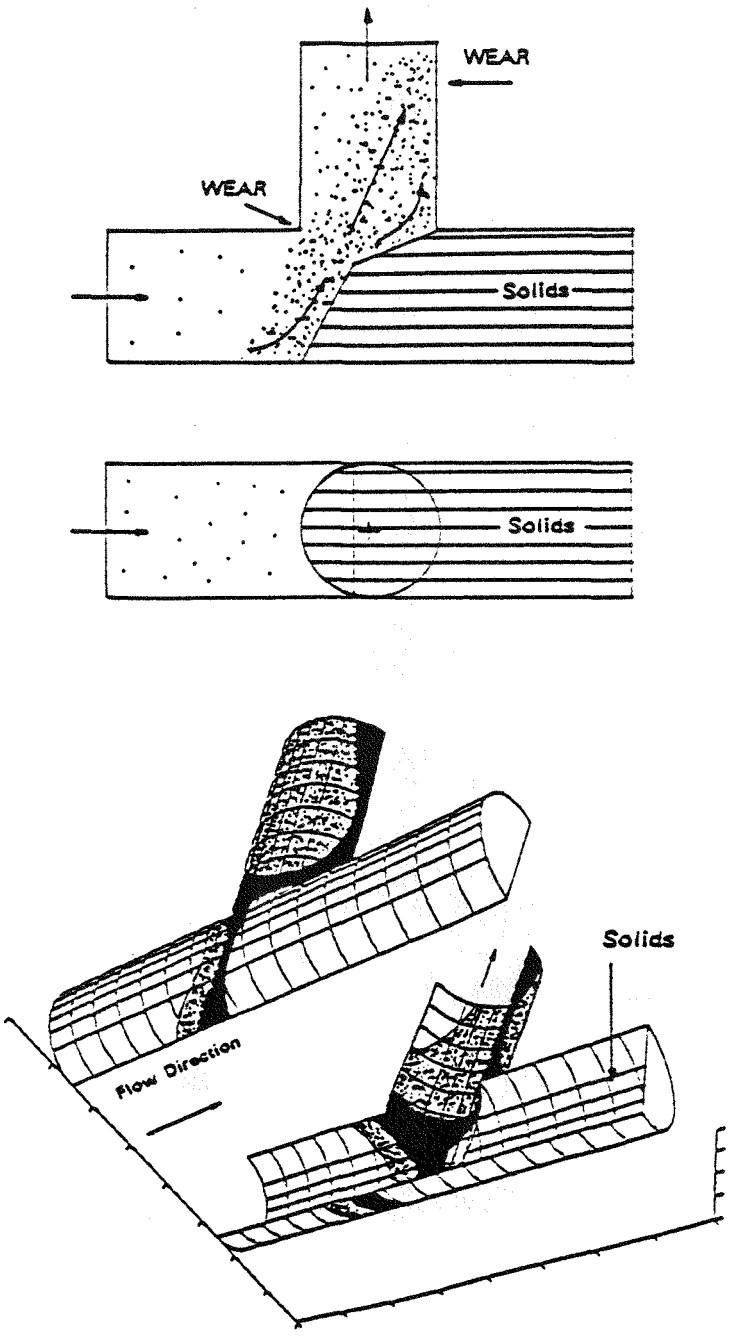

Figure 58. T-Bend wear pattern. Case 4 : Horizontal to Vertical Upflow

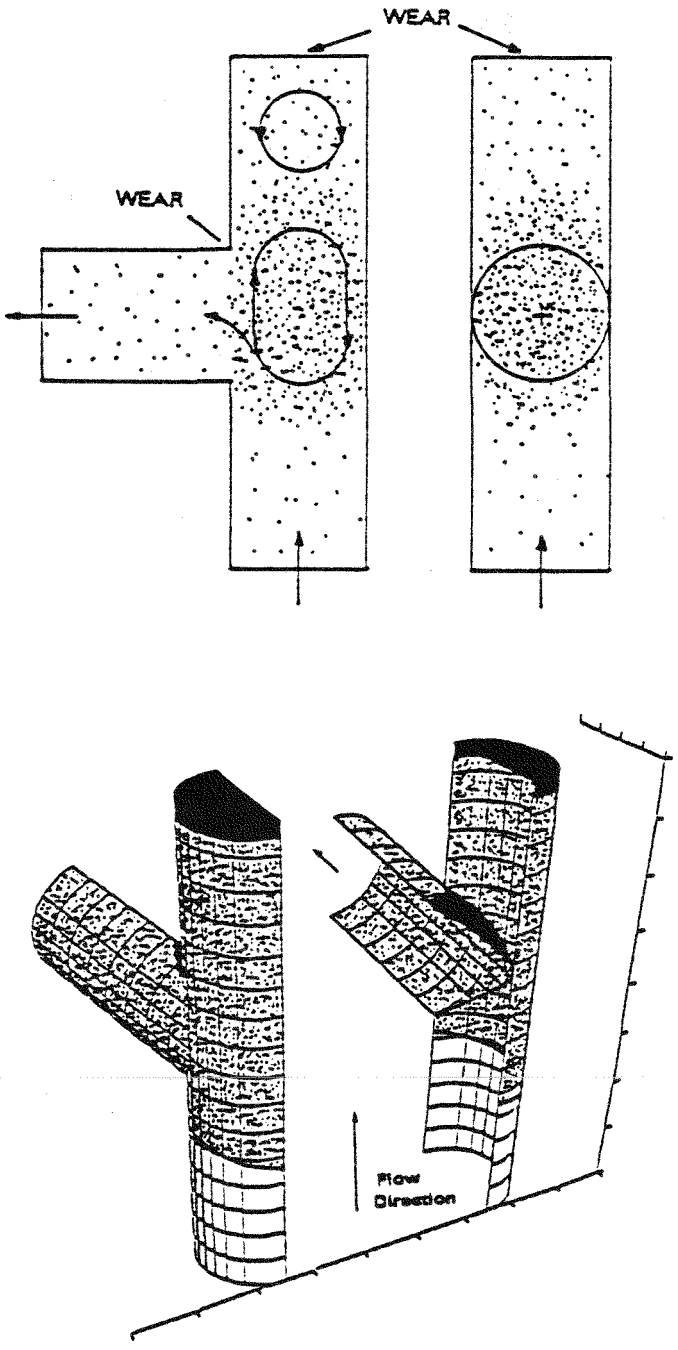

Figure 59. T-Bend wear pattern. Case 5 : Vertical Upflow to Horizontal

4.5 EROSION OF OTHER COMPONENTS

Valves, cyclones, and measuring devices exposed to the gas- solids stream are likely to suffer failure due to erosive wear. As in the case of bends, the wear profile in these components is not uniform, but there are smaller sections in which wear thru will probably occur. The identification of these points is useful for the design of the transport line components, since once the primary wear points are known it is possible to modify the design for extended life of the component. One of the alternatives is the use of expensive advanced materials in small quantities, only to protect primary wear points.

During the last series of experiments with alumina as erodent material (wedge sample tests), a buttefly valve made of Fraxcast concrete was inserted in the test section. Two positions were tried: half open and completely open. After eight hours exposed to the alumina bombardment at 530 °C, with a gas velocity of 34 m/s and solids flow rate of 48 kg/h, the valves showed significant wear in parts of them. The points affected with significant wear are shown in Figure 60. In the case of the fully open valve, the walls of the pipe surrounding the fin presented little evidence of erosion, while the border of the fin confronted to the gas-solids stream showed significant wear. The half open valve case was different because the flow field was highly disturbed. Significant erosion occured in the side of the fin exposed to the flow stream, while the other side there was little wear. The deviation of the particles caused severe damage in the pipe walls, both upstream and downstream. A picture of the fin is shown in Figure 61.

The hot cyclone of the pneumatic transport facility also suffered damage during the erosion tests. A first wear thru occured during the coal slag test performed at high gas velocity (34 m/s). The wall of the cyclone was holed at the site opposite to the gas-solids entrance, where the primary impact occurs, as shown in Figure 62. An important observation is that the wear was confined to a small region, of about a half inch, with the surface nearby in very good condition. A pausible explanation is that there was a beaming effect caused by the bend from which the solids are coming into the cyclone. As it was noted in the section of circular bends simulation, the solids tend to accumulate towards the outer radius of the bend, generating a zone with the solids confined into a beam. These solids leave the bend in such a way that they can hit a small region of the next component, either a pipe or, as in the case of the test facility, a cyclone. Failure then can be expected after pipe bends due to increased collision rates.

The cyclone was repaired by welding a 1/16 in. steel plate outside the worn region of the cyclone, but a second failure occured in the same point as before towards the ending of the slag test series. A 1/8 plate was welded above the other one, and that allowed continuous operation until the end of the alumina tests, being holed a few minutes before the programmed test runs. The wear thru point this time was displaced, occuring in one of the edges of the 1/8 steel plate (the downstream edge).

Besides the cyclone, there was a number of failures occuring in other components of the test facility, mainly thermocouples. To measure accurately the temperatures of the gas solids mixture, the thermocouples had to reach the surface of the samples, and the particle bombardment was severe enough to erode the tips and the bimetallic connection. Thermocouples had to be replaced several times during the execution of the erosion tests.

Pipe bends in the recirculation line of the pneumatic transport test facility were carbon steel blinded end T-bends. The effectiveness of these components was proved after examining them after the slag test experiments, showing no sign of appreciable wear. The solids deposition inside the T-bends was appreciated by looking at the corrosion patterns on them. Moisture during the inactivity periods caused the Tees to

corrode, forming an oxide layer. During operation, this layer was removed in all places, except the ones protected by the solids. As a result, the solids deposition could be traced by noticing the places that still contained rust, and the patterns obtained were in agreement with the flow patterns observed in the last section of this chapter.

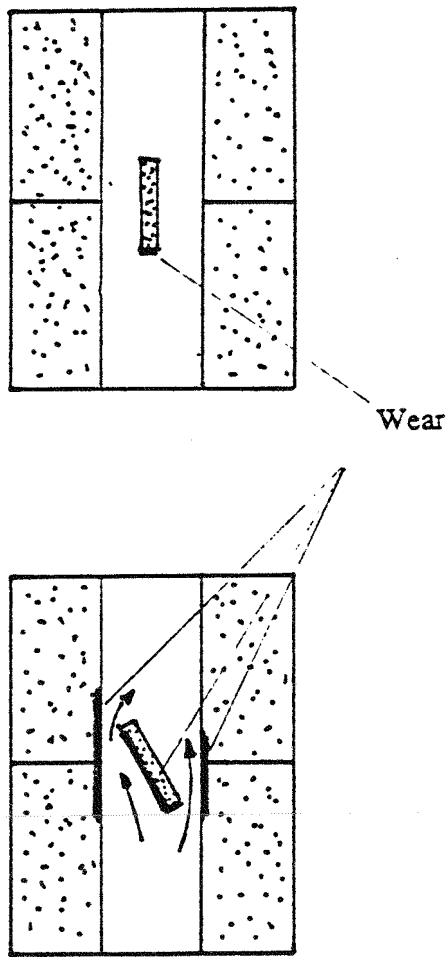

Figure 60. Wear points in a butterfly valve

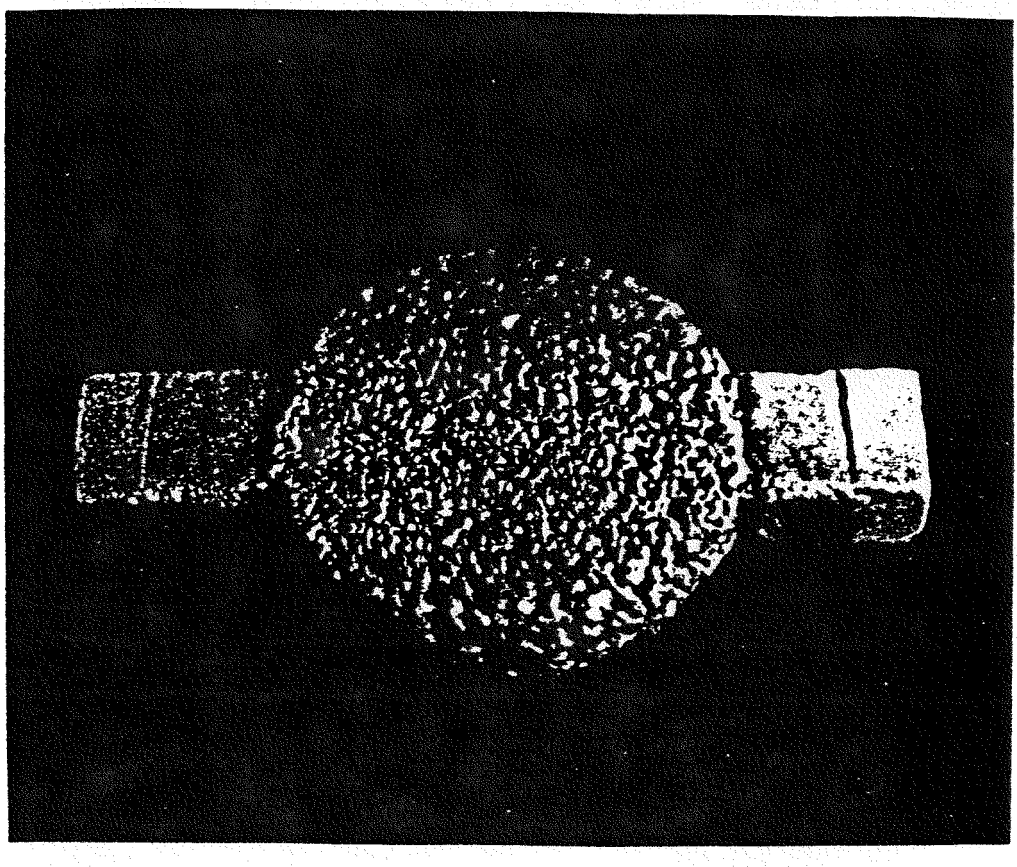

Figure 61. Erosion of the valve fin

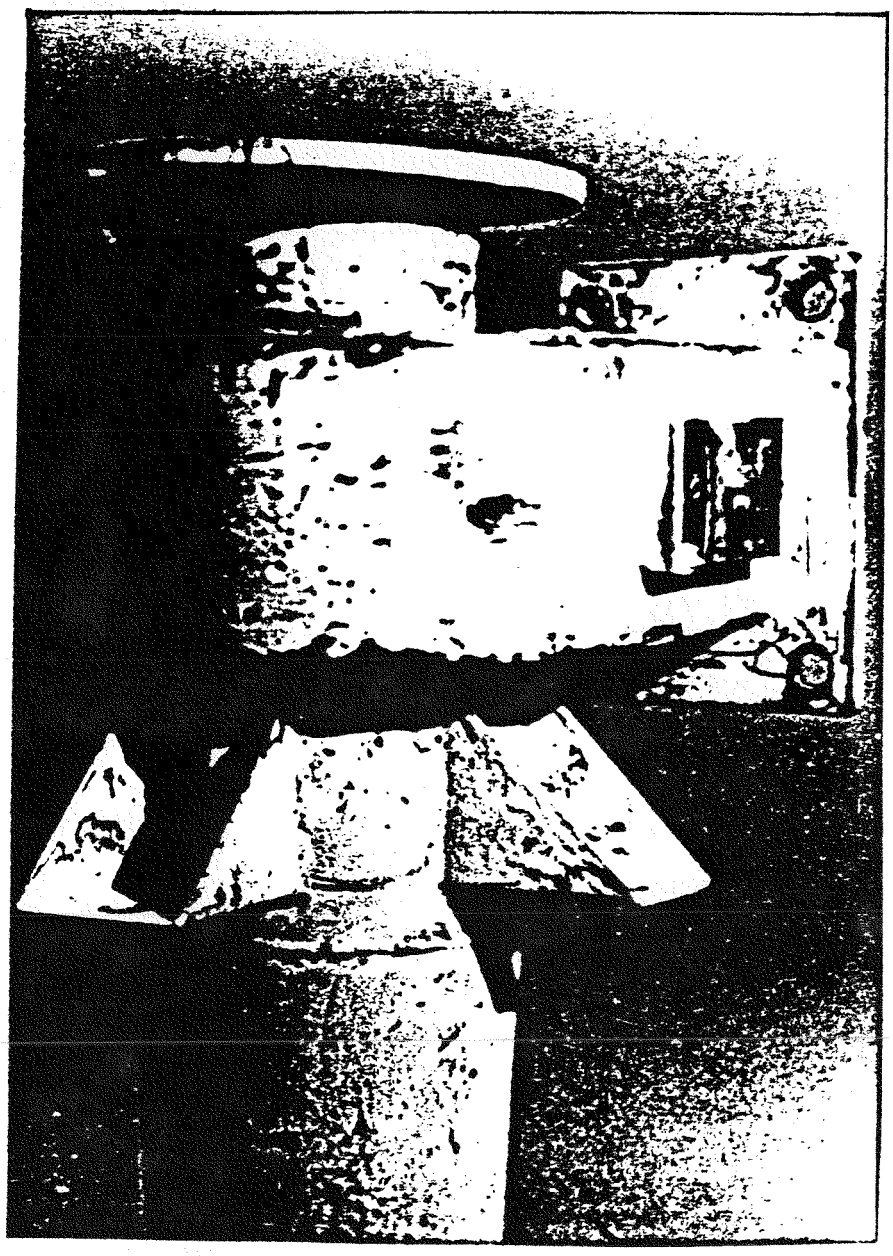

Figure 62. Cyclone erosion

5.0 CONCLUSIONS

The mechanisms of erosion of refractory concrete lined pipes were identified and the erosion rates were measured as a function of gas velocity, solids flow rate and temperature. The erosion of high alumina, alumino-silica and silicon carbide concretes, all bonded with high purity calcium aluminate cement, was found to proceed in stages, in which increasingly larger aggregates were undercutted and hit loose by the erodent. The extent of damage depended on the particular aggregate size distribution, with small and intermediate size aggregates resisting the penetration of the matrix, and large size grains shielding the underlying matrix in the so called shadowing effect. The optimum concrete structure appears to be consistent with the requirement of minimum amount of bonding material, which is the phase most susceptible to particle bombardment.

The erosion process in a freshly casted sample presents a transient period in which shadowing effects have not developed. The completion of this stage can be evaluated by a purely geometrical technique. For this work, fractal analysis was tried and, although fractal parameters are not directly related to the erosion rates, they can show the initiation of a steady state of erosion.

Erosion rates proved to be very sensitive to particle shape and particle size distribution. Coal slag, the most irregular and sharp pointed of the erodent materials, presented the highest erosion rates even at temperatures above the softening point.

The effect of gas velocity on the erosion rates of straight pipe sections was correlated in terms of a power law. The value of this exponent was insensitive to the type of erodent material, being determined mainly by the target properties. The high values for this exponent emphasize the necessity to operate the transport lines at the minimum velocity possible in order to obtain a reasonable life for the conveying system.

The effect of solids concentration on the erosion rates of straight pipe sections was also correlated in terms of a power law. The exponents were sensitive to the type of erodent as well as target materials. Specific erosion rates actually decreased as the solids concentration increased. The effect was explained in term of shielding effects by the particles in the gas-solids stream, as well as local effects due to particles residing temporarily in the surface of the concretes.

Temperature effects depended on both target and erodent properties. Experiments performed with alumina, a stable material in the temperature range of interest, showed an increase of the erosion rates of the refractory samples at temperatures above 530°C. River sand showed the same kind of behavior. This behavior seems to be related to the behavior of the hot modulus of rupture of the concretes. For the case of coal slag, there is an initial increase on the erosion rates followed by a sharp decrease as the slag reaches its softening point. The temperature behavior was affected also by the particle velocity.

Pressure drop data showed an increase in frictional losses as the surface was eroded. These losses were determined by the solids static and frictional contributions to the pressure drop, and the variation was caused by an increase in the particle wall collision rate inside the pipe as a result of the new surface topology.

The effect of angle of impingment on the erosion rates was correlated assuming that shadowing by large aggregates played a mayor role in the process. In this case, the behavior of the erosion rates was determined by geometrical factors.

Particle wall interactions were correlated using polynomial expressions. The kinetic energy after rebound of alumina particles was relatively well determined while angles of rebound presented a high dispersion, being worse when the surface was eroded.

The erosion of circular bends was successfully simulated using a two dimensional model. Primary wear points, as well as secondary and tertiary wear points were accurately predicted. The model uses basic data on erosion rates and particle-wall interactions, and can be applied to a variety of situations.

Flow and wear patterns in a blinded T-bend were determined and characterized as a function of gas velocity and solids flow rate. The deposition of solids inside the bend acted like a shield, protecting the bend walls from erosive wear. The geometry of the deposition can be manipulated by changing the operating conditions inside the bend.

Future work in this area should concentrate in :

1. The assessment of temperature effects using radically different binding materials for the concretes, such as phosphate cements, to formulate correlations based on their mechanical properties at high temperatures.
2. The study of collisional processes in rough samples.
3. The development of simulation algorithms for more complex components, such as T-bends and cyclones, using the same basic approach applied in the case of circular bends.

APPENDIX A.
EQUIPMENT'S DESCRIPTION

A.1 The High Temperature Pneumatic Transport Test Facility

The High Temperature Pneumatic Transport Test Facility was designed and constructed at Westinghouse R&D Center in Pittsburgh. This facility was built to measure the erosion of refractory materials, attrition of the transported solids and to study flow characteristics. The flow diagram for the test facility, modified to accomplish the objetives of this project, is shown in Figure 63. A layout of the different major components is shown in Figure 64. A detailed desription of the major components follows.

A.2 The Main Burner

The hot gas required for the experiments is provided by burning natural gas under oxygen rich conditions in the horizontal leg of the facility. This Model 4422-4 XSA natural gas burner was supplied by the North American Manufacturing Co. with a working range of 50% excess fuel up to 2100% excess air.

A.3 The Pneumatic Transport Leg

The L-shaped pneumatic transport leg shown in Figure 65 has been deigned to carry the high temperature combustion gas and solid particles. This leg is constructed from sections of nominal 14 in., schedule 40 steel pipes. There are two tee sections making up the horizontal run, four 2.5 ft. acceleration sections, and five 1 ft. test sections

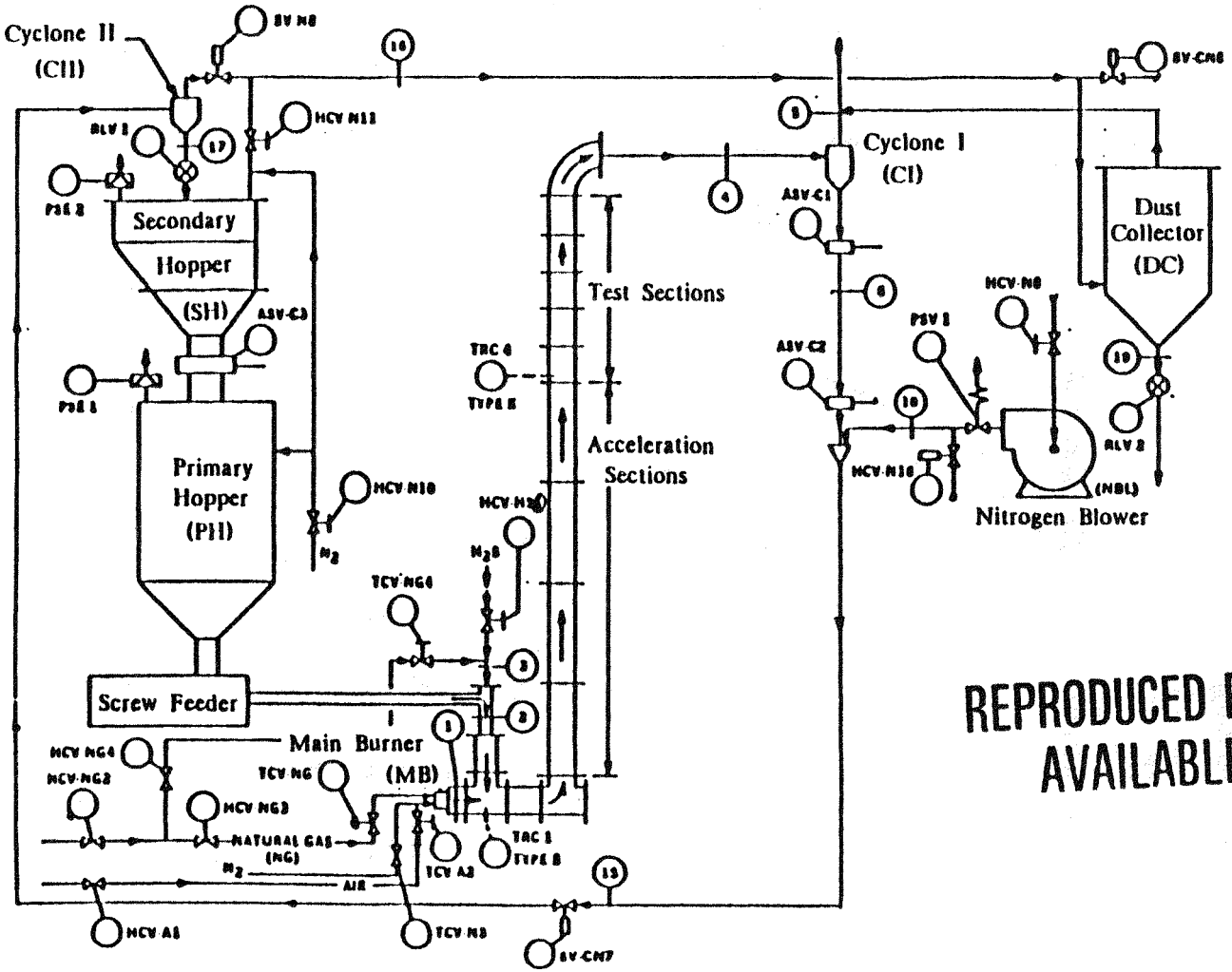

Figure 63. Flow Diagram of the Pneumatic Transport Test Facility

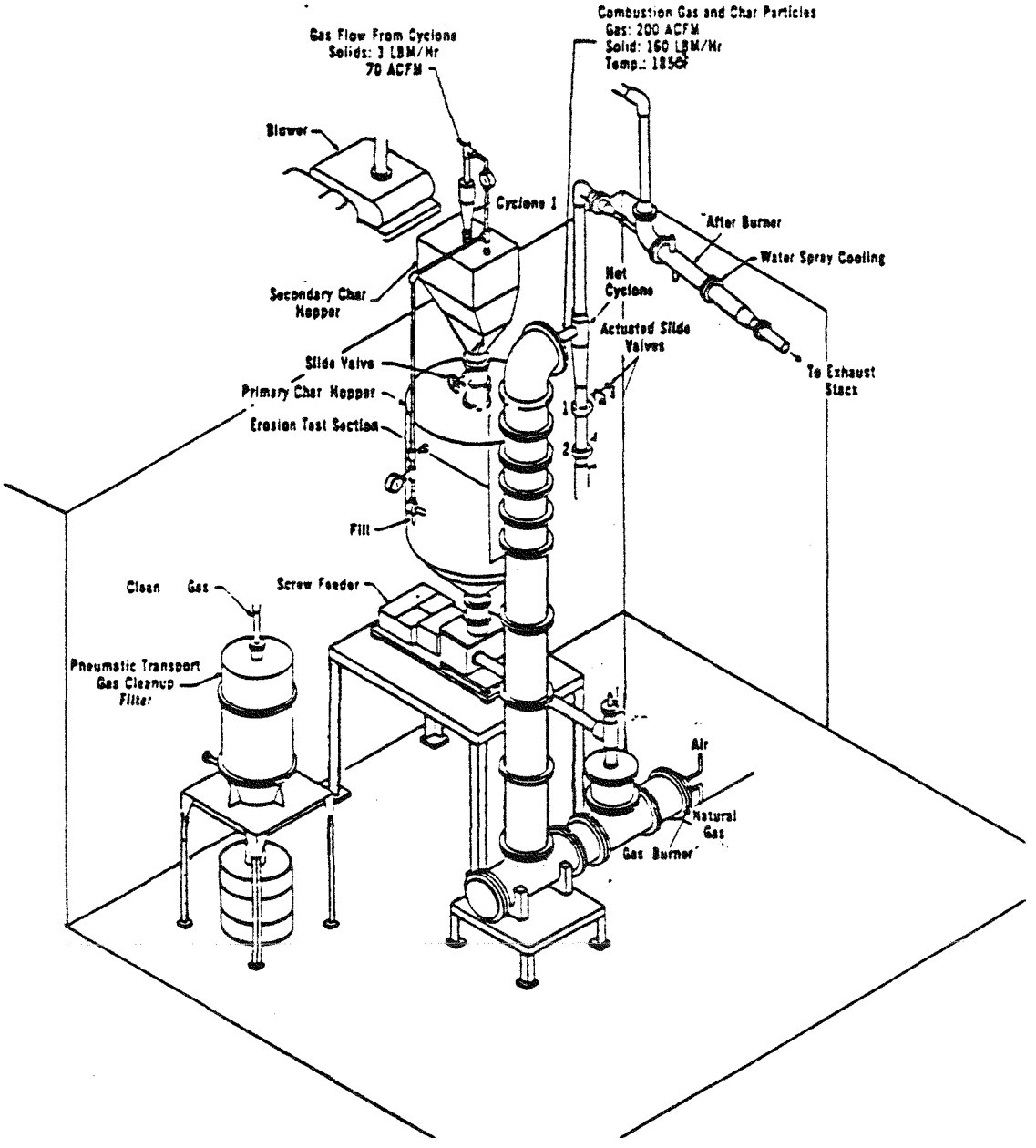

Figure 64. Layout of the major components of the test unit

in the vertical run. An elbow section on top of the column directs the gas-solids mixture into a cyclone. The acceleration sections are lined with Harbison-Walker Altec high alumina tubes of 2 in. I.D. x 4 in. O.D. x 15 in. long to resist erosion and high temperatures in the acceleration region. The back up insulation is provided by about 5 in. of Harbison-Walker Light-weight Castable ES. The test sections are also lined with refractory tubes and Light-weight Castable ES. Four curved sections of Harbison-Walker Siltec, a clay bonded silicon carbide refractory 2 in. I.D. x 4 in. O.D. are used to form the 21 in. radius elbow backed by about 5 in. of light-weight castable insulation. The sections are held together by 150 lb. slip-on flanges. Flexitalic gaskets with 304 stainless steel backing are used between the flanges to prevent leakage. The column is provided with 2 in. thick Fiberfrax insulation to reduce heat losses from the unit, and is surrounded by a steel structure to prevent its lateral movement while allowing vertical growth during hot operation. Each flange is provided with two holes to accept a thermocouple and a pressure probe. Each section of metal surface is provided with a thermocouple to indicate refractory break-down.

A.4 The Hot Cyclone CI

A cyclone made of 310 stainless steel by Fisher-Klostermann Inc. (size XQ-3) is used to separate the erodent particles from the combustion gas stream. The cyclone wall temperature is monitored by a skin thermocouple.

A.5 The Recycle Blower

A Roots 33XA Gas Pump supplied by the Dresser Industries Inc. is used to provide an air stream in the recirculation loop. By using room air, hot particles are carried to the secondery hopper while being cooled. This blower is driven by a 2 H.P. totally enclosed motor running at 1800 rpm.

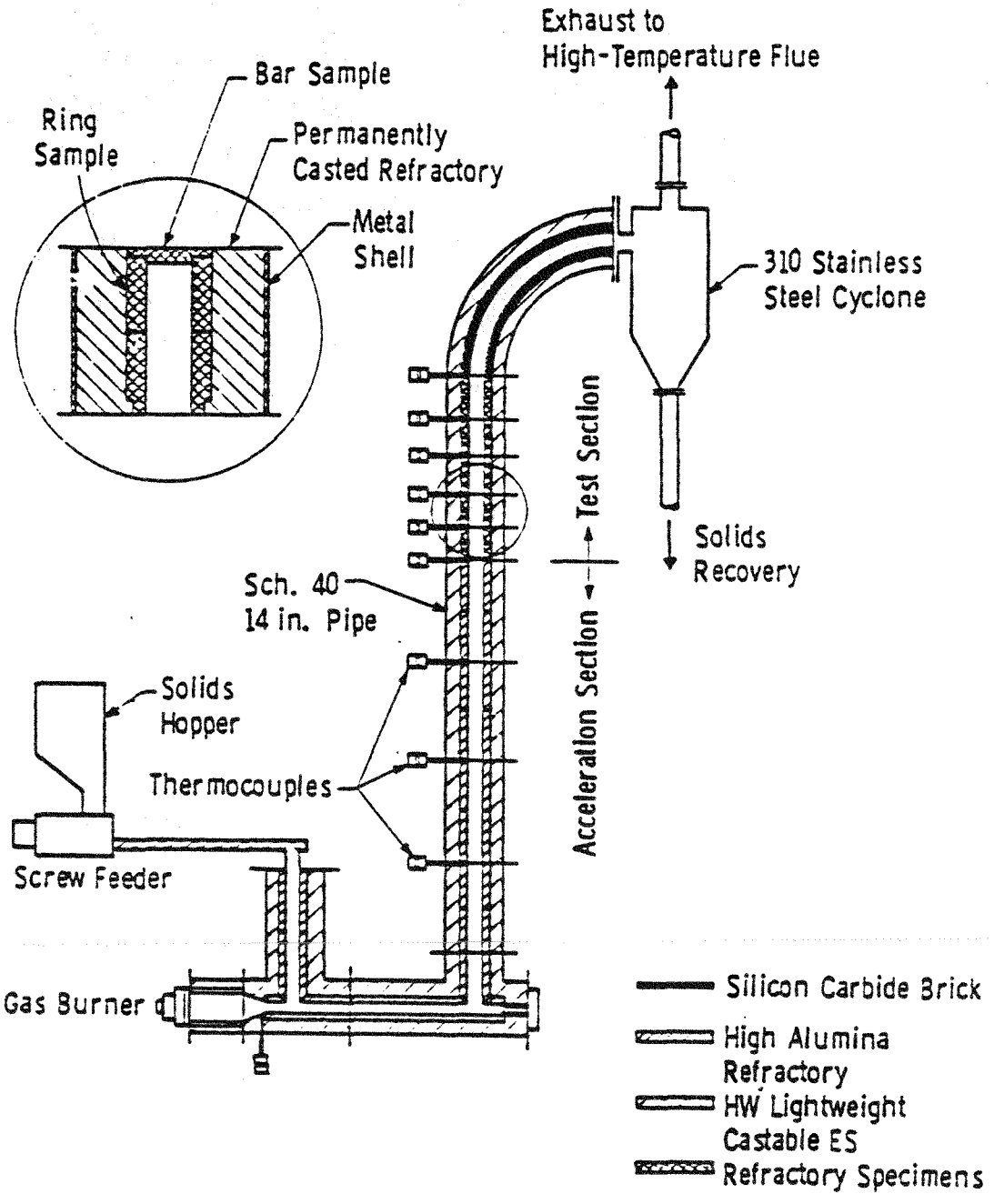

Figure 65. The Pneumatic Transport Leg

A.6 Dust Collector

A Model TD-162 Cartridge Dust Collector supplied by the Duskey Company Inc. is used to clean the air coming from the recirculating loop. Dust is deposited on the filter media, consisting of three filter cartridges with 162 square feet of filter area. The filter cartridges are cleaned automatically and continuously by jets of air. Dust removed from the filter settles in the bottom of the collector.

A.7 Primary Hopper

A LBB-4-50 live bottom bin with 50 cubic feet capacity supplied by the Vibra Screw Inc is used to store the erodent material and to feed them to the screw feeder. The vibrating section of the live bottom bin incorporates an integral vibrating baffle which promotes the flow of material from the upper regions of the static bin and relieves headload and compaction at the final outlet. The vibratory force is generated by the gyrator assembly. The material in the bin is kept constantly mobile as the vibrations from the baffle are transmitted upward in all directions. This combination assures a constant mass flow.

A.8 The Screw Feeder

A model HD-22 Heavy Duty Screw Feeder provided by Vibra Screw Inc. is used to feed the erodent material from the primary hopper into the pneumatic transport leg. The screw speed is controlled by a variable speed drive capable of turn-down ratio ranging from 10 to 1. The screw length is such that the discharge comes directly into the first tee section of the pneumatic transport leg's horizontal section.

APPENDIX B.
MATERIAL'S DATA

B.1 Fraxcast ES Cement

Fraxcast ES is an extra-strength, dry, abrasion resistant, hydraulic setting, aluminosilica castable. It gives outstanding performance at far less cost than prefired and phosphate-bonded monilithic shapes. It is highly abrasion resistant, equaling almost the silicon carbide brick. Fraxcast cement comes in 100 lb. bags. Instructions for preparation are indicated by the manufacturer as follows. Properties of Fraxcast concrete are presented in Table 8.

Water: Should be clean and cool. Adjust slightly to exact job requirements. Pouring/Rodding: 10%, 4.75 qts. per 100 lb. Vibration: use 1/5 less. Ram/Tamp: 1/2 less.

Mixing: Plaster-mortars paddle mixers are preferred. Use a clean mixer or mortar box. Clean out hardened mix frequently. Dry powder-mix 1 minute. Wet powder-mix 2-3 minutes. Mix no more than can be placed in 20 minutes.

Forms: Wood or metal forms should be reasonably watertight. Coat with oil or grease. Coat and taper internal cores for easy withdrawal. If pouring inside refractory or insulation, wet it down before pouring, or seal with plastic sheet or asphalt mastic.

Placing: Pour into forms and rod or vibrate to work out air voids. Do not work the mix more than 15 minutes after pouring. Withdraw vibrator slowly to avoid air pockets. Do not slick-trowel exposed surfaces. It will delay drying and will cause surface flaking.

Curing: Cure in forms for 24 hours or longer. Hot weather speeds set, cold retards

it. Keep exposed surfaces damp by covering with plastic film, foil, tar paper; or spray lightly with water every few hours begining when casting has hardened to touch (4-6 hours). Remove internal cores 4-6 hours after casting. Avoid freezing while casting is wet.

Aid dry: Strip forms, air dry 24 hours. Keep air moving with fans, open doors and flues.

Force dry: Avoid flame impingment. Raise at 50°F per hour, holding at 200°F, 650°F, 1550°F 40 to 60 min per inch of thickness.

The following plot gives the behavior of HMOR for 60 percent alumina conventional castables.

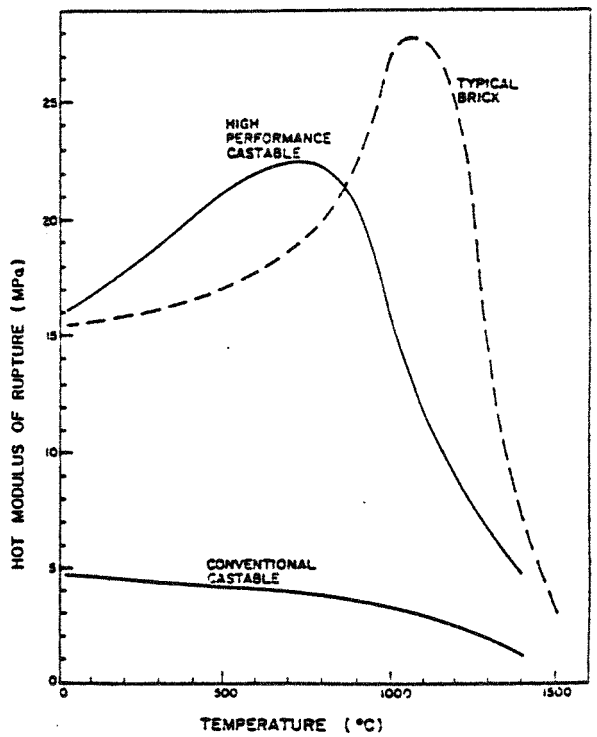

B.2 Carbofrax 11 LI Cement

Carbofrax 11LI castable is an hydraulic setting silicon carbide based castable with a moderately high thermal conductivity, good resitance to acids and good bend strength. It is intended for use to a maximum temperature of 1480 °C, resisting abrasion and slag attack. Properties of this concrete are presented in Table 9. Carbofrax 11 LI cements also come in 100 lb. bags. Instructions for preparation are as follows.

Water: Should be clean and cool. Adjust slightly to fit exact job requirements. Pouring/Rodding: 11.5 %, 5.5 qts. per 100 lb. Vibration: Use 1/5 less. Ram/Tamp: 1/2 less.

Mixing, forms, placing, curing, aid dry and force dry, all the same as Fraxcast.

B.3 Kaotab 95

Kaotab 95 is a high alumina, high purity, calcium aluminate bonded castable. Some of the properties of the concrete are presented in Table 10 B&W Kao-tab 95 comes in 100 lb. bags. This product is not recommended for pneumatic placement. It is designed for casting applications. Highest strength is obtained with refractory castables by using the least amount of mixing water which will allow thorough working of the material into place. When machine mixed, (paddle-type mixer best suited) add one half recommended amount of water to mixer before adding dry material. Place contents of bag directly in mixer, add remaining water immediately and mix for 3 minutes. When hand mixed, contents of bag should be dry mixed on a clean, dry surface before adding water. Place material within 20 minutes after mixing. Forms may be removed 8 hours after placing. The following amounts of clean water are recommended according to the method of placement. Hand rodding and tamping: 4.5 to 5 U.S. qts./bag (100 lb.). External vibrating: 4 to 4.5 U.S. qts./bag (100 lb.). High speed external vibrator: 4 to 4.5 U.S. qts./bag (100 lb.). Ramming: 2 to 3 U.S. qts./bag (100 lb.). Use watertight forms. When

placing against porous surface, waterproof the surfaces. Material should be used within 20 minutes after mixing. For maximum strength, allow 24 hours curing in damp atmosphere before first heat-up. Heat slowly the first time. Keep freshly placed castable warm during cold weather.

B.4 Kaocrete HS Cement

B&W Kaocrete HS is a 2600°F castable suitable for casting and gunning. Highest strength is obtained with castable using the least amount of clean mixing water which will allow thorough working of the material. After adding the recommended amount of water to achieve a ball-in-hand consistency, mix for 3 minutes. Place material within 30 minutes after mixing. The recommended water ranges are as follow. Casting by hand rodding: 6.5 to 7 U.S. qts./100 lb. bag. Casting by vibrating: 6.0 to 6.5 U.S. qts./100 lb. bag. Ramming: 3.0-4.0 U.S. qts./100 lb. bag. Use a water tight form. For maximum strength, cure 24 hours under damp conditions before initial heat-up.

B.5 Kaolite 2000HS Cement

B&W Kaolite 2000HS is a 2000°F castable suitable for casting and gunning. Casting and curing procedure is similar to Kaocrete HS. The recommended water range for casting is 11.5-12.0 U.S. qts./40 lb. bag.

B.6 River sand

River sand with an average particle size of 210 μm was bought from ESCO Company. Some of the properties of this erodent material are presented in Table 11.

B.7 Coal slag

The coal salg used in the experiments came from a wet bottom boiler at Ohio Edison Power Plant. This material was characterized by a wide distribution of particle sizes, allowing to simulate industrial materials. Some of the properties of this material are shown in Table 12.

B.8 Alumina T-64

Alcoa T-64 tabular alumina is a massive sintered alumina that has been thoroughly shrunk and has coarse, well developed alpha alumina crystals. The alumina has been converted to the corundum form by heating to a temperature slightly below 3700°F, near the fusion point of the aluminum oxide. The shape of the crystals is predominantly tabular. This material has an extremely high refractoriness and volume stability at high temperatures, being available in graded granular sizes. The size used in this work corresponds to a 28-48 mesh fraction, with 2% maximum on the 28 mesh and 5% maximum through mesh 65 Tyler. In Table 13 are summarized the properties of this material.

Table 8. Properties of Fraxcast concrete

Product Description:
Dry, extra-strength, hydraulic set, low-iron.

Typical Chemical Analysis:

Al_2O_3	58.3%
SiO_2	32.8%
CaO	6.2%
TiO_2	1.2%
Fe_2O_3	0.8%
Na_2O	0.1%
MgO	0.1%

Typical Physical Properties:

Particle size	Through 8 mesh sieve		
Maximum hot face temperature.	1371°C (2500°F) (higher for shorter periods)		
Amount required/ft³	135 lbs. dry material		
Method of placing	All usual castable techniques		
Water content	10 to 11 pints/100 lbs. dry ingredients		
Fired properties:			
After firing to:	104°C (220°F)	816°C (1500°F)	1094°C (2000°F)
Linear change % cold	nil	-0.36	-0.03
Cold modulus of rupture, psi	1,500-1,700	1,600-1,800	1,200-1,400
Cold crushing strength, psi	8,000-10,000	12,000-14,000	9,000-11,000

Abrasion Resistance:
Abrasion and strength tests
In I and II, the lower the index number, the better the abrasion resistance (the less the sample wore).

	Temperature	ES
I. "Sandblast" Abrasion Test 30 mesh alumina @ 80 psi, 90° angle of impingement, approx. 16 minutes, all relative to controls of Carbofrax® D type SiC prefired bricks at 1.0 value. This test is run cold after samples are prefired to temperatures shown.	121°C (250°F)	2.30
	538°C (1000°F)	2.10
	816°C (1500°F)	3.80
	1094°C (2000°F)	3.48
II. Hot Rubbing Test measured at temperatures shown.	538°C (1000°F)	0.55
	816°C (1500°F)	0.40
	1094°C (2000°F)	0.27
III. Compressive Strength measured cold after firing to temperatures shown, relative.	121°C (250°F)	100%
	816°C (1500°F)	135%
	1094°C (2000°F)	105%
IV. Modulus of Rupture measured cold after firing to temperature shown, relative.	121°C (250°F)	100%
	816°C (1500°F)	104%
	1094°C (2000°F)	85%

Table 9. Properties of Carbofrax concrete

Product Description:
Dry, hydraulic setting, low-iron type.

Typical Chemical Analysis:

SiC	83.0%
Al_2O_3	12.5%
CaO	2.8%
SiO_2	1.3%
Fe_2O_3	0.2%
Na_2O	0.1%
MgO	0.1%

Standard Containers:
100 lb. bags, 300 lb. drums.

General Information:
General purpose applications requiring ruggedness, high thermal conductivity, resistance to acid slags and metals, resistant to flame abrasion. In boiler and incinerator plants use it for studded tube facings, and lining wet ash pits and troughs.

Maximum temperature stated is for continuous duty, "dry" heat, hot face service. This will be affected by slags, metals, fumes, etc.

All data shown are typical but not guaranteed values.

Typical Physical Properties:

Particle size	6 mesh and finer
Maximum use temperature	1482°C (2700°F)
Method of placing	Pouring, tamping, trowelling, gunning
Amount required/ft³	145 to 150 lbs. dry material at pouring consistency
Water content	9 to 9½ pints/100 lbs. of dry material at pouring consistency (9½ to 10%)
Thermal conductivity	65 to 75 BTU, dependent on method of placing and temperature
Physical strength	Prefired to temperature shown and measured cold
Modulus of Rupture	
93°C (200°F)	1000-1200 psi
538°C (1000°F)	900-1100 psi
816°C (1500°F)	900-1100 psi
1093°C (2000°F)	1000-1300 psi
1371°C (2500°F)	1300-1600 psi
Compressive Strength	
93°C (200°F)	2600-2800 psi
538°C (1000°F)	1500-1800 psi
816°C (1500°F)	1400-1600 psi
1093°C (2000°F)	2000-2500 psi
1371°C (2500°F)	2500-3000 psi

Table 10. Properties of Kaotab concrete

Max. hot face temperature (^{o}F)	3300
Bulk density (kg/m^{3})	2650
Composition (%)	
Al_2O_3	96.7
SiO_2	0.1
Fe_2O_3	0.1
CaO	2.7
Alkalis	0.3
Porosity (%)	26.0
Compressive strength (psi)	9000
Abrasion resistance	Very good
Thermal shock resistance	Good

Table 11. Properties of river sand

Sieve analysis

mesh	size (μm)	% passing
30	595	99.9
40	420	95.0
50	297	71.9
70	210	36.0
100	149	7.4
140	105	1.9
200	74	0.5

Main mineral constituent	Quartzite
Particle density (kg/m^3)	2650
Bulk density(kg/m^3)	1580
Hardness (Moh's)	7

Table 12. Properties of coal slag

Particle density (kg/m^3)	2810
Bulk density (kg/m^3)	1580
Composition (%)	
SiO_2	51.8
Al_2O_3	22.4
TiO_2	1.08
Fe_2O_3	18.0
CaO	2.30
MgO	1.19
K_2O	1.26

Table 13. Properties of Alumina T-64

Particle density (kg/m^3)	3650
Bulk density (kg/m^3)	1700
Apparent porosity (%)	3
Water absorption (%)	0.8
Hardness (Moh's)	9
Composition (%)	
Al_2O_3	99.5+
SiO_2	0.05
Fe_2O_3(total)	0.07
Fe_2O_3(soluble)	0.02
Na_2O	0.16
CaO	0.04

APPENDIX C.
PIPE EROSION DATA

Table 14. Operating conditions for the test series

Erodent	Run #	t (h)	U_g (m/s)	W_s (Kg/h)	W_s/W_g	T (°C)
Sand	1	17.5	17.8	50	0.89	530
	2	21.3	17.8	50	0.32	23
	3	15.0	17.8	91	1.61	530
	4	14.2	17.8	159	2.76	530
	5	20.0	26.0	50	0.62	530
	6	22.0	12.9	50	1.25	530
	7	36.8	17.8	50	0.83	530
	8	17.5	17.8	50	1.20	830
	9	20.0	17.8	50	0.32	23
	10	5.5	17.8	50	1.20	830
Slag	1	18.0	17.8	64	0.66	200
	2	11.8	17.8	64	0.87	350
	3	11.0	17.8	64	0.41	22
	4	8.5	26.0	64	0.45	200
	5	4.7	26.0	64	0.59	350
	6	5.6	26.0	64	0.69	450
	7	5.0	34.0	64	0.45	350
	8	4.9	34.0	64	0.34	200
	9	3.5	34.0	64	0.52	450
	10	2.7	34.0	64	0.60	550
	11	6.2	17.8	119	1.22	200
	12	3.7	17.8	171	1.76	200
	13	3.0	17.8	225	2.32	200
	14	1.0	34.0	64	0.65	630
Alumina	1	9.0	17.8	48	0.86	530
	2	5.0	26.0	48	0.59	530
	3	4.5	34.0	48	0.45	530
	4	9.0	17.8	112	2.01	530
	5	5.0	17.8	172	3.08	530
	6	4.5	34.0	48	0.55	700
	7	5.0	34.0	48	0.63	850
	8	5.5	34.0	48	0.63	850

Table 15. Erosion rates ($cm^3/cm^2/h$) for the test series

Erodent	Run #	Kaotab	Fraxcast	Carbofrax	Kaocrete
Sand	3	4.1E-4	5.8E-4	1.6E-3	2.5E-3
	4	4.7E-4	7.3E-4	2.0E-3	4.1E-3
	5	1.7E-3	1.3E-3	3.2E-3	3.4E-3
	6	1.5E-4	1.9E-4	2.0E-4	6.2E-4
	7	1.6E-4	3.8E-4	8.3E-4	1.9E-3
	9	2.4E-4	2.5E-4	6.5E-4	-
	10	8.5E-4	2.1E-3	1.4E-3	-
Slag	1	1.4E-3	2.7E-3	2.0E-3	-
	2	1.8E-3	2.7E-3	3.1E-3	-
	3	1.3E-3	3.2E-3	2.1E-3	-
	4	5.7E-3	8.0E-3	7.0E-3	-
	5	6.4E-3	8.9E-3	7.7E-3	-
	6	6.2E-3	9.6E-3	7.9E-3	-
	7	1.3E-2	1.9E-2	1.3E-2	-
	8	1.2E-2	1.4E-2	1.0E-2	-
	9	1.4E-2	2.1E-2	1.5E-2	-
	10	1.4E-2	1.4E-2	1.4E-2	-
	11	2.3E-3	4.2E-3	2.1E-3	-
	12	2.7E-3	4.8E-3	2.2E-3	-
	13	3.2E-3	5.2E-3	2.3E-3	-
	14	9.9E-3	9.8E-3	7.9E-3	-
Alumina	1	4.4E-4	8.0E-4	7.9E-4	-
	2	1.4E-3	1.6E-3	2.3E-3	-
	3	3.9E-3	4.2E-3	3.8E-3	-
	4	7.3E-4	1.0E-3	1.1E-3	-
	5	8.6E-4	1.4E-3	1.2E-3	-
	6	4.8E-3	6.8E-3	5.5E-3	-
	7	6.2E-3	1.3E-2	8.7E-3	-
	8	6.8E-3	9.2E-3	8.4E-3	-

Table 16. Specific erosion rates ($cm^3/cm^2/kg$) for the test series

Erodent	Run #	Kaotab	Fraxcast	Carbofrax	Kaocrete
Sand	3	4.5E-6	6.4E-6	1.8E-5	2.7E-5
	4	3.0E-6	4.6E-6	1.2E-5	2.6E-5
	5	3.4E-5	2.6E-5	6.4E-5	6.8E-5
	6	3.0E-6	3.8E-6	4.0E-6	1.2E-5
	7	3.2E-6	7.6E-6	1.7E-5	3.7E-5
	9	4.8E-6	5.0E-6	1.3E-5	-
	10	1.7E-5	4.2E-5	2.8E-5	-
Slag	1	2.2E-5	4.2E-5	3.1E-5	-
	2	2.8E-5	4.2E-5	4.8E-5	-
	3	2.0E-5	5.0E-5	3.3E-5	-
	4	8.9E-5	1.3E-4	1.1E-4	-
	5	1.0E-4	1.4E-4	1.2E-4	-
	6	9.7E-5	1.5E-4	1.2E-4	-
	7	2.0E-4	3.0E-4	2.0E-4	-
	8	1.9E-4	2.2E-4	1.6E-4	-
	9	2.2E-4	3.3E-4	2.3E-4	-
	10	2.2E-4	2.2E-4	2.2E-4	-
	11	1.9E-5	3.5E-5	1.8E-5	-
	12	1.6E-5	2.8E-5	1.3E-5	-
	13	1.4E-5	2.3E-5	1.0E-5	-
	14	1.5E-4	1.5E-4	1.2E-4	-
Alumina	1	9.2E-6	1.7E-5	1.6E-5	-
	2	2.9E-5	3.3E-5	4.8E-5	-
	3	8.1E-5	8.8E-5	7.9E-5	-
	4	6.5E-6	9.3E-6	1.0E-5	-
	5	5.6E-6	8.2E-6	6.7E-6	-
	6	1.0E-4	1.4E-4	1.1E-4	-
	7	1.3E-4	2.7E-4	1.8E-4	-
	8	1.4E-4	1.9E-4	1.8E-4	-

Table 17. Sand test run #2

Temperature : 23 °C
Gas velocity : 17.8 (m/s)
Solids flow : 50 (Kg/h)
Time : 21.3 (h)

Sample	#	h_s (cm)	Δm (g)	E ($g/cm^2/h$)	E ($cm^3/cm^2/h$)
Kaotab	1	6.3	3.8	0.00177	0.000670
	2	6.4	2.9	0.00133	0.000503
	3	6.2	7.4	0.00351	0.00132
	4	6.7	4.3	0.00187	0.000705
	5	6.8	5.8	0.00251	0.000947
Fraxcast	1	6.4	1.5	0.000689	0.000373
	2	6.5	0.4	0.000181	0.000098
	3	5.9	0.4	0.000199	0.000108
	4	6.9	0.4	0.000169	0.000091
Carbofrax	1	6.2	7.2	0.00342	0.00159
	2	6.4	9.8	0.00450	0.00209
	3	6.3	6.4	0.00298	0.00139
	4	6.0	1.1	0.00054	0.00026
Kaocrete	1	5.5	0.1	0.000053	0.000032
	2	6.5	0.4	0.000182	0.000110
	3	6.5	0.1	0.000045	0.000027
	4	6.5	0.6	0.000272	0.000164

Table 18. Sand test run #3

Temperature : 504-560 °C
Gas velocity : 17.7 (m/s)
Solids flow : 91 (Kg/h)
Time : 15.0 (h)

Sample	#	h_s (cm)	Δm (g)	E ($g/cm^2/h$)	E ($cm^3/cm^2/h$)
Kaotab	1	6.7	1.5	0.000935	0.000353
	2	6.4	1.9	0.00124	0.000468
Fraxcast	1	6.5	1.8	0.00116	0.000625
	2	5.9	1.3	0.000920	0.000497
	3	6.5	1.8	0.00116	0.000625
Carbofrax	1	6.4	6.1	0.00398	0.00185
	2	6.3	5.5	0.00364	0.00169
	3	6.0	4.2	0.00292	0.00136
	4	5.5	4.6	0.00349	0.00162
Kaocrete	1	6.4	6.5	0.00424	0.00256
	2	5.4	6.4	0.00495	0.00298
	3	6.5	5.4	0.00347	0.00209

Table 19. Sand test run #4

Temperature : 493-554 °C
Gas velocity : 17.8 (m/s)
Solids flow : 159 (Kg/h)
Time : 14.2 (h)

Sample	#	h_s (cm)	Δm (g)	E ($g/cm^2/h$)	E ($cm^3/cm^2/h$)
Kaotab	1	6.6	2.0	0.00134	0.000505
	2	6.5	1.5	0.00102	0.000384
	3	6.2	1.5	0.00107	0.000403
	4	6.5	2.0	0.00136	0.000512
	5	6.4	2.0	0.00138	0.000520
Fraxcast	1	7.0	2.1	0.00132	0.000716
	2	6.5	2.2	0.00149	0.000807
	3	6.4	2.1	0.00145	0.000783
	4	5.9	1.5	0.00112	0.000606
Carbofrax	1	6.4	7.0	0.00483	0.00224
	2	5.9	5.8	0.00434	0.00202
	3	6.5	6.5	0.00355	0.00165
	4	5.6	4.5	0.00441	0.00205
	5	6.2	5.6	0.00399	0.00186
Kaocrete	1	6.4	12.9	0.00889	0.00535
	2	6.4	9.3	0.00683	0.00411
	3	6.2	8.5	0.00605	0.00364
	4	5.4	6.1	0.00498	0.00300
	5	6.5	11.2	0.00760	0.00458

Table 20. Sand test run #5

Temperature : 532-579 °C
Gas velocity : 26.0 (m/s)
Solids flow : 50 (Kg/h)
Time : 20.0 (h)

Sample	#	h_s (cm)	Δm (g)	E ($g/cm^2/h$)	E ($cm^3/cm^2/h$)
Kaotab	1	6.6	8.2	0.00389	0.00147
	2	6.5	7.5	0.00361	0.00136
	3	6.2	7.2	0.00364	0.00137
	4	6.5	11.6	0.00559	0.00211
	5	6.5	7.3	0.00347	0.00131
	6	6.4	12.9	0.00631	0.00238
Fraxcast	1	7.0	8.0	0.00358	0.00194
	2	6.5	5.8	0.00280	0.00151
	3	6.4	2.6	0.00127	0.000692
	4	5.9	3.0	0.00159	0.000860
Carbofrax	1	6.4	18.1	0.00886	0.00412
	2	5.9	8.0	0.00425	0.00198
	3	6.5	23.4	0.0113	0.00524
	4	5.6	5.1	0.00285	0.00133
	5	6.2	14.6	0.00738	0.00343
Kaocrete	1	6.4	13.9	0.00690	0.00410
	2	6.5	9.1	0.00439	0.00264

Table 21. Sand test run #6

Temperature : 543-585 °C
Gas velocity : 12.9 (m/s)
Solids flow : 50 (Kg/h)
Time : 22.0 (h)

Sample	#	h_s (cm)	Δm (g)	E ($g/cm^2/h$)	E ($cm^3/cm^2/h$)
Kaotab	1	6.6	1.2	0.000518	0.000194
	2	6.5	0.4	0.000175	0.000066
	3	6.2	1.2	0.000551	0.000208
	4	6.5	0.7	0.000307	0.000115
	5	6.5	0.9	0.000394	0.000149
	6	6.4	1.0	0.000445	0.000170
Fraxcast	1	7.0	0.7	0.000285	0.000154
	2	6.5	0.9	0.000394	0.000213
	3	6.4	1.0	0.000445	0.000241
	4	5.9	0.7	0.000338	0.000183
Carbofrax	1	6.4	1.2	0.000534	0.000248
	2	5.9	0.6	0.000290	0.000135
	3	6.5	1.5	0.000657	0.000306
	4	5.6	0.7	0.000356	0.000165
	5	6.2	0.8	0.000367	0.000171
Kaocrete	1	6.4	1.8	0.000801	0.000482
	2	6.4	2.4	0.00107	0.000641
	3	5.4	2.3	0.00121	0.000730

Table 22. Sand test run #7

Temperature : 520-565 °C
Gas velocity : 17.8 (m/s)
Solids flow : 50 (Kg/h)
Time : 36.8 (h)

Sample	#	h_s (cm)	Δm (g)	E ($g/cm^2/h$)	E ($cm^3/cm^2/h$)
Kaotab	1	6.6	2.3	0.000593	0.000224
	2	6.5	1.2	0.000314	0.000118
	3	6.2	1.3	0.000357	0.000135
	4	6.5	2.3	0.000602	0.000227
	5	6.5	0.9	0.000236	0.000089
Fraxcast	1	7.0	3.5	0.000851	0.000460
	2	6.5	3.1	0.000812	0.000378
	3	6.4	1.7	0.000452	0.000244
	4	6.4	3.4	0.000905	0.000421
Carbofrax	1	6.4	6.8	0.00181	0.000841
	2	6.2	8.1	0.00222	0.00103
	3	5.9	5.0	0.00144	0.000671
	4	5.6	4.5	0.00137	0.000636
	5	6.2	7.7	0.00211	0.000984
Kaocrete	1	6.5	12.2	0.00320	0.00193
	2	6.4	13.0	0.00346	0.00208
	3	5.4	8.5	0.00268	0.00161

Table 23. Sand test run #9

Temperature : 23 °C
Gas velocity : 17.8 (m/s)
Solids flow : 50 (Kg/h)
Time : 20.0 (h)

Sample	#	h_s (cm)	Δm (g)	E ($g/cm^2/h$)	E ($cm^3/cm^2/h$)
Kaotab	1	6.5	1.5	0.000723	0.000273
	2	6.3	1.2	0.000598	0.000225
	3	6.6	1.2	0.000570	0.000215
	4	6.7	1.5	0.000701	0.000265
Fraxcast	1	6.4	1.3	0.000636	0.000344
	2	6.4	0.8	0.000392	0.000211
	3	6.4	0.7	0.000342	0.000185
Carbofrax	1	5.5	2.4	0.00137	0.000635
	2	6.4	2.5	0.00122	0.000569
	3	5.9	3.0	0.00159	0.000741

Table 24. Sand test run #10

Temperature : 821 - 858 °C
Gas velocity : 17.8 (m/s)
Solids flow : 50 (Kg/h)
Time : 5.5 (h)

Sample	#	h_s (cm)	Δm (g)	E ($g/cm^2/h$)	E ($cm^3/cm^2/h$)
Kaotab	1	10.4	1.98	0.00217	0.000818
	2	12.0	2.12	0.00201	0.000760
	3	10.2	2.53	0.00823	0.00107
	4	18.1	3.39	0.00213	0.000805
Fraxcast	1	8.0	2.86	0.00407	0.00220
	2	11.5	3.14	0.00311	0.00168
	3	12.6	4.08	0.00369	0.00199
	4	17.5	7.21	0.00469	0.00254
Carbofrax	1	6.5	1.36	0.00238	0.00111
	2	5.6	1.43	0.00291	0.00135
	3	18.3	6.05	0.00376	0.00175

Table 25. Slag test run #1

Temperature : 196-206 °C
Gas velocity : 17.8 (m/s)
Solids flow : 64 (Kg/h)
Time : 18.0 (h)

Sample	#	h_s (cm)	Δm (g)	E ($g/cm^2/h$)	E ($cm^3/cm^2/h$)
Kaotab	1	6.5	5.4	0.00289	0.00109
	2	6.3	7.3	0.00403	0.00152
	3	6.6	8.0	0.00422	0.00159
	4	6.7	7.1	0.00369	0.00139
Fraxcast	1	6.4	9.4	0.00511	0.00276
	2	6.4	7.9	0.00430	0.00232
	3	5.8	8.9	0.00534	0.00289
Carbofrax	1	5.5	8.8	0.00557	0.00259
	2	6.4	9.1	0.00495	0.00230
	3	5.9	4.5	0.00265	0.00123

Table 26. Slag test run #2

Temperature : 337-355 °C
Gas velocity : 17.8 (m/s)
Solids flow : 64 (Kg/h)
Time : 11.8 (h)

Sample	#	h_s (cm)	Δm (g)	E ($g/cm^2/h$)	E ($cm^3/cm^2/h$)
Kaotab	1	6.5	7.6	0.00621	0.00234
	2	6.6	5.7	0.00459	0.00173
	3	6.7	4.7	0.00372	0.00141
Fraxcast	1	6.4	5.6	0.00465	0.00251
	2	6.4	7.5	0.00622	0.00336
	3	6.4	5.0	0.00415	0.00224
	4	6.6	4.9	0.00394	0.00213
	5	5.8	6.9	0.00632	0.00341
Carbofrax	1	5.5	9.4	0.00908	0.00422
	2	5.9	10.3	0.00927	0.00431
	3	6.5	5.2	0.00424	0.00198
	4	6.3	4.7	0.00396	0.00184

Table 27. Slag test run #3

Temperature : 22 °C
Gas velocity : 17.8 (m/s)
Solids flow : 64 (Kg/h)
Time : 11.0 (h)

Sample	#	h_s (cm)	Δm (g)	E ($g/cm^2/h$)	E ($cm^3/cm^2/h$)
Kaotab	1	6.5	2.6	0.00228	0.000860
	2	6.3	5.9	0.00533	0.00201
	3	6.6	4.1	0.00354	0.00134
	4	6.7	3.0	0.00255	0.000962
Fraxcast	1	6.4	7.0	0.00623	0.00337
	2	6.4	9.4	0.00837	0.00452
	3	6.4	4.0	0.00356	0.00192
	4	6.4	6.4	0.00570	0.00308
	5	6.6	9.0	0.00777	0.00420
	6	5.8	4.0	0.00393	0.00212
Carbofrax	1	5.5	2.9	0.00300	0.00140
	2	6.4	4.9	0.00436	0.00203
	3	5.9	2.8	0.00270	0.00126
	4	6.5	7.9	0.00692	0.00322
	5	6.3	5.7	0.00515	0.00240
	6	6.3	6.4	0.00579	0.00269

Table 28. Slag test run #4

Temperature : 195-204 °C
Gas velocity : 26.0 (m/s)
Solids flow : 64 (Kg/h)
Time : 8.5 (h)

Sample	#	h_s (cm)	Δm (g)	E ($g/cm^2/h$)	E ($cm^3/cm^2/h$)
Kaotab	1	6.5	8.6	0.00975	0.00368
	2	6.3	20.7	0.0242	0.00914
	3	6.6	15.3	0.0171	0.00645
	4	6.7	9.5	0.0105	0.00394
Fraxcast	1	6.4	15.9	0.0183	0.00999
	2	6.4	10.6	0.0122	0.00660
	3	6.6	13.1	0.0146	0.00791
	4	5.8	11.2	0.0142	0.00769
Carbofrax	1	5.5	12.1	0.0162	0.00754
	2	5.9	11.3	0.0141	0.00657

Table 29. Slag test run #5

Temperature : 342-364 °C
Gas velocity : 26.0 (m/s)
Solids flow : 64 (Kg/h)
Time : 4.7 (h)

Sample	#	h_s (cm)	Δm (g)	E ($g/cm^2/h$)	E ($cm^3/cm^2/h$)
Kaotab	1	6.5	5.6	0.0115	0.00433
	2	6.3	10.4	0.0220	0.00830
	3	6.6	8.4	0.0170	0.00640
	4	6.7	6.7	0.0133	0.00503
	5	6.1	9.7	0.0212	0.00799
Fraxcast	1	6.4	6.7	0.0140	0.00754
	2	6.4	7.7	0.0160	0.00807
	3	6.6	9.0	0.0182	0.00983
	4	5.8	7.8	0.0179	0.00969
Carbofrax	1	5.5	5.4	0.0131	0.00608
	2	5.9	6.8	0.0154	0.00715
	3	6.3	10.1	0.0214	0.00994

Table 30. Slag test run #6

Temperature : 451-483 °C
Gas velocity : 26.0 (m/s)
Solids flow : 64 (Kg/h)
Time : 5.6 (h)

Sample	#	h_s (cm)	Δm (g)	E ($g/cm^2/h$)	E ($cm^3/cm^2/h$)
Kaotab	1	6.3	10.5	0.0186	0.00704
	2	6.6	10.6	0.0179	0.00678
	3	6.1	6.6	0.0121	0.00458
Fraxcast	1	6.4	11.1	0.0194	0.0105
	2	6.4	8.9	0.0156	0.00841
	3	6.4	9.8	0.0171	0.00926
	4	6.6	11.1	0.0188	0.0102
Carbofrax	1	6.4	8.7	0.0152	0.00707
	2	6.5	11.0	0.0189	0.00881

Table 31. Slag test run #7

Temperature : 320-369 °C
Gas velocity : 34.0 (m/s)
Solids flow : 64 (Kg/h)
Time : 5.0 (h)

Sample	#	h_s (cm)	Δm (g)	E ($g/cm^2/h$)	E ($cm^3/cm^2/h$)
Kaotab	1	6.5	20.0	0.0385	0.0146
	2	6.3	21.2	0.0422	0.0159
	3	6.6	13.7	0.0260	0.00980
	4	6.7	18.6	0.0348	0.0131
Fraxcast	1	6.4	24.1	0.0472	0.0255
	2	6.4	19.4	0.0380	0.0205
	3	6.4	14.5	0.0284	0.0153
	4	6.6	19.7	0.0374	0.0202
	5	20.0	23.0	0.0144	0.00779
Carbofrax	1	5.5	13.7	0.0312	0.0145
	2	6.4	16.9	0.0331	0.0154
	3	5.9	10.7	0.0227	0.0106

Table 32. Slag test run #8

Temperature : 193-214 °C
Gas velocity : 34.0 (m/s)
Solids flow : 64 (Kg/h)
Time : 4.9 (h)

Sample	#	h_s (cm)	Δm (g)	E ($g/cm^2/h$)	E ($cm^3/cm^2/h$)
Kaotab	1	6.5	16.0	0.0314	0.0118
	2	6.3	20.4	0.0414	0.0156
	3	6.6	18.2	0.0353	0.0133
	4	6.7	9.4	0.0179	0.00677
Fraxcast	1	6.4	11.6	0.0232	0.0125
	2	6.4	14.7	0.0294	0.0158
	3	6.6	18.6	0.0360	0.0194
	4	20.0	28.0	0.0179	0.00967
Carbofrax	1	5.5	8.7	0.0202	0.00939
	2	6.4	12.7	0.0254	0.0118
	3	5.9	8.5	0.0184	0.00856

Table 33. Slag test run #9

Temperature : 438-473 °C
Gas velocity : 34.0 (m/s)
Solids flow : 64 (Kg/h)
Time : 3.5 (h)

Sample	#	h_s (cm)	Δm (g)	E ($g/cm^2/h$)	E ($cm^3/cm^2/h$)
Kaotab	1	6.5	16.9	0.0465	0.0176
	2	6.3	8.5	0.0242	0.00911
	3	6.6	14.8	0.0401	0.0151
Fraxcast	1	6.4	14.3	0.0400	0.0216
	2	6.4	14.0	0.0392	0.0212
	3	6.4	14.4	0.0403	0.0218
	4	6.6	-13.2	0.0358	0.0193
Carbofrax	1	5.5	7.4	0.0241	0.0112
	2	6.4	13.5	0.0377	0.0176
	3	6.5	13.6	0.0375	0.0174

Table 34. Slag test run #10

Temperature : 512-556 °C
Gas velocity : 34.0 (m/s)
Solids flow : 64 (Kg/h)
Time : 2.7 (h)

Sample	#	h_s (cm)	Δm (g)	E ($g/cm^2/h$)	E ($cm^3/cm^2/h$)
Kaotab	1	6.5	12.5	0.0446	0.0168
	2	6.3	9.0	0.0332	0.0125
	3	6.6	13.7	0.0482	0.0182
	4	6.7	7.3	0.0253	0.00954
Fraxcast	1	6.4	6.1	0.0221	0.0120
	2	6.4	7.2	0.0261	0.0141
	3	6.4	8.3	0.0301	0.0163
	4	6.6	8.0	0.0281	0.0152
Carbofrax	1	5.5	5.2	0.0219	0.0102
	2	6.4	8.8	0.0319	0.0149
	3	5.9	9.2	0.0362	0.0168

Table 35. Slag test run #11

Temperature : 196-216 °C
Gas velocity : 17.8 (m/s)
Solids flow : 119 (Kg/h)
Time : 6.2 (h)

Sample	#	h_s (cm)	Δm (g)	E ($g/cm^2/h$)	E ($cm^3/cm^2/h$)
Kaotab	1	6.5	4.8	0.00746	0.00281
	2	6.3	4.5	0.00722	0.00272
	3	6.6	3.2	0.00490	0.00185
	4	6.7	2.8	0.00422	0.00159
Fraxcast	1	6.4	4.5	0.00711	0.00384
	2	6.4	5.2	0.00821	0.00444
	3	20.0	16.4	0.00829	0.00448
Carbofrax	1	5.5	2.5	0.00459	0.00213
	2	6.4	3.1	0.00489	0.00227
	3	5.9	1.7	0.00291	0.00135
	4	18.3	10.4	0.00574	0.00267

Table 36. Slag test run #12

Temperature : 196-215 °C
Gas velocity : 17.8 (m/s)
Solids flow : 171 (Kg/h)
Time : 3.7 (h)

Sample	#	h_s (cm)	Δm (g)	E ($g/cm^2/h$)	E ($cm^3/cm^2/h$)
Kaotab	1	6.5	2.5	0.00651	0.00246
	2	6.3	3.7	0.00994	0.00375
	3	6.6	3.1	0.00795	0.00300
	4	6.7	2.2	0.00556	0.00210
	5	16.8	6.0	0.00605	0.00228
Fraxcast	1	6.4	3.5	0.00926	0.00501
	2	6.4	3.3	0.00873	0.00472
	3	20.0	10.0	0.00846	0.00456
Carbofrax	1	5.5	1.7	0.00523	0.00243
	2	6.4	1.5	0.00397	0.00185
	3	5.9	1.8	0.00517	0.00240

Table 37. Slag test run #13

Temperature : 189 - 226 °C
Gas velocity : 17.8 (m/s)
Solids flow : 225 (Kg/h)
Time : 3.0 (h)

Sample	#	h_s (cm)	Δm (g)	E ($g/cm^2/h$)	E ($cm^3/cm^2/h$)
Kaotab	1	6.5	2.9	0.00932	0.00351
	2	6.6	1.9	0.00601	0.00227
	3	6.7	2.4	0.00748	0.00282
	4	6.1	3.3	0.0113	0.00426
Fraxcast	1	6.4	2.7	0.00881	0.00476
	2	6.4	3.1	0.0101	0.00547
	3	20.0	9.4	0.00982	0.00531
Carbofrax	1	5.5	1.4	0.00532	0.00248
	2	6.4	1.5	0.00489	0.00228
	3	5.9	1.2	0.00425	0.00197

Table 38. Slag test run #14

Temperature : 648 - 671 °C
Gas velocity : 34.0 (m/s)
Solids flow : 64 (Kg/h)
Time : 1.0 (h)

Sample	#	h_s (cm)	Δm (g)	E ($g/cm^2/h$)	E ($cm^3/cm^2/h$)
Kaotab	1	6.5	2.9	0.0280	0.0105
	2	6.3	2.2	0.0219	0.00826
	3	6.6	2.6	0.0247	0.00931
	4	6.7	3.2	0.0299	0.0113
Fraxcast	1	6.4	2.3	0.0225	0.0122
	2	6.4	1.4	0.0137	0.00741
Carbofrax	1	5.5	1.3	0.0148	0.00689
	2	6.4	1.5	0.0234	0.0109
	3	5.9	1.2	0.0127	0.00593

Table 39. Alumina test run #1

Temperature : 512-559 °C
Gas velocity : 17.8 (m/s)
Solids flow : 48 (Kg/h)
Time : 9.0 (h)

Sample	#	h_s (cm)	Δm (g)	E ($g/cm^2/h$)	E ($cm^3/cm^2/h$)
Kaotab	1	10.4	1.48	0.000991	0.000374
	2	12.0	3.16	0.00183	0.000692
	3	10.2	1.01	0.000689	0.000260
	4	18.1	3.1	0.00119	0.000449
Fraxcast	1	7.8	1.53	0.00136	0.000738
	2	8.0	1.90	0.00165	0.000894
	3	11.5	1.95	0.00118	0.000638
	4	12.6	2.78	0.00154	0.000830
	5	17.5	4.12	0.00164	0.000886
Carbofrax	1	6.5	1.67	0.00179	0.000832
	2	5.6	1.43	0.00177	0.000823
	3	18.3	4.01	0.00153	0.000710

Table 40. Alumina test run #2

Temperature : 508-579 °C
Gas velocity : 26.0 (m/s)
Solids flow : 48 (Kg/h)
Time : 5.0 (h)

Sample	#	h_s (cm)	Δm (g)	E ($g/cm^2/h$)	E ($cm^3/cm^2/h$)
Kaotab	1	10.4	1.80	0.00217	0.000818
	2	12.0	3.96	0.00414	0.00156
	3	10.2	3.68	0.00452	0.00171
	4	18.1	5.8	0.00402	0.00152
Fraxcast	1	7.8	1.70	0.00273	0.00148
	2	8.0	2.48	0.00388	0.00210
	3	11.5	2.09	0.00228	0.00123
	4	12.6	2.55	0.00254	0.00137
	5	17.5	4.32	0.00309	0.00167
Carbofrax	1	6.5	2.05	0.00395	0.00184
	2	5.6	2.21	0.00495	0.00230
	3	18.3	8.32	0.00569	0.00265

Table 41. Alumina test run #3

Temperature : 521-535 °C
Gas velocity : 34.0 (m/s)
Solids flow : 48 (Kg/h)
Time : 4.5 (h)

Sample	#	h_s (cm)	Δm (g)	E ($g/cm^2/h$)	E ($cm^3/cm^2/h$)
Kaotab	1	10.4	6.54	0.00876	0.00330
	2	12.0	7.47	0.00867	0.00327
	3	10.2	7.85	0.0107	0.00404
	4	18.1	16.6	0.0128	0.00482
Fraxcast	1	8.0	5.31	0.00924	0.00500
	2	11.5	6.02	0.00729	0.00394
	3	12.6	5.95	0.00657	0.00355
	4	17.5	9.93	0.00790	0.00428
Carbofrax	1	6.5	3.07	0.00658	0.00306
	2	5.6	3.92	0.00975	0.00453
	3	18.3	11.02	0.00838	0.00390

Table 42. Alumina test run #4

Temperature : 525-546 °C
Gas velocity : 17.8 (m/s)
Solids flow : 112 (Kg/h)
Time : 9.0 (h)

Sample	#	h_s (cm)	Δm (g)	E ($g/cm^2/h$)	E ($cm^3/cm^2/h$)
Kaotab	1	10.4	2.97	0.00199	0.000750
	2	12.0	3.62	0.00210	0.000793
	3	10.2	3.12	0.00213	0.000804
	4	18.1	4.0	0.00154	0.000581
Fraxcast	1	8.0	2.92	0.00254	0.00137
	2	11.5	3.05	0.00185	0.00100
	3	12.6	2.72	0.00150	0.000811
	4	17.5	4.37	0.00174	0.000940
Carbofrax	1	6.5	1.93	0.00207	0.000962
	2	5.6	1.84	0.00229	0.00106
	3	18.3	7.37	0.00280	0.00130

Table 43. Alumina test run #5

Temperature : 516-535 °C
Gas velocity : 17.8 (m/s)
Solids flow : 172 (Kg/h)
Time : 5.0 (h)

Sample	#	h_s (cm)	Δm (g)	E ($g/cm^2/h$)	E ($cm^3/cm^2/h$)
Kaotab	1	10.4	1.58	0.00190	0.000718
	2	12.0	1.99	0.00208	0.000784
	3	10.2	2.31	0.00284	0.00107
	4	18.1	3.3	0.00228	0.000862
Fraxcast	1	8.0	1.30	0.00204	0.00110
	2	11.5	1.80	0.00196	0.00106
	3	12.6	2.85	0.00283	0.00153
	4	17.5	4.52	0.00324	0.00175
Carbofrax	1	6.5	1.26	0.00243	0.00113
	2	5.6	1.20	0.00269	0.00125
	3	18.3	4.05	0.00277	0.00129

Table 44. Alumina test run #6

Temperature : 688 - 720 °C
Gas velocity : 34.0 (m/s)
Solids flow : 48 (Kg/h)
Time : 4.5 (h)

Sample	#	h_s (cm)	Δm (g)	E ($g/cm^2/h$)	E ($cm^3/cm^2/h$)
Kaotab	1	10.4	9.28	0.0124	0.00468
	2	12.0	8.75	0.0105	0.00383
	3	10.2	10.11	0.0138	0.00521
	4	18.1	19.1	0.0147	0.00554
Fraxcast	1	8.0	6.74	0.0117	0.00634
	2	11.5	9.49	0.0115	0.00621
	3	12.6	12.48	0.0138	0.00745
	4	17.5	16.63	0.0132	0.00715
Carbofrax	1	6.5	4.48	0.00960	0.00446
	2	5.6	4.20	0.0104	0.00486
	3	18.3	20.64	0.0157	0.00731

Table 45. Alumina test run #7

Temperature : 818 - 870 °C
Gas velocity : 34.0 (m/s)
Solids flow : 48 (Kg/h)
Time : 5.0 (h)

Sample	#	h_s (cm)	Δm (g)	E ($g/cm^2/h$)	E ($cm^3/cm^2/h$)
Kaotab	1	10.4	11.70	0.0141	0.00532
	2	12.0	14.23	0.0148	0.00561
	3	10.2	15.38	0.0189	0.00713
	4	18.1	26.0	0.0180	0.00679
Fraxcast	1	8.0	9.87	0.0155	0.00836
	2	11.5	18.01	0.0196	0.0106
	3	12.6	22.96	0.0228	0.0123
	4	17.5	50.04	0.0358	0.0193
Carbofrax	1	6.5	7.13	0.0137	0.00640
	2	5.6	9.52	0.0213	0.00991
	3	18.3	31.08	0.0213	0.00991

Table 46. Alumina test run #8

Temperature : 832 - 869 °C
Gas velocity : 34.0 (m/s)
Solids flow : 48 (Kg/h)
Time : 5.5 (h)

Sample	#	h_s (cm)	Δm (g)	E ($g/cm^2/h$)	($cm^3/cm^2/h$)
Kaotab	1	10.4	14.91	0.0163	0.00616
	2	12.0	19.04	0.0181	0.00682
	3	10.2	16.93	0.0190	0.00714
	4	18.1	29.5	0.0186	0.00701
Fraxcast	1	8.0	12.71	0.0181	0.00978
	2	11.5	16.50	0.0163	0.00884
	3	12.6	16.24	0.0147	0.00794
	4	17.5	29.35	0.0191	0.0103
Carbofrax	1	6.5	8.86	0.0155	0.00722
	2	5.6	10.74	0.0218	0.0102
	3	18.3	26.69	0.0166	0.00772

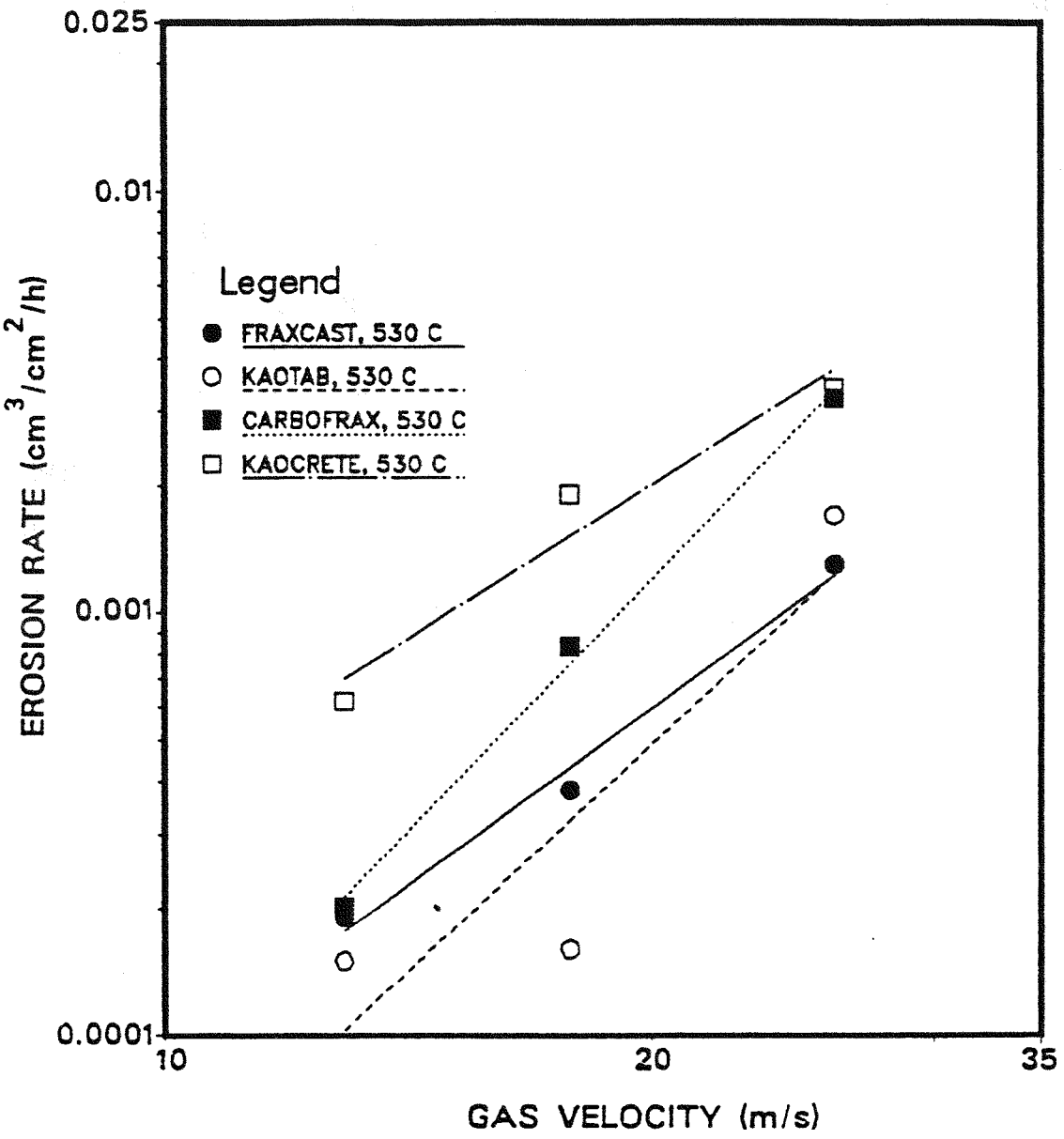

Figure 66. Effect of gas velocity on the erosion rates by river sand, W_s= 50 kg/h

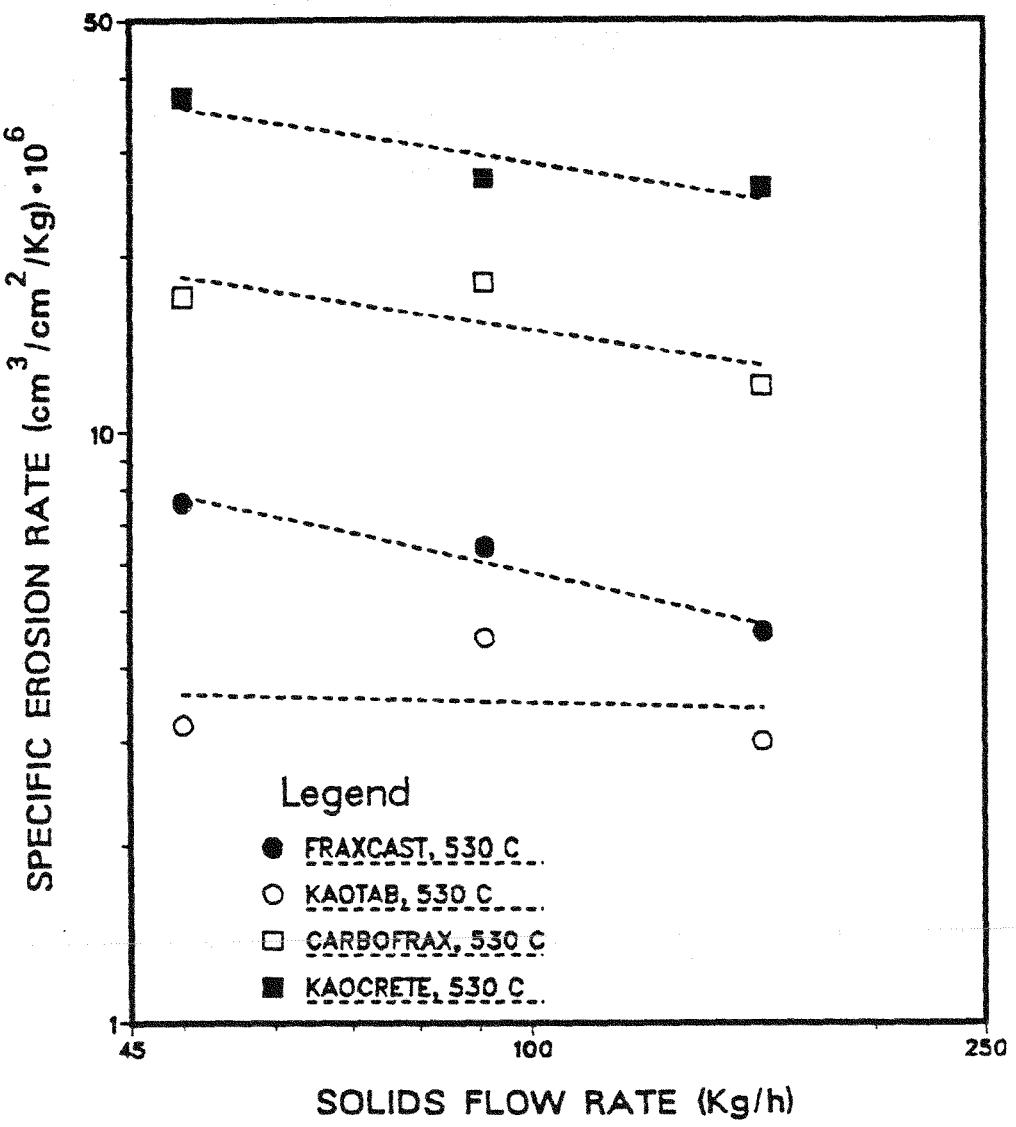

Figure 67. Effect of solids concentration on the erosion rate by river sand, U_g = 17.8 m/s

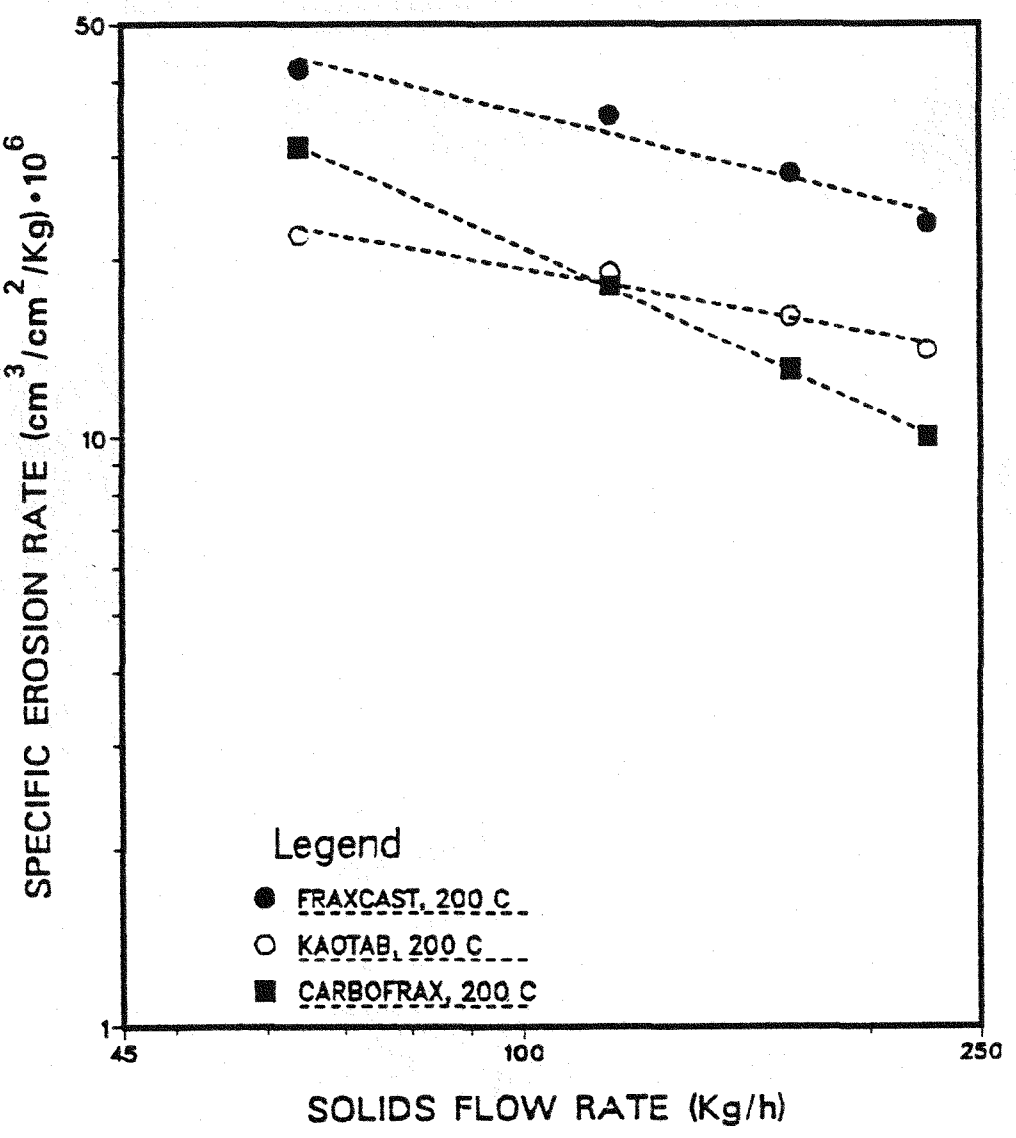

Figure 68. Effect of solids concentration on the erosion rate by coal slag, U_s = 17.8 m/s

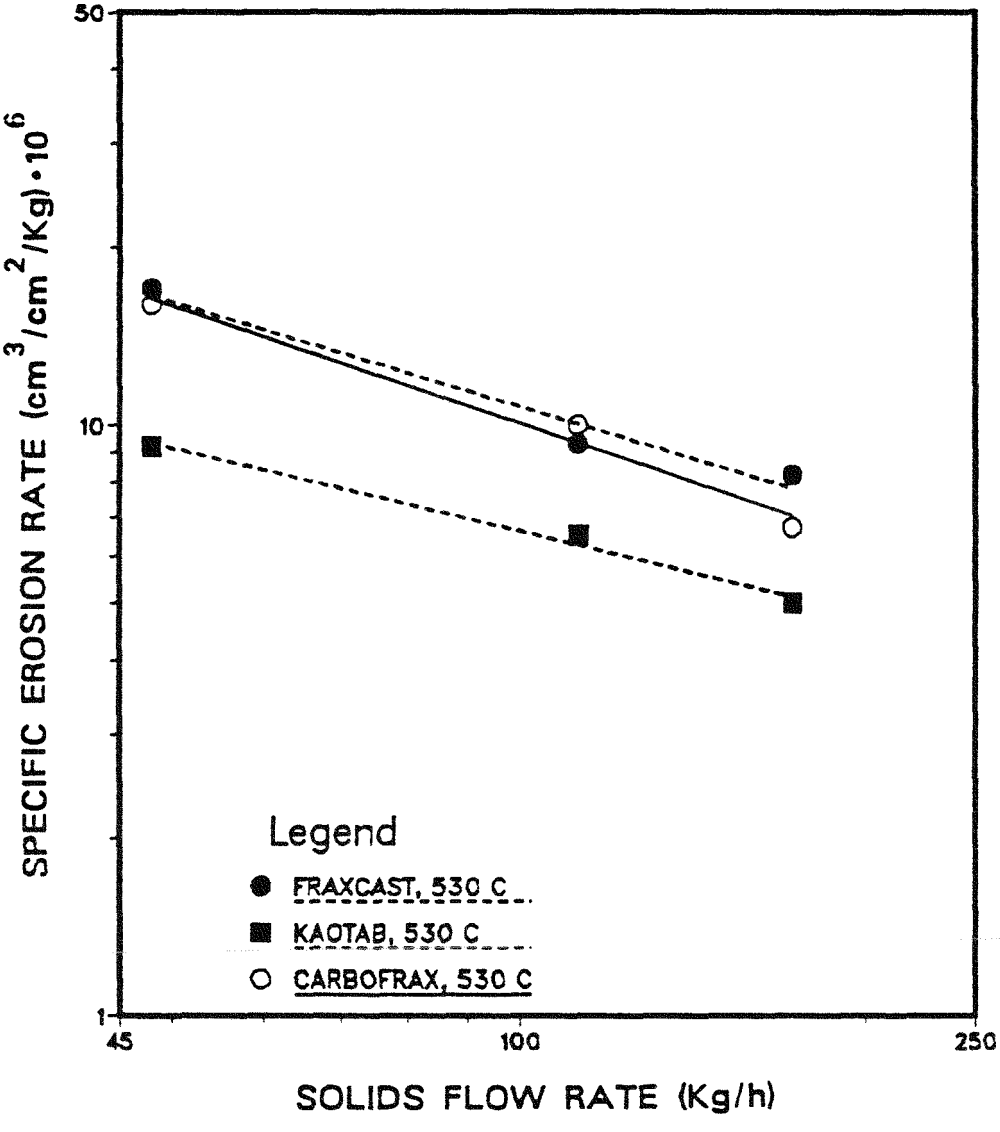

Figure 69. Effect of solids concentration on the erosion rate by alumina, U_s = 17.8 m/s

APPENDIX D.
CONCRETE SURFACES

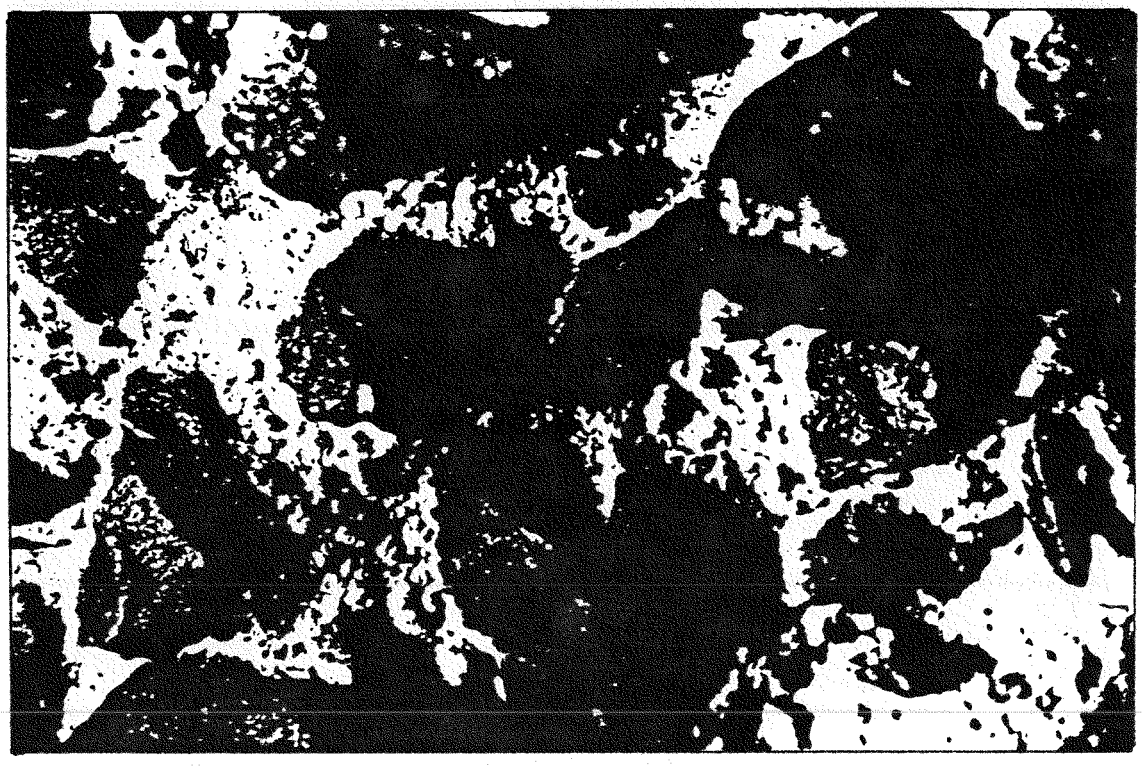

Figure 70. Micrograph of a steady state Fraxcast surface eroded by coal slag

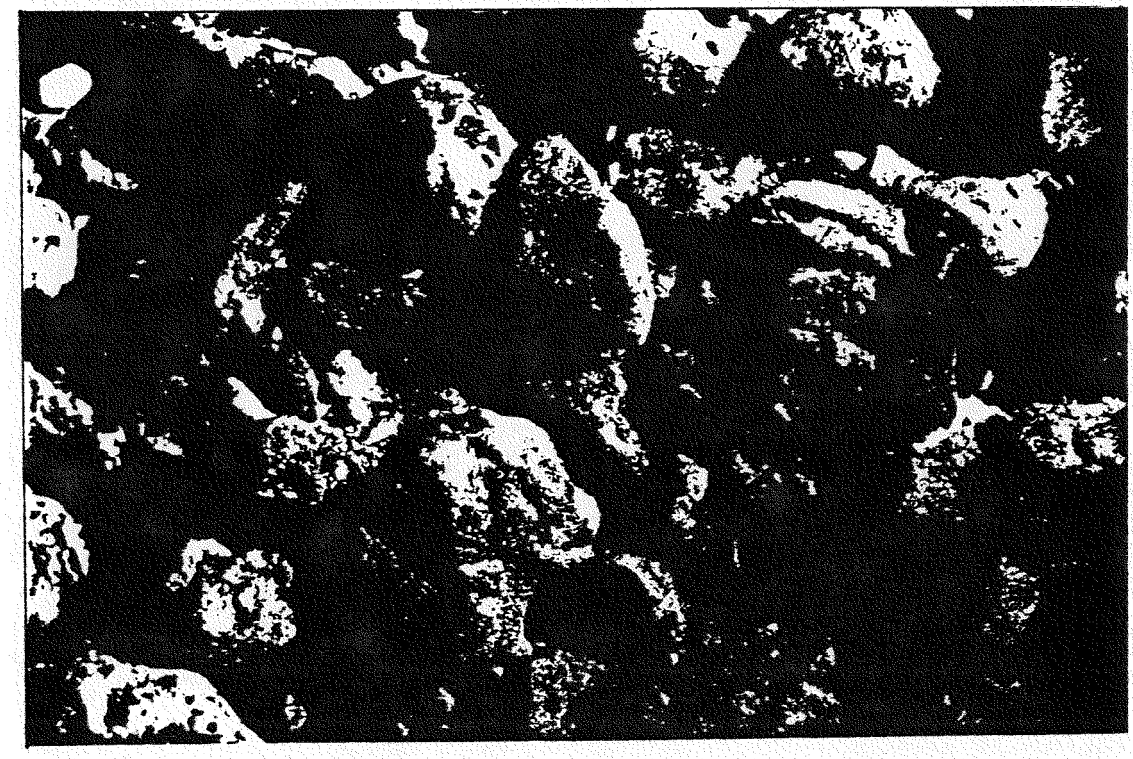

Figure 71. Micrograph of a steady state Kaocrete surface eroded by sand

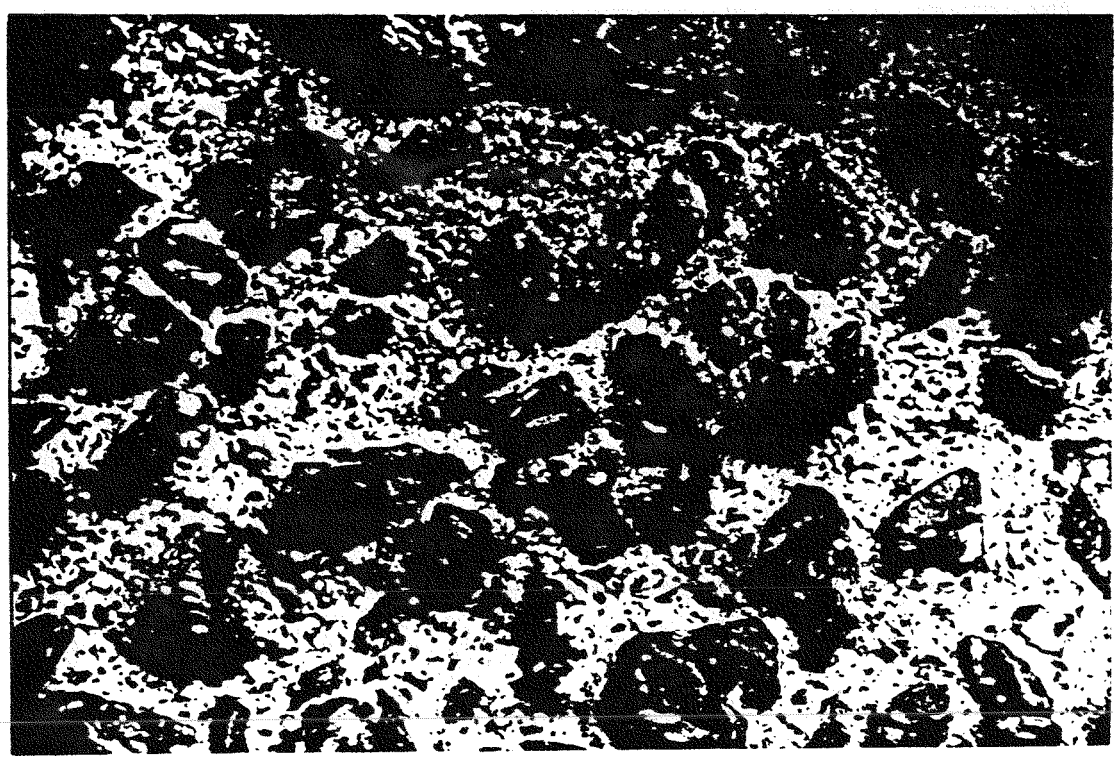

Figure 72. Micrograph of a transient Carbofrax surface eroded by alumina

Figure 73. Micrograph of a steady state Carbofrax surface eroded by alumina

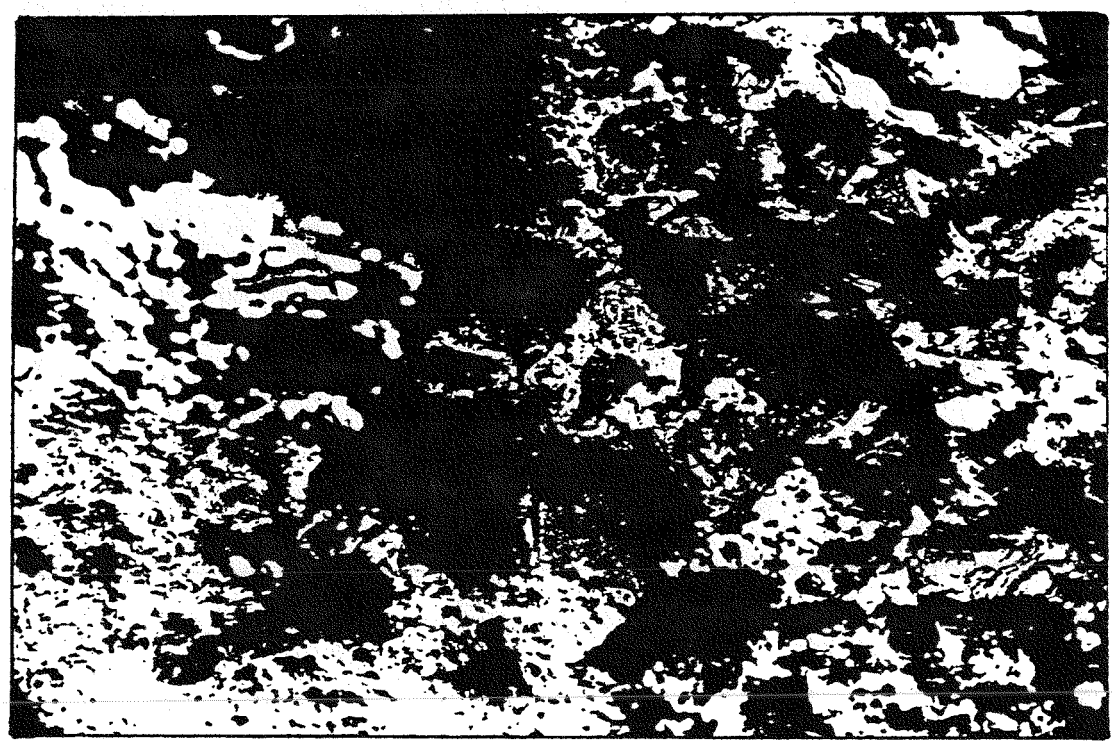

Figure 74. Micrograph of a steady state Carbofrax surface eroded by coal slag

Figure 75. Micrograph of a steady state Carbofrax surface eroded by sand

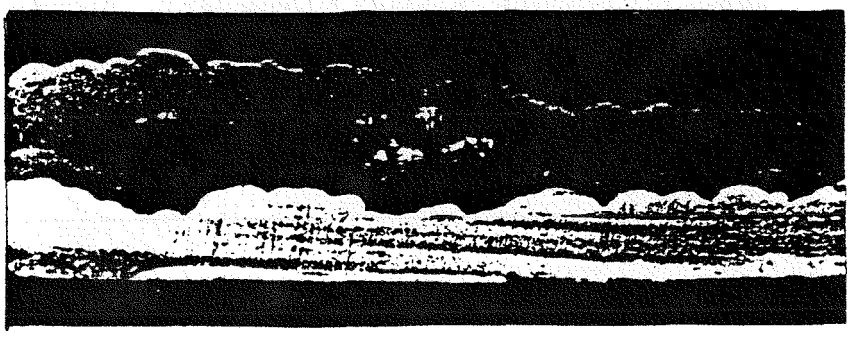

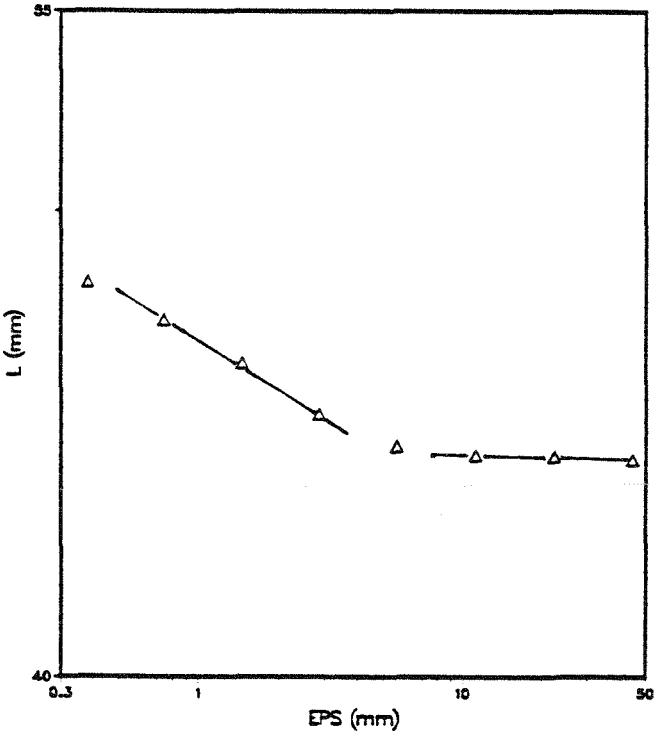

Figure 76. Fractal analysis for a steady state Carbofrax surface eroded by sand

APPENDIX E.
PRESSURE DROP DATA

Table 47. Pressure drop (kPa/m) for coal slag on initial samples

T (°C)	U_g (m/s)	W_s (Kg/h)					
		0	64	74	119	171	225
22	6.3	0.017	-	-	-	-	-
	8.1	0.034	0.118	0.139	0.189	0.233	0.273
	10.0	0.040	-	-	-	-	-
	11.5	0.057	0.187	0.219	0.275	0.322	0.371
	13.6	0.078	-	-	-	-	-
	16.1	0.098	0.261	0.296	0.364	0.458	0.524
	18.6	0.119	-	-	-	-	-
	21.3	0.158	0.369	0.401	0.506	0.583	0.644
200	7.5	0.013	-	-	-	-	-
	8.6	0.020	-	-	-	-	-
	10.8	0.027	0.155	0.206	0.248	0.324	0.366
	13.0	0.042	-	-	-	-	-
	15.3	0.062	0.212	0.290	0.347	0.433	0.512
	17.5	0.084	-	-	-	-	-
	20.5	0.105	0.347	0.396	0.493	0.601	-
	24.3	0.135	-	-	-	-	-
	26.6	0.163	0.448	0.503	0.633	-	-
	29.3	0.192	-	-	-	-	-
	32.5	0.228	0.535	0.589	-	-	-
	34.2	0.261	-	-	-	-	-
350	10.9	0.026	-	-	-	-	-
	13.0	0.033	0.188	0.287	0.338	0.372	0.412
	15.5	0.045	-	-	-	-	-
	18.2	0.064	0.316	0.360	0.433	0.534	0.595
	20.8	0.084	-	-	-	-	-
	24.0	0.102	0.396	0.448	0.557	-	-
	26.5	0.129	0.422	0.476	0.603	-	-
	29.4	0.155	0.470	0.512	-	-	-
	32.7	0.182	-	-	-	-	-
	34.8	0.200	-	-	-	-	-
	38.0	0.252	-	-	-	-	-
450	11.8	0.027	-	-	-	-	-
	14.9	0.033	0.232	0.288	0.380	0.485	-
	17.1	0.047	-	-	-	-	-
	20.0	0.064	0.310	0.371	0.499	0.627	0.775
	22.5	0.078	-	-	-	-	-
	24.7	0.099	0.399	0.467	0.631	0.817	-
	28.2	0.121	-	-	-	-	-
	31.2	0.139	0.472	0.564	0.767	-	-
	33.4	0.162	-	-	-	-	-
	36.6	0.182	0.567	0.655	-	-	-
	37.7	0.197	-	-	-	-	-

Table 48. Pressure drop (kPa/m) for coal slag on rough samples

T (°C)	U_g (m/s)	W_s (Kg/h)					
		0	64	74	119	171	225
22	6.3	0.026	-	-	-	-	-
	8.1	0.037	0.153	0.185	0.230	0.276	0.353
	10.0	0.054	-	-	-	-	-
	11.5	0.066	0.236	0.272	0.362	0.426	0.532
	13.6	0.094	-	-	-	-	-
	16.1	0.121	0.340	0.395	0.497	0.569	0.645
	18.6	0.166	-	-	-	-	-
	21.3	0.229	0.426	0.468	0.601	0.739	0.918
100	6.1	0.010	-	-	-	-	-
	7.7	0.016	-	-	-	-	-
	9.3	0.032	0.192	0.222	0.278	0.347	0.408
	10.4	0.042	-	-	-	-	-
	12.5	0.063	0.259	0.286	0.372	0.472	0.538
	13.7	0.084	-	-	-	-	-
	15.7	0.098	0.330	0.359	0.477	0.580	-
	18.2	0.120	-	-	-	-	-
	20.4	0.138	0.362	0.421	0.527	0.647	0.770
	22.1	0.175	-	-	-	-	-
200	7.9	0.013	-	-	-	-	-
	10.7	0.034	0.188	0.234	0.315	0.388	0.489
	13.8	0.059	-	-	-	-	-
	16.4	0.080	0.337	0.389	0.500	0.626	0.690
	20.5	0.116	-	-	-	-	-
	23.2	0.138	0.435	0.508	0.645	0.738	-
	26.2	0.177	-	-	-	-	-
	28.4	0.230	0.480	0.544	0.682	0.856	-
	31.1	0.274	-	-	-	-	-
	33.4	0.313	-	-	-	-	-
	35.9	0.369	-	-	-	-	-
350	12.1	0.028	-	-	-	-	-
	14.7	0.040	0.271	-	0.421	-	-
	16.8	0.059	-	-	-	-	-
	19.6	0.076	0.357	-	0.527	-	-
	21.7	0.101	-	-	-	-	-
	24.9	0.123	0.479	-	0.717	-	-
	27.3	0.145	-	-	-	-	-
	30.1	0.197	-	-	-	-	-
	32.4	0.202	-	-	-	-	-
	36.0	0.252	-	-	-	-	-
	37.3	0.286	-	-	-	-	-

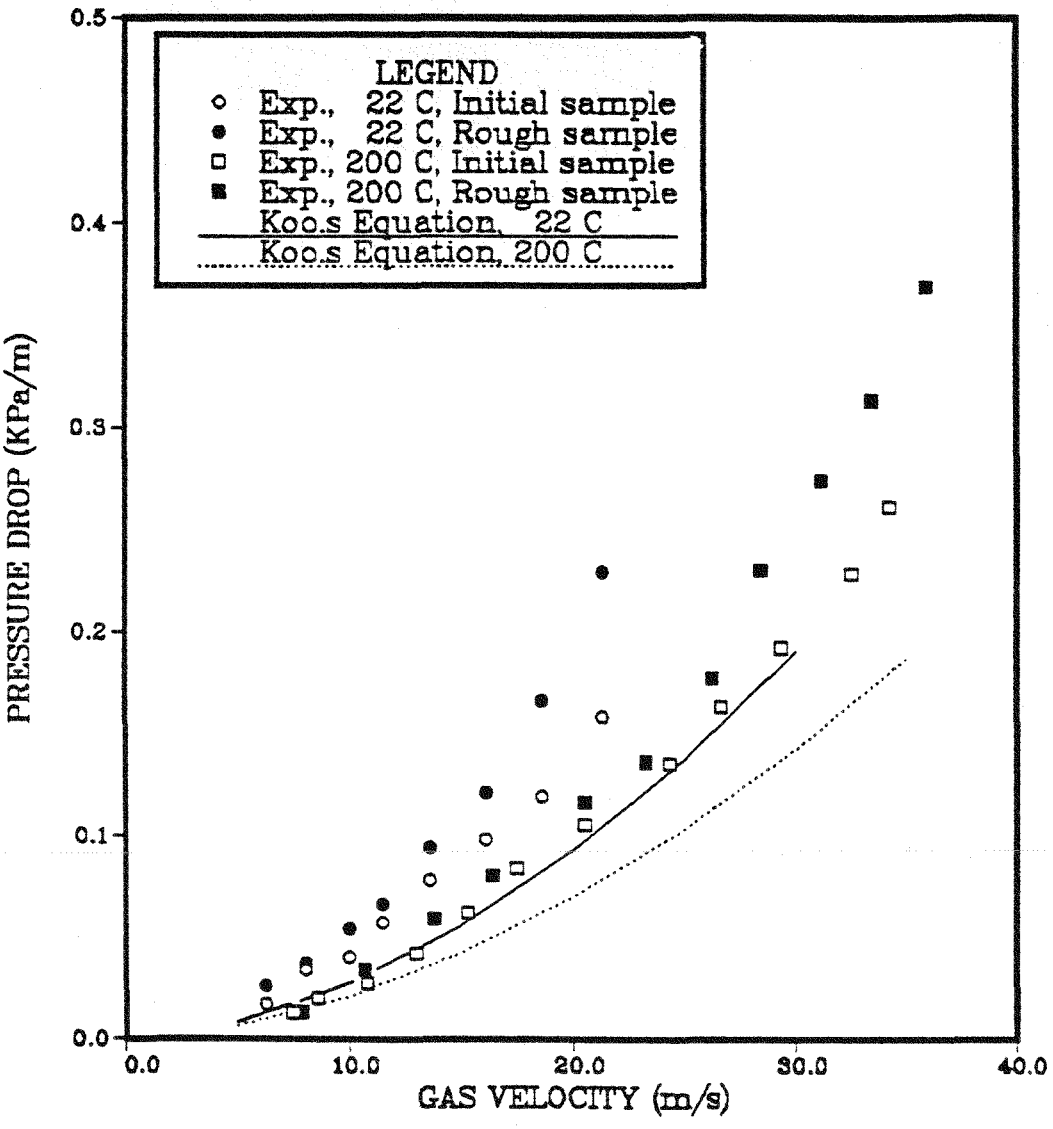

Figure 77. Pressure drop of combustion gases alone compared to Koo's equation

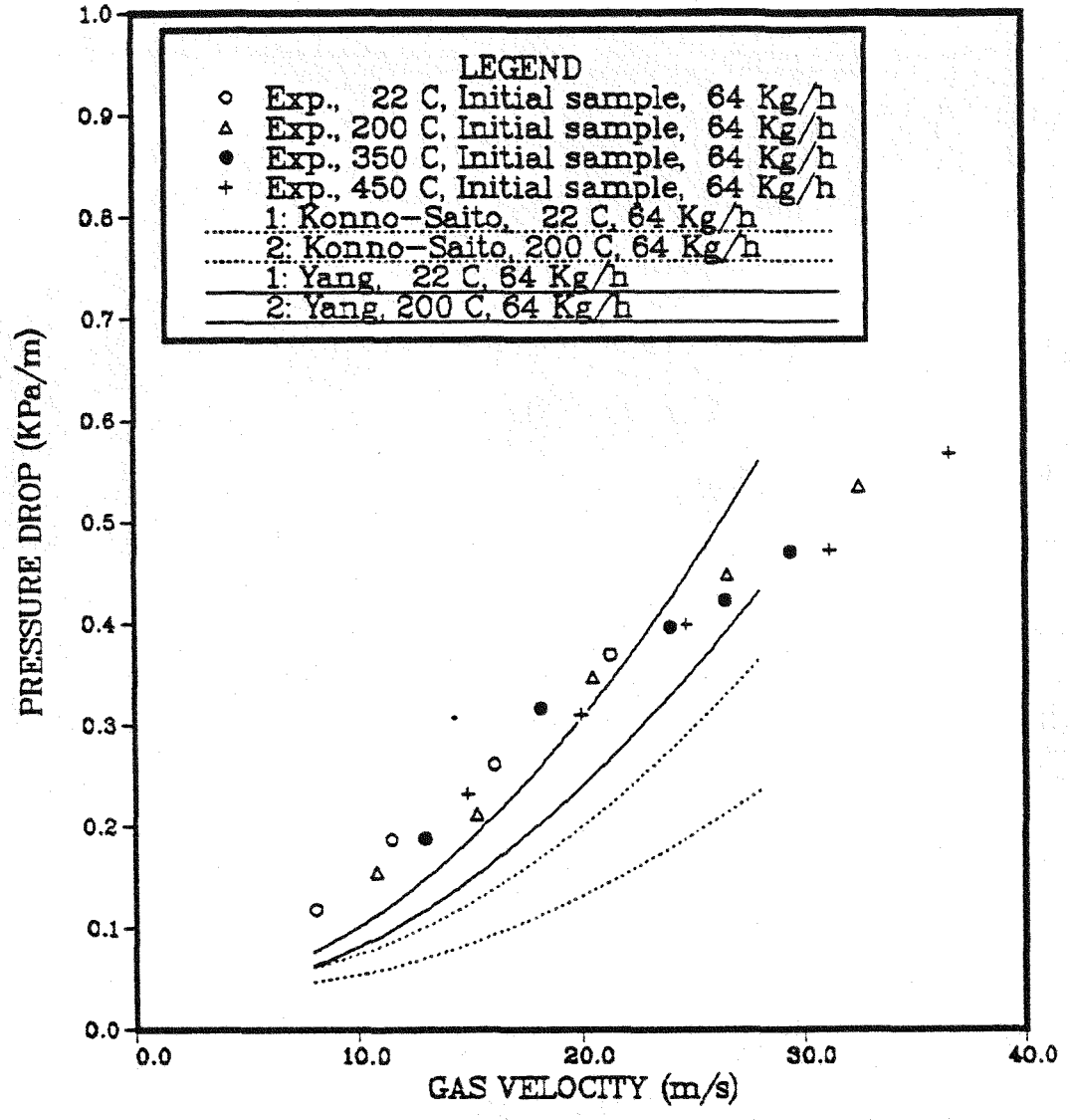

Figure 78. Comparison of pressure drop on initial sample with Konno-Saito and Yang correlations

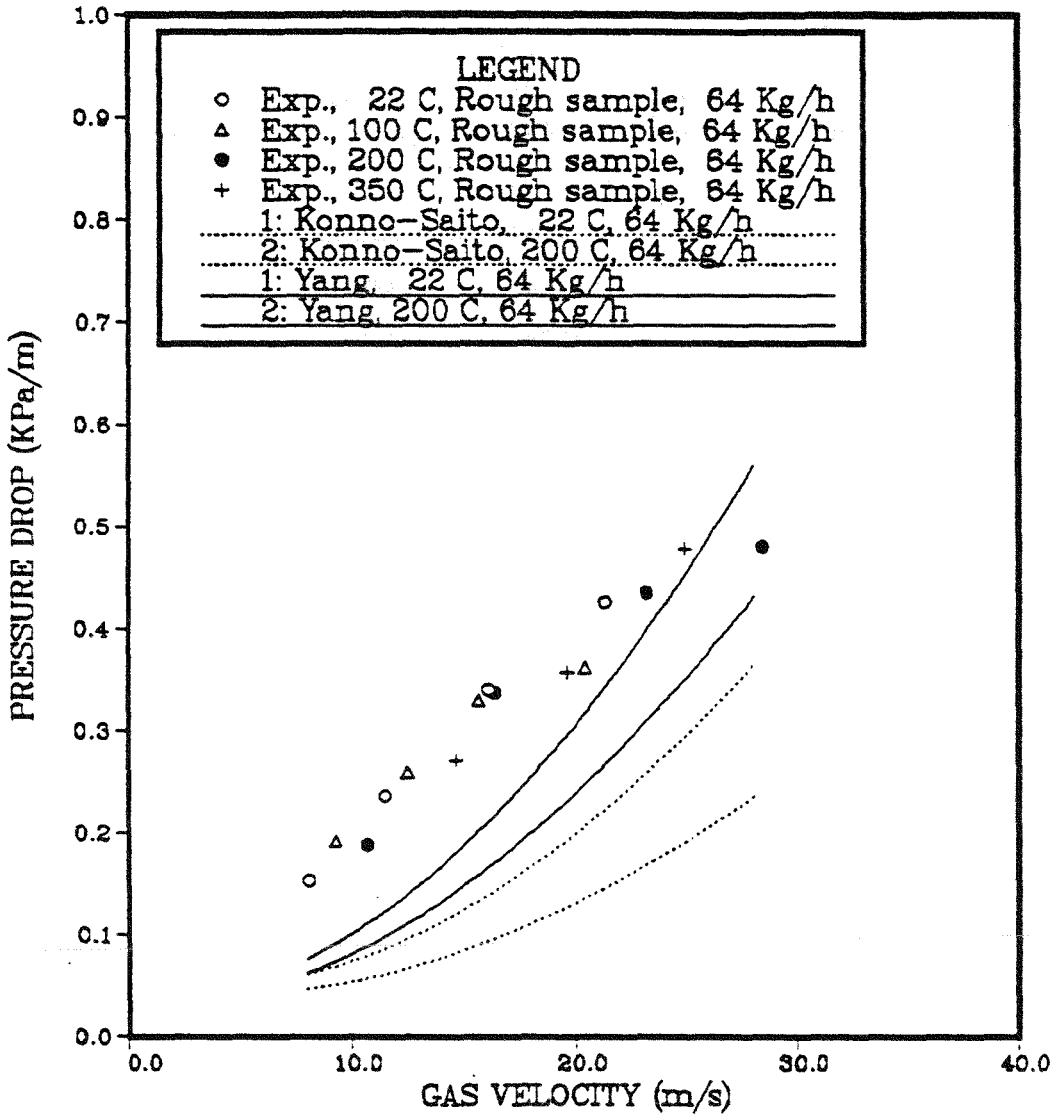

Figure 79. Comparison of pressure drop on rough sample with Konno Saito and Yang correlations

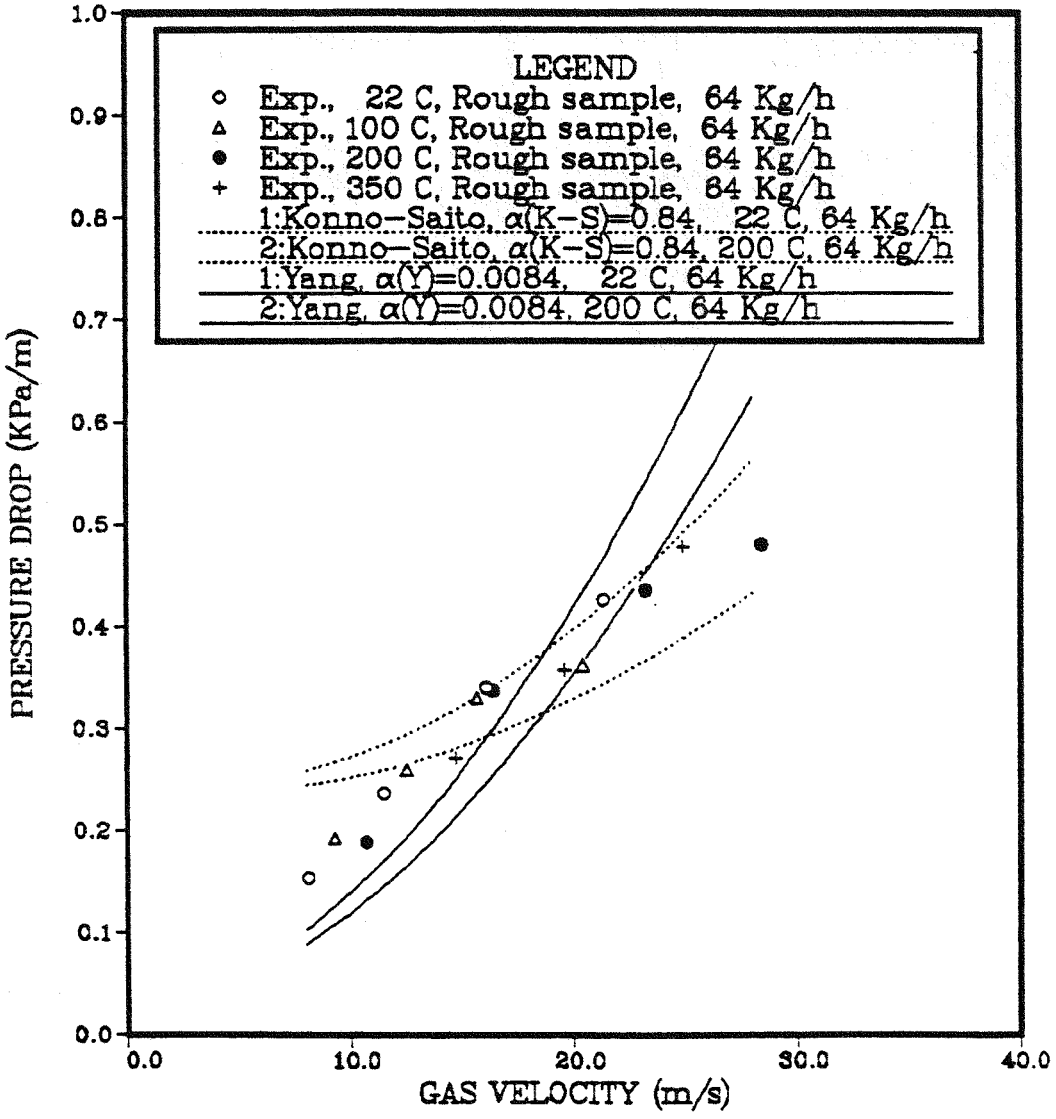

Figure 80. Comparison of pressure drop on rough sample with single parameter fitted Konno-Saito and Yang correlations

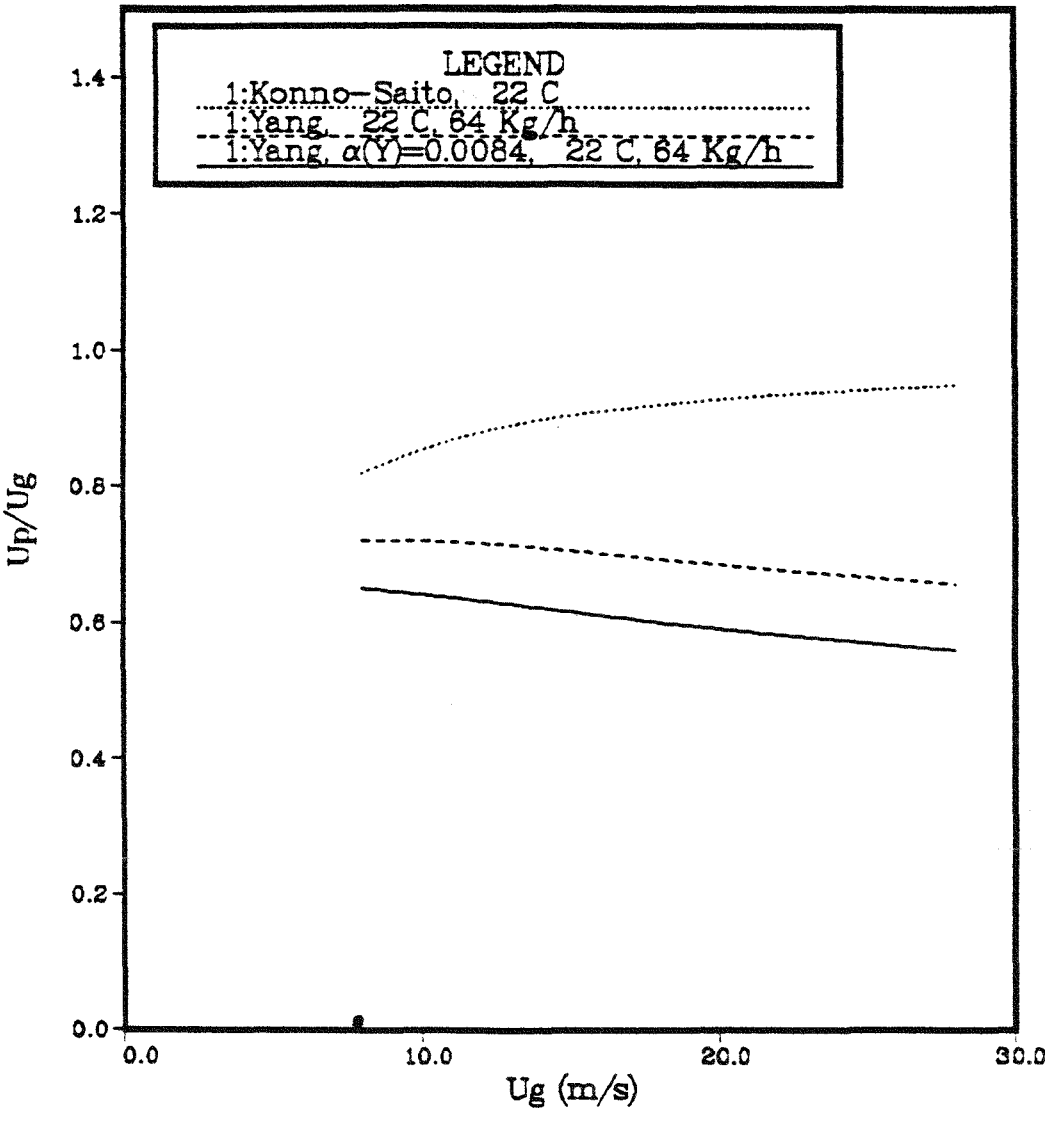

Figure 81. Particle to gas velocity ratio as a function of gas velocity predicted by different correlations

APPENDIX F.
BEND EROSION SIMULATION

Table 49. Erosion data for Fraxcast wedges eroded by sand at 530°C

Sample	α(°)	Dimensions (cm)	A_E (cm²)	E_W (cm³/cm²/kg)
1	22.5	1.8 x 1.8 x 7.6	18.3	4.7E-5
2	30.	2.7 x 2.7 x 7.6	27.4	4.6E-5
3	30.	2.0 x 2.0 x 7.6	20.9	11.3E-5
4	45.	1.8 x 1.8 x 7.6	18.3	13.3E-5
5	90.	1.9 x 7.6	9.7	13.3E-5

Sample	α°	Δm_E (g)	t (h)	Erosion (g/h)
1	22.5	1.9	3.83	0.496
		0.2	5.18	0.0386
		0.1	3.90	0.0256
		0.2	5.0	0.0400
2	30.	5.0	4.66	1.0730
		0.4	4.45	0.0899
		0.3	4.45	0.0674
3	30.	3.5	4.45	0.7978
		0.5	4.45	0.1123
4	45.	1.9	3.83	0.496
		0.7	5.18	0.135
		0.6	3.90	0.154
		0.6	5.0	0.120
5	90.	2.9	3.90	0.744
		0.3	5.0	0.0600
		0.3	4.66	0.0644
		0.2	4.45	0.0449

Table 50. Erosion data for different concrete wedges eroded by alumina at 530°C

Fraxcast

Sample	α(°)	Dimensions (cm)	A_E (cm^2)	E_w ($cm^3/cm^2/kg$)
1	22.5	1.8 x 1.8 x 7.6	18.3	4.1E-4
2	30.	1.8 x 1.8 x 7.6	18.3	12.0E-4
3	45.	1.8 x 1.8 x 7.6	18.3	14.5E-4
4	90.	1.7 x 7.6	8.6	14.7E-4

Kaotab

Sample	α(°)	Dimensions (cm)	A_E (cm^2)	E_w ($cm^3/cm^2/kg$)
1	22.5	1.8 x 1.8 x 7.6	18.3	3.5E-4
2	30.	2.0 x 2.0 x 7.6	20.9	11.1E-4
3	45.	1.8 x 1.8 x 7.6	18.3	14.0E-4
4	90.	1.7 x 7.6	8.6	13.6E-4

Carbofrax

Sample	α(°)	Dimensions (cm)	A_E (cm^2)	E_w ($cm^3/cm^2/kg$)
1	22.5	2.0 x 2.0 x 7.6	20.9	7.5E-4
2	30.	2.0 x 2.0 x 7.6	20.9	13.0E-4
3	45.	1.8 x 1.8 x 1.8	18.3	13.0E-4
4	90.	1.7 x 7.6	8.6	13.1E-4

BEND EROSION SIMULATION PROGRAM

```
      DIMENSION XP(1000),YP(1000)
      DIMENSION UPX(1000),UPY(1000)
      DIMENSION B1(200),B2(200)
      DIMENSION SL1(200),SL2(200)
      DIMENSION DY1(200),DY2(200),DX1(200),DX2(200)
      DIMENSION RM(200)
      DIMENSION ALF1(10000),ALF2(10000)
      DIMENSION TET1(10000),TET2(10000)
      DIMENSION UPC1(10000),UPC2(10000)
      DIMENSION DB1(200),DB2(200)
      DIMENSION UPC(1000)
      DIMENSION SXI1(90),SXI1D(90),SXI2(90),SXI2D(90)
      DIMENSION BOUN(1000)
C
      COMMON/VEL/UGX,UGY,UPX,UPY
      COMMON/VE1/US
      COMMON/FOR/FX,FY
      COMMON/PRP/RG,VG
      COMMON/GEO/DP
      COMMON/GE1/AP
      COMMON/ANG/FIYX
      COMMON/PASS/U1,U2,FUP
C
C     ***************************************************************************
C
C        DATA AND CONSTANTS
C
C     ***************************************************************************
C
      DATA R,RO,DP/0.3048,0.0254,2.E-4/
      DATA RG,RP,VG/0.42,2900.,5.4E-4/
      DATA G,PI/9.8,3.1415926/
      DATA UGMAX/17.8/
      DATA ET/0.0002/
      DATA ETE/36000./
      DATA WS/51./
      DAF=0.87
      NC1=0
      NC2=0
      NINV=0
      TIME=0.
      WRITE(5,100)
  100 FORMAT(1HO,3X,'DISK UNIT:')
      ACCEPT *,ND
      WRITE(5,101)
  101 FORMAT(1HO,3X,'NUMBER OF PARTICLES:')
      ACCEPT *,NPART
      WRITE(5,102)
  102 FORMAT(1HO,3X,'TIME SIMULATION (HRS):')
      ACCEPT *,ENDTIM
      ENDTIM=ENDTIM*3600.
      WRITE(5,1022)
 1022 FORMAT(1HO,3X,'EROSION INTEGRATION TIME (HRS):')
      ACCEPT *,ETH
      ETE=ETH*3600.
C
C     PARTICLE CONSTANTS
C
      D=DP*1.E6
C
```

```
C       PROJECTED AREA OF SPHERE
C
        AP=PI*(DP/2)**2
C
C       VOLUME OF SPHERE
C
        VOL=4./3.*PI*(DP/2)**3
C
C       MASS OF PARTICLE
C
        PMASS=RP*VOL
C
C       PIPE DIAMETER
C
        DT=2*R0
C
        WS=WS/3600.
C
C       EROSION DATA
C       ************
C
        NDAT=0
        XM=0.44
        XN=2.6
        XK1=2.875E-11/(17.8**XN)
        EO=XK1
C       EO=XK1*RP*VOL/WS**XM
        XNPS=WS/VOL/RP
C
C       WRITE DATA
C
        WRITE(ND,103) R,DT,D,UGMAX
 103    FORMAT(1HO,3X,'OUTER RADIUS     : ',F7.4,' m',/,
     *             3X,'PIPE DIAMETER    : ',F7.4,' m',/,
     *             3X,'PARTICLE SIZE    : ',F7.2,' microns',/,
     *             3x,'GAS VELOCITY     : ',F7.1,' m/s',//)
C
C       ********************************************************************
C
C       INITIAL CONDITIONS
C
C       ********************************************************************
C
C       PARTICLES ASSUMED TO BE EVENLY DISTRIBUTED IN A LINE.
C       NO PARTICLE INTERACIONS
C
C       INITIAL POSITION
C
        EPSP=2*(R0-0.003)/(NPART-1)
C
C       INITIAL VELOCITY
C       ASSUME TURBULENT
C
        US=SQRT(4*DP*G*(RP-RG)/3./0.44/RG)
        REP=DP*US*RG/VG
        IF(REP.LT.1000) GO TO 10
        GO TO 50
C
C       ASSUME STOKES
C
```

```
  10    US=DP**2*G*(RP-RG)/18./VG
        REP=DP*US*RG/VG
        IF(REP.GT.0.3) GO TO 20
        GO TO 50
C
C       ASSUME INTERMEDIATE REGION
C
  20    VAR1=DP**1.6*G*(RP-RG)/RG**0.4/VG**0.6
        US=0.152*VAR1**0.7143
        REP=DP*US*RG/VG
        IF(REP.GT.0.3.OR.REP.LT.1000) GO TO 50
        WRITE(5,150)
 150    FORMAT(1X0,'REGIME INCONSISTENCY')
  50    UPINIT=UGMAX-US
        UP=UPINIT
C
C       EROSION CONSTANT
C
C       E00=E0/(WS**XM)*UP**XN
        VOLPI=UP*PI*R0**2
        CONC=XNPS/VOLPI
        DM=1/CONC**(1./3.)
        NDP=2*R0/DM-1
C
        E0=E0*NDP
        XPART=NPART
        XNDP=NDP
        TAUR=XPART/XNDP*DM/UP
        TYPE *,TAUR,NPART,NDP,DM
C
C       ********************************************************************
C
C       INITIAL BOUNDARIES
C
C       ********************************************************************
C
C       CIRCULAR BOUNDARIES, 90 DEGREES BEND
C       SLOPES AT B1 AND B2
C       K CORRESPONDS TO ONE DEGREE IN ZETA
C
        DO 52 K=1,90
        B1(K)=R
        B2(K)=R-2*R0
        SXI1(K)=0.
        SXI2(K)=0.
        SXI1D(K)=0.
        SXI2D(K)=0.
  52    CONTINUE
C
C       ********************************************************************
C       ********************************************************************
C       ********************************************************************
C
C       LOOP THAT CALCULATES PARTICLE TRAJECTORIES AND COLLISIONS
C       FROM BEGINING TO END OF BEND
C
C       ********************************************************************
C
C       REAL TIME FOR NEXT OUTPUT
C
```

```
  15    TIME=TIME-ETE
        TIMEW=TIME/3600.
        ETEW=ETE/3600.
        WRITE(5,290) TIMEW, ETEW
 290    FORMAT(1H0,5X,'TIME:',F7.2,'HRS',F7.2)
C
C       INITIAL POSITION AND VELOCITY OF PARTICLES
C
        DO 210 I=1,NPART
        XP(I)=EPSP*I+0.003
        YP(I)=0.
        UPX(I)=0.
        UPY(I)=UPINIT
C        TYPE *,XP(I),YP(I),UPX(I),UPY(I)
 210    CONTINUE
C
C       CARTESIAN COORDINATES OF WALLS
C
        DO 522 K=1,90
        A=K
        XSIA=SIND(A)
        CSIA=COSD(A)
        DY1(K)=S1(K)*XSIA
        DX1(K)=R-S1(K)*CSIA
        DY2(K)=S2(K)*XSIA
        DX2(K)=R-S2(K)*CSIA
 522    CONTINUE
C
C       SLOPE FOR EACH BOUNDARY
C
        SL1(1)=(DY1(2)-DY1(1))/(DX1(2)-DX1(1))
        SL1(89)=(DY1(89)-DY1(88))/(DX1(89)-DX1(88))
        SL1(90)=0.
        SL2(1)=(DY2(2)-DY2(1))/(DX2(2)-DX2(1))
        SL2(89)=(DY2(89)-DY2(88))/(DX2(89)-DX2(88))
        SL2(90)=0.
        DO 54 K=2,88
        SL1(K)=((DY1(K+1)-DY1(K))/(DX1(K+1)-DX1(K))+(DY1(K)-DY1(K-1))/
     1  (DX1(K)-DX1(K-1)))/2.
        SL2(K)=((DY2(K+1)-DY2(K))/(DX2(K+1)-DX2(K))+(DY2(K)-DY2(K-1))/
     1  (DX2(K)-DX2(K-1)))/2.
  54    CONTINUE
C
C       ACTUAL PIPE DIAMETER
C
        DO 57 K=1,90
        RM(K)=S1(K)-S2(K)
  57    CONTINUE
C
C       RESET COUNTERS FOR PARTICLE COLLISIONS
C
        NC1=0
        NC2=0
C
C       ************************************************************************
C       ************************************************************************
C
C       LOOP THAT CALCULATES TRAJECTORIES AND COLLISIONS
C       FOR EACH PARTICLE IN THE INTERVAL ET
C
```

```
C       ************************************************************.
C
  16    DO 55 L=1,NPART
C
C       POLAR ANGLE FOR PARTICLE POSITION
C
        ZETA=ATAND(YP(L)/(R-XP(L)))
        R=ZETA+1
        IF(ABS(ZETA).LT.1.E-3) GO TO 60
        RL=YP(L)/SIND(ZETA)
        GO TO 70
  60    RL=R-XP(L)
        RR=ABS(R-RL-R0)
        RA=R0
        IF(ZETA.GE.0) GO TO 72
        WRITE(5,124)
 124    FORMAT(1H0,5X,'INVERTED TRAJECTORY')
        NINV=NINV+1
        XP(L)=R0
        YP(L)=0
        UPX(L)=UPINIT
        UPY(L)=0.
        GO TO 55
  70    RR=ABS(R1(K)-RM(K)/2.-RL)
        RA=RM(K)/2.
  72    UGO=UGMAX*(RA/R0)
        UG=UGO*(1-RR/RA)**(1./7.)
        UGX=UG*SIND(ZETA)
        UGY=UG*COSD(ZETA)
C
C       CALCULATE DRAG FORCE
C
        CALL REY(REP,L)
        CALL FORCE(REP)
C
C       PARTICLE TRAJECTORY
C
        XO=XP(L)
        YO=YP(L)
        TIMEP=TIME/3600.
c        IF(TIMEP.LT.1.1) GO TO 231
C        GO TO 233
C 231    I1=L/10
C        I2=I1*10-L
C        IF(ABS(I2).GE.0.5) GO TO 233
C        WRITE(51,*) XO,YO
C        NDAT=NDAT+1
         XP(L)=XP(L)+UPX(L)*ET+FX*ET**2/2./PMASS
         ACC=FY/PMASS-G*(RP-RG)/RP
         YP(L)=YP(L)+UPY(L)*ET+ACC*ET**2/2.
         UPX(L)=UPX(L)+FX*ET/PMASS
         UPY(L)=UPY(L)+ACC*ET
         IF(XP(L).GE.R) GO TO 17
C
C        ************************************************************************
C
C        CHECK FOR COLLISIONS
C
C        ************************************************************************
C
```

```
C         RADIAL COORDINATE OF PARTICLE
C
          H=SQRT(YP(L)**2+(R-XP(L))**2)
C
C         POLAR COORDINATE OF PARTICLE
C
          ZETAP=ATAND(YP(L)/(R-XP(L)))
          K1=ZETAP+1
C
C         ********************************************************************
C
C         COLLISION WITH OUTER WALL B1
C
C         ********************************************************************
C
          IF(H.LE.B1(K1)) GO TO 80
C
C         INCREASE COUNTER NC1
C
          NC1=NC1+1
C
C         ANGLE OF PARTICLE TRAJECTORY
C
          U1=UPX(L)
          U2=UPY(L)
          CALL ANGLE1
          FUP0=FUP
C
C         ANGLE BETWEEN THE WALL AND X-AXIS
C
          BETA=ATAND(SL1(K1))
          IF(BETA.GE.0) GO TO 778
          BETA=BETA+180
C
C         IMPACT ANGLE FOR COLLISION NC1
C
  778     ALF1(NC1)=FUP0-ZETA
          IF(ALF1(NC1).LE.90) GO TO 77
          ALF1(NC1)=180-ALF1(NC1)
   77     IF(ALF1(NC1).GT.0) GO TO 777
          ALF1(NC1)=ALF1(NC1)+180
C
C         SAVE POLAR ANGLE FOR COLLISION POINT
C
  777     TET1(NC1)=ZETAP
C
C         ANGLE OF REFLECTION
C
          FUP=2*BETA-FUP
          IF(FUP.GE.0) GO TO 78
          FUP=FUP+360
C
C         PARTICLE VELOCITY AFTER COLLISION
C
   78     UP=SQRT(UPX(L)**2+UPY(L)**2)
          UPC(L)=UP*DAF
          UPC1(NC1)=UP
          UPX(L)=UPC(L)*COSD(FUP)
          UPY(L)=UPC(L)*SIND(FUP)
          XP(L)=X0
```

```
      YP(L)=Y0
      GO TO 55
C
C     ********************************************************************
C
C     COLLISION WITH INNER WALL
C
C     ********************************************************************
C
 80   IF(H.GE.B2(K1)) GO TO 55
C
C     INCREASE COLLISION COUNTER NC2
C
      NC2=NC2+1
C
C     ANGLE OF PARTICLE TRAJECTORY
C
      U1=UPX(L)
      U2=UPY(L)
      CALL ANGLE1
      FUP0=FUP
C
C     ANGLE BETWEEN INNER WALL AND X-AXIS
C
      BETA= ATAND(SL2(K1))
      IF(BETA.GE.0) GO TO 889
      BETA=BETA+180
C
C     IMPACT ANGLE FOR COLLISION NC2
C
 889  IF(FUP0.GE.180) GO TO 891
      ALF2(NC2)=BETA-FUP0
      FUP=BETA+2*ALF2(NC2)
      IF(ALF2(NC2).GE.0) GO TO 888
      ALF2(NC2)=ALF2(NC2)+180
      GO TO 888
 891  ALF2(NC2)=360-FUP+BETA
      FUP=360-FUP-2*BETA
      IF(ALF2(NC2).GE.0) GO TO 888
      ALF2(NC2)=ALF2(NC2)+180
C
C     SAVE COLLISION POINT WITH INNER WALL
C
 888  TET2(NC2)=ZETAF
C
C     ANGLE OF REFLECTION
C
C
      FUP=FUP
C
C     PARTICLE VELOCITIES AFTER COLLISION NC2
C
      UP=SQRT(UPX(L)**2+UPY(L)**2)
      UPC(L)=UP*DAF
      UPC2(NC2)=UP
      UPX(L)=UPC(L)*COSD(FUP)
      UPY(L)=UPC(L)*SIND(FUP)
      XP(L)=X0
      YP(L)=Y0
      GO TO 55
```

```
  55    CONTINUE
        NDAT=NDAT+1
        GO TO 16
C
C       ************************************************************************.
C       ************************************************************************
C       ************************************************************************
C
C       WALL EROSION
C
C       ************************************************************************
C
  17    DO 300 K=1,90
        DS1(K)=0.
        DS2(K)=0.
 300    CONTINUE
        ND2=ND+1
        WRITE(ND2,3001) TIMEW,NC1,NC2
 3001   FORMAT(1H ,3X,F8.2,2(3X,I5))
        TYPE *,NC1,NC2
        IF(NC1.EQ.0) GO TO 330
        DO 310 L=1,NC1
        LA=TET1(L)
        E=EO*(SIND(ALF1(L))**2)*UPC1(L)**XN
        DS1(LA)=E+DS1(LA)
 310    CONTINUE
 330    IF(NC2.EQ.0) GO TO 360
        WRITE(5,308) TIMEW
 308    FORMAT(1H0,3X,'COLLISION TYPE 2 AT',2X,F7.2,2X,'HRS')
        DO 390 L=1,NC2
        LA=TET2(L)
C       E=....
        E=EO*(SIND(ALF2(L))**2)*UPC2(L)**XN
        DS2(LA)=E+DS2(LA)
 390    CONTINUE
 360    TIMEC=ETE/TAUR
        TYPE *,TIMEC,ETE,TAUR
        DO 391 J=1,90
        D1T=TIMEC*DS1(J)
        D2T=TIMEC*DS2(J)
        SXI1(J)=SXI1(J)+D1T/100.
        SXI2(J)=SXI2(J)+D1T/100.
 391    CONTINUE
        TIMEP=TIME/3600.
        WRITE(ND,2012) TIMEP
 2012   FORMAT(1H0,5X,'TIME',2X,F7.2,'HRS')
C
C       CONVOLUTION WINDOW
C
        SXI1D(1)=(SXI1(1)+SXI1(2)+SXI1(3))/5.
        SXI1D(2)=(SXI1(1)+SXI1(2)+SXI1(3)+SXI1(4))/5.
        SXI2D(1)=(SXI2(1)+SXI2(2)+SXI2(3))/5.
        SXI2D(2)=(SXI2(1)+SXI2(2)+SXI2(3)+SXI2(4))/5.
        DO 2033 I=3,88
        SXI1D(I)=(SXI1(I-2)+SXI1(I-1)+SXI1(I)+SXI1(I+1)+SXI1(I+2))/5.
        SXI2D(I)=(SXI2(I-2)+SXI2(I-1)+SXI2(I)+SXI2(I+1)+SXI2(I+2))/5.
 2033   CONTINUE
        SXI1D(89)=(SXI1(87)+SXI1(88)+SXI1(89)+SXI1(90))/5.
        SXI1D(90)=(SXI1(88)+SXI1(89)+SXI1(90))/5.
        SXI2D(89)=(SXI2(87)+SXI2(88)+SXI2(89)+SXI2(90))/5.
```

```
      SXI2D(90)=(SXI2(88)-SXI2(89)-SXI2(90))/5.
      DO 2010 K=1,90
      SXI1(K)=SXI1D(K)
      SXI2(K)=SXI2D(K)
      B1(K)=SXI1(K)+R
      B2(K)=(R-2*R0)-SXI2(K)
 2010 CONTINUE
      IF(TIMEP.LT.240.) GO TO 1160
      DO 2020 K=1,90
      AJ=K-1
      RAN=AJ
      CAJ=COSD(AJ)
      SAJ=SIND(AJ)
      XC1=(R-B1(K)*CAJ)/R
      ED3=R-B1(K)
      YC1=(B1(K)*SAJ)/R
      XC2=(R-B2(K)*CAJ)/R
      YC2=(B2(K)*SAJ)/R
      WRITE(61,*) XC1,YC1
 2020 CONTINUE
C2011  FORMAT(1H ,I4,6(2X,F8.6))
 1160 IF(TIME.GE.ENDTIM) GO TO 2001
C      IF(TIME.GE.ENDTIM) GO TO 2001
      GO TO 15
 2001 TYPE *,NDAT,NDAT,NDAT
      END

      SUBROUTINE REY(REP,L)
      DIMENSION UPX(1000),UPY(1000)
      COMMON/VEL/UGX,UGY,UPX,UPY
      COMMON/PRP/RG,VG
      COMMON/GEO/DP
      COMMON/ANG/FIYX
      COMMON/VE1/US
      USX=UGX-UPX(L)
      USY=UGY-UPY(L)
      US=SQRT(USX**2+USY**2)
      IF(ABS(USX).LE.1.E-6) GO TO 10
      FIYX=ATAND(USY/USX)
      IF(USX.LT.0.AND.USY.LE.0) GO TO 11
      IF(USX.LT.0.AND.USY.GT.0) GO TO 11
      GO TO 20
   11 FIYX=FIYX+180
      GO TO 20
   10 FIYX=90.
   20 REP=DP*US*RG/VG
      RETURN
      END

      SUBROUTINE FORCE(REP)
      COMMON/GE1/AP
      COMMON/VE1/US
      COMMON/FOR/FX,FY
      COMMON/PRP/RG,VG
      COMMON/ANG/FIYX
      IF(REP.GE.0.3) GO TO 10
      IF(REP.GE.1000) GO TO 20
      IF(ABS(REP).GE.1.E-5) GO TO 5
      FD=0.
      GO TO 35
```

```
    5     CD=24/REP
          GO TO 30
   10     CD=18.5/REP**0.6
          GO TO 30
   20     CD=0.44
   30     FD=CD*AP*RG*US**2/2.
   35     FX=FD*COSD(FIYX)
          FY=FD*SIND(FIYX)
          RETURN
          END

          SUBROUTINE ANGLE1
C
          COMMON/PASS/X,Y,ZETA
          IF(ABS(X).GT.1.E-6) GO TO 10
          IF(Y.LT.0) GO TO 5
          ZETA=90.
          GO TO 50
    5     ZETA=270
          GO TO 50
   10     ZETA0=ATAND(Y/X)
          ZETA=ZETA0
          IF(X.GT.0) GO TO 20
          ZETA=ZETA0+180
          GO TO 50
   20     IF(Y.GT.0) GO TO 50
          ZETA=ZETA0+360
   50     RETURN
          END
```

BIBLIOGRAPHY

1. Dial, R.E., *Refractories for Coal Gasification and Liquefaction*, Am.Cer.Soc.Bull.,Vol. 54, 1975, pp. 640-643.
2. Proceedings Corrosion/Erosion of Coal Conversion Systems Materials Conference, NACE, Berkeley, California, 1979, Industrial Experience and Design Requirements with respect to Erosion and Corrosion in Coal Conversion Systems, by J. Stringer
3. Proceedings Corrosion/Erosion of Coal Conversion Systems Materials Conference, NACE, Berkeley, California, 1979, Introductory Remarks on Erosion, by A. Ruff
4. Proc. Conversion 1984, NACE, New Orleans, LA, 1984, Erosion/Wear Monitor Development, by C. Youngdahl
5. Yang, W.C. et al., *A High Temperature Pneumatic Transport Line Test Facility*, I&EC Process Design and Development,Vol. 18, 1979, pp. 695-703.
6. C. Preece, Treatise on Materials Science and Technology, volume 16, Erosion, Academic Press, New York, 1979, Impact Damage Mechanics, by A.G. Evans
7. Finnie, I. et al., *Erosion of Metals by Solid Particles*, Journal of Materials,Vol. 2, 1967, pp. 682-700.
8. Tilly, G.P., *Erosion Caused by Airborne Particles*, Wear,Vol. 14, 1969, pp. 63-80.
9. C. Preece, Treatise on Materials Science and Technology, volume 16, Erosion, Academic Press, New York, 1979, Erosion by Solid Particle Impact, by A.W. Ruff and S.M. Wiederhorn
10. Tilly, G.P., *A Two-stage mechanism for ductile erosion*, Wear,Vol. 23, 1973, pp. 87-96.

11. Evans. A.G. et al., *Impact Damage in Brittle Materials in the Elastic/Plastic Response Regime*, Proc. R. Soc. of London,Vol. 361, 1978, pp. 343-65.

12. Marshal, D.B. et al., *Elastic/Plastic Indentation Damage in Ceramics: The Lateral Crack System*, Journal Am. Cer. Soc.,Vol. 11, 1982, pp. 561-6.

13. Wiederhorn, S.M. and B.R. Lawn, *Strength Degradation in Glass Impacted with Sharp Particles: Annealed Surfaces*, Jour. Am. Cer. Soc.,Vol. 62, 1979, pp. 66-71.

14. Wiederhorn, S.M. and D.E. Roberts, *A Technique to Investigate High Temperature Erosion of Refractories*, Ceramic Bulletin,Vol. 55, 1976, pp. 185-9.

15. Hutchings, I.M., _, Proc.ASTM Symp. Eros. Prevent. Useful Appl, STP 664

16. Yust, C.S. and R.S. Crouse, *Melting at Particle Impact Sites During Erosion of Ceramics*, Wear,Vol. 51, 1978, pp. 193-196.

17. Finnie, I., *Erosion of Surfaces by Solid Particles*, Wear,Vol. 3, 1960, pp. 87.

18. Arundel, P.A. et al., *The Rapid Erosion of Various Pipe-Wall Materials by a Stream of Abrasive Alumina Particles*, Pneumotransport 2,Vol. E, 1973, pp. E1-1,15.

19. Morrison, C.T. and J.L.Roubert, *Solid Particle Erosion of Mullite*, Wear,Vol. 105, 1985, pp. 19-27.

20. Mills, D., Mason, J.S., *Particle Concentration Effects in Bend Erosion*, Powder Technology,Vol. 17, 1977, pp. 37-53.

21. ACI, Refractory concrete, American Concrete Institute, Detroit, 1978, Properties of Refractory Concrete, by W. Bakker

22. Briebach, A.V., *A Review of Refractory Hydraulic Cements*, J. British Cer. Soc.,Vol. 71, 1972, pp. 153-158.

23. Giva. G.V. et al., *Curing and Firing of High Purity Calcium Aluminate Bonded Tabular Alumina Castables*, Am. Cer. Soc. Bull.,Vol. 54, 1975, pp. 710-13.

24. Wygant, J.F. and M.S. Crowley, *Curing Refractory Castables*, Amer. Cer. Soc. Bull.,Vol. 43, 1964, pp. 1-5.

25. Bakker, W.T. and B.E. Dunworth, Strength of Calcium Aluminate Bonded Castables at Intermediate Temperatures, Paper 2-R-74F, ACS, Refractory Division Meeting, Bedford Springs, 1974

26. R. Fisher, Advances in Ceramics, vol 13, American Ceramic Society, Columbus, Ohio, 1985, High Performance Castables for Severe Applications, by C. Richmond

27. McCullough, J.M. and G.R. Rigby, *Mechanical Properties of Refractory Castables*, J. British Cer. Soc,Vol. 71, 1972, pp. 233.

28. Crowley, M.S., *Refractory Problems in Coal Gasification Units*, Am. Cer. Soc. Bull.,Vol. 54, 1975, pp. 1072-4.

29. Crowley, M.S., *Influence of Particle Size on Erosion Resistance of Refractory Concretes*, Ceramic Bulletin,Vol. 48, 1969, pp. 707-10.

30. Bitter, J.G.A., *A Study of Erosion Phenomena*, Wear,Vol. 6, 1963, pp. 5-21.

31. Vojnovich, T. et al., Design of Refractories for Coal Gasification and Combustion Systems, Final Report, EPRI RP625-1, 1978

32. Wiederhorn, S.M. et al., *Effect of Hydrothermal Environments on the Erosion of Castable Refractories*, Trans. ASME: Jour. Mat. and Technol.,Vol. 99, 1977, pp. 143-46.

33. Raask, E., Erosion wear in Coal Utilization, Hemisphere Publishing Corporation, Washinghton, 1988.

34. Mohlmann, J.D., Parameters Influencing the Pneumatic Conveying of Large Rock Particles, PhD dissertation, University of Witwatersrand, Johannesburg, 1985 .

35. Michelides E., *A model for the flow of Solid Particles in gases*, Int. J. of Multiphase Flow,Vol. 10, 1984, pp. 61-77.

36. Verba, R. and R.D. Salman, Particle Trajectory in a Horizontal Pipe and a Bend, II Koloquium der Staubtechnikabsteilung, I-20 Karpacz von 14 bis 29 Oktober 1978, Polen

37. Matsumoto, S. et al., , J. Chem. Eng. of Japan,Vol. 3, 1970, pp. 83.

38. Scott, A., _, PNEUMOTRANSPORT 4, paper A3 BHRA, 1978

39. Ottjes, J.A., *A Measuring System for Particle Impact Velocities and Application in a Pneumatic Transport Line*, Chem. Eng. Sci.,Vol. 36, 1981, pp. 1337-1347.

40. Brauer, H., *Report on Investigations on Particle Movement in Straight Horizontal Tubes*, J. of Powder & Bulk Solids Technol.,Vol. 4, 1980, pp. 3-12.

41. Vaux, W.G. et al., Design of Refractories for Resistance to High Temperature Erosion, EPRI AP1955, Final Report, 1981, Palo Alto, CA

42. Mandelbrot, B.B., The Fractal Geometry of Nature, W.H. Freeman and Co, New York, 1977.

43. Bayles, G., New Pore Characterization Techniques for Flow Dynamics in Porous Media, PhD dissertation, University of Pittsburgh, 1988.

44. Sreenivasan, K. and C. Meneveau, *The Fractal Facets of Turbulence*, J.Fluid Mechanics,Vol. 1986, 1986, pp. 357-386.

45. Zaltash, A., Stability Analysis of Gas-Solid Transport with Electrostatics, Master's thesis, University of Pittsburgh, 1985.

46. Drew, T.B., R.C. Koo and W.H. McAdams, , Trans. AIChE,Vol. 28, 1932.

47. Haaland, S.E., *Simple and Explicit Formulas for the Friction Factor in Turbulent Pipe Flow*, J. of Fluids Engineering,Vol. 105, 1983, pp. 89-90.

48. Yang, W.C., *A Correlation for Solid Friction Factor in Vertical Pneumatic Conveying Lines*, AIChE Journal,Vol. 24, (1978, pp. 548-51.

49. Konno. H and S. Saito, *Pneumatic Conveying of Solids through Straight Pipes*, Chem. Eng. Japan,Vol. 21, 1969, pp. 211-17.

50. Myler, C., Gas-Solid Transport in a 0.0508 m Pipe at Various Inclinations with and without Electrostatics, Master's thesis, University of Pittsburgh, 1985.

51. Danziger, W.J., *Heat Transfer to Fluidized Gas-Solis Mixtures in Vertical Transport*, I & EC Process Design and Development,Vol. 2, 1963, pp. 269-273.

52. Soo,S.L., Fluid Dynamics of Multiphase Systems, Blaisdell Publishing Co. Waltham, Massachusetts, 1967.

53. Arastoopour, H. and C.Y. Chen, *Attrition of Char Agglomerates*, Powder technology,Vol. 36, 1983, pp. 99-106.

54. Mason, J.S., Smith, B.V., *The Erosion of Bends by Pneumatically Conveyed Suspensions of Abrasive Particles*, Powder Technology,Vol. 6, 1972, pp. 323-335.

55. Agarwal, V.K., Mills, D., Mason, J.S., *Some Aspects of Bend Erosion in Pneumatic Conveying Systems Pipelines*, Bulk Solids Handling,Vol. 5, 1985, pp. 111-116.

56. Mason, J.S. and B.U. Smith, Pressure Drop and Flow Behavior for the Pneumatic Transport of Fine Particles around 90 degrees bends. PNEUMOTRANSPORT 2, 1973

57. Hawthorne, W.H., *Secondary Circulation in Fluid Flow*, Proc. Roy. Soc.,Vol. A206, 1951, pp. 374-387.

58. Solt, P., Bends in Pneumatic Conveying Systems, Fuller Company Research Department, Internal Report

59. Hilbert, J.D., *Alternatives in Pneumatic Conveying Pipeline Bends*, Bulk Solids Handling,Vol. 4, 1984, pp. 107-110.

60. Tsuji, Y. and Y. Morikawa, Computer Simulation for the Pneumatic Transport in Pipes with bends, Pneumotransport 4, 1978, paper B1

61. Soo, S.L. et al., *Concentration and Mass Flow Distributions in a Gas-solids Suspension*, I&EC Fundamentals,Vol. 3, 1964, pp. 98-105.

62. Tabakoff, W., *Review - Turbomachinery Performance Determination Exposed to Solid Particulates Environment*, Journal of Fluids Engineering,Vol. 106, 1984, pp. 125-134.

63. Shames, I., Engineering Mechanics. Vol II. Dynamics, Prentice-Hall, New Jersey, 1966.

64. Tsuji, Y. et al., *Numerical simulation of Pneumatic conveying in a horizontal pipe*, KONA,Vol. 3, 1985, pp. 38-51.

65. Tsuji, Y. et al., *Numerical Simulation of Gas Solid Two-Phase Flow in a Two Dimensional Horizontal Channel*, Int. J. of Multiphase Flow,Vol. 13, 1987, pp. 671-684.

66. Tabakoff, W. et al., *Erosion Study of Different Materials Affected by Coal Ash Particles*, Wear,Vol. 52, 1979, pp. 161-173.

67. Park, Y., Zenz, F., Pressure Loss in Horizontal to Vertical Upflow Elbows, PNEUMOTRANSPORT 5